

IRIA

State of the Art Reports

Military Utility of Multispectral and Hyperspectral Sensors



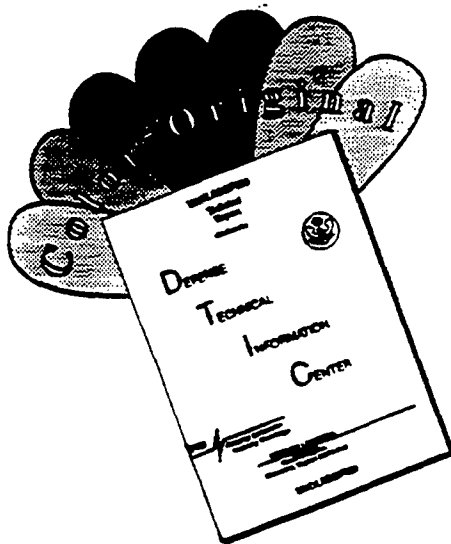
19970605 110

Faint, illegible text.

Infrared Information Analysis Center
Environmental Research Institute of Michigan
P.O. Box 134001
Ann Arbor, MI 48113-4001

1. Report No. 246890-3-F	2. Government Accession No.	3. Recipient's Catalog No.	
4. Title and Subtitle Military Utility of Multispectral and Hyperspectral Sensors		5. Report Date November 1994	
		6. Performing Organization Code ERIM	
7. Author(s) R. Anderson, W. Malila, R. Maxwell, and L. Reed		8. Performing Organization Report No.	
9. Performing Organization Name and Address Infrared Information Analysis Center Environmental Research Institute of Michigan PO Box 134001 Ann Arbor, Michigan 48113-4001		10. Work Unit No.	
		11. Contract or Grant No.	
12. Sponsoring Agency Name and Address Defense Technical Information Center Cameron Station Alexandria, Virginia 22304-6145		13. Type of Report and Period Covered	
		14. Sponsoring Agency Code DTIC	
15. Supplementary Notes DTIC is under Defense Logistic Agency <i>For Announcement ONLY, No distribution by DTIC</i>			
16. Abstract This State-of-the-Art Report (SOAR) reviews the science and technology related to detection and discrimination of militarily useful objects through the use of multiple regions of the optical and infrared electromagnetic spectrum. The report examines the phenomenological basis of many spectral features found in the reflected and emitted radiation from typical materials. Elements of sensor design important in multispectral detection are also reviewed, as a sensor components critical to multispectral operation. A key challenge in multispectral detection is the necessity of extracting the requisite information from a massive amount of data in a reasonably short time. An overview of the advanced signal processing algorithms required to perform the detection and discrimination tasks is furnished. A number of multispectral sensors are currently in use, in space-based and airborne environments. The characteristics of these sensors are summarized. Potential applications of multispectral sensing in both military and civilian contexts are also covered.			
17. Key Words		18. Distribution Statement Unlimited	
19. Security Classif. (of this report) Unclassified	20. Security Classif. (of this page) Unclassified	21. No. of Pages	22. Price

DISCLAIMER NOTICE



THIS DOCUMENT IS BEST QUALITY AVAILABLE. THE COPY FURNISHED TO DTIC CONTAINED A SIGNIFICANT NUMBER OF COLOR PAGES WHICH DO NOT REPRODUCE LEGIBLY ON BLACK AND WHITE MICROFICHE.

IRIA State of the Art Reports

***Military Utility
of Multispectral and Hyperspectral
Sensors***

R. Anderson, W. Malila, R. Maxwell, and L. Reed

Infrared Information Analysis Center

Environmental Research Institute of Michigan
Ann Arbor, Michigan

NOVEMBER 1994

DISTRIBUTION STATEMENT A
Approved for public release
Distribution Unlimited

The IRIA Center is Administratively Managed by the
Defense Technical Information Center
Cameron Station
Alexandria, VA 22304-6145
under Defense Logistics Agency
Contract No. DLA900-88-D-0392/0042
ERIM Report No. 246890-3-F

DTIC QUALITY INSPECTED 4

CONTENTS

1.0 OVERVIEW	1-1
2.0 BACKGROUND	2-1
2.1 DEFINITION OF TERMS	2-1
2.2 SOLAR REFLECTION AND THERMAL EMISSION	2-2
2.3 REFLECTANCE, EMITTANCE, AND ABSORPTION	2-3
2.4 DIRECTIONAL REFLECTANCE, BIDIRECTIONAL REFLECTANCE, AND DIRECTIONAL EMITTANCE: DEFINITIONS	2-4
2.5 DIRECTIONAL REFLECTANCE, DIRECTIONAL EMITTANCE, AND BIDIRECTIONAL REFLECTANCE: MEASUREMENTS	2-6
3.0 PHENOMENOLOGY	3-1
3.1 PHYSICAL ORIGINS OF SPECTRAL PROPERTIES	3-1
3.1.1 Electronic, Vibrational, and Rotational Transitions	3-1
3.1.2 Characteristic Bandwidths of Spectral Phenomena	3-2
3.1.3 Resonance Phenomena	3-2
3.2 ATMOSPHERIC SPECTRAL PROPERTIES	3-4
3.3 SURFACE AND VOLUME CONTRIBUTIONS TO REFLECTANCE	3-6
3.4 OPTICAL PROPERTIES OF MATERIALS	3-7
3.4.1 Reflectance and Emittance	3-8
3.4.2 Thermal Properties	3-8
3.4.3 Radiance Measurements	3-8
3.4.4 Imagery	3-9
4.0 MULTISPECTRAL AND HYPERSPECTRAL SENSING	4-1
4.1 DETECTOR AND DETECTOR ARRAYS	4-1
4.2 SPECTRAL RADIOMETRIC MEASUREMENTS	4-2
4.3 MULTISPECTRAL SCANNERS	4-2
4.4 IMAGING SPECTROMETERS	4-3
4.5 CURRENT AND PLANNED AIRBORNE SENSORS	4-6
4.5.1 Airborne Multispectral Imaging Scanners	4-7
4.5.2 Airborne Hyperspectral Sensors	4-9
4.5.3 System Profiles	4-9
4.6 CURRENT AND PLANNED SPACEBORNE SENSORS	4-15
4.6.1 Merits of Satellite Multispectral Sensing	4-15
4.6.2 Classes of Multispectral Satellite Sensors	4-16
4.6.3 History of Satellite Multispectral Sensing	4-16
4.6.4 High-Resolution Multispectral Imagers	4-16
4.6.5 Wide-Field-of-Coverage Multispectral Systems	4-23
4.7 BIBLIOGRAPHY	4-25

CONTENTS (Continued)

5.0 MODELING AND SIMULATION	5-1
5.1 TARGET AND BACKGROUND MODELING	5-1
5.1.1 SIRIM, PRISM, GTSIG, and SPIRITS	5-3
5.1.2 TARSIS and SSTIRS	5-3
5.1.3 SPF and SIRRM-AB	5-4
5.1.4 CREEP, ERIM, and Aerodyne Models	5-4
5.1.5 Suits Vegetation Canopy Model	5-5
5.1.6 GENESIS	5-5
5.1.7 CLDSIM	5-6
5.2 ENVIRONMENT MODELING	5-6
5.2.1 LOWTRAN, MODTRAN, FASCODE, and APART	5-6
5.2.2 EOSAEL	5-7
5.3 STRATEGIC SCENE GENERATOR MODEL	5-7
5.4 MULTISPECTRAL AND HYPERSPECTRAL BAND SELECTION AND PERFORMANCE ANALYSIS	5-9
5.4.1 Optimum Band Specification	5-9
5.4.2 Spatial Resolution Requirements Specification	5-10
5.4.3 Radiometric Sensitivity Analysis	5-10
5.5 FLAT PLATE MODELING	5-10
5.6 BIBLIOGRAPHY	5-15
6.0 SPECTRAL ALGORITHMS	6-1
6.1 SINGLE SPECTRAL-BAND PROCESSING	6-1
6.2 LOG LIKELIHOOD RATIO DETECTOR	6-4
6.3 TWO BAND LOG LIKELIHOOD RATIO DETECTOR	6-6
6.4 MULTISPECTRAL CHANGE DETECTION	6-11
6.4.1 General Discussion	6-11
6.4.2 Example Change Detection Procedures	6-13
6.5 PREPROCESSING OR SIGNAL CONDITIONING TECHNIQUES	6-14
6.5.1 Corrections for Sensor Radiometric Effects	6-14
6.5.2 Corrections for Scene Observation Conditions and Atmospheric Haze Effects	6-16
6.5.3 Corrections for Sensor Geometric Effects	6-18
6.5.4 Data Screening and Masking Procedures	6-19
6.6 TERRAIN CATEGORIZATION	6-19
6.6.1 Supervised Techniques	6-19
6.6.2 Unsupervised Techniques	6-20
6.6.3 Target Detection	6-21
6.7 SUBPIXEL SPECTRAL MIXTURE ESTIMATION	6-21
6.7.1 Background	6-22
6.7.2 Discussion of Approaches	6-23

CONTENTS (Continued)

6.8	UNIQUE ASPECTS OF SPECTRAL PROCESSING IN THE THERMAL INFRARED	6-27
6.8.1	Emissivity Mapping	6-28
6.8.2	Spectrally Correlated Background Clutter Suppression	6-28
6.9	BIBLIOGRAPHY	6-29
7.0	POTENTIAL DEFENSE APPLICATIONS OF MULTISPECTRAL AND HYPERSPECTRAL TECHNIQUES	7-1
7.1	CLASSES OF APPLICATIONS	7-1
7.1.1	Strategic	7-1
7.1.2	Tactical	7-1
7.2	DEFENSE APPLICATIONS AND ASSOCIATED SENSOR REQUIREMENTS	7-1
7.3	IMPLEMENTATION CONSIDERATIONS	7-3
7.3.1	Existing Software/Hardware Systems and Facilities	7-3
7.3.2	Tactical-Unit Availability	7-5
7.4	BIBLIOGRAPHY	7-7
8.0	EXAMPLE DATA PRODUCTS FOR DEFENSE APPLICATIONS OF SPECTRAL PHENOMENA	8-1
8.1	TARGET DETECTION IN THE VISIBLE AND REFLECTIVE IR	8-1
8.2	MATERIALS CLASSIFICATION IN THE LWIR	8-5
8.3	EMISSIVITY MAPPING IN THE LWIR	8-5
8.4	SPECTRALLY CORRELATED BACKGROUND CLUTTER SUPPRESSION IN THE MWIR AND LWIR	8-10
8.5	HYPERSPECTRAL IMAGING IN THE MWIR	8-10
8.6	HYPERSPECTRAL DETECTION OF ETHYL ETHER VAPOR IN THE LWIR	8-14
8.7	PRODUCTS FROM COMMERCIALY AVAILABLE SATELLITE DATA	8-22
8.7.1	Types of Color Composite Images	8-23
8.7.2	Image Mapping	8-23
8.7.3	Feature Extraction	8-23
8.7.4	Visualization and Image Fusion	8-35
APPENDIX A: MATERIALS PHENOMENOLOGY		A-1
APPENDIX B: AIRBORNE HYPERSPECTRAL SENSOR SYSTEMS		B-1

FIGURES

2-1.	Directional Reflectance Healthy Green and Mature Brown Corn Leaves	2-7
2-2.	Directional Hemispherical Reflectance Spectra of Representative Samples of Vegetation Cover	2-9
2-3.	Directional Hemispherical Reflectance Spectra of Representative Samples of Vegetation Cover	2-10
2-4.	Near Zero Bistatic Bidirectional Reflectance at 0.63 μm	2-11
2-5.	Near Zero Bistatic Bidirectional Reflectance at 10.6 μm	2-12
3-1.	Transmittance and Reflectance of 0.002 cm of Sea Water	3-3
3-2.	The Complex Index of Refraction: (a) type alpha crystalline silicon dioxide (SiO_2) and (b) amorphous silicon dioxide (SiO_2) (Glass)	3-3
3-3.	The Atmospheric Absorption Spectral of Several Molecular Species	3-5
4-1.	M-7 Mapper Optical-Mechanical Layout	4-4
4-2.	Band Comparison of Multispectral Data Collection Systems	4-5
4-3.	Summary of Sensor Sampling Characteristics	4-17
4-4.	Observation Characteristics of Multispectral Satellite Imagers	4-18
4-5.	Future Improvements to Observation Characteristics of Multispectral Satellite Imagers	4-20
4-6.	Observation Characteristics of Present and Planned Wide-Field Multispectral Satellite Sensors	4-24
5-1.	Target/Background Hemispherical Spectral Reflectances. (a) In the MWIR (8 cm^{-1} Spectral Resolution) and (b) in the LWIR (8 cm^{-1} Spectral Resolution)	5-12
5-2.	Actual and Modeled Target and Conifer Background Signatures. (a) In the MWIR and (b) in the LWIR	5-13
5-3.	Actual and Modeled Target and Grass Background Signatures. (a) In the MWIR and (b) in the LWIR	5-14
6-1.	Probability of Detection vs. Peak Signal to RMS Noise Ratio	6-3
6-2.	Single Band and Two Band Mean and Variance	6-8
6-3.	Single Band and Two Band Mean and Variance Differences for Target/Background Discrimination	6-10
6-4.	Optimal Multispectral Processor Gain vs. Target/Background Color	6-12
8-1.	Multispectral Discrimination of Construction Materials	8-2
8-2.	Multispectral Detection of Vehicular Targets	8-3
8-3.	Illustration of LWIR Spectral Diversity	8-6
8-4.	Use of LWIR Spectral Emissivity Differences to Discriminate Among Construction Materials	8-7
8-5.	TIMS Imagery of Adelaide Scene	8-8
8-6.	TIMS Imagery of Adelaide Scene	8-9
8-7.	Low Contrast Target Detection With Spectral Correlation Sensor	8-11
8-8.	AT&SF Railroad at Kingman AZ	8-15
8-9.	Off-Nadir Images of Solar Reflections From High-Altitude (~12,000 ft) Lakes at 2.2 μm	8-16
8-10.	Graphic Depiction of a Multispectral Image	8-17
8-11.	Simultaneous Multispectral Images of Oahu	8-18

FIGURES (Continued)

8-12.	An Example of Wide-Band Differencing	8-19
8-13.	A Second Example of Wide-Band Differencing	8-20
8-14.	A Second Example of Narrow-Band Differencing	8-21
8-15.	Image Map Produced From Landsat TM Data	8-24
8-16.	Landsat-Based Terrain Categorization, Camp Grayling, MI	8-25
8-17.	Examples of TM-Based Categorization of Ice Types (Saginaw Bay of Lake Huron, near Tawas City, MI)	8-27
8-18.	Water Temperature Map Derived From Landsat TM Data	8-28
8-19.	Landsat TM Change Image Near Kazan, Russia, 31 May 85 to 2 May 86	8-29
8-20.	TM-Based Change Detection of Storage Areas in Iraq	8-31
8-21.	Change Detection Mapping of Flooded Area (St. Louis, MO)	8-32
8-22.	Landsat-Based Bathymetric Image (North Cat Cay, Bahamas, 30 June 86, Mercator Projection)	8-33
8-23.	Contoured Version of Landsat-Based Depth Image (North Cat Cay, Bahamas, 30 Jan 86)	8-34
8-24.	LOC Extraction From Landsat TM Data	8-36
8-25.	Comparison Between SPOT-Derived Terrain Elevation Data and USGS DEM Data	8-37
8-26.	Multisensor Perspective View, Using Data From SPOT, Landsat TM, and AVHRR Sensors (Lake Mead, NV)	8-39
8-27.	Mobility and Routing Analysis Using Multispectral Inputs	8-40

TABLES

4-1. Observation Characteristics of Airborne Multispectral Imaging Sensors	4-8
4-2. Observation Characteristics of Airborne Hyperspectral Imaging Sensors	4-10
5-1. Summary of Vehicle Model Features	5-2
5-2. Phenomenology Models and Databases for SSGM Baseline R5.0	5-8
7-1. Illustrative Defense Applications of Multispectral Sensors (To the Task Level)	7-2
7-2. Representative Commercial Image Processing Software Products	7-6
8-1. Airborne Instrument Program (AIP) Sensor Characteristics	8-13
8-2. Band Combinations For Common Color Composite Images	8-23

ACRONYMS

AAHIS-1	Advanced Airborne Hyperspectral Imaging System-1
ADRI	Arc Digital Raster
AF	Air Force
AFB	Air Force Base
AFMSS	Air Force Mission Support System
AHS	Airborne Hyperspectral Scanner
AIP	Airborne Instrument Program
AIS	Airborne Imaging Spectrometer
ALRSS	Advanced Land Remote Sensing System
AMSS	Airborne Multispectral Sensor System
APART	Atmospheric Propagation and Radiative Transfer
ARC	Ames Research Center
ARPA	Advanced Research Projects Agency
ASAS	Advanced Solid-State Array Spectroradiometer
ASTER	Advanced Spaceborne Thermal Emission and Reflection Radiometer
ATM	Airborne Thematic Mapper
AVHRR	Advanced Very High Resolution Radiometer
AVIRIS	Airborne Visible-Infrared Imaging Spectrometer
BRDF	Bidirectional Reflectance Distribution Function
BRL	Ballistic Research Laboratories
CAMS	Calibrated Airborne Multispectral Scanner
CASI	Compact Airborne Spectrographic Imager
CBW	Chemical and Biological Warfare
CHRISS	Compact High-Resolution Imaging Spectrograph System
CLDSIM	Cloud Simulation (program)
CREEP	Coatings Reflectance Engineering and Evaluation Program
CSG	Combinatorial Solid Geometry
CVA	Change Vector Analysis
DAIRS	Defense Intelligence Agency Advanced Imagery Reproduction System
DARPA	Defense Advanced Research Projects Agency (now ARPA)
DIA	Defense Intelligence Agency
DIRDL	DARPA Infrared Data Library
DLPO	Defense Landsat Program Office
DMA	Defense Mapping Agency
DoD	Department of Defense
DTED	Digital Terrain Elevation Data
EOS	Earth Observing System
EOSAEL	Electro-Optical Systems Atmospheric Effects Library
ERTS	Earth Resources Technology Satellite
ETM	Enhanced Thematic Mapper
FLIR	Forward-Looking Infrared
FTS	Fourier Transform Spectrometer

ACRONYMS (Continued)

GENESSIS	Generic Scene Simulation Software
GER	Geophysical Environmental Research
GIS	Geographic Information System
GPS	Global Positioning System
GSD	Ground Spatial Dimension
GSFC	Goddard Space Flight Center
GTSIG	Georgia Tech Signature Model
HICAMP	High Resolution Calibrated Airborne Measurements Program
HIPS	Hyperspectral Image Processing System
HIRIS	High Resolution Imaging Spectrometer
HRMSI	High Resolution Multispectral Imagery
HRV	High Resolution Visible
HYDICE	Hyperspectral Digital Imagery Collection Experiment
IFOV	Instantaneous Field of View
IPB	Intelligence Preparation of the Battlefield
IR	Infrared
IRAMMP	Infrared Analysis and Measurements and Modeling Program
IRIS	Infrared Intelligent Spectroradiometer
IRSS	Indian Remote Sensing Satellites
JERS-1	Japanese Earth Resources Satellite
JPL	Jet Propulsion Laboratory
LIMMIX	Limited Mixtures
LISS	Linear Self-Scanning
LMSC	Lockheed Missiles and Space Company
LOC	Line of Communication
LOWTRAN	Low-Resolution Atmospheric Transmittance Model (Air Force Geophysics Lab)
LWIR	Long-Wave Infrared
MAGISTIC	MATRIX Geographic Information System and Turnkey Imagery Capability
MATRIX	Multisensor Automatic Target Recognition With Interactive Exploitation
MEIS	Multidetector Electro-Optical Imaging Sensor
MIMES	Multispectral Imagery Materials Exploitation System
MISR	Multiangle Imaging Spectroradiometer
MIVIS	Multispectral Infrared and Visible Imaging Spectrometer
MODTRAN	Moderate-Resolution Version of LOWTRAN
MSI	Multispectral Imagery
MSS	Multispectral Scanner Subsystem
MSS	Multispectral Scanner
MSS-II	Mission Support System-II
MUSIC	Multispectral Infrared Camera
MWIR	Medium-Wave Infrared
NASA	National Aeronautics and Space Administration
NIR	Near Infrared
NIST	National Institute of Science and Technology

ACRONYMS (Continued)

NRL	Naval Research Laboratory
ONR	Office of Naval Research
PISCES	Production Image Screening and Change Editing System
PRA	Photon Research Associates
PRISM	Physically Realizable Infrared Signature Model
RBV	Return Beam Vidicon Camera
ROC	Receiver Operating Characteristic
ROSIS	Reflective Optics Systems Imaging Spectrometer
SAC	Strategic Air Command
SAIC	Science Applications International Corporation
SAM	Spectral Angle Metric
SCR	Signal-to-Clutter Ratio
SDI	Strategic Defense Initiative
SIPS	Spectral Image Processing System
SIRIM	Simulated Infrared Imaging Model
SIRRAM-AB	Standardized Infrared Radiation Model for Air Breathing Vehicles
SMIFTS	Spatially Modulated Imaging Fourier Transform Spectrometer
SNR	Signal-to-Noise Ratio
SPACECOM	Space Command
SPECTRA	Standardized Production Environment for the Classification of Terrain and Resource Analysis
SPF	Standard Plume Flowfield
SPIRITS	Spectral IR Imaging of Targets and Scenes Model
SPOT	Système Pour l'Observation de la Terre
SSGM	Strategic Scene Generator Model
SSTIRS	Spectral Sciences Target IR Signature (code)
SWIR	Short-Wave Infrared
TAMPS	Tactical Aircraft Mission Planning System
TARSIS	Target Signature Simulation
TIMS	Thermal Infrared Multispectral Sensor
TIR	Thermal Infrared
TM	Thematic Mapper
TMD	Theater Missile Defense
TMS	Thematic Mapper Simulator
TSAC	Target Signature Analysis Center
USAF	United States Air Force
USGS	U.S. Geological Survey
VIS	Visible Imaging Spectrometer
VNIR	Visible and Near Infrared
WIS	Wedge Imaging Spectrometer
WL	Wright Laboratory

1.0 OVERVIEW

The optical spectrum from 0.4 μm to 14 μm is a rich source of information about objects in the environment. This region is particularly useful because both optical properties of materials and incident illumination change drastically over its breadth. In the solar region (0.4 μm to 0.7 μm) the sun, of course, dominates, and only reflectance properties matter. At the other end of the region (10 μm to 12 μm), the solar component is negligible, and thermal self-emission becomes the principal source of radiation. By exploiting these characteristics, we may extract considerable information from the scene.

The utility of multispectral sensing comes at the cost of increased complexity. In order to use the wealth of information, one must construct sensors capable of detecting the required spectra, and develop data processing algorithms to extract the desired target features. Both these necessities stress the current state of the art in hardware and software development.

Although the associated phenomena are complex and the reduction to practice of hardware and software difficult, the potential payoff of multispectral sensing is too great to ignore. Indeed, visible and near-infrared sensing is a key component in all current earth observation satellites. These daylight only systems have limited the military utility. Extension of multispectral sensing to the thermal bands has been a major thrust of the Department of Defense (DoD) since the Gulf War, since this will allow day-night operation.

This State of the Art Report surveys the standing of the community in key disciplines relevant to multispectral sensing:

phenomenology: optical properties of materials and radiance modelling validation

sensor design: multi- and hyper-spectral design, including components such as array

multispectral algorithms: determination of multi-band payoff, data conditioning

In order to place these disciplines in context, we also have included some examples of multispectral sensing. These include an assessment of potential defense applications and a summary of data products currently available from existing systems.

A broad overview of the report is shown below.

Topic	Location
Phenomenology/Including Modeling	Chapter 3, Chapter 5, Appendix A
Sensor Design	Chapter 4, Appendix B
Algorithms	Chapter 6
Examples	Chapter 7, Chapter 8

2.0 BACKGROUND

Section 2.1 defines multispectral, hyperspectral, and ultraspectral imaging sensors.

Section 2.2 describes solar reflection in the visible, near infrared (NIR), and short-wave infrared (SWIR) between 0.4 and 2.5 μm , solar reflection and thermal emission in the medium-wave infrared (MWIR) between 3 and 5.5 μm , and thermal emission in the long-wave infrared (LWIR) between 8 and 14 μm .

Section 2.3 discusses the optical properties of materials including reflectance and emittance in terms of their complex index of refraction.

Section 2.4 defines the spectral directional reflectance, directional emittance, bidirectional reflectance and their interrelationships.

Finally, Section 2.5 describes the spectral measurement of directional reflectance, directional emittance, and bidirectional reflectance.

2.1 DEFINITION OF TERMS

The optical spectrum is generally considered to include the ultraviolet from 0.2 to 0.4 μm , the visible from 0.4 to 0.7 μm , the NIR from 0.7 to 1.1 μm , the SWIR between 1.1 and 2.5 μm , the MWIR from 3 to 5.5 μm , and the LWIR from 8 to 14 μm . Solar reflection dominates between 0.2 and 2.5 μm and thermal emission dominates the spectrum between 8 and 14 μm . Solar reflection makes a significant contribution between 3 and 5.5 μm during the daytime.

Many sensors detect reflected and/or thermally emitted radiance in a single broad spectral band. For example panchromatic photography is sensitive in the visible between 0.4 and 0.7 μm , and forward-looking infrared (FLIR) sensors generally operate in the thermal infrared between 8 and 12 μm . Bright and dark in a panchromatic or FLIR image generally represent high and low surface reflectances or warm or cold surfaces, respectively. Contrast and high spatial resolution are important to detecting targets of interest.

Targets frequently have spectral signatures that uniquely separate them from their backgrounds. Two and three band sensors are frequently designed to detect targets in the presence of background clutter. Three band missile warning systems, for example, exploit the spectral differences between a missile plume, solar glints, and warm terrain backgrounds.

Multispectral imaging sensors are imaging sensors having 10-20 spectral bands between 0.4 and 14 μm with a spectral resolution of $\Delta\lambda/\lambda = 0.1$ (e.g., 0.05 μm in the visible and 1 μm in the thermal infrared). Processing of multispectral imagery is used for many military and civilian applications such as terrain classification, soils analysis, moisture content, trafficability analysis, bathymetry, camouflage detection, change detection, crop inventory, land use assessment, and others. Multispectral sensing dates back to the early 1960s and has led to a variety of airborne sensors and spaceborne sensors including the current generation of Landsat and SPOT sensors.

Hyperspectral imaging sensors have 100-200 spectral bands with a spectral resolution $\Delta\lambda/\lambda = 0.01$ (e.g., 0.005 μm in the visible and 0.1 μm in the thermal infrared). Hyperspectral

imaging sensors have been realized largely due to the technology development associated with large one- and two-dimensional detector arrays. The finer spectral resolution available with hyperspectral imaging provides significantly more capability for materials identification.

Ultraspectral sensors are sensors with a resolution of $1\text{--}2\text{ cm}^{-1}$ (e.g., $0.02\text{ }\mu\text{m}$ at $10\text{ }\mu\text{m}$, and $0.0008\text{ }\mu\text{m}$ at $2\text{ }\mu\text{m}$). Ultraspectral sensors are generally useful for detecting narrow band spectral phenomena over a limited part of the spectrum in applications that do not require high spatial resolution imaging. Detection of chemical vapor clouds is an example.

2.2 SOLAR REFLECTION AND THERMAL EMISSION

The target and background spectral radiance characteristics of interest at the aperture of a remote airborne or spaceborne sensor have their origin in differences in spectral reflectance and emittance properties. Differences in these characteristics are the basis of target detection and discrimination with today's multispectral and hyperspectral imaging sensors. However, spectral reflectances and emittances may be quite variable within a particular target or background class, and these variations may limit the probability of correct detection, or classification. There are, in addition, many other factors that also affect the target and background spectral radiance characteristics, and the variability of these characteristics, at a remote sensor.

The sun is the primary source of reflected radiance in the visible and reflective portion of the infrared spectrum. Other sources are stellar, galactic, and airglow radiance. Atmospheric scattering and transmission affects the spectral characteristics of the solar illumination and hence also the reflected radiance. Atmospheric scattering and transmission by the atmosphere between the reflecting surface and the sensor aperture further alter the spectral characteristics of the reflected radiance as observed at the remote sensor aperture.

Emission in the thermal infrared depends both on the spectral emittance and temperature of the surface. The temperature is determined by the solar loading, internal heat sources, thermal conductivity, specific heat, density, moisture content, convective, radiative, and evaporative cooling, and transpiration processes. Higher temperatures cause all radiances to increase but also cause a change in the spectral distribution characteristics of the emitted radiance as described by the Planck equation. Thermal emission by clouds and by the atmosphere contribute an important reflected component to the spectral radiances of the surfaces in the thermal infrared, and atmospheric transmission, emission, and scattering between the surface and the sensor aperture further impact the spectral characteristics that are sensed.

The utility of multispectral and hyperspectral sensors in any particular application is related to the differences in the spectral emittances of the target and its background. Variations and uncertainties in all the other factors that drive the spectral radiances and spectral radiance differences are, to the maximum extent possible, accounted for in the data processing. To the extent that these factors are well known for a particular scenario, performance will approach that limited by the spectral emittance differences between the target of interest and its background. If these factors are not well known and only incompletely accounted for, the performance will be lower.

2.3 REFLECTANCE, EMITTANCE, AND ABSORPTION

The fundamental equations governing the propagation of electromagnetic waves are Maxwell's equations. They provide the basis for understanding reflection and transmission of radiation in matter. The optical properties of a dielectric medium can be described in terms of a complex index of refraction, $N = n + ik$. The complex index of refraction, in terms of the relative permeability μ and relative permittivity ϵ , is

$$N = \sqrt{\mu\epsilon} \quad (2-1)$$

The specular reflectance from a smooth dielectric surface is given by the Fresnel equations

$$R_{\parallel} = \frac{\tan^2(\theta - \theta')}{\tan^2(\theta + \theta')} \quad (2-2)$$
$$R_{\perp} = \frac{\sin^2(\theta - \theta')}{\sin^2(\theta + \theta')}$$

where R_{\parallel} and R_{\perp} are the reflectances for energy polarized parallel and perpendicular to the plane of incidence. θ is the angle of incidence and θ' is the angle of transmission given by Snell's law

$$N_1 \sin(\theta_1) = N_2 \sin(\theta_2) \quad (2-3)$$

where N_1 and N_2 are the indices of refraction in the medium of incidence and transmission. The emittance of an opaque surface is related to the reflectance by Kirchhoff's law, namely

$$\epsilon(\theta) = 1 - \rho(\theta) \quad (2-4)$$

The imaginary part of the complex index of refraction, k , is related to the absorption in the medium, and is given by Beers law

$$I = I_0 e^{-\frac{4\pi k d}{\lambda}} \quad (2-5)$$

where d is the depth in the medium. The intensity is reduced by a factor of e^{-1} at a depth $d = \lambda/(4\pi k)$. The imaginary part of the complex index of refraction does not have to be very large to cause the absorption to be very high. However, the Fresnel reflectances are not very sensitive to k for $k < 0.1$, and the k dependence of the Fresnel equations can frequently be ignored.

A conductor can be described by a complex index of refraction with large k . For a good conductor the transmission is very small and the reflectance very nearly unity.

Spectral variations in the reflectance and emittance properties of materials are caused by electronic, vibrational, and rotational resonant absorptions in the material. Electronic transitions and molecular vibrational resonances dominate in the visible, near, and midwave infrared, and molecular vibrational and rotational resonances dominate in the midwave and longwave infrared. Common examples include absorption due to chlorophyll at 0.675 μm , absorption in water at 2.7, 6.3 μm , and 15 μm , absorption in CO_2 at 2.7, 4.2, and 15 μm , and absorption in silicon dioxide between 8.5 and 10 μm .

2.4 DIRECTIONAL REFLECTANCE, BIDIRECTIONAL REFLECTANCE, AND DIRECTIONAL EMITTANCE: DEFINITIONS

Maxwell's and Fresnel's equations describe reflection and absorption of electromagnetic energy from specular surfaces in terms of the complex index of refraction. Most surfaces are not specular, so knowledge of the complex index of refraction does not provide an adequate characterization of the reflectance properties of real surfaces.

In practice it is necessary to measure the spectral reflectance and/or emittance properties of materials of interest. Reflectance generally depends on the wavelength considered, on the angles of incidence and reflection, and on the polarization characteristics of the source and receiver. A variety of instrumentation exists for measuring a directional reflectance as a function of wavelength. A typical reflectometer is fitted with a broad band source, a scanning monochromator, and an integrating sphere. The directional reflectance, $\rho_d(\theta_i, \lambda)$, is the ratio of total power reflected into the hemisphere to the incident power from direction θ_i at wavelength λ , namely

$$\rho_d(\theta_i, \lambda) = \frac{P_R(\lambda)}{P_i(\theta_i, \lambda)} \quad (2-6)$$

An alternative measurement uniformly illuminates the sample over the hemisphere and views the sample from a direction θ_r at wavelength λ . The ratio of the radiance reflected to the radiance incident is the directional reflectance $\rho_d(\theta_r, \lambda)$, namely

$$\rho_d(\theta_r, \lambda) = \frac{L_r(\theta_r, \lambda)}{L_i(\theta_i, \lambda)} \quad (2-7)$$

where $\rho_d(\theta_i, \lambda) = \rho_d(\theta_r, \lambda)$ by reciprocity.

Spectral emissivities are sometimes determined directly from the ratio of spectral radiance from the material to the spectral radiance (computed) from a blackbody at the same temperature. The sample is frequently either heated, or kept at ambient and placed in a cold chamber, to minimize any reflected radiance. The spectral emissivity, $\varepsilon(\theta, \lambda)$, is defined as

$$\varepsilon(\theta, \lambda) = \frac{L(\theta, \lambda, T)}{L_{bb}(\lambda, T)} \quad (2-8)$$

The directional emissivity is related to the directional reflectance by reciprocity, namely

$$\epsilon(\theta, \lambda) = 1 - \rho_d(\theta, \lambda) . \quad (2-9)$$

Spectral directional reflectivities and emissivities show the spectral characteristics of materials and indicate where spectral bands should be chosen for discriminating between various types of materials. However, they are an incomplete specification of the optical properties of materials. A complete specification requires the bidirectional reflectance distribution function (BRDF), denoted by $\rho'(\theta_i, \phi_i, \theta_r, \phi_r, \lambda, P)$ where P represents the polarization state of the incident and reflected radiance. The BRDF is the ratio of the radiance reflected at wavelength λ into direction θ_r, ϕ_r $L(\theta_r, \phi_r, \lambda)$ to the incident irradiance at wavelength λ from direction θ_i, ϕ_i $E(\theta_i, \phi_i, \lambda)$, namely

$$\rho'(\theta_i, \phi_i, \theta_r, \phi_r, \lambda) = \frac{L(\theta_r, \phi_r, \lambda)}{E(\theta_i, \phi_i, \lambda)} . \quad (2-10)$$

In the most general case the polarization characteristics of the BRDF for a given $\theta_i, \phi_i, \theta_r, \phi_r$ are specified by a 4 by 4 Mueller matrix.

The directional reflectance is related to the bidirectional reflectance as follows

$$\rho_d(\theta_i, \lambda) = \int \rho'(\theta_i, \phi_i, \theta_r, \phi_r, \lambda) \cos(\theta_r) d\Omega_r . \quad (2-11)$$

Since the spectral directional reflectance, and hence the spectral directional emittance, can both be specified in terms of the BRDF, the BRDF is a complete specification of the optical properties of the surface. A diffuse reflector is one with ρ' independent of the angles of incidence and reflection. It follows that the diffuse reflectance and the bidirectional reflectance for a diffuse reflector are related as follows,

$$\rho_d(\theta, \lambda) = \pi \rho'(\lambda) . \quad (2-12)$$

Finally, the relationship between the radiance at a remote sensor and the optical properties of the surface can be written as follows

$$L = \text{transmission [reflected + emitted]} + \text{path}$$

$$L = \tau \left[\int \rho' L_i \cos(\theta_i) d\Omega_i + \epsilon_d L_{bb}(T) \right] + L_p \quad (2-13)$$

$$L = \tau \left[\frac{\rho_d}{\pi} E_i + \epsilon_d L_{bb}(T) \right] + L_p$$

where $\tau = \tau(R, \theta, \lambda)$ is the atmospheric transmission,
 $L = L(\theta_r, \phi_r, \lambda)$ is the observed radiance,
 $L_i = L_i(\theta_i, \phi_i, \lambda)$ is the incident radiance,
 $E_i = E_i(\lambda)$ is the incident irradiance,
 $\rho' = \rho'(\theta_i, \phi_i, \theta_r, \phi_r, \lambda)$ is the BRDF,
 $\rho_d = \rho_d(\theta_i, \phi_i, \lambda)$ is the directional reflectance,
 $\epsilon_d = \epsilon_d(\theta_r, \phi_r, \lambda)$ is the directional emittance,
 $L_{bb} = L_{bb}(T, \lambda)$ is the blackbody radiance, and
 $L_p = L_p(R, \theta, \lambda)$ is the atmospheric path radiance.

The incident radiance is primarily from direct and scattered sunlight in the visible and reflective infrared out to 2.5 μm . Self emission dominates in the thermal infrared between 8 and 14 μm , and both solar reflection and thermal emission contribute in the midwave infrared between 3 and 5.5 μm . Although the dominant contribution to the radiance in the thermal infrared is self emission, it should be noted that the effect of clouds in the thermal infrared is to provide a source of greybody radiance for reflection, and an increase in spectral reflectance in one portion of the spectrum is necessarily accompanied by a decrease in the spectral emittance in that portion of the spectrum. As a consequence the spectral characteristics that distinguish the targets of interest from background clutter in the thermal infrared are reduced under partly cloudy and overcast conditions.

2.5 DIRECTIONAL REFLECTANCE, DIRECTIONAL EMITTANCE, AND BIDIRECTIONAL REFLECTANCE: MEASUREMENTS

A variety of laboratory-type instruments are used for making spectral directional reflectance, directional emittance, and bidirectional reflectance measurements.

A very simple instrument configuration for making spectral directional measurements in the visible and reflective infrared between 0.4 and 2.5 μm uses a broadband source, such as a tungsten filament lamp, a prism or grating monochromator for spectrally scanning the wavelength of the source, optics to collimate the narrow band radiation from the monochromator onto the sample, and an integrating sphere attachment to collect radiance reflected into the hemisphere onto a detector. Many laboratories are equipped with instrumentation used to measure reflectance (and transmittance) in the visible and reflective infrared between 0.4 and 2.5 μm .

Examples of spectral directional reflectance for vegetation are shown in Figure 2-1 with a spectral resolution of 0.002 μm at 0.4 μm , 0.05 μm at 1 μm , and 0.1 μm at 2 μm . The data shown are directional reflectance spectra for green and senescent corn leaves. These are characteristic of a wide variety of green and senescent vegetation. For healthy vegetation, the reflectance is low in the blue, 10-20 percent in the green, very low in the red portion of the spectrum at 0.675 μm due to absorption by chlorophyll, and low at 1.4, 1.9, and 2.7 μm due to absorption by water. Senescent leaves lose chlorophyll and water with significantly weaker spectral absorptions from chlorophyll and water.

Spectral directional reflectance measurements may also be made at longer wavelengths using appropriate infrared sources and detectors. An infrared integrating sphere is coated with a material that is highly reflective and diffuse in the infrared, for example gold. Spectral

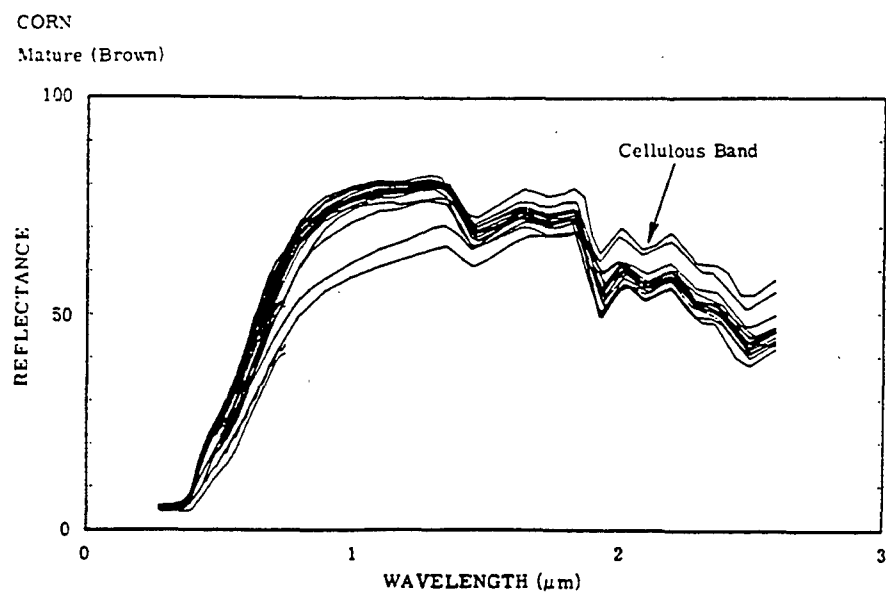
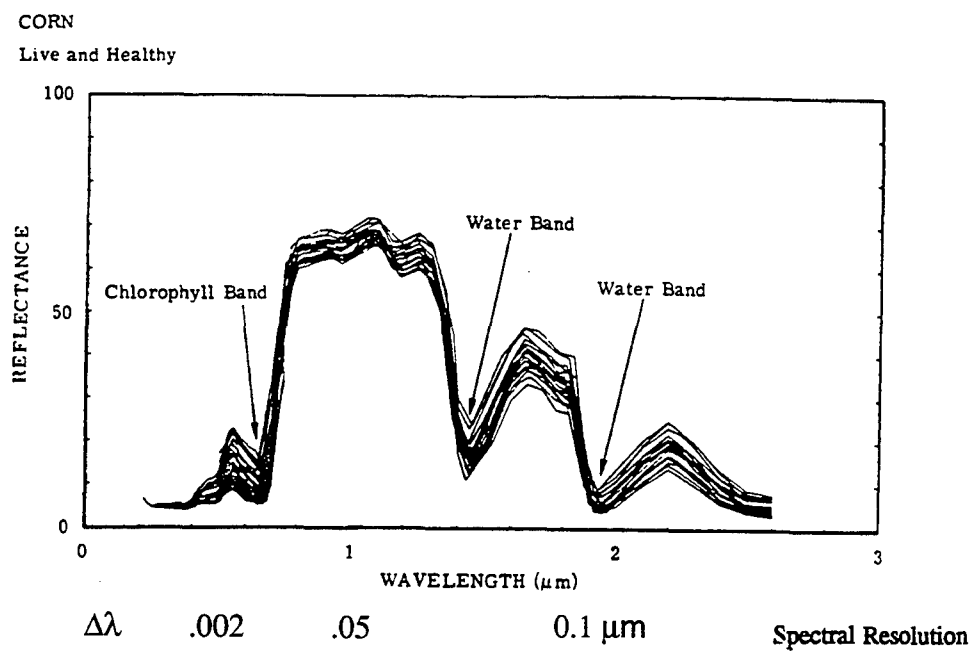


Figure 2-1. Directional Reflectance Healthy Green and Mature Brown Corn Leaves

measurements may be made by dispersing the source with a prism or grating or by analyzing the spectral characteristics of the reflected broadband source with a wedge filter or with a Fourier transform spectrometer. The Fourier transform spectrometer can provide very high spectral resolution. Examples of high spectral resolution, spectral directional reflectance measurements of green and senescent foliage in the 3-5 μm band are shown in Figure 2-2. The spectral resolution in these data is 4 cm^{-1} ($0.0064\text{ }\mu\text{m}$ at $4\text{ }\mu\text{m}$). The reflectance of green vegetation in the MWIR, between 3 and 5 μm , is very low. The increase in reflectance between 3.4 and 3.55 μm is caused by a C-H vibration in the cellulose. The reflectance of senescent vegetation is significantly higher due to loss in water and because the waxy cuticle flakes off of the broad leaves after senescence.

The reflectance of green and senescent vegetation in the 8-14 μm band, with a resolution of 4 cm^{-1} ($0.04\text{ }\mu\text{m}$ at $10\text{ }\mu\text{m}$), is shown in Figure 2-3. The increase in reflectance after senescence is also due to a loss of water and flaking off of waxy cuticle.

Bidirectional reflectance measurements are made using specially designed goniometric facilities not generally available in most laboratories. Lasers are frequently used because they provide high energy narrow spectral band sources. Sources that are frequently used are He:Ne (0.63 and $3.39\text{ }\mu\text{m}$), Nd:YAG ($1.06\text{ }\mu\text{m}$), and CO_2 ($10.6\text{ }\mu\text{m}$ or $5.3\text{ }\mu\text{m}$ doubled). With a typical goniometric facility, a sample is mounted on a 3 axis platform so that the angle of incidence can be varied, and a sensor is located on a mount that can be positioned anywhere on a hemisphere above the illuminated sample. Figure 2-4 shows an example of the bidirectional reflectance of a painted sample at $0.63\text{ }\mu\text{m}$ as a function of receiver angle, with the receiver in the plane of incidence, and with the source at an angle of incidence of 40 degrees. The large increase in the BRDF at 40 degrees in the forward scatter direction is due to first surface scattering at the rough surface dielectric interface. Figure 2-5 shows the bidirectional reflectance at $10.6\text{ }\mu\text{m}$ for the same sample. The forward scatter peak is much sharper because the surface is much more specular at longer wavelengths.

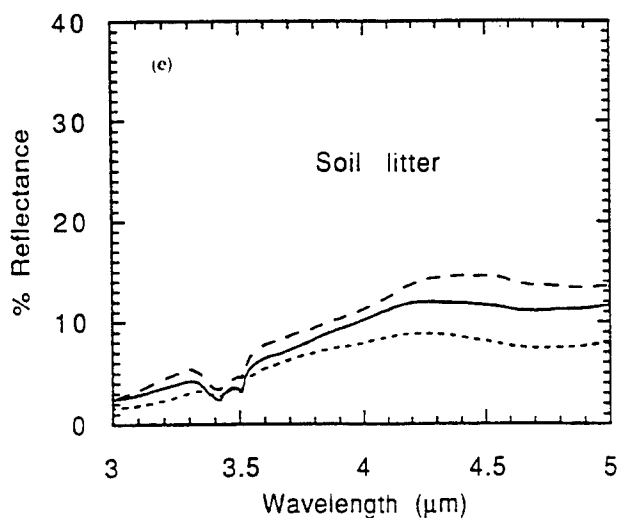
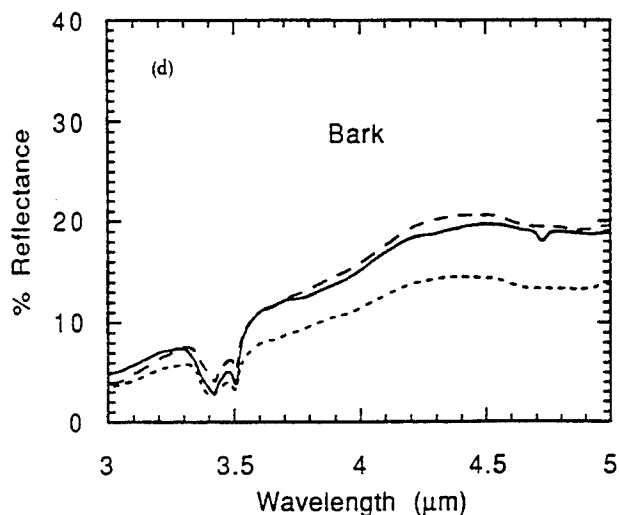
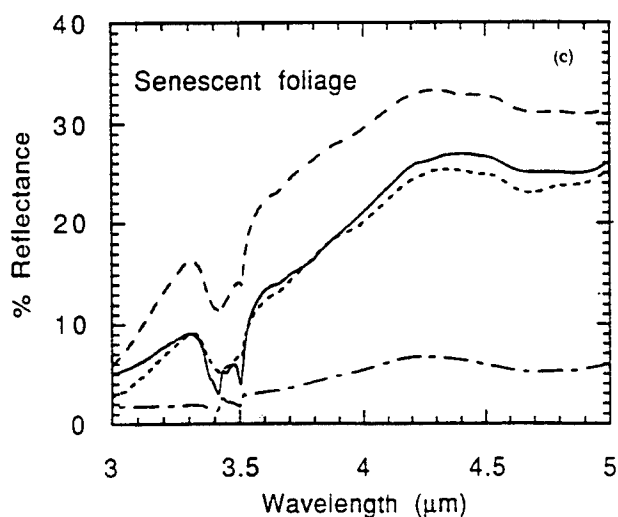
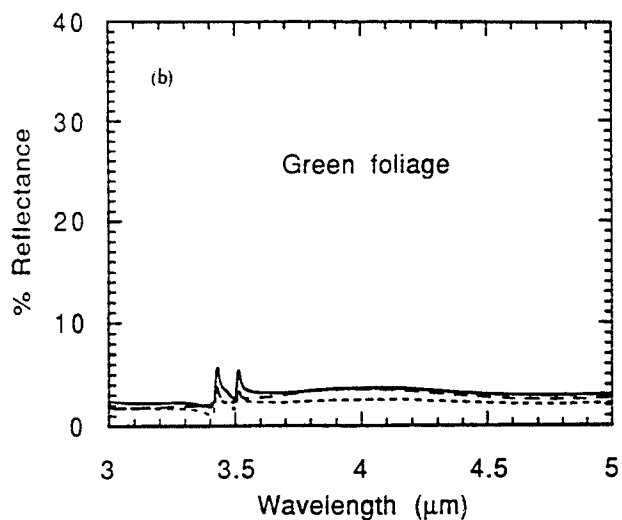
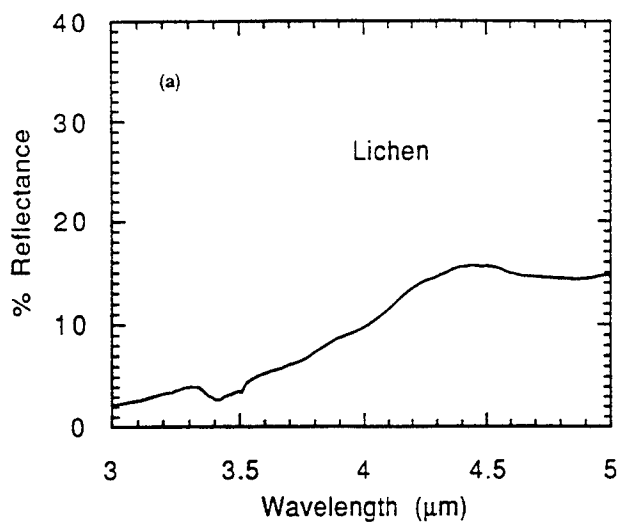


Figure 2-2. Directional Hemispherical Reflectance Spectra of Representative Samples of Vegetation Cover: a) spectrum of the foliose lichen *Parmotrem*, a tree lichen from Maryland; b) spectra of typical green foliage, including red oak leaves (solid curve), Indiangrass blades (dashed curve), and white pine needles (dotted curve); c) spectra of typical senescent foliage, including beech (dashed curve), red oak leaves (solid curve), rye grass (dotted curve), and white pine needles (dash-dot curve); d) spectra of typical bark samples, including white oak (solid curve), yellow poplar (dashed curve), and Loblolly pine (dotted curve); e) spectra of typical decaying soil litter, including deciduous leaf fragments and twigs (solid curve), mostly decaying wood (dashed curve), and decaying white pine needles (dotted curve).

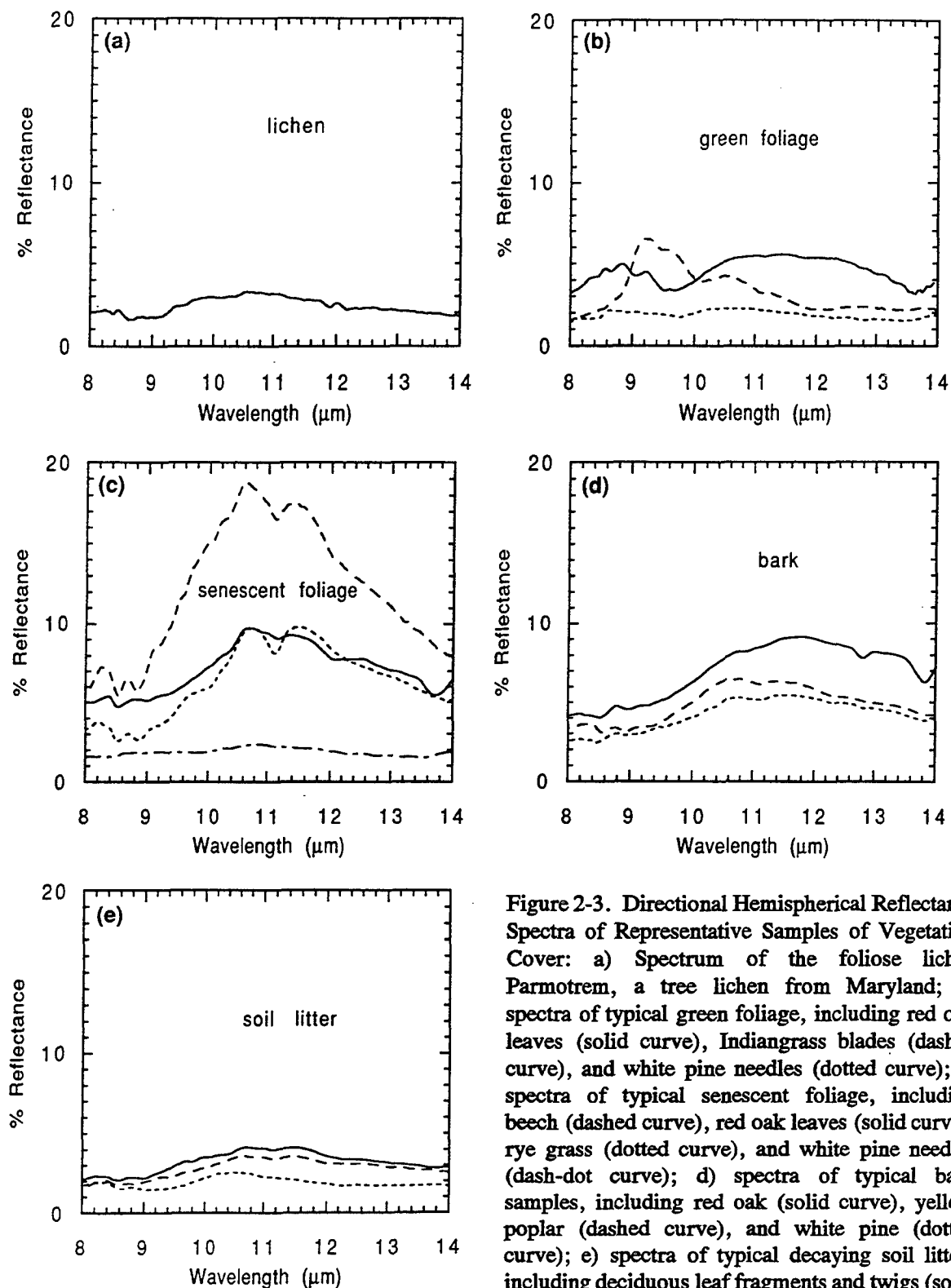


Figure 2-3. Directional Hemispherical Reflectance Spectra of Representative Samples of Vegetation Cover: a) Spectrum of the foliose lichen *Parmotrem*, a tree lichen from Maryland; b) spectra of typical green foliage, including red oak leaves (solid curve), Indiangrass blades (dashed curve), and white pine needles (dotted curve); c) spectra of typical senescent foliage, including beech (dashed curve), red oak leaves (solid curve), rye grass (dotted curve), and white pine needles (dash-dot curve); d) spectra of typical bark samples, including red oak (solid curve), yellow poplar (dashed curve), and white pine (dotted curve); e) spectra of typical decaying soil litter, including deciduous leaf fragments and twigs (solid curve), mostly decaying wood (dashed curve), and decaying white pine needles (dotted curve).

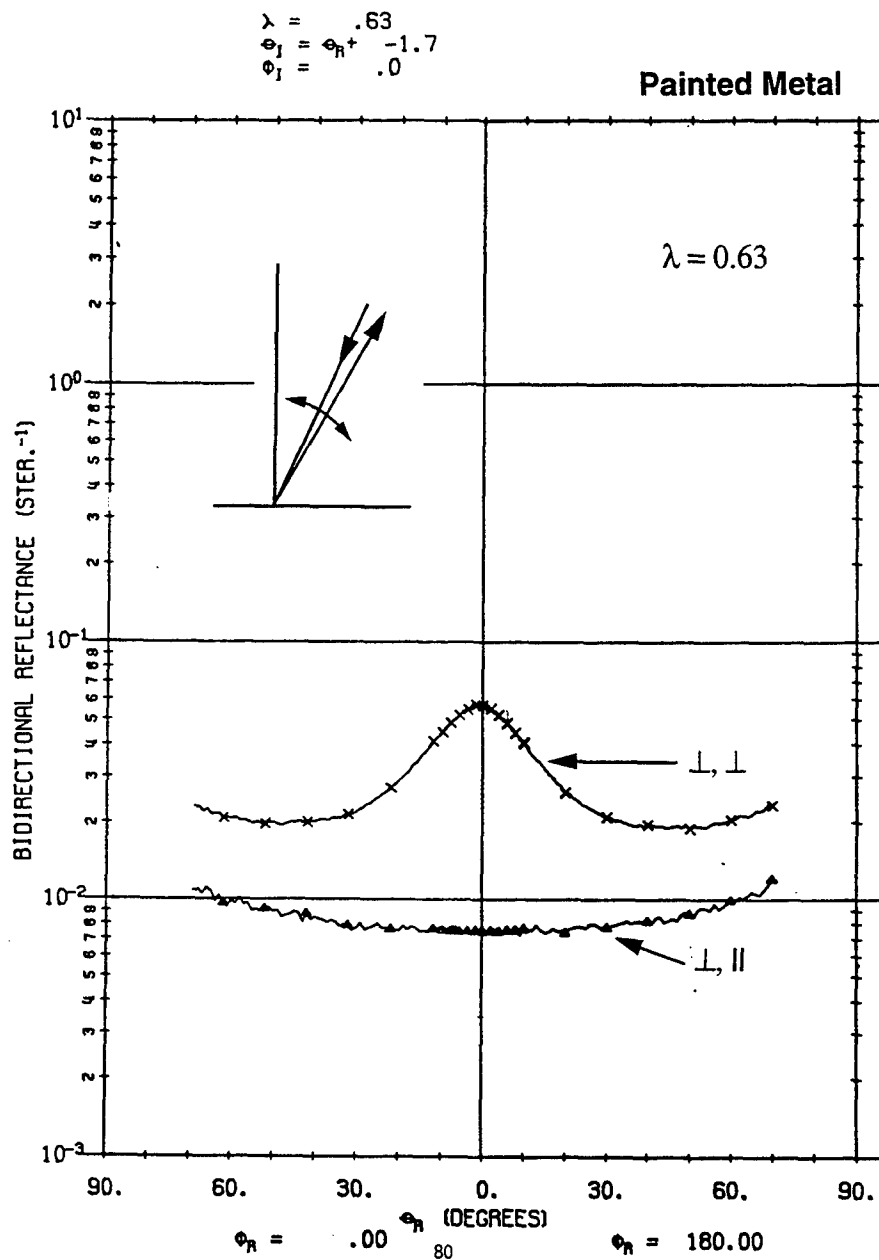


Figure 2-4. Near Zero Bistatic Bidirectional Reflectance at 0.63 μm

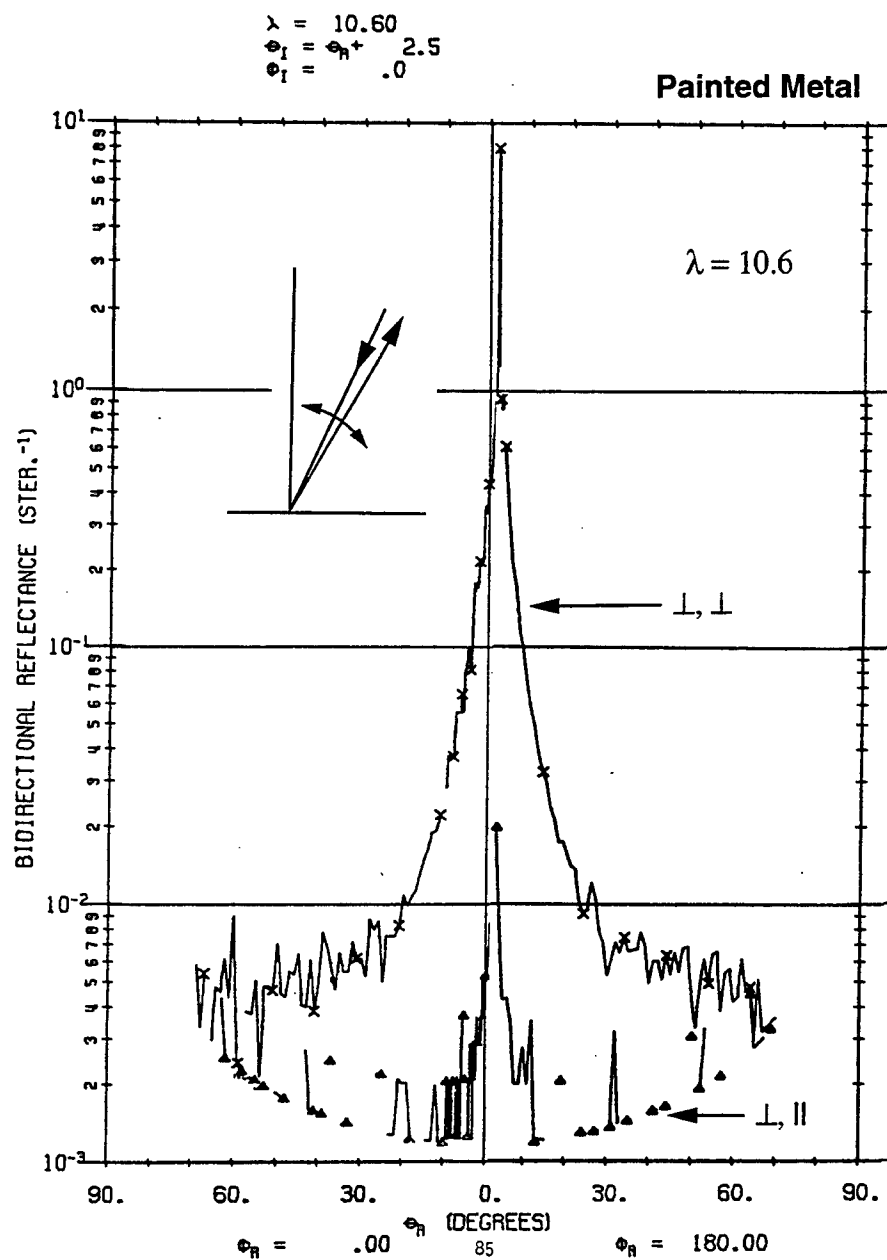


Figure 2-5. Near Zero Bistatic Bidirectional Reflectance at 10.6 μm

3.0 PHENOMENOLOGY

This section provides a brief summary of the optical properties of materials and material property databases. A detailed discussion is contained in Appendix A.

Section 3.1 discusses the physical origins of the spectral properties of materials. Section 3.2 discusses the spectral properties of the atmosphere. Section 3.3 provides a discussion of the surface and volume contributions to the reflectance. Finally, Section 3.4 identifies several sources for optical properties data.

3.1 PHYSICAL ORIGINS OF SPECTRAL PROPERTIES

Radiance in the visible and infrared includes both reflected and emitted radiance. Reflection of energy from the sun, moon, earth, and from atmospheric scattering dominate in the visible and near IR between 0.4 and 2.5 μm . Solar reflection contributes significantly in the MWIR between 3 and 4.2 μm during the daytime. Thermal emission from ambient temperature surfaces generally dominates from 4.2 to 5.5 μm in the MWIR and between 8 and 14 μm in the LWIR.

The reflectances of many materials differ spectrally in the visible which accounts for the many variations in color. Reflectances also vary in the NIR and SWIR which gives rise to a more general concept of color in the spectral range between 0.4 and 2.5 μm .

Thermal emission is the dominant source of radiation in the MWIR beyond 4.2 μm and in the LWIR. A blackbody emitter radiates according to the Planck radiation law. Thermal emission of real surfaces is less than that of a blackbody. The ratio of the thermal emission of a surface at temperature T at wavelength λ to that of an ideal blackbody at the same temperature and wavelength is the spectral emissivity. The spectral emissivity is always less than or equal to one. Spectral variations in emittances provide spectral radiance variations in the thermal IR analogous to those caused by variations in the reflectance at shorter wavelengths.

There are a variety of sources for the observed spectral variations in the spectral reflectance and emittance. Section 3.1.1 discusses the role of electronic, vibrational, and rotational transitions in absorption, reflection, and emission. Section 3.1.2 discusses the characteristic bandwidths of spectral phenomena, and Section 3.1.3 discusses the resonance phenomenon that give rise to strong emissivity effects in the infrared.

3.1.1 Electronic, Vibrational, and Rotational Transitions

Transitions occur between electronic energy levels in atoms and between vibrationally and rotationally excited states in molecules. These transitions are the source for line structure emission from a variety of atoms and molecules. Electronic energy transitions are typically measured in electron volts (1 eV corresponds to a wavelength of 1.2 μm). The Lyman series of transitions in atomic hydrogen is a typical example with the transition between the first excited state and the ground state in the ultraviolet at 0.1216 μm . Vibrational levels are typically separated by a few μm . They are more closely spaced than electronic transitions, and

the 10.6 μm radiation between vibrational bands in CO_2 is a familiar example. Rotational levels are more closely spaced yet, typically 60 GHz or 0.02 μm . The closely spaced rotational lines in CO_2 allow for tuning the CO_2 over a small wavelength range. The main absorption lines in water vapor at 2.7, 6.3, and 15 μm and in carbon dioxide gas at 2.7, 4.2, and 15 μm are absorptions associated with vibrational bands. The fine structures in the absorption spectra are due to rotational states.

3.1.2 Characteristic Bandwidths of Spectral Phenomena

Atoms and molecules in the gaseous state generally absorb and emit energy in very narrow spectral bands. The spectral lines are frequently pressure and temperature broadened, and spectral line widths depend on temperature and pressure. Typical linewidths are fractions of wavenumber (where, for example, 1 cm^{-1} corresponds to 0.0025 μm at 5 μm).

Absorption lines in liquids and solids are much broader than in their corresponding gaseous state from the perturbations arising from bonding into the liquid and solid state. Liquid water strongly absorbs at 2.7, 6.3, and 14 μm . None of the fine structure caused by the presence of rotational levels is observed. Figure 3-1 shows the reflectance and transmittance through 0.002 cm of sea water. Absorption lines are observed at 1.4, 1.9, 2.7, 6.3, and very broadly at 15 μm . The effects of the strong absorptions at 2.7, 6.3, and 15 μm are very pronounced.

Reflectance spectra for vegetation, water, and a number of mineral types of interest to geologic remote sensing, terrain categorization, trafficability, target detection, and target/background/camouflage discrimination are included in Appendix A.

3.1.3 Resonance Phenomena

Absorption in liquids and solids is associated with atomic and molecular bonding. Absorption can be measured directly, and the absorption can be related to the imaginary index of refraction, k , as follows:

$$I = I_0 e^{-\frac{4\pi k d}{\lambda}} \quad (3-1)$$

The reflectance and emittance for pure specular surfaces can be determined from the real and imaginary components of the index of refraction, where the real component of the index of refraction can be determined by a variety of ellipsometric and polarimetric techniques.

Figure 3-2 shows the real and imaginary components of the index of refraction for crystalline and amorphous SiO_2 . The large increase in k at about 9.5 μm is related to a large increase in the absorption at 9.5 μm in the thermal infrared. The effect is very strong and causes the imaginary component of the index to reach a value of nearly 10 at 9.8 μm and the real component to go through a typical resonance peak with the index decreasing with wavelength near the strong absorption (anomalous dispersion). The real component of the

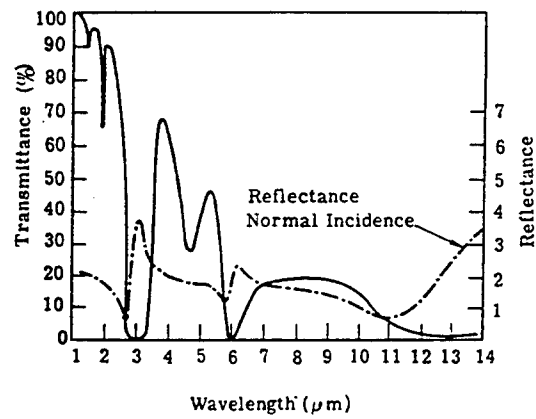


Figure 3-1. Transmittance and Reflectance of 0.002 cm of Sea Water.

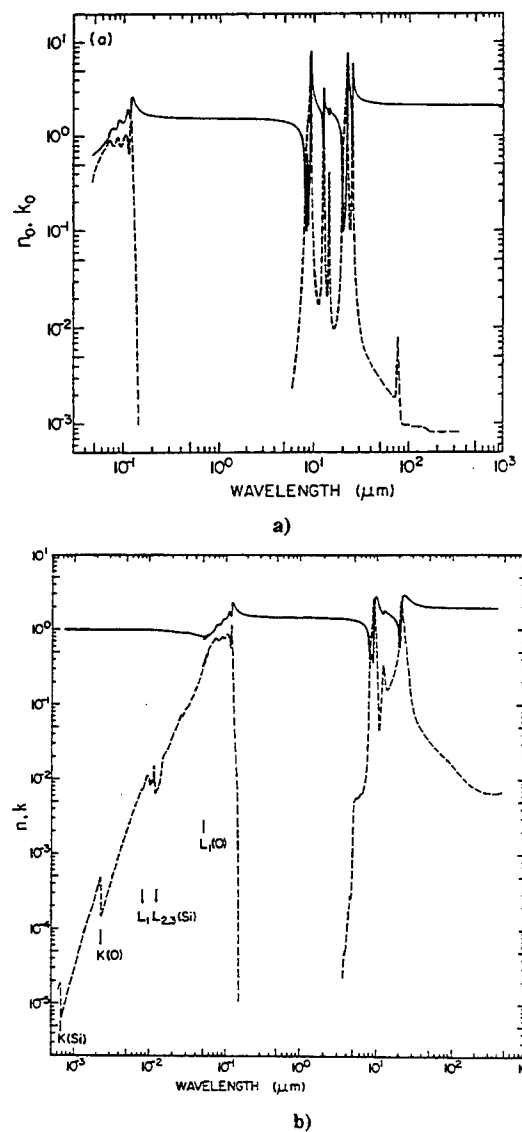


Figure 3-2. The Complex Index of Refraction: a) type alpha crystalline silicon dioxide (SiO_2) and b) amorphous silicon dioxide (SiO_2) (Glass).

index of refraction can become less than one at wavelengths just short of the absorption peak. A strong absorption with these characteristics is frequently referred to as a "reststrahlen" band.

Absorption lines in liquids and solids can be modeled using a classical forced damped harmonic oscillator (Lorentz) model. Using such a model, for example, for SiO_2 , with a resonant frequency at $9.5 \mu\text{m}$, it is possible to derive the equivalent complex dielectric constant in terms of the electric field forcing function, damping coefficient, restoring force, and charge and mass of the electron. The Lorentz model explains the large increase in transmission below the reststrahlen band where the real component of the index of refraction approaches one and the imaginary component of the index of refraction is small. These peaks in the transmission spectra are known as Christiansen peaks.

Absorptions in a variety of liquids and solids occur in the visible, reflective infrared, and thermal infrared that give rise to spectral variations in their reflectances and emittances. These are the fundamental sources of signature information for distinguishing between different materials using techniques of multispectral, hyperspectral, and ultraspectral sensing.

3.2 ATMOSPHERIC SPECTRAL PROPERTIES

The atmosphere affects the spectral radiance at a remote sensor in several ways. In the visible part of the spectrum the atmosphere attenuates and scatters solar radiation. This alters the spectrum of solar radiation and provides a diffuse source of sky illumination. Atmospheric effects in the visible also include transmission losses between the target and sensor and scattering of nontarget radiance into the sensor field of view. In the thermal infrared the atmosphere emits where it absorbs and thus provides a diffuse source of infrared illumination. Path losses between the target and the sensor also alter the spectral characteristics at the sensor.

Figure 3-3 shows the atmospheric absorption for several molecular species found in the atmosphere. The absorptions due to water and CO_2 largely define the atmospheric "windows" which include the visible from 0.4 to $0.7 \mu\text{m}$, the NIR from 0.7 - $1.1 \mu\text{m}$, the SWIR from 1.1 - 1.4 , 1.5 - 1.9 , and 2.0 - $2.5 \mu\text{m}$, the MWIR from 3 - $5.5 \mu\text{m}$ spanning the CO_2 absorption band at $4.2 \mu\text{m}$, and the LWIR from 8 - $14 \mu\text{m}$. Another important atmospheric constituent is ozone with a strong absorption at $9.8 \mu\text{m}$. Ozone is concentrated in the upper atmosphere so that the primary effect is ozone emission and a source of reflected radiance for many applications.

The data in Figure 3-3 are low resolution spectra (approximately 20 cm^{-1} resolution, $0.032 \mu\text{m}$ at $4 \mu\text{m}$). This resolution is typical of that utilized in multispectral sensor applications and can be easily obtained using the low-resolution atmospheric transmittance model (LOWTRAN). More spectral resolution is required for hyperspectral sensor applications and is available with the moderate-resolution version of LOWTRAN (MODTRAN). For very high ultraspectral and laser applications it is necessary to use atmospheric models based on a line-by-line catalog of absorption data on various gases in the atmosphere.

Scattering and absorption of solar energy in clouds has a significant effect on the magnitude and the spectral character of the radiance in the visible and reflective infrared portions of the spectrum.

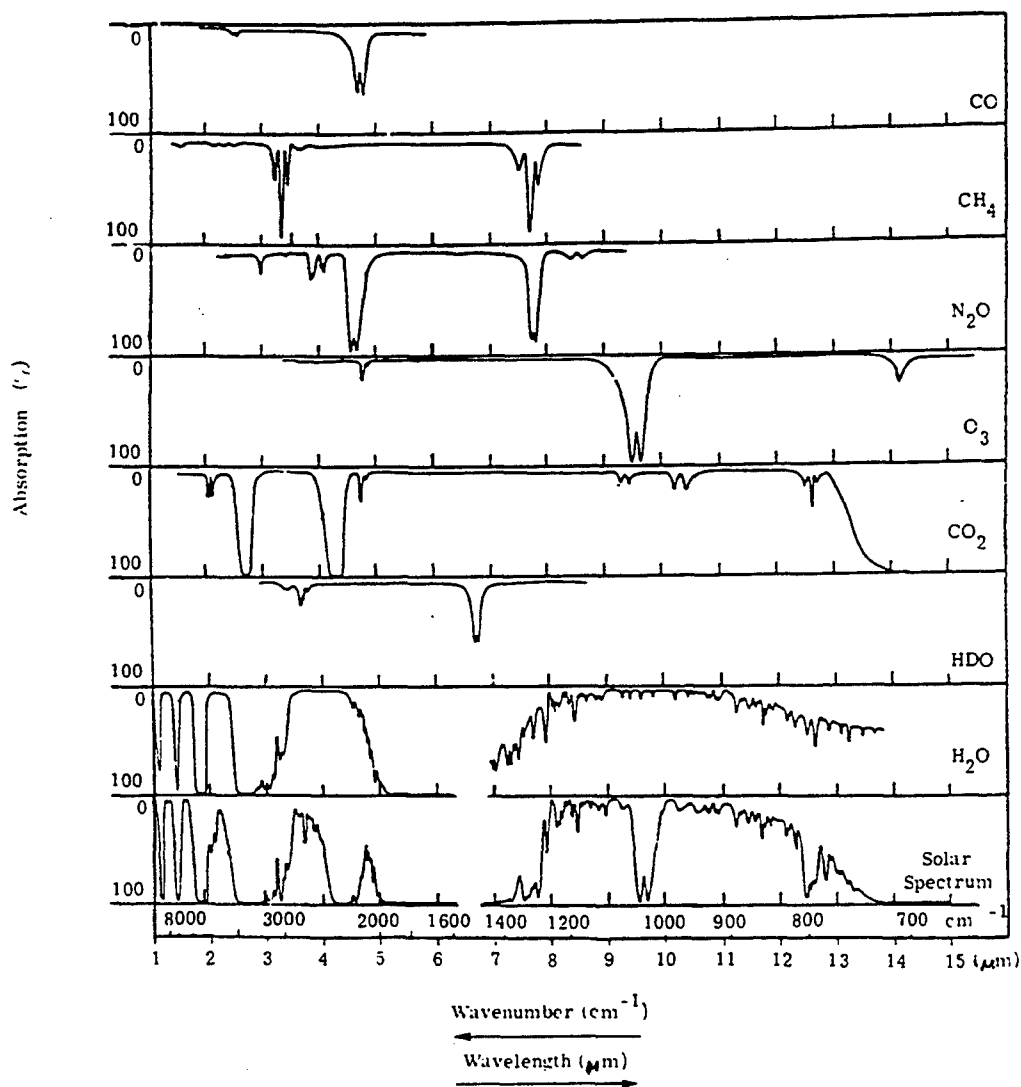


Figure 3-3. The Atmospheric Absorption Spectral of Several Molecular Species

Clouds can also significantly affect the spectral characteristics of the radiance in the thermal infrared. The water in clouds almost completely absorbs energy in the thermal infrared, hence clouds are nearly perfect blackbody emitters at air temperature at altitude. Clouds increase the reflected radiance in those parts of the spectrum where the emitted radiance is reduced due to a lower spectral emittance (i.e., $\epsilon(\lambda) = 1 - \rho(\lambda)$). The net result is that spectral variations in the radiance at a remote sensor can be significantly reduced under conditions of cloud cover as shown with an approximate form of the radiative transfer equation, namely

$$L(\lambda) \approx \tau \left[\frac{\rho_d(\lambda)}{\pi} E_i(\lambda) + \epsilon_d(\lambda) L_{bb}(\lambda, T_{tgt}) \right] + L_p$$

(3-2)

$$\approx \tau \left[\frac{\rho_d(\lambda)}{\pi} E_i(\lambda) + (1 - \rho_d(\lambda)) L_{bb}(\lambda, T_{tgt}) \right] + L_p .$$

3.3 SURFACE AND VOLUME CONTRIBUTIONS TO REFLECTANCE

The reflectance properties of real materials are fully characterized by the BRDF. This requires measurements as a function of source wavelength, source and receiver angles, and source and receiver polarizations. Source coherence may also be required for a complete specification. Emittance properties can be derived from the BRDF.

Insight into the physical phenomena giving rise to the reflectance properties of various types of materials provides guidance both into the type and number of measurements required to characterize the material and to the development of reflectance modeling.

Most surfaces are not specular so that the Fresnel equations and a complex index of refraction are not adequate for characterizing the reflectance. Departures from specularity are due to scattering caused by surface roughness and scattering from radiation propagating—into the material (volume effects). Some man-made surfaces are metallic, and many others, metallic or nonmetallic, are painted.

Metallic surfaces may be rough or smooth. Reflectance from metals occurs at the air-metal interface. The BRDF may show a pronounced specular peak if the surface is smooth, or it may be quite diffuse if the surface is rough. The reflectance will be high for most clean metallic surfaces, and the reflectance generally increases with wavelength. For a rough surface, the scale of the surface roughness relative to the wavelength is an important parameter. The width of the specular lobe in the BRDF is generally narrower for longer wavelengths.

The reflectance properties of paint can be characterized in terms of binder and pigment properties. Paint binders are generally dielectric. Reflection from a painted surface is due primarily to reflection from the surface of the paint (the "surface" component) and to radiation that is transmitted into the binder, scattered and absorbed by the pigment, binder, and substrate, and reflected back out through the first surface interface. This is the "volume" scattering component.

The first surface component of the reflectance from a paint or coating depends on the surface roughness of the binder and on its complex index of refraction. Most dielectrics do not have a large imaginary component to the index of refraction so that the first surface reflection is well characterized by the real component of the index of refraction. A "glossy" surface is one for which the first surface is very smooth and quite specular. A "diffuse" surface is one for which the first surface is rough. Reflection away from the specular direction arises from a distribution of local surface normals about the average surface normal. The first surface reflectance from typical dielectric coatings (with index of refraction 1.4-1.6) is 3-5 percent for normal incidence and higher for nonnormal incidence. The surface reflectance approaches unity near grazing.

The volume component of the reflectance due to pigment scattering depends on the pigment index of refraction, number density and size distribution, on the binder thickness and absorption, and for thin coatings on the substrate reflectance. In general the reflectance component due to pigment scattering is quite diffuse for viewing angles between normal and about 70 degrees (corresponding to the critical angle for transmission from the binder to air). Volume scattering gives rise to most of the spectral variations in the reflectance of paints and determines whether they are high or low reflectance paints.

The reflectance properties of water can also be explained in terms of a surface component and a volume component. In the visible part of the spectrum, where the transmission of water is relatively high, volume scattering can be a significant contributor to the reflectance from water. In the infrared, where water is opaque, first surface reflection dominates.

The bidirectional reflectance properties of leaves also consist of a surface and volume component. The surface component of the reflectance from leaves may be quite specular for waxy leaves. Volume scattering arises from scattering by the cell structure within the leaf and is very diffuse. The volume component of reflectance in the visible is quite small due to absorption within the leaf, especially due to chlorophyll at 0.675 μm . The volume scattering (and also the diffuse transmission) is very high in the near infrared where there is little absorption in the leaf.

The bidirectional reflectance from natural vegetation is much more diffuse than from a single leaf because of the random orientation of leaf surfaces within the canopy.

The bidirectional reflectance from dry soils is dominated by scattering and is generally quite diffuse. Wet soil may have a water surface giving rise to a surface component.

3.4 OPTICAL PROPERTIES OF MATERIALS

Databases of optical properties of materials including spectral reflectances, spectral emittances, and spectral indices of refraction are important for selecting wavelength bands for particular multispectral sensor applications and for estimating expected performance. In addition, thermal properties including specific heats, conductivities, and heat capacities are important in the infrared. Radiance measurements are important for characterizing the spectral radiances in the field and for validating models that relate optical and thermal properties to radiance. Multispectral imagery databases are important for determining the characteristics of extended backgrounds and for validating models, developing algorithms, and evaluating performance with real data.

3.4.1 Reflectance and Emittance

The Target Signature Analysis Center (TSAC) compilation was prepared between 1967 and 1972 for the Avionics Laboratory at Wright Patterson Air Force Base. It was the first comprehensive database of optical properties. This data compilation contains a large number of spectral directional reflectance curves between 0.4 and 2.5 μm natural and man-made materials. This compilation also contains BRDF data at several wavelengths including 0.6328, 1.06, and 10.6 μm , spectral emittance measurements between 4 and 14 μm , and field spectral radiance measurements on various backgrounds between 4 and 14 μm . This compilation includes all measurement data available at the time including data collected by the Environmental Research Institute of Michigan (ERIM), then the Willow Run Laboratories of the University of Michigan. A large portion of the TSAC database has since been published as part of the NASA Data Compilation.

Many spectral reflectance measurements between 0.4 and 14 μm have been made since publication of the TSAC Data Compilation. Surface Optics has measured the optical properties of many materials over the last 20 years that are contained in a variety of their reports.

Much of the earlier data have sufficient spectral resolution to support multispectral analyses. More recently Fourier transform spectrometer measurements with higher spectral resolution in support of hyperspectral analysis have become available. Dr. John Salisbury has collected many high spectral resolution measurements between 3 and 14 μm that have been published and that are part of a Spectral Catalog assembled and maintained by SETS Technology, Inc. Measurements have been made for a variety of natural and man-made materials.

Index of refraction data are frequently published in the *Journal of the Optical Society of America* and *Applied Optics*. A summary of index of refraction data is available in the form of a State-of-the-Art report from IRIA, and many of these data are contained in the most recent IR/EO Systems Handbook published by IRIA. Additional data are available in the *Handbook of Infrared Optical Materials*, edited by Paul Klocek and published by Dekker in 1991.

3.4.2 Thermal Properties

Most thermophysical properties required for analysis in the thermal infrared can be obtained from the *Handbook of Chemistry and Physics*. Additional data are available in the *Handbook of Infrared Optical Materials* edited by Paul Klocek.

3.4.3 Radiance Measurements

Field radiance measurements are most useful only if they are well ground truthed. This is because solar, sky, and cloud radiances significantly affect the magnitude and spectral quality of the reflected radiance throughout the spectrum. In the thermal infrared, surface temperatures affect the magnitude and spectral quality through the dependence on the Planck equation.

Field spectral radiance measurements are often used to validate models that are based on reflectance and emittance properties of target and background materials to spectral radiances at

a sensor including all solar and sky emission illumination sources, surface temperatures, BRDF effects, and atmospheric transmission and path radiance effects. However field measurements are of only limited value in directly understanding the fundamental reflectance and emittance properties of materials.

Field spectral radiance measurements are especially useful for characterizing statistical characteristics of target and background radiances. A catalog of hyperspectral radiance measurements between 3 and 14 μm has been generated by ERIM. This catalog contains data collected using a BOMEM Fourier Transform Spectrometer on a computer controlled pan-tilt mount. These data have been collected under contract to the Air Force as part of the Advanced Research Projects Agency (ARPA) Multispectral Program and under contract to Naval Research Laboratory (NRL) as part of the Navy Multispectral Program. These data show that narrow band radiance in the MWIR and LWIR for vegetative and desert backgrounds are very highly correlated. The correlation coefficients are frequently larger than 0.99 and sometimes as high as 0.9999 between bands away from the atmospheric absorption edges and away from the shorter end of the MWIR and the influence of solar reflection.

High spectral correlations in the MWIR and LWIR suggest that the spectral emittance variations are small and that almost all of the variation in the data is caused by temperature variation. Temperature variations affect all thermal spectral bands in nearly the same way, hence temperature-induced variation should be expected to cause highly correlated variations. The surprising result is that the uncorrelated variations in the thermal infrared spectral emissivities are so very small.

Diurnal variations in the solar input and variable cloud cover can affect the data in the reflective visible and SWIR in much the same way as variations in temperature in the thermal IR. They give rise to correlated variations in the visible and SWIR although the spectral correlations the visible and SWIR tend to be smaller than in the thermal infrared. This is presumably to the electronic transitions and a variable chemical content in many materials in the visible and SWIR.

3.4.4 Imagery

There are several sources of readily available airborne and spaceborne multispectral data. ERIM has flown several multispectral scanners along flight lines over much of the United States beginning in the mid 1960s. The original multispectral scanner included 12 visible and near IR bands between 0.4 and 0.9 μm ; three SWIR bands (1.0-1.4, 1.5-1.9, and 2.0-2.6 μm); a MWIR or LWIR band; and an analog recorder system. The most recent version has 30 available bands, digital recording of 16 bands at a time, and a motion measurement system for geocoding the data.

Daedalus has a commercial product line of multispectral scanners that have collected data for a wide variety of programs. For example, data over a number of backgrounds are available as part of the DARPA InfraRed Data Library (DIRDL) at ERIM. These data were collected in support of the High Resolution Calibrated Airborne Measurements Program (HICAMP) and TEAL RUBY programs.

HICAMP is a staring focal plane array imaging sensor that collects data both in a staring mode and in a pushbroom scanner mode. Data in selected MWIR (filter selectable) and LWIR

(filter selectable) bands over a variety of backgrounds and aircraft targets are available in DIRD L.

Infrared Analysis and Measurements and Modeling Program (IRAMMP) is a two-band sensor operating in the MWIR (filterwheel selectable) and in the LWIR. Two bands over clouds, blue sky, and terrain are cataloged and available from QuestTech.

Data from the Landsat and Système Pour l'Observation de la Terre (SPOT) satellite multispectral sensors from almost anywhere in the world is available from the Sioux Falls Data Center in South Dakota and from SPOT Inc. in Washington D.C.

4.0 MULTISPECTRAL AND HYPERSPECTRAL SENSING

Multispectral and hyperspectral remote sensing across the visible and thermal infrared has become practical in large part because of the advances in detector technology over the last two decades. Section 4.1 will describe these developments very briefly (detailed discussions can be found in the IR Handbook and in the IRIS IR Detector Specialty Group Proceedings). Section 4.2 presents a brief review of the principles of spectral radiometry. Section 4.3 discusses the main characteristics of multispectral scanning, and Section 4.4 discusses several approaches to hyperspectral imaging. Section 4.5 and 4.6 present design characteristics of several current and planned airborne and spaceborne multispectral and hyperspectral imaging sensors.

4.1 DETECTORS AND DETECTOR ARRAYS

Optical detectors operate on a variety of photoemissive, photoconductive, and photovoltaic principles. Photocathodes in the visible and very near IR, silicon detectors in the visible and near infrared (out to about 1.1 μm), InSb photovoltaic detectors from 1 to about 5.5 μm , and HgCdTe photoconductors in the infrared from 3 to 12 μm offer high performance operation and are frequently used detectors. PtSi detectors for operation in the MWIR from 2 to about 5.5 μm have a lower quantum efficiency but can be produced in the form of large two-dimensional focal plane arrays. Extrinsic Si (e.g., Si:In in the MWIR and Si:Ga in the LWIR) detectors require a very low operating temperature but may be preferred for low background applications, and monolithic silicon two-dimensional focal plane detector assemblies are easier to fabricate for use in the LWIR than HgCdTe arrays which normally must be bump-bonded to silicon readout.

Imaging with a single detector requires two-dimensional scanning over the entire object field of view. Linear arrays can reduce the requirement for scanning to one dimension. HgCdTe linear arrays developed for the Army Common Module Program are used for a wide variety of LWIR imaging sensors. More recent developments of two-dimensional detector arrays have further reduced the requirement for scanning.

The development of one- and two-dimensional detector arrays is very significant for several reasons. The first is the significant increase in sensitivity available with the large number of detectors in the detector arrays. The second is the temporal processing that becomes practical with detector arrays. A two-dimensional rigid focal plane significantly reduces the number of degrees of freedom of motion between subsequent image frames so that image registration and clutter suppression by frame-to-frame subtraction become a practical reality. Third, two-dimensional detector arrays permit hyperspectral scanning with one dimension used for spatial information and the other dimension for spectral information.

4.2 SPECTRAL RADIOMETRIC MEASUREMENTS

Spectral radiometric measurements of a nonimaging type are used to obtain the spectral characteristics of radiance, reflectance, emittance, and transmittance. These measurements have been the basis for many of the developments of modern physics and astronomy and are also frequently used as a means of materials identification. Interferometric techniques, long a mainstay of atomic and molecular physics, provide very high spectral resolution data, and prism and grating spectrometers, spectral filters, and variable spectral filters can be found in many common instrument designs.

The recent development and use of the Fourier transform spectrometer (FTS) is largely due to the availability of the laboratory computer and electronic digital signal processing technology. The principle of the FTS is that of a Michelson interferometer with a variable path length in one arm. A time varying path length causes the fringes in the output of the spectrometer to vary in intensity due to constructive and destructive interference. The temporal output of a detector at the output of the interferometer is then the Fourier transform of the spectrum at the input. The FTS allows high resolution spectra to be collected using a single detector.

High resolution (ultraspectral) techniques can be used to monitor an area for the presence of chemical and biological warfare (CBW) agents or vapors produced in the production of illegal substances by detecting a unique "fingerprint" signature. Military applications of high resolution, ultraspectral imaging sensors are, however, limited because of the general requirement for high spatial resolution with imaging systems.

The development of one- and two-dimensional detector arrays has provided for a number of sensor developments that have led to high spectral resolution (multispectral and hyperspectral) scanners and imaging spectrometers.

4.3 MULTISPECTRAL SCANNERS

Multispectral scanners are most frequently configured to scan a detector across the ground beneath an aircraft to provide imaging in the cross-track direction. Aircraft motion provides the second dimension to the image. Multispectral imaging can be achieved with a dispersing element and an array of detectors behind the field stop. Multispectral scanners can also be configured with a linear array of detectors in the image plane of the scanner with each detector spectrally filtered separately and brought into spatial registration by appropriate time delay techniques.

ERIM developed the first multispectral scanner in 1963 with subsequent developments leading to the current ERIM M-7 mapper multispectral scanner. This scanner included a dispersive element in the visible near-infrared and spectrally filtered linear arrays in the infrared. The instantaneous field of view (IFOV) is scanned orthogonal to the direction of motion of the aircraft to provide imaging in one dimension. Aircraft motion provides motion in the other dimension. The field stop defines the IFOV (spatial resolution). A dichroic beam splitter in the optical path divides the beam. The transmitted beam (in the visible and near IR) is dispersed through a prism and imaged onto a fiber optic bundle coupled to an array of detectors. The spectral data are collected simultaneously and are spatially registered. The

reflected beam is imaged onto a linear array of detectors, each with its own spectral filter. These data are collected simultaneously and are brought into spatial registration by appropriate time delay. Additional spectral coverage is obtained by deflecting a portion of the beam onto another linear array of filtered detectors. An optical schematic is shown in Figure 4-1 with the spectral bands shown in Figure 4-2.

The ERIM M-7 scanner has been used in support of many DoD and National Aeronautics and Space Administration (NASA) multispectral programs and currently covers 30 spectral bands with 18 in the visible and very near IR, 6 bands in the SWIR (1-2.5 μm), and 6 bands in the 3-12 μm range). The sensor IFOV is 2.5 mrad and the sensitivity is typically $\text{NE}\Delta\rho \leq 0.05\%$ in the reflective bands and $\text{NE}\Delta T \leq 0.10\text{K}$ in the thermal bands. The ERIM M-7 mapper utilizes a state-of-the-art high bandwidth, six degree of freedom, motion measurement system for precision geometric image correction, orthorectification, geocoding, and multipass mosaics.

A family of multispectral scanners based on similar principles is available from Daedalus and is both widely used and commercially available. One is the Daedalus 1268 Thematic Mapper Simulator (TMS); among its 11 bands are 6 spectral bands in the visible and reflective IR and one band in the LWIR to match the spectral bands of the Landsat Thematic Mapper. This scanner has been used to collect a wide variety of data in support of various DoD and other government sponsored programs.

The Thermal Infrared Multispectral Sensor (TIMS) is a Daedalus scanner configured with an array of 6 bands in the LWIR selected primarily for geologic remote sensing brought into registration by appropriate time delay. The TIMS sensor was one of the first sensors to collect multispectral data in the thermal infrared.

Multispectral scanners typically have a small number of detectors, one for each spectral band, that scan a two-dimensional image space. Sensitivity is generally limited by the number of photons that can be collected in a dwell time, and this then limits the number of spectral bands and the spectral resolution available using typical multispectral scanner technology as represented by the ERIM or Daedalus multispectral scanners.

4.4 IMAGING SPECTROMETERS

The development of large one- and two-dimensional focal plane arrays has led to the development of a variety of imaging spectrometers. NASA and the Jet Propulsion Laboratory (JPL) developed the first hyperspectral imaging spectrometer known as the Airborne Imaging Spectrometer (AIS) in 1983 (and retired in 1987). The AIS was a pushbroom scanner using a 64 by 64 two-dimensional focal plane array. One dimension of the array provides the cross track image along the flight line. The other dimension is spectral. The AIS could be configured to operate between 0.78 and 2.14 μm for vegetation studies or 1.19 and 2.53 μm for geological studies.

The JPL Airborne Visible-Infrared Imaging Spectrometer (AVIRIS) was developed in 1987 to collect data in 224 spectral bands between 0.4 and 2.5 μm . The AVIRIS is a scanning spectrometer. Four optical fibers are connected to four spectrometers which define the field stop for the AVIRIS telescope. Spectrometer A contains a linear array of Si detectors, and spectrometers B, C, and D each contain a linear array of indium antimonide detectors. There

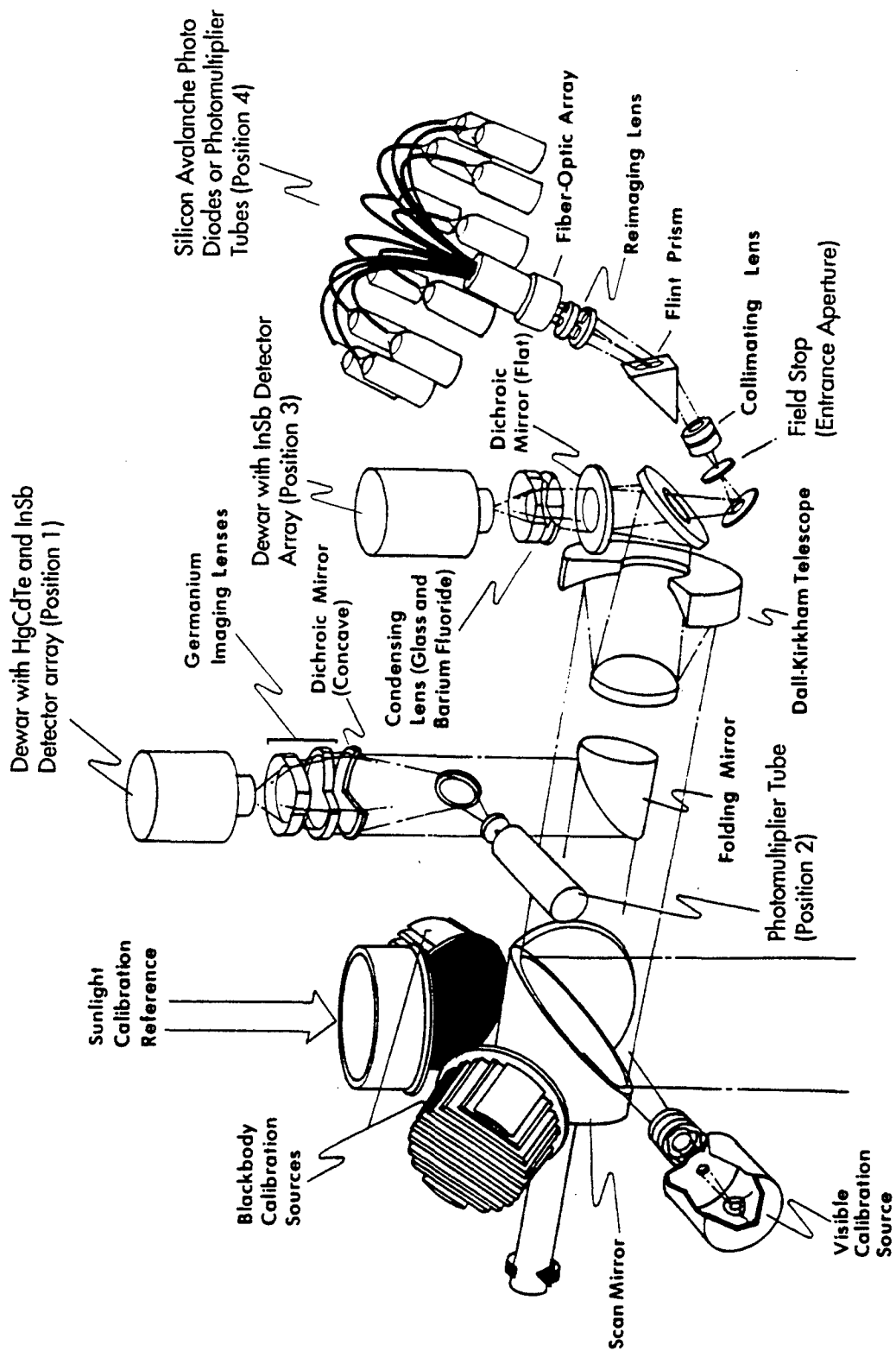


Figure 4-1. M-7 Mapper Optical-Mechanical Layout

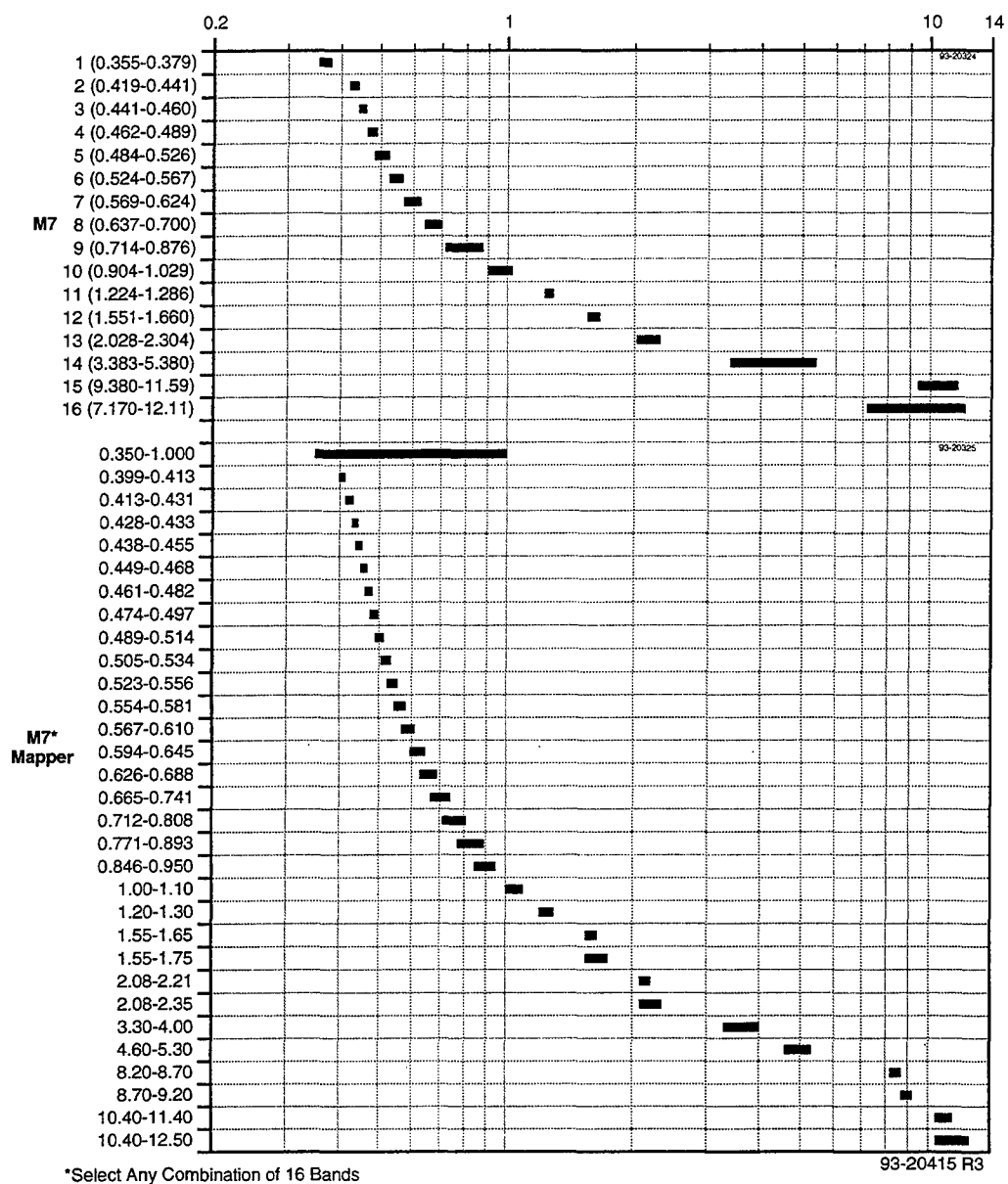


Figure 4-2. Band Comparison of Multispectral Data Collection Systems

are 224 spectral bands of which 220 are usable. The spectral ranges of spectrometers A, B, C, and D are 0.40 to 0.71, 0.68 to 1.28, 1.24 to 1.86, and 1.83 to 2.45 μm . There are 210 spectral bands after spectral resampling.

The most recent development has been the sensor being developed for the Hyperspectral Digital Imagery Collection Experiment, HYDICE, covering the spectrum between 0.4 and 2.5 μm with 206 spectral channels. HYDICE represents a significant advance in the state of the art in hyperspectral sensors by combining higher signal-to-noise ratio (SNR) and significantly better spatial and spectral resolution and radiometric accuracy than earlier systems. The optical system consists of an off-axis telescope and a double pass prism spectrometer, and the heart of the sensor is a 320 x 210 pixel InSb detector array which is "pushbroomed" along the flight path.

The MultiSpectral Infrared Camera (MUSIC) sensor is a modification of the HICAMP sensor with a 45 by 90 extrinsic Si detector array in the LWIR. Data are collected in 45 spectral bands. A spectrally variable filter is placed just in front of the focal plane detector array. The sensor is operated in a pushbroom fashion. The data are read out once for each pixel of forward motion of the aircraft, and data are brought into spatial-spectral registration with appropriate time delays as part of the post processing.

The Spatially Modulated Imaging Fourier Transform Spectrometer (SMIFTS) represents an alternative to using a dispersive element or variable spectral filter in the optical path. Developed by Defense Advanced Research Projects Agency (DARPA), Office of Naval Research (ONR), and University of Hawaii, SMIFTS is based on the Sagnac interferometer. Rather than varying the optical path length of one arm of the interferometer to generate a temporal Fourier transform of the input (as in the Fourier transform spectrometer), SMIFTS captures the interferogram spatially at the output of the interferometer. The other spatial dimension at the output of the interferometer contains a one-dimensional spatial image of the input. A two-dimensional hyperspectral image is then obtained by operating the SMIFTS in a pushbroom fashion.

SMIFTS is a hyperspectral imaging spectrometer with 100 spectral bands between 1.0 and 2.5 μm . There are a number of practical trade-offs to be considered between a SMIFTS design and a more traditional design using a dispersive element in the optical path such as HYDICE. However, both designs take full advantage of the two-dimensional focal plane technology and use one dimension for spatial imaging and the other for spectral imaging. The high spectral resolution, the large number of spectral bands, the high spatial resolution, and the longer dwell times all result from the availability of the two-dimensional focal planes.

HYDICE and SMIFTS represent state of the art approaches to hyperspectral imaging spectrometers, but there are many hyperspectral imaging sensors available today. Brief descriptions of a number of these are included in Sections 4.5 and 4.6.

4.5 CURRENT AND PLANNED AIRBORNE SENSORS

This section presents brief summaries of current and planned airborne multispectral imaging scanners and hyperspectral imaging sensors.

4.5.1 Airborne Multispectral Imaging Scanners

Characteristics of six commonly used current airborne multispectral imaging scanners are summarized in Table 4-1. The sensors are presented in alphabetical order.

4.5.1.1 ATM and ATMX (Airborne Thematic Mappers) (AADS 1268 and AADS 1278)

These sensors have been designed and build by Daedalus, Inc. At least a dozen are in use in various parts of the world. The instrument was designed to spectrally match the six reflective spectral bands of the Landsat Thematic Mapper, which was first launched in 1982. The thermal channel has a broader bandpass to improve SNRs in airborne mapping operations. In addition, there are four other visible and near infrared (VNIR) bands, for a total of 11.

4.5.1.2 Calibrated Airborne Multispectral Scanner (CAMS)

This NASA-sponsored and -operated instrument is flown in the NASA/SSC Learjet 23. Like the ATM, it was designed to provide spectral matches to the Landsat Thematic Mapper bands, plus two additional visible bands.

4.5.1.3 Multidetector Electro-Optical Imaging Sensor (MEIS)

This pushbroom scanner was developed and is available from MacDonald Dettwiler and Associates in Canada. It acquires data in eight narrow spectral band selectable from the VNIR spectral region.

4.5.1.4 M-7 Multispectral Mapper

This pioneering sensor was developed in the early 1970s by ERIM (Environmental Research Institute of Michigan). It still is operational and was upgraded in 1993. Selection and recording is done on any of 16 individual bands or band combinations selected from a possible 31 spectral bands. The M-7 is the only system to provide capability for coverage simultaneously in all spectral regions from the ultraviolet (UV) through visible, NIR, SWIR, MWIR, and LWIR. It also has been used with special position measurement equipment, allowing accurate mosaicking of adjacent passes.

4.5.1.5 NS001 (Thematic Mapper Simulator)

The NASA-developed NS001 is another simulator of the Landsat Thematic Mapper spectral bands. It has one additional SWIR band.

4.5.1.6 Thermal Infrared Multispectral Scanner (TIMS)

This six-band thermal scanner was developed by Daedalus, Inc., to specifications developed by NASA/JPL. Its purpose was primarily for geological mapping, taking advantage of spectral emissivity differences in the LWIR spectral region. TIMS is flown on NASA aircraft, for example, C-130 or ER-2.

Table 4-1. Observation Characteristics of Airborne Multispectral Imaging Sensors

	0.2 μm	0.4 μm	Visible	NIR	SWIR	MWIR	5.5 μm	7.5 μm	LWIR	IFOV (mrad)	FOV	Pixels /Line	Digitization	Oper. Date
ATM and ATMX										14.0 μm				
VIS/NIR	0.42-1.05		8 bands							1.25/2.50	43°/86°	716	8 bits (10 bits for some ATMX channels)	1982
SWIR	1.55-2.35				2 bands				1 band					
LWIR	8.50-12.50													
CAMS														
VIS/NIR	.045-0.90		6 bands											
SWIR	1.55-2.35				2 bands					2.5	100°	700	8 bits	1987
LWIR	10.20-12.50								1 band					
MEIS														
VIS/NIR	.39-1.10		8 bands							0.7	40°	1024	8 bits	1983
M7 Mapper														
UV/Pan	0.35-1.00		1 band											
VIS/NIR	.040-1.00		18 bands											
SWIR	1.00-2.35				6 bands					2.5	90°	738	8 bits	1972, upgraded in 1993
MWIR	3.30-5.30				(16 bands or combinations of 31 bands are recorded)	2 bands			4 bands					
LWIR	8.20-12.50													
NS001														
VIS/NIR	0.46-0.91		4 bands											
SWIR	1.130-2.38				3 bands					2.5	100°	699	8 bits	
LWIR	10.90-12.30								1 band					
TIMS														
LWIR	8.20-12.60								6 bands	2.5	86°	714	8 bits	1981

4.5.2 Airborne Hyperspectral Sensors

This section presents brief profiles of 19 airborne hyperspectral sensor systems currently (May, 1994) or nearly available for data acquisition. These 19 systems are summarized in Table 4-2. This section was contributed by Ronald J. Birk, Commercial Remote Sensing Program, Sverdrup Technology, Inc., Stennis Space Center, MS, and Thomas B. McCord, SETS Technology, Inc., Mililani, HI, and Hawaii Institute of Geophysics and Planetology, University of Hawaii, Honolulu, HI. The paper was presented at the 47th National Aerospace and Electronics Conference, Dayton, OH, May 23-27, 1994 and is included in its entirety in Appendix B.

4.5.3 System Profiles

AAHIS-1 - SETS Technology, Inc.

The Advanced Airborne Hyperspectral Imaging System-1 (AAHIS-1) is being developed by SETS Technology, Inc., to demonstrate the value of very high quality hyperspectral imaging data for a variety of land surface and underwater applications. This fully funded system will first fly in May 1994 and should be available as a service starting in the summer of 1994. This first system is optimized for the visible and blue portions of the spectrum (440-835 nm, 36 or 73 channels) to concentrate on littoral, vegetation, and underwater applications. The AAHIS-1 uses the latest technology, including a two-dimensional focal plane, to achieve the highest data quality in a pushbroom mode. Performance expected includes 1 m ground spatial dimension (GSD) at 1 km altitude with SNR > 500:1 per spectral channel for 20% albedo. The system will first be flown on a Piper Aztec in Hawaii but is available for flight around the world. The compact AAHIS-1 is easily operated and can be carried from place to place as personal baggage. Several applications flights are already planned and funded. Over the next year, the system will be extended to cover the spectral range out to about 2.5 μm . The data are collected directly onto a 1.2 GB hard drive as measured through a high-speed port at about 0.3 Mb/s so that approximately a 40 km-long swath can be recorded before downloading to Exabyte tape. The data are to be processed by SETS Technology, Inc. using their existing Hyperspectral Image Processing System (HIPS) and its related tools. Several data sets have already been collected and processed using a prototype sensor of similar specifications to prove the technology.

AHS-Daedalus Enterprises, Inc.

The Airborne Hyperspectral Scanner (AHS) (formerly MAS), developed by Daedalus Enterprises, Inc., has been operational since 1991. Applications for this system include environmental studies, mineral exploration, oceanography, satellite simulation, and forest fire environmental impact. The NASA Ames Research Center (ARC) and Goddard Space Flight Center (GSFC) are using Daedalus' spectrometer to develop an airborne simulator for the MODIS-N instrument. When flown with the TIMS, the system can approximate the Advanced Spaceborne Thermal Emission and Reflection Radiometer (ASTER) (Grant and Myers, 1992).

Table 4-2. Observation Characteristics of Airborne Hyperspectral Imaging Sensors

	0.2 μm	0.4 μm	Visible	NIR	SWIR	2.5 μm	3.0 μm	MWIR	5.5 μm	7.5 μm	LWIR	IFOV (mrad)	FOV	Pixels /Line	Digitiz- ation
AAHIS VIS			30-72 bands									1.0	193 mr	193	12 bits
AHS VIS			20 bands												
SWIR					15 bands							2.5	85.92°	715	12 bits
MWIR								7 bands							
LWIR											6 bands				
AIS VIS/NIR				24 bands											
SWIR					7 bands							2.5-4.5	90°	512-1024	16 bits
SWIR						32 bands									
AMSS VIS/NIR				32 bands											
SWIR					8 bands							2.1 x 3	92.16°	768	8 bits
LWIR											8 bands				
ASAS VIS/NIR				62 bands								0.7	19°	512	12 bits
AVIRIS VIS/NIR/SWIR				224 bands											
												1.0	30°	614	12 bits
CASI VIS/NIR				<288 bands								1.2	35.4°	578	12 bits
CHRS VIS/NIR				125 bands								0.17-0.5	10.3°	1024	digital/ analog data
DAIS-2815 NIR				1 band											
MWIR								3 bands				1.0	82°	512-2048	15 bits
LWIR											20 bands	2.5 5.0			

Table 4-2. Observation Characteristics of Airborne Hyperspectral Imaging Sensors (Continued)

	0.2 μm	0.4 μm	Visible	NIR	SWIR	2.5 μm	3.0 μm	MWIR	5.5 μm	LWIR	IFOV (mrad)	FOV	Pixels /Line	Digitization
DAIS-7915														
VIS/NIR	.40-1.00		32 bands								1.1			16 bits
SWIR	1.00-1.80		8 bands								2.2	78°		
SWIR	1.97-2.45				32 bands						3.3			
MWIR	3.00-5.00							1 band						
LWIR	8.00-12.30									6 bands				
HYDICE														
VIS/NIR/SWIR	.40-2.50			206 bands							0.5	8.94°	312	12 bits
MVIS														
VIS/NIR	.43-.83		20 bands											
SWIR	1.15-1.55				8 bands						2.0	72°	755	12 bits
SWIR	2.00-2.50				64 bands									
LWIR	8.20-12.70									10 bands				
MUSIC														
MWIR	2.500-7.0							90 bands			0.5	1.3° swath width x 2.6°	45	80 f/sec digital PCM
LWIR	6.00-14.50									90 bands				
ROSIS														
VIS/NIR	.43-.88		256 bands								0.55	±16°	512	12 bits
SMIFTS														
NIR/SWIR/MWIR	1.00-5.20					100 bands					0.66	9.7°	256	12 bits
TRWIS B														
VIS/NIR	.46-.88		90 bands								1	14°	240	8 bits
TRWIS-SC														
VIS/NIR	.46-.88		90 bands								1	60°	1000	8 bits
TRWS-II														
SWIR	1.50-2.50										.5/1	7/14°	240	8 bits
WIS														
VIS	.40-.60		17 bands											
NIR	.60-1.00													
SWIR	1.00-1.80		67 bands								0.65	20°	512	12 bits
SWIR	1.80-2.50									45 bands				

AIS-Geophysical Environmental Research

The AIS developed by Geophysical Environmental Research (GER) is a 63-channel AHS. This system began operating in 1987, providing surface mineral direct mapping for commercial use. Between 1987 and 1990, this system was flown over the U.S.A., Australia, Germany, Great Britain, France, Spain, Italy, and Israel (Collins and Chang, 1990). Applications for this sensor include environmental monitoring, oil and mineral exploration, mapping, and military targeting.

AMSS-Geoscan PTY LTD

The Airborne Multispectral Sensor System (AMSS) was developed by Geoscan PTY LTD of Australia. This AHS, which was built for commercial mineral exploration, has been operational since 1989. Its applications include mineral, oil, and gas exploration as well as environmental monitoring. The SNR of the AMSS imagery is high enough to enable band differences to be used for simplified image processing in mineral detection. By use of two or three band differences, the band shapes for specific minerals can be outlined. In addition, single black and white band difference images can show major mineral types directly in an alteration envelope. The minerals can be shown to be present in GER Infrared Intelligent Spectroradiometer (IRIS) ground spectra taken in the scanner-indicated zones (Lyon and Honey, 1990).

ASAS-NASA/Goddard Space Flight Center

The Advanced Solid-State Array Spectroradiometer (ASAS) was developed by NASA/GSFC. In its current configuration, this AHS has been operational since 1992. ASAS is currently the only airborne imaging system with off-nadir pointing capability. Off-nadir pointing imaging devices offer multidirectional observations of bidirectional reflectances and increased temporal coverage potential. With its bidirectional and spectral characteristics, ASAS is ideally suited to provide data for Earth Observing System (EOS) era research: pointing capabilities are proposed for the Multiangle Imaging Spectroradiometer (MISR) on EOS (NASA/GSFC, unpublished). Applications for the sensor include bidirectional reflectance studies, off-nadir viewing, stereo-image analysis, terrestrial ecosystem field experiments, and simulator for EOS spaceborne instruments.

AVIRIS - NASA/Jet Propulsion Laboratory

The AVIRIS AHS was developed by NASA/JPL. This AHS is designed to measure the upwelling spectral radiance in the region where solar reflected energy from the Earth's surface is dominant. AVIRIS is the first Earth-looking imaging spectrometer to cover the entire solar surface-reflected portion of the electromagnetic spectrum in narrow contiguous spectral channels (Green et al., 1992). AVIRIS is calibrated at better than 5 percent. The sensor produced its first airborne images in 1986 and its first science data in 1987. The system has been fully operational since 1989. Applications for AVIRIS include imaging spectrometry research and applications, terrestrial land ecology, ocean ecology and bathymetry, geology and soil science, hydrology, atmospheric aerosols and gases, environmental monitoring, and spaceborne system calibration and modeling.

CASI-ITRES Research Ltd.

ITRES Research Ltd. of Canada has developed the Compact Airborne Spectrographic Imager (CASI), which has been operational since 1988. CASI is a highly sensitive pushbroom imager that captures both spatial and spectral information from each line image without any scanning or other mechanical motions. CASI provides programmable spectral band sets and easy switching between spectral and spatial information during data acquisition. Water applications include pollution and algae bloom monitoring, benthic weed surveys, and bathymetry and subsurface feature investigations. Vegetation applications include vitality analysis, species discrimination, cover estimation, right of way surveillance, illicit crop detection, and soil evaluations. In addition, CASI can be used as a tool for providing direct digital input data for Geographic Information System (GIS). ITRES is developing a companion system for CASI that will generate the necessary navigation and pointing information to provide direct inputs for GIS (Babey and Anger, 1993).

CHRISS-Science Applications International Corporation

The Compact High-Resolution Imaging Spectrograph System (CHRISS) developed by Science Applications International Corporation (SAIC) has been operational since 1992. The system features high spectral and spatial resolution, decreased weight, small size, and both digital and analog data recording. CHRISS uses a staring optical design and a high throughput, low aberration spectrograph in a pushbroom imaging format (Speer et al., 1992). Applications include petroleum seepage, vegetation identification, environmental and global change, DoD camouflage discrimination and reconnaissance, and NASA forestry and ocean color. SAIC is currently building a new version of CHRISS; parameters for the new system will soon be available.

DAIS-2815 - Geophysical Environmental Research

The ASTER Simulator (DAIS-2815) developed by Geophysical Environmental Research has been operational since 1991. This system is designed to simulate ASTER's VNIR band 3 and Thermal Infrared (TIR) bands 10-14. In addition, the scanner has three MWIR bands between 3 μm and 5 μm to investigate this region's use for geological and environmental remote sensing. All data from this instrument can be used in general image processing software, such as ERDAS or GenIsis (Watanabe et al., 1991).

DAIS-7915 - Geophysical Environmental Research

The 79-channel DAIS-7915 was developed by Geophysical Environmental Research for detection, analysis, and mapping. The system is currently under development (Birk, 1992).

HYDICE - Naval Research Laboratory

The HYDICE AHSS is being developed by the Naval Research Laboratory under the Congressional Dual-Use Initiative for transfer of military technology to the civil sector. Researchers are exploring the use of hyperspectral data for problems in agriculture, geology, the environment, coastal ocean processes, ocean optics, the marine atmospheric boundary layer, bathymetry, and water clarity measurements. HYDICE is being build to research the use of an

advanced imaging spectrometer to evaluate the data's usefulness and to determine how to build a truly operational system (Rickard et al., 1993).

MIVIS - Daedalus Enterprises, Inc.

The Multispectral Infrared and Visible Imaging Spectrometer (MIVIS) produced by Daedalus Enterprises, Inc., has been operational since 1993. MIVIS contains a 10-channel TIR band, a 64-channel spectrometer covering the 2-2.5 μm region and 8-channel NIR, and a 20-channel visible imaging spectrometer (VIS). The 102-channel MIVIS is designed primarily for mineral and oil exploration (Baker, 1991). Other applications may include oceanography, environmental studies, plant stress, and thermal mapping applications.

MUSIC - Lockheed Missiles and Space Company, Inc.

MUSIC was developed by Lockheed Missiles and Space Company, Inc. (LMSC) for ARPA. The current version has been operational since 1989. MUSIC is a cryogenic staring thermal infrared sensor with dual telescopes. The telescopes produce data frames in two bands simultaneously. Spectral filtering by multilayer interference filters is provided in each telescope to define the spectral band of radiation reaching the detectors. Either fixed spectral filters or a circular variable filter can be commanded in each telescope. An on-board computer controls the operation of the sensor, including selection of spectral filters, detector array frame rate, operation of the tape recorders, and pointing of the gimbaled mirror pointing and stabilization system (Kulgein et al., 1992). MUSIC's applications include chemical vapor sensing, plume diagnostics, and target and background spectral signatures.

ROSIS - DLR

The Reflective Optics Systems Imaging Spectrometer (ROSIS), developed by DLR in Germany, has been operational since 1992. Because of its purely reflective concept, ROSIS extends in both spectral directions. This system was particularly tailored to measure ocean parameters, including chlorophyll fluorescence, but the range of applications is growing beyond ocean and coastal zones. Water applications for ROSIS include measurement of water pollution, chlorophyll-fluorescence, plankton blooms and biomass, mesoscale eddies and currents, coastal erosion, mapping of flooded areas, and sea-ice mapping. Land and atmospheric applications include mapping of deforestation, crop status, land use, glacier and snow coverage, clouds, and aerosol amount (Kunkel et al., 1991).

SMIFTS - Advanced Research Projects Agency, Office of Naval Research, University of Hawaii

ARPA, ONR, and the University of Hawaii have developed SMIFTS. The instrument is cryogenically cooled, is robust and compact, and provides simultaneous measurement of all spectral channels. SMIFTS uses spatial modulation and a detector array to sample the interferogram and therefore uses no moving parts to obtain data (Lucey et al., 1992). Applications for this system include airborne imaging spectroscopy, plume observations, thermal profiling, Lightsat emulation, and HYDICE data simulation.

TRWIS-B, TRWIS-SC, TRWIS-II - TRW

TRW is currently flying three models of Imaging Spectrometers: TRWIS-B and TRWIS-SC, which operate in the VNIR regions (0.46-0.88 μm), and TRWIS-II, which operates in the SWIR (1.5-2.5 μm). These instruments have been operated from fixed-wing aircraft, helicopters, and ground platforms. TRWIS-B and TRWIS-II are pushbroom instruments with a swath width of 240 pixels. TRWIS-SC is a cross-track whiskbroom scanner with a swath width of 1000 pixels. All instruments feature simultaneous measurements of all spectral channels to avoid spectral contamination. Extensive software and special-purpose hardware are available to perform sophisticated, rapid processing of data. The data can also be processed in real time in the aircraft to receive immediate identification or quantification of surface material. Applications for these instruments include infrastructure mapping; environmental, agriculture, and forestry monitoring; oil and natural gas exploration; maritime research; and general research (Dr. Donald Davies, personal communication).

WIS - Hughes Aircraft Company/Santa Barbara Research Center

The Wedge Imaging Spectrometer (WIS) developed by Hughes Aircraft Company has been in operation since 1989. This system joins the spectral separation filters to the detector array, eliminating the need for a complex aft-optics assembly and bringing imaging spectrography into an affordable cost range. Its resulting smaller size and weight make it compatible with lightweight satellite or small aircraft use. In addition, its simple, rugged design is well suited to operation by relatively unskilled personnel (Demro and Woody, 1993). WIS sensor data collection is flexible; data acquisition is synchronized with aircraft velocity and focal plane integration times. A wide range of altitudes and velocities are available, and data rectification does not require aircraft attitude information or global positioning system (GPS) (Hughes/SBRC, unpublished). Applications for the WIS include hyperspectral imaging, airborne monitoring, environmental observations, terrain and site classification, crop assessment, and identification of specific materials. Hughes is currently building the next generation WIS. Specifications for Hughes' new WIS, as well as for the other systems profiles above, are listed in Table 4-2.

4.6 CURRENT AND PLANNED SPACEBORNE SENSORS

4.6.1 Merits of Satellite Multispectral Sensing

Satellite multispectral sensing provides synoptic, repeated, broad-area coverage of the entire Earth, with spectral diversity, radiometric quality, and geometric fidelity. Its digital form is important, because it allows for interactive and automated data exploitation. It provides data continuity, with one archive (Landsat MSS) dating back to the early 1970s. Stereo coverage is another advantage of some systems (with off-axis pointing or simultaneous viewing), allowing for extraction of digital terrain elevation data.

On the other hand, temporal revisit frequency is a weakness of some systems, but can be offset by inclusion of off-axis pointing capability. Spatial resolution is moderate to coarse, in comparison to aerial photography or other systems, and obscuration by clouds can be a problem.

4.6.2 Classes of Multispectral Satellite Sensors

For purposes of this report, two classes of spaceborne multispectral sensors are discussed, high-resolution imagers and wide-field systems. System designers have had to make trades between spatial resolution, swath width, and revisit interval, under constraints imposed by telemetry downlinks and other factors. Some of the choices that have been made are summarized in Figure 4-3.

Wide-field systems have large (e.g., 1 km) pixels which permit wide swaths and (up to) daily revisits; they have been designed primarily for meteorological and sea-surface observations. High-resolution imagers have smaller (10- to 30-meter) pixels which lead to more narrow swaths and revisits at two- to six-week intervals, unless they have off-nadir pointing of the sensor which can provide next-day coverage; they have been designed primarily for land remote sensing.

4.6.3 History of Satellite Multispectral Sensing

The satellite multispectral imaging era began in 1972, with USA's launch of Landsat-1, then called the Earth Resources Technology Satellite (ERTS). It had two sensors on board, the Multispectral Scanner Subsystem (MSS) and the Return Beam Vidicon Camera (RBV). The 80-meter-resolution MSS proved to be the more durable and useful of the two instruments. Its four channels of multispectral VNIR data set the stage for the similar and improved sensors which have followed. Like Landsat-1, they are in sun-synchronous polar orbits.

The first major wide-field multispectral system was the USA's Advanced Very High Resolution Radiometer (AVHRR), initially carried in 1978 by the TIROS-N satellite and subsequently by National Oceanic and Atmospheric Administration (NOAA) satellites, beginning with NOAA 6 in 1979.

4.6.4 High-Resolution Multispectral Imagers

Figure 4-4 summarizes the salient characteristics of those systems which have produced the currently available, high-resolution, digital multispectral image data. Looking to the future, characteristics of planned systems are presented in Figure 4-5. The sensors have on-board sources which permit radiometric calibration of the data; however, the primary data applications generally do not rely on absolute calibration of the data.

Landsat MSS data, with 80-meter resolution and finer GSD, were collected continuously and archived from 1972 to 1993 by at least one and often two systems, on Landsats 1 through 5. The Thematic Mapper (TM), a more capable sensor with 30-meter resolution, began collecting data in parallel with the MSS in 1982, from Landsat-4, and continues to this day from Landsat-5. Landsat-6 failed on launch in the fall of 1993, but EOSAT expects the Landsat-5 TM to continue producing good data for several more years. Launch of the Landsat Enhanced Thematic Mapper (ETM) is expected in 1997.

The current Landsat TM has seven spectral bands (three visible, one near infrared, two short-wave infrared, and one long-wave thermal infrared). All bands have 30-meter resolution, except the thermal band which is 120 meters. The normal GSD of the data is 28.5 meters.

The other four current sources of multispectral data are foreign systems. The most important of these is the French SPOT system which has two High Resolution Visible (HRV)

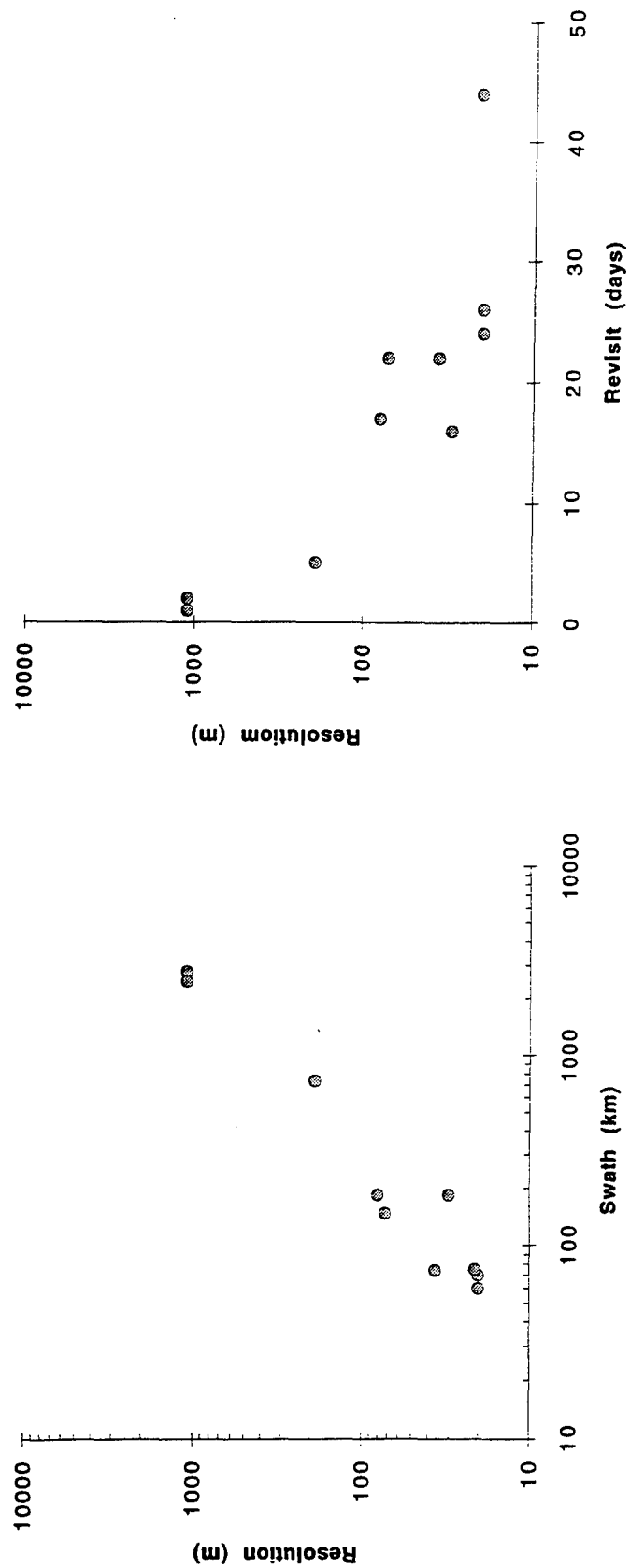


Figure 4-3. Summary of Sensor Sampling Characteristics

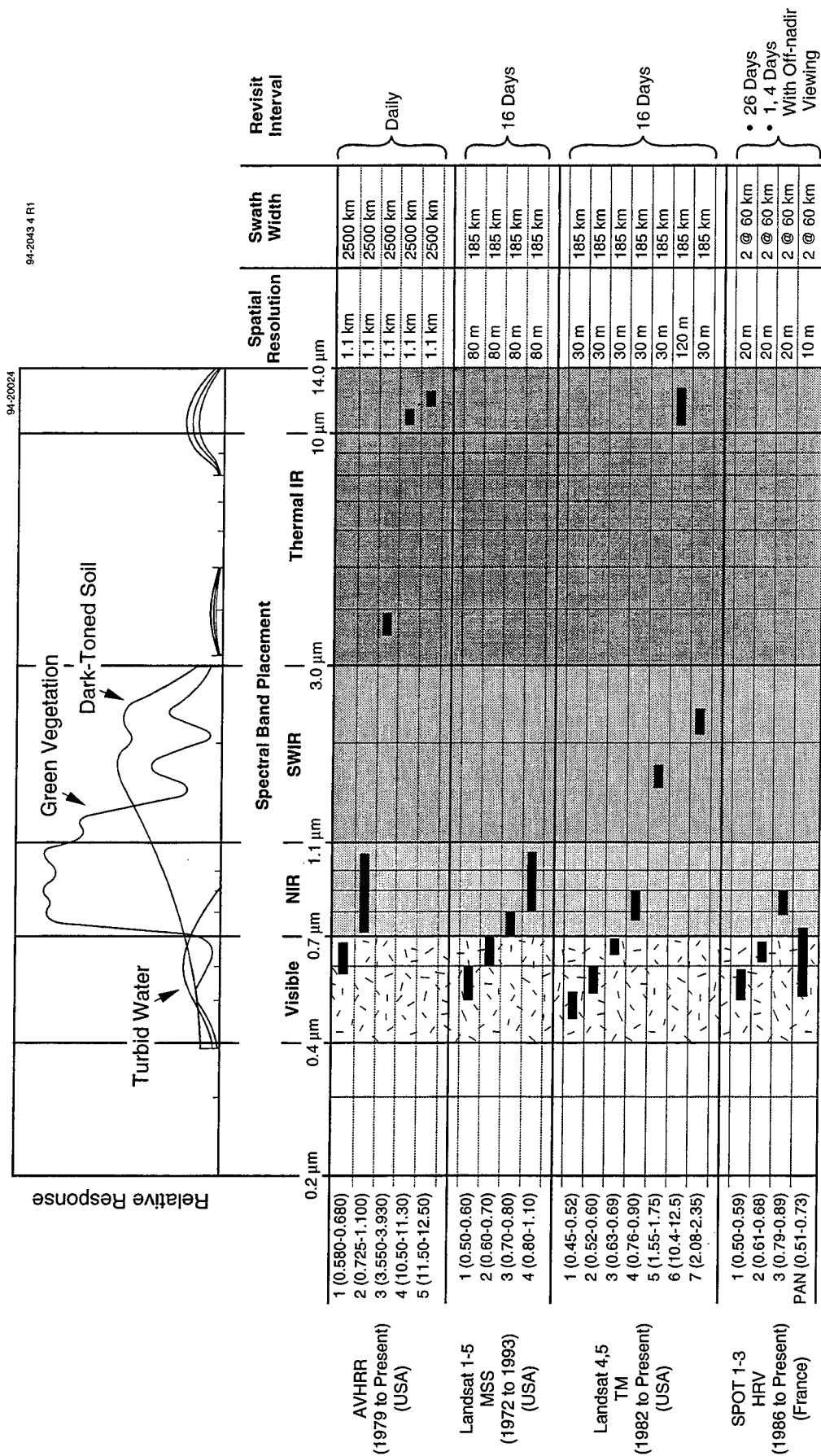
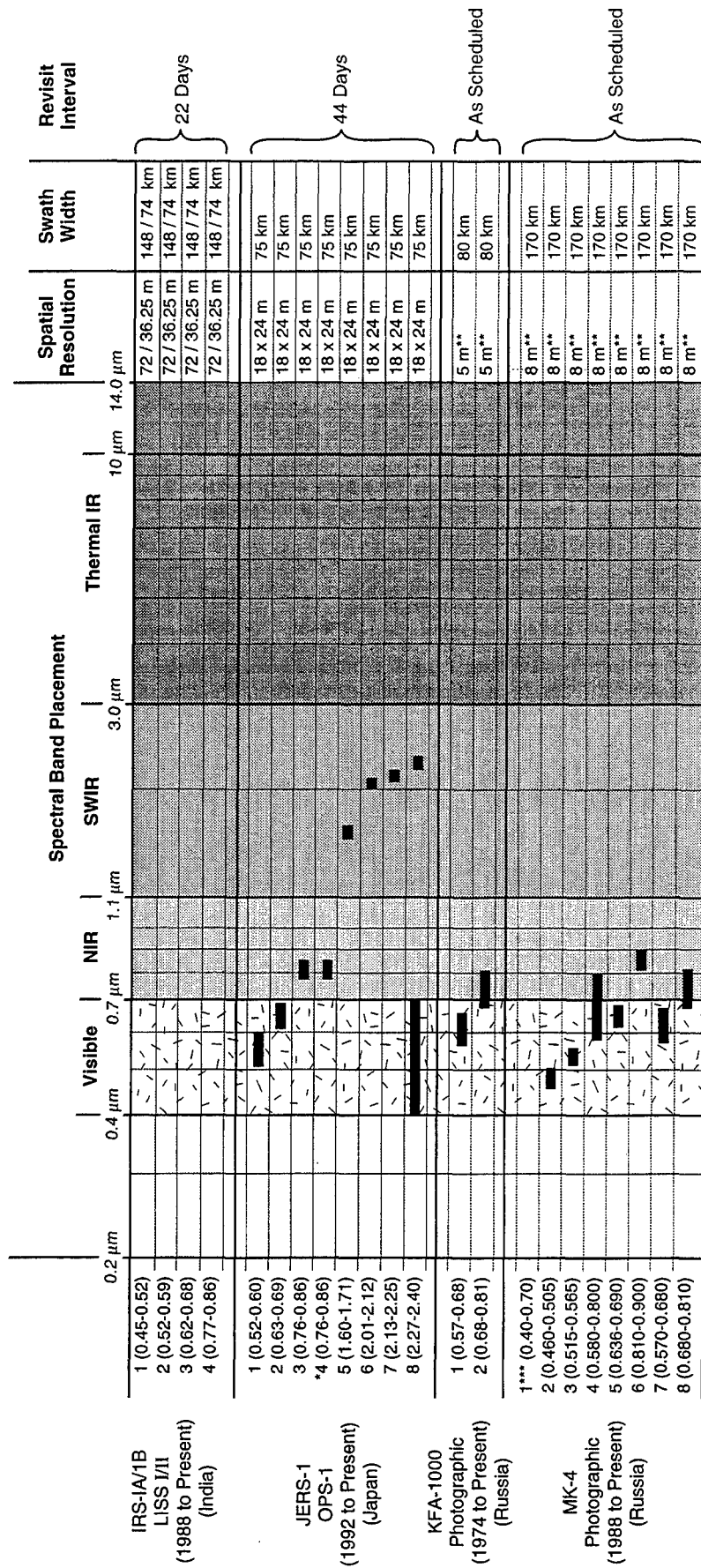


Figure 4-4. Observation Characteristics of Multispectral Satellite Imagers



*Band 4 is 15' forward-looking, for stereo

**Nominal Resolution of Photography, Effective Resolution of Digital Scanned Data Likely Is Larger

***Only Panchromatic and Three MS Bands per Mission

Figure 4-4. Observation Characteristics of Multispectral Satellite Imagers (Continued)

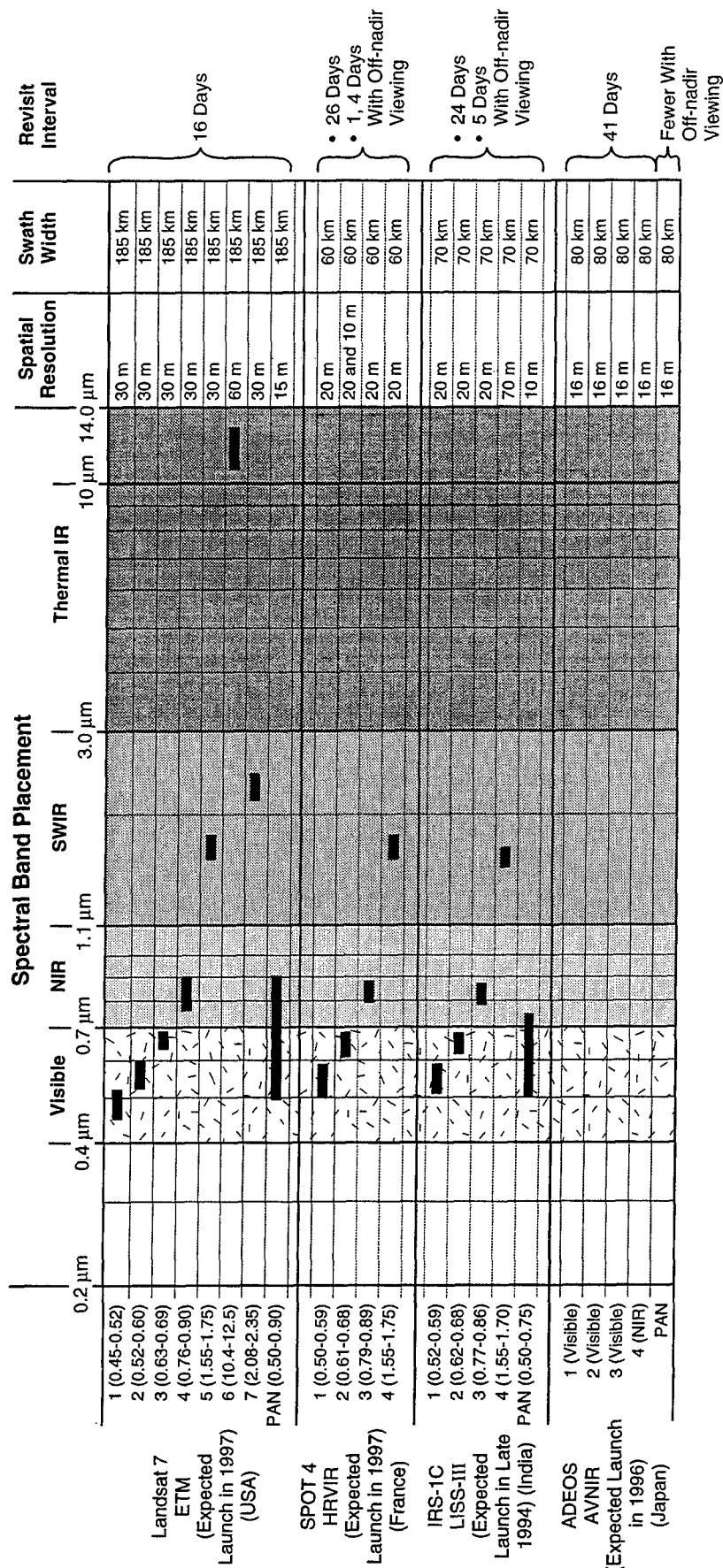


Figure 4-5. Future Improvements to Observation Characteristics of Multispectral Satellite Imagers

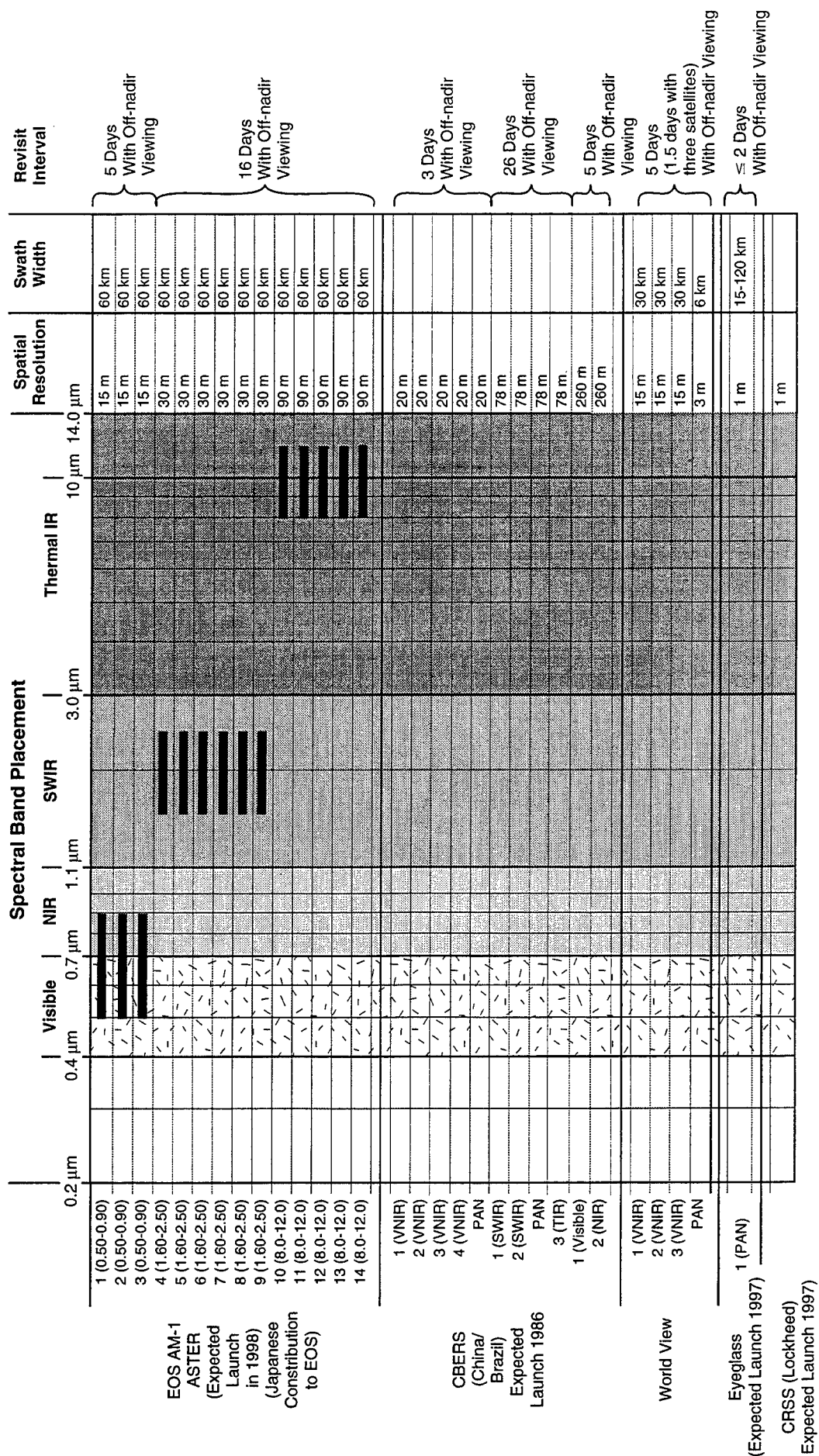


Figure 4-5. Future Improvements to Observation Characteristics of Multispectral Satellite Imagers (Continued)

sensors, each of which has the capability of collecting either three-band VNIR multispectral data at 20-meter resolution or panchromatic data at 10-meter resolution. With its off-axis pointing capability, revisits can occur at 1 and 4 days after viewing any given location. The scene size of SPOT data is 60 by 60 km, which means that more than nine SPOT scenes are required to cover the same area as one 185 by 185 km Landsat scene. While the first three SPOT systems are currently operational, an improved SPOT 4 system is expected in 1997.

The next most important source is from the Indian Remote Sensing Satellites (IRSS) with their Linear Self-Scanning (LISS) sensors. Their 37-meter data are now being marketed in the USA by the EOSAT Corporation. An upgraded, SPOT-like system is expected to be launched later in 1994.

The Japanese Earth Resources Satellite (JERS-1) carries the OPS multispectral sensor, in addition to a SAR sensor. The OPS system has 18 x 24-meter resolution and spectral bands similar to TM, except that a TM 1 match is missing and three narrower SWIR bands cover the spectral band sensed by TM 7; also, a forward-looking NIR band is collected to provide stereo coverage with a spectrally similar down-looking band. Intended primarily as a research system, the quantities of data have been somewhat limited and until recently were restricted to designated researchers or members of the sponsoring Japanese resource companies. After the failure of Landsat-6, the Japanese have made their archives available for purchase to other interested parties. The SWIR portion of the system has produced no data since December 1993.

Russian data are derived by digitizer scanning of space-based multiband photography. Data from two multispectral systems are available for sale through representatives in the U.S. and other Western countries. The KFA-1000 system has two bands, 0.57-0.68 and 0.68-0.81 micrometers, with a nominal photographic spatial resolution of 5 meters; its archive dates back to 1974. Since 1988, the MK-4 sensor has had one panchromatic band and a choice of three multispectral bands from a selection of seven bands between 0.46 and 0.90 micrometers, all at a photographic resolution of 8 meters. It is noted, however, that the effective resolution of the digital products likely are somewhat more coarse than these nominal values. The scene size of the KFA-1000 is 80 x 80 km and that of the MK-4 is 170 x 170 km.

The Japanese plan to launch an improved AVNIR sensor aboard the ADEOS satellite in 1996 and will be the providers of the ASTER sensor for the EOS AM-1 mission in 1998.

In addition, China and Brazil have a joint venture aimed at launching a multisensor earth resources satellite in 1996. Called CBERS, it will include three multispectral sensors. The first is a five-band VNIR system with 19.5-meter resolution (one panchromatic and four VNIR bands) and off-nadir pointing allowing three-day revisits. The second will be an infrared multispectral scanner with three 78-meter reflective bands (panchromatic, two SWIR, and one LWIR) and 26 day revisit. Finally, there will be a wide-field imaging sensor with two bands (visible red and NIR) at 260-meter resolution and three- to five-day revisits.

Important pieces of the future multispectral satellite puzzle may be provided by commercial interests within the U.S. and associates. Several private companies or consortia have recently announced plans for providing future multispectral imaging systems with very competitive characteristics. Three of these systems are: CRSS, Eyeglass, and WorldView.

WorldView Imaging Corp. has indicated plans to launch a sensor in 1995 with three 15-meter VNIR multispectral bands and a 3-meter panchromatic band. With its off-nadir pointing capability, revisits will be 5 days with one satellite and 1.5 days with three satellites. Fore/aft stereo coverage will be included. The swath width will be 30 km for the spectral data and 6 km for the panchromatic data. Accurate geolocation is intended.

Eyeglass, International, expects to launch a 1-meter panchromatic sensor in 1997. With its off-nadir pointing, it will have revisits every two days or less. Stereo coverage is optional, as are a variety of scanning modes using an agile pointing system. Scene size will be 15 x 15 km and swath widths will vary from 15 km to 120 km, depending on the collection mode.

Lockheed Corp. has announced plans for a 1-meter sensor (CRSS) to be launched in 1997. Other details are not presently available.

We observe that it will be important for continued development and growth of defense applications that the U.S. develop reliable, low cost sources of improved multispectral data.

4.6.5 Wide-Field-of-Coverage Multispectral Systems

Figure 4-6 summarizes the major characteristics of some present and planned wide-field systems. Of current systems, only the AVHRR is listed.

Although the AVHRR has been collecting data since 1978, its data were not archived systematically during early stages of that period. Only in recent years have the digital data been made readily available. The major interest for sensor calibration has been for the thermal channels, used for sea-surface temperature measurements. More recently, the VNIR channels have been used for vegetation index measurements.

Note that along with the improved AVHRR planned for 1995, a privately-funded SeaWiFS system will be launched later this year, along with a two-band wide-field sensor on the Indian satellite. Japan will include one on the ADEOS platform in 1996, and France plans a wide-field addition to SPOT 4 in 1997.

	Spectral Band Placement						Thermal IR	Spatial Resolution	Swath Width	Revisit Interval
	0.2 μ m	0.4 μ m	Visible	0.7 μ m	NIR	SWIR	3.0 μ m	10 μ m	14.0 μ m	
AVHRR (1979 to Present) (USA)	1 (0.58-0.68)									Daily
	2 (0.73-1.10)								1.1 km	
	3 (3.55-3.93)								1.1 km	
	4 (10.50-11.3)								1.1 km	
	5 (11.50-12.5)								1.1 km	
Improved AVHRR (Expected) Launch in 1995 (USA)	1 (0.58-0.68)								1.1 km	Daily
	2 (0.73-1.10)								1.1 km	
	3 (3.55-3.93)								1.1 km	
	3a (1.58-1.64)								1.1 km	
	4 (10.50-11.30)								1.1 km	
Sea WiFS (Expected) Launch Late 1994 (USA)	5 (11.50-12.50)								1.1 km	2 Days
	1 (0.40-0.42)								1.1/4.5 km	
	2 (0.43-0.45)								1.1/4.5 km	
	3 (0.48-0.50)								1.1/4.5 km	
	4 (0.50-0.52)								1.1/4.5 km	
IRS-1C WiFS (Expected Launch Late 1994) (India)	5 (0.55-0.57)								1.1/4.5 km	5 Days
	6 (0.66-0.68)								1.1/4.5 km	
	7 (0.75-0.79)								1.1/4.5 km	
	8 (0.85-0.89)								1.1/4.5 km	
	1 (0.62-0.68)								188 m	
SPOT VMI (Expected) Launch in 1997 (France)	2 (0.77-0.86)								188 m	Daily
	1 (0.43-0.47)								1.1 km	
	2 (0.50-0.59)								1.1 km	
	3 (0.61-0.68)								1.1 km	
	4 (0.79-0.89)								1.1 km	
ADEOS OCTS (Expected) Launch in 1996 (Japan)	5 (1.58-1.75)								1.1 km	Daily
	1-6 (Visible)								700 m	
	7-8 (Near IR)								700 m	
	9 (Mid IR-3.7)								700 m	
	10-12 (Thermal IR)								700 m	

Figure 4-6. Observation Characteristics of Present and Planned Wide-Field Multispectral Satellite Sensors

4.7 BIBLIOGRAPHY

- Babey, S.K., and C.D. Anger, "Compact Airborne Spectrographic Imager (casi): A Progress Review," presented at SPIE Conference, Orlando, FL, 15 April 1993.
- Baker, W.T., "Hyperspectral Imaging: An Environmental Monitor," *Sensors*, pp. 19-24, December 1991.
- Birk, R.J., "Airborne Hyperspectral Sensor Profiles." In *Proceedings of the International Symposium on Spectral Sensing Research*, Maui, HI, 15-20 November 1992.
- Birk, R.J. and T.B. McCord, "Airborne Hyperspectral Sensor Systems," presented at the 47th National Aerospace and Electronics Conference, Dayton, OH, 23-27 May 1994.
- Davies, D., personal communication.
- Demro, J.C. and L.M. Woody, "Flight Demonstration of the Wedge Imaging Spectrometer." In *Tactical Technologies and Wide-Area Surveillance International Symposium Proceedings*, Counterdrug Technology Center, 1993.
- Green, R.O., J.E. Conel, and T.G. Chrien, "Airborne Visible-Infrared Imaging Spectrometer (AVIRIS): Sensor System, Inflight Calibration and Reflectance Calculation." In *Proceedings of the International Symposium on Spectral Sensing Research*, Vol. I, Maui, HI, pp. 198-214, 1992.
- Kramer, H.J., "Observation of the Earth and Its Environments - Survey of Missions and Sensors," 2nd Ed., Springer-Verley, 1994.
- Kulgein, N.G., S.P. Richard, W.P. Rudolf, and E.M. Winter, "Airborne Chemical Vapor Detection Experiment." In *Proceedings of the International Symposium on Spectral Sensing Research*, Vol. II, Maui, HI, pp. 1119-1130, 1992.
- Kunkel, B., F. Blechinger, D. Viehmann, H. Van Der Piepen, and R. Doerffer, "ROSIS Imaging Spectrometer and Its Potential for Ocean Parameter Measurements (Airborne and Space-borne)," *International Journal of Remote Sensing*, Vol. 12, No. 4, pp. 753-761, 1991.
- Lucey, P.G., T. Williams, K. Horton, K. Hinck, C. Budney, J.B. Rafert, and T.B. Rusk, "SMIFTS: A Cryogenically Cooled, Spatially Modulated, Imaging, Fourier Transform Spectrometer for Remote Sensing Applications." In *Proceedings of the International Symposium on Spectral Sensing Research*, Vol. I, Maui, HI, pp. 251-262, 1992.

- Lyon, R.J.P. and F.R. Honey, "Direct Mineral Identification (DMI) With Geoscan MK II Advanced Multispectral Scanner (AMSS)," SPIE Proceedings, *Imaging Spectroscopy of the Terrestrial Environment*, Vol. 1298, Orlando, FL, pp. 50-61, 1990.
- Rickard, L.J., R. Basedow, E. Zalewski, P. Silverglate, and M. Landers, "HYDICE: An Airborne System for Hyperspectral Imaging." In *Proceedings of Imaging Spectrometry of the Terrestrial Environment*, Vol. 1937, SPIE, p. 173, 1993.
- Speer, B., C. Coyle, R. Anderson, and G. Mooradian, "Compact, High Resolution Airborne Hyperspectral Imaging Sensor at SAIC." In *Proceedings of the International Symposium on Spectral Sensing Research*, Vol. II, Maui, HI, pp. 948-955, 1992.
- Watanabe, H., M. Sano, F. Mills, S.H. Change, and S. Masuda, "Airborne and Spaceborne Thermal Multispectral Remote Sensing," 1991.

5.0 MODELING AND SIMULATION

Simulation and modeling play an important role in the design of multispectral sensors, in the development of target detection and discrimination algorithms for processing multispectral data, and in estimating probabilities of detection and false alarm. The basis for multispectral detection and discrimination is found in the optical and thermal properties of materials. These properties include spectral reflectance, spectral emittance, bidirectional reflectance, solar absorptivity, thermal emissivity, heat capacity, thermal conductivity, internal heat sources, and so forth, as described in Section 3. Although significant insight into the potential advantages of multispectral sensing can be obtained from an analysis of optical properties, many other factors affect the spectral radiances at a remote sensor. A variety of computer models have been developed that account for all of the significant factors that are based on well understood physical principles.

The design of a multispectral sensor and processor requires spectral radiance data from validated models and simulations. Measurements from a multispectral sensor with higher sensitivity, with more bands and with more spectral resolution, and with higher spatial resolution over appropriate targets and backgrounds under a variety of conditions are generally required before committing to an operational system for any specific application(s).

Models and simulations are discussed in the next four subsections of this report. Section 5.1 describes several deterministic target and cloud and terrain background models. The target models described in Section 5.1 are primarily aircraft and ground target models and models for backgrounds. Section 5.2 describes models for the environment. The Strategic Scene Generator Model (SSGM), is described in Section 5.3 and represents an integration of all of the capabilities for modeling the spectral radiance characteristics of any target and background related to strategic surveillance and especially to Strategic Defense Initiative (SDI) missions. Section 5.4 describes an approach to using multispectral data, based on laboratory-measured optical properties data and simulation models, to design and predict the performance of a multispectral sensor system. Section 5.5 discusses a flat plate model for spectral radiance in the infrared that validates the use of measured BRDFs and measured atmospheric parameters to account for the spectral radiance features in the field.

5.1 TARGET AND BACKGROUND MODELING

This section of the report describes models for targets and backgrounds as sources of multispectral radiance. They include vehicle thermodynamic, reflectance and radiance models, plume flow field and radiance models, and background models. For more information on target modeling, we invite the reader to examine the State-of-the-Art report, *Infrared Signature Simulation of Military Targets*, a companion to this volume.

Vehicle models discussed can be divided into those which predict vehicle surface temperatures and those which do not. SIRIM GTSIG, PRISM, and SPIRITS are all predictive models in that they model internal heat sources as well as external sources and sinks to predict vehicle surface temperatures. TARSIS and SSTIRS require the user to specify target surface

temperatures. These temperatures are then used in conjunction with BRDF data or models to compute target spectral signatures that include emitted and reflected components. A summary of the different features of these models is presented in Table 5-1.

Table 5-1. Summary of Vehicle Model Features

Model Name	Target Types	Model Type	Solar Loading Calculations	Recovery Temperature Calculations	Internal Heat Source	BRDF	Polarization Capability?
SIRIM	Ground Vehicles	CSG	Yes	No	Yes	Beard-Maxwell	Yes
GTSIG	Ground Vehicles Helicopters	Faceted	Yes	No	Yes	Robertson-Sandford Model	No
PRISM	Ground Vehicles	Faceted*	Yes	No	Yes	Diffuse, currently being upgrded	No
SPIRITS	Aircraft/Missiles/ Helicopter	Faceted	Yes	Yes	Yes	Robertson-Sandford Model	No
TARSIS	Aircraft	Faceted	Yes	Yes	No	BRDF Data	Yes
SSTIRS	Aircraft	4 Simple Surfaces	Yes	Yes	No	Robertson-Sandford BRDF	No

*SPIRITS includes software to translate CSG models into faceted models.

The Coatings Reflectance Engineering Evaluation Model (CREEP) is a state of the art first principles model for predicting the BRDF characteristics of a paint coating based on binder, pigment, surface roughness, and substrate characteristics.

The JANNAF Standard Plume Flowfield (SPF, SPF2 and SPF3) codes are programs for calculating the gas dynamic structure of an exhaust plume from rocket powered engines below 70 km. The output from SPF must be used with a radiative transfer model such as SIRRM-AB for spectral signature prediction.

The Standardized Infrared Radiation Model for Air Breathing Vehicles, SIRRM-AB, is a model for computing aircraft or missile signatures including the signature of the plume. SIRRM-AB uses a faceted surface model for the surface of the aircraft; it includes reflection and emission, atmospheric transmission, and the Standard Plume flowfield model with a plume with plume radiative transfer.

Vegetation is a very common background. A number of vegetation canopy reflectance (and emittance) models have been developed. A model developed by Suits is described which embodies most of the essential features of any canopy model.

Background scene spatial structure (as well as spectral structure) is important and can be modeled statistically. However, with the limited statistics that are usually available, there is no guarantee that any particular realization has the spatial structure actually found in nature. GENESSIS (GENERIC Scene SIMulation Software) uses Landsat multispectral data to identify specific scene structure and material/background types in an image. Then elevations data from

a digital terrain elevation data (DTED) database are used with solar illumination and radiative and convective heat transfer to compute thermal infrared images.

CLDSIM is a CLOUD SIMulation program for computing the radiance characteristics of clouds.

5.1.1 SIRIM, PRISM, GTSIG, and SPIRITS

The Simulated InfraRed Imaging Model (SIRIM), was developed by ERIM to predict radiometric signature distributions and histories. The solid target modeling is based on the combinatorial solid geometry (CSG) techniques from Ballistic Research Laboratories (BRL). One of the unique advantages of the CSG modeling is that it includes the solid three-dimensional characteristics of the target. Extension of the BRL modeling includes an automated decomposition of the target into an adaptively sampled grid of volume elements (voxels) suitable for a finite volume method computation of heat conduction in the target. Solar loading, convection, conduction, radiative exchange and internal heat sources are included in the thermal modeling portion of SIRIM. The target radiometric signature is based on the resulting surface temperatures, surface emittances and reflectances, a Stokes-vector based description of the polarization, and a ray tracing procedure employed using the original CSG target description. The SIRIM ray trace method treats multiple target surface reflections, polarization, and background reflection. By using the CSG-defined geometry in the ray trace, renderings at very high image resolutions are possible and are not limited by the resolution of discrete geometry used for heat transfer calculations.

The Physically Realizable Infrared Signature Model, PRISM, is a faceted target model developed by the Keweenaw Research Center at Michigan Technical University. GTSIG, is the Georgia Tech Signature model and it is similar to PRISM. SPIRITS, the Spectral IR Imaging of Targets and Scenes model, is the JANNAP standard for aircraft modeling developed by Aerodyne. These models represent the surface of a target by small planar facets in sufficient number to adequately represent the surface of the target. Facet thicknesses and conductivities and internal heat nodes are chosen to allow surface temperature prediction. PRISM and GTSIG require the vehicle model builder to specify the internal heat nodes, in contrast to SIRIM which specifies internal nodes automatically using ray tracing. Alternatively, temperatures can be assigned. The ray tracing for the optical rendering and radiometric calculation methods are similar to those in SIRIM.

5.1.2 TARSIS and SSTIRS

TARSIS is the TARget Signature Simulation aircraft modeling program developed by Photon Research Associates (PRA). Target surfaces are represented by an appropriate collection of planar facets. Facet temperatures are specified by the user but are then input to thermodynamic calculations which iteratively determine the skin temperature by balancing facet temperature, aerodynamic, and solar heating with radiative losses. TARSIS utilizes BRDF tables for radiometric calculations. These can be generated offline from the various reflectance models.

SSTIRS is the Spectral Sciences Target IR Signature code that represents the surface using a selection from four simple geometric shapes: planes, hemi-ellipsoids, cylinders, and discs.

SSTIRS requires facet skin temperatures from the users and utilizes the Robertson-Sandford BRDF model in its radiometric calculations.

None of the above aircraft signature models includes skin temperature prediction. Skin temperatures can be assigned from available measurements, or equilibrium skin temperatures can be calculated due to aerodynamic heating, solar input, and radiative cooling.

5.1.3 SPF and SIRRM-AB

The calculation of the spectral signature characteristics of an aircraft or missile plume involve very complex calculations of the aerodynamic flow of the exhaust gases in the plume and of the chemical reactions occurring in the plume. In addition to a calculation for the spatial distribution of plume specie density, temperature, and pressure profiles, it is also necessary to calculate the emission from and transmission through a nonequilibrium plume.

SPF, SPF-2 and SPF-3 are Standard Plume Flowfield (SPF) models for calculating the spatial distribution of species in aircraft or missile plumes along with their temperature and pressure profiles. SIRRM-AB is the Standardized Infrared Radiation Model for Air Breathing vehicles, an aircraft signature similar to SPIRITS, TARSIS, and SSTIRS, for calculating the radiance from the plume defined by SPF along with the emitted and reflected radiance from the skin of an aircraft.

5.1.4 CREEP, ERIM, and Aerodyne Models

The spatial-spectral characteristics of a target depend on target geometry and on both emission and reflection. Specification of the full spectral, angular, and polarization dependence of the BRDF is required for an accurate representation of the target image. Such detailed BRDF data are easily determined for surfaces that are specular or surfaces that are perfectly diffuse (or approximately so). For other samples measurement data are generally required. Either measured BRDFs or a model for the BRDF of the surface is required for accurate target modeling in the visible or infrared.

The Coatings Reflectance Engineering and Evaluation Program (CREEP) is a program developed by PRA based on first-principles modeling reflection and scattering from rough surfaces and particulate matter. CREEP is used to calculate the BRDF from a coating consisting of a number of layers of binder, each loaded with pigment, on a substrate. Large- and small-scale surface roughness at each interface, binder indices of refraction for each layer, and pigment and pigment coating index of refraction, number density, and size distribution are required inputs. CREEP uses large- and small-scale surface roughness models from Barrick, Mie scattering routines from Boren and Hufmann, and doubling and adding routines from Hansen and Travis with extensions due to PRA for multiple layer coatings.

CREEP is a state-of-the-art BRDF code for coatings and for use in target modeling. However the detailed input parameters are often not available or they are inadequately characterized. For this reason empirical models with parameters based on actual measurement data are frequently used to model the BRDF characteristics of the target surfaces.

The ERIM and Aerodyne models are two BRDF models that are widely used for characterizing the surface optical properties of targets. The ERIM model derives a surface roughness distribution function from a limited measurement database. The BRDF is assumed

to arise from specular reflections from the rough surface along with a diffuse reflectance component from "volume" or pigment scattering within the binder. Over small spectral intervals the spectral characteristics of the BRDF are well characterized by the spectral directional reflectance because the index of refraction is generally only weakly dependent on wavelength. BRDF measurements are required at several wavelengths between the visible and thermal IR because the surface appears to be smoother at the longer wavelengths. This model is used in SIRIM and is used as a means of characterizing the BRDF of surfaces measured at the Materials Laboratory at Wright-Patterson Air Force Base.

The Aerodyne model is similar to the ERIM model. However, the Aerodyne model uses an analytical expression for the surface roughness with parameters derived from a limited measurement database. The Aerodyne model does not include polarization, but polarization could be included with only minor modification. This model is utilized in PRISM and SSTIRS.

5.1.5 Suits Vegetation Canopy Model

Vegetation represents a significant portion of the background for many down-looking imaging systems. There are numerous measurements of the spectral directional reflectance of leaf surfaces from various types of vegetation in the visible and infrared. However, surface measurements alone often are inadequate to predict reflectance properties of the canopy since the effects of the canopy structure on the spectral reflectance properties of vegetation can be very strong.

The Suits model characterizes a vegetative canopy with multiple layers of equivalent horizontal and vertical leaf area over a substory of soil and/or dead vegetation. The reflectance of the canopy is the result of the solution to a set of differential equations describing the attenuation of the direct solar radiation and the upward and downward flow of diffuse flux in the canopy. Inputs to the model are horizontal and vertical leaf area indices, equivalent leaf (and other vegetative matter) reflectance and transmittance, row structure in the case of crops, and substory reflectance. All of these parameters are related to the canopy and can be measured.

5.1.6 GENESSIS

One of the most difficult problems in simulating targets and backgrounds is to accurately represent the spatial structure of real cloud and terrain background scenes. Statistical techniques are frequently used in which specific image realizations are generated from measured background scene statistics. However, the spatial structure in such a realization may not be representative of actual scenes due to the limited statistical information used in the simulation, usually only the first and second moments.

GENESSIS (GENERIC Scene Simulation Software) is a program developed by PRA under NRL sponsorship to generate visible and infrared scenes between 0.2 and 15 μm from Landsat imagery. Multispectral Landsat imagery is processed to define scene content of a Landsat image. Spatial scene content and Digital Terrain Elevation Data (DTED) are then combined with environmental inputs (solar input and meteorological conditions) to simulate the spatial distribution of reflected radiances, temperatures, and emitted radiances in the scene.

5.1.7 CLDSIM

Clouds are a common background for many systems. CLDSIM is a program developed by PRA under NRL sponsorship that is used to calculate two-dimensional radiance maps of clouds between 1 and 12.5 μm using a process very similar to that used by GENESIS. The clouds are defined by a two-dimensional array of cloud top altitudes. Surface temperatures of the clouds are set equal to the ambient temperature at cloud top altitude. Cloud types include water, water-ice, and ice. Surface reflectance is specified by a BRDF and emittance by a directional emittance.

5.2 ENVIRONMENT MODELING

The sun, moon, stars, airglow, clouds, atmospheric scattering, and atmospheric emission all provide sources of illumination throughout the visible and thermal infrared. In addition the atmosphere also absorbs some of the energy from the target between the target and the sensor. Varying spectral quality of the incident radiation and of the atmospheric transmission all cause a coloring of the target over and above that intrinsic to the reflectance and emittance optical properties.

Several atmospheric models have been developed for atmospheric effects. LOWTRAN, MODTRAN, and FASCODE (which uses a HITRAN database) are state of the art models for various spectral resolutions. APART is an Atmospheric Propagation and Radiative Transfer model developed by PRA that is a modification of LOWTRAN for propagation and transport of radiance through the atmosphere.

EOSAEL is the Electro-Optical Systems Atmospherics Effects Library, a model developed by the Atmospheric Sciences Laboratory for battlefield smokes and obscurants.

5.2.1 LOWTRAN, MODTRAN, FASCODE, and APART

LOWTRAN has been an accepted standard for computing atmospheric transmission since its first release in 1972. The current version, LOWTRAN 7, computes atmospheric transmittance and background radiance for a given atmospheric path at low spectral resolution. LOWTRAN 7 calculates atmospheric transmittance, atmospheric background radiance, single scattered solar and lunar radiance, direct solar irradiance, and multiple scattered solar and thermal radiance. The spectral resolution of the model is 20 cm^{-1} in steps of 5 cm^{-1} from 0 to $50,000\text{ cm}^{-1}$ ($0.2\text{ }\mu\text{m}$ to infinity). A single-parameter band model is used for molecular line absorption and the effects of molecular continuum-type absorption; molecular scattering, aerosol, and hydrometer absorption and scattering are included. Refraction and earth curvature are considered in the calculation of the atmospheric slant path and attenuation amounts along the path. Representative atmospheric aerosol, cloud, and rain models are provided in the code with options to replace them with user-provided theoretical or measured values.

A database consisting of separate molecular profiles (0-100 km) for 13 minor and trace gases is provided for use with the LOWTRAN 7 model. Six reference atmospheres, each defining temperature, pressure, density, and mixing ratios for H_2O , O_3 , CH_4 , CO , and N_2O , all as a function of altitude, allow a range of climatological choices.

Separate band models and band model absorption parameters are included in LOWTRAN 7 for the following molecules: H_2O , O_3 , N_2O , CH_4 , CO , O_2 , CO_2 , NO , NO_2 , NH_3 ,

and SO₂. These models were developed with and based on degraded line-by-line spectra and validated against laboratory measurements.

An efficient and accurate multiple scattering parameterization has been implemented that is based on the two-stream approximation and adding method for combining atmospheric layers.

MODTRAN is a model to calculate atmospheric transmission at 2 cm⁻¹ resolution. MODTRAN uses the LOWTRAN method and at 20 cm⁻¹ is identical to LOWTRAN 7. MODTRAN is the currently supported U.S. standard atmospheric transmission program.

FASCODE is a high resolution atmospheric transmission code based on absorption by all contributing resolved lines in a HITRAN database. In principle the transmission can be computed at arbitrarily high spectral resolution. The accuracy is limited by the HITRAN database.

5.2.2 EOSAEL

EOSAEL is a state-of-the-art collection of computer codes that models the degrading effects of natural and man-made gases, aerosols, and dusts on the propagation of radiation. Modules in EOSAEL address the visible to millimeter region of the spectrum plus individual laser lines from the visible to the far infrared.

Specifically, EOSAEL 82 calculates extinction coefficients, atmospheric effects on laser beam propagation, contrast transmittance, and target detection probabilities. A climatology module is included, which provides easy access to an extensive climatology database for a number of climatic regions.

5.3 STRATEGIC SCENE GENERATOR MODEL

The SSGM integrates state of science knowledge, databases, and computerized phenomenology models to simulate strategic engagement scenarios and to support the design, development, and test of advanced sensor systems. Multiphenomenology scenes are produced from validated codes to serve as a traceable standard against which different concepts and designs can be tested. The SSGM was developed by PRA under the sponsorship of NRL.

The baseline model (SSGMB) has been designed for application to SDI applications. The phenomenology models and databases for SSGMB are listed in Table 5-2 and include models for terrestrial backgrounds, the earth limb, aurora, space, missile and RV targets, and nuclear effects. Details for each of the components of SSGMB can be found in the literature and in the technical reference manuals for SSGMB R5.0.

Enhancements to SSGM are being developed for Theater Missile Defense (TMD) applications and include targets, backgrounds, and engagement scenarios appropriate for any number of likely global threats which might be confined to a region or "theater" of operation. The TMD requirements involve four major areas: formulation of the Third World missile threat (countries and missiles), definition of missile parameters (trajectories, fuels, thrust, burn times, range, number of stages, hard body specifications, etc.), expansion of target model treatments (primitive fuels and propellants, hardbody heating from ascent to re-entry, and debris resulting from kinetic kill impact), and the development of global and theater background databases for input into SSGM terrestrial models including terrain, cloud, and atmospheric. Many of these are included in SSGMB R5.0.

Table 5-2. Phenomenology Models and Databases for SSGM Baseline R5.0

Category	Observable	Model	Description	Agency/ Developer
TERRESTRIAL	Hard Earth Cloud	■ GENESIS ■ CLDSIM	Terrain Scenes (Rad.) Cloud Scenes (Rad. & Trans.)	NRL/PRA NRL/PRA
EARTH LIMB (RAD_E)	LTE Atmosphere NLTE Limb LTE/NLTE	■ MODTRAN ■ APART ■ SHARC 2.1 db FASTLIMB	LTE Band Model (Rad. & Trans.) Propagation and Radiative Transport NLTE (Rad.) Earthlimb Spectral Radiance Database (2:30 μm in 1% energy bins) derived from MODTRAN & SHARC	PL PRA PL MRC/PL
AURORA (RAD_A)	Perturbed Limb	db AURORA	Aurora Volumetric Emission Spectra Database (2-20 μm at 1 cm^{-1} resolution) derived from ARCTIC, MSIS90, PRISM, ARCHON, NLTE, DOUBPI & SINGLET	MRC/PL/DNA
SPACE (RAD_S)	Celestial Phenomena	■ CBSD ■ CBPOINTS ■ CBZODY ■ CBAMP	Celestial Background Scene Descriptor Point Source model for galactic stars Zodiacal Background (Diffuse & Structured) (Asteroids, Moons, Planets, & Sun)	PL/MRC PL/NASA/MRC PL/MRC PL/MRC
TARGET	Missile Plume Plume Transients Debris Post-Boost Vehicle Plume Illumination Target Illumination Target Hard Body	■ SIRRIM II db SPF2 & SPF3 ■ CHARM 1.3 SPURC SFM ■ DEBRA/KIDD CHAMP HALT DELTAS db OSC XVII ■ OPTISIG ■ MDOSC ■ MCOSIG ■ MCOIMG	Plume Radiance for 2D/3D Geometries (used in SSGM for altitudes <50 km) Couples Missile Body, Base, & Flowfield Plume Flowfield & Radiance (used in SSGM for altitudes >50 km) Plume Flowfield & Radiance (0.1-0.7 μm) Plume Flowfield & Transients (staging, chuffing, thrust vector control) Debris from KKV intercepts PBV Hardbody & Plumes Plume/Laser Retroreflectance Target/Laser Retroreflectance Optical Signatures Code Point Image Signature Code Run-Time Midcourse Data OSC Sensor/Target Engagements Scenarios and Resolved Image Signatures Run-Time Resolved Image Capability	PL/MICOM, GAC, SSI PL/MICOM, PST PL/MSC, SSI, AOI, CALSPAN, GAC PL/GAC, AOI, SSI, PSI PL/SEA, AOI PL+SSDC+SMC/Aerospace PLL+WL/AOI PL SDIO/NRC SSDC/TBE SSDC/TBE NRL/TBE NRL/TBE NRL/TBE
NUCLEAR	Perturbed Atmosphere	db NORSE ■ PEM 3.3 ■ IRSim ■ HISEMM	Analytic Application Code (Rad.) Engagement Code (Rad.) Engagement Code (Rad.) Engagement Code (Rad. & RF Prop.)	DNA/VI, MRC DNA/VI DNA/VI DNA+SSDC/VI
Key: ■ = On-line SSGM R5.0 code db = Off-line computed database				

5.4 MULTISPECTRAL AND HYPERSPECTRAL BAND SELECTION AND PERFORMANCE ANALYSIS

Section 3 described the phenomenology underlying the spectral characteristics of the radiance at a remote sensor, and Section 4 discussed the measurement and sensing of the spectral characteristics of radiance at a remote sensor. Sections 5.1-5.3 included a variety of models used to predict the spectral signatures of targets and backgrounds in a realistic environment from the visible through the infrared. In this section a methodology is presented for utilizing laboratory spectral properties of materials, phenomenology, and simulation models for sensor specification and performance evaluation.

The approach described in this section has been developed and used at ERIM for a variety of multispectral and hyperspectral applications. While it has been applied only to reflective data (0.4 to 2.5 μm), its primary elements apply equally to longer wavelength data (e.g., 3 to 5 μm or 8 to 14 μm). The ERIM approach is meant to illustrate the techniques involved in selecting spectral bands and evaluating performance. In general, the successful implementation of the program depends very strongly on the data based of optical properties used as input to the program.

Specification of a new sensor system aimed at providing information to support a given mission or set of missions is a complex process involving consideration of a wide variety of factors including the sensor, targets, backgrounds, and environmental conditions at the time of measurement. The performance model developed at ERIM defines (1) band number, location and width, (2) spatial resolution, and (3) radiometric sensitivity.

5.4.1 Optimum Band Specification

A materials reflectance library containing over 2000 spectra from a wide variety of materials and classes covering the range 0.4 to 2.5 μm underlies the simulations of spectral radiances at the remote sensor. These data are used along with atmospheric models to simulate spectral radiances.

Steps are first taken to reduce the original number of high spectral resolution samples down to a manageable number of bands that capture the pieces of information required for target discrimination or interrogation. This involves a principal components analysis for defining the spectral directions having the greatest variability. These directions are sorted based on target/background separability. Contiguous wavelengths with the same sign in the eigenvectors that provide the greatest target/background separation are grouped together into bands. In this way the number of spectral bands is reduced from as many as 200 to 20 or less.

The performance of all (approximately 20) combinations of the bands defined above is determined by evaluating two-class separability, on a single pixel basis, taking into account class spectral characteristics, target and pixel size, shape, orientation, and alignment, sensor point spread function, detector response function, sensor noise characteristics, and atmospheric far-field turbulence. The model first adjusts the class signatures based on the above factors and then computes the statistical separation between the class signatures in a maximum likelihood context.

The best set of bands is based on a comparison and ranking of all combinations of one band through n bands including relative gains in performance associated with the addition of bands and the requirements of the mission or missions of interest.

The band set selected above is evaluated in greater detail by incrementally adjusting the edges of each band and re-computing the class separability metric. The final band set selected is the smallest set that provides performance near that associated with the full n band set.

Any given mission will typically have several class pair discrimination problems of interest. At this stage, the optimum band sets defined for each class pair are combined into a band set providing the best performance over all class pairs. The performance of the "compromise" band set derived from all the separate sets is then evaluated for all class pairs, again considering all combinations of one band through n bands.

Analysis of empirical data (e.g., from an airborne sensor) requires that the best subset of bands from the total available set be identified. This selection is made by clustering pixels in the image into spectrally similar categories, manually extracting samples from the target and background clusters, and applying maximum likelihood classification techniques to select the best bands.

5.4.2 Spatial Resolution Requirements Specification

Spatial resolution requirements are typically evaluated using high-resolution empirical data. Starting from the base data, a series of images is derived that simulate a range of spatial resolutions. Each degraded image is classified using the same target and background signatures defined for the original image. All pixels in the degraded image that contain more than 50 percent target are typically considered to be target pixel. Classification results for the various degraded resolution data are evaluated as a means for specifying the required resolution.

5.4.3 Radiometric Sensitivity Analysis

Requirements for radiometric sensitivity ($NE\Delta L$, $NE\Delta\rho$, $NE\Delta T$, etc.) are derived by adjusting the noise characteristics of the sensor and determining the effect on classification performance directly. Typically a threshold in performance (classification accuracy) is set, after which the maximum acceptable noise level is determined. Alternatively the performance curve as a function of noise characteristics can be evaluated to determine at what noise level classification accuracy begins to degrade significantly.

5.5 FLAT PLATE MODELING

Complex targets can, in principle, be modeled to arbitrary accuracy, limited only by the completeness and accuracy of the input to the model. However, it is useful to model single pixel spectral radiances from a flat plate for comparison with actual measurement data in order to assess the accuracy and completeness of the radiometric portion of the model.

A flat plate model can be expressed as

$$L(\theta_r, \lambda) = \tau(R, \lambda) \left[\int \rho'(\theta_i, \phi_i, \theta_r, \phi_r, \lambda) L_i(\theta_i, \phi_i, \lambda) \cos(\theta_i) d\Omega_i \right. \\ \left. + \varepsilon(\theta_r, \lambda) L_{bb}(T, \lambda) \right] + L_p(\theta, \phi, R, \lambda) \quad (5-1)$$

where

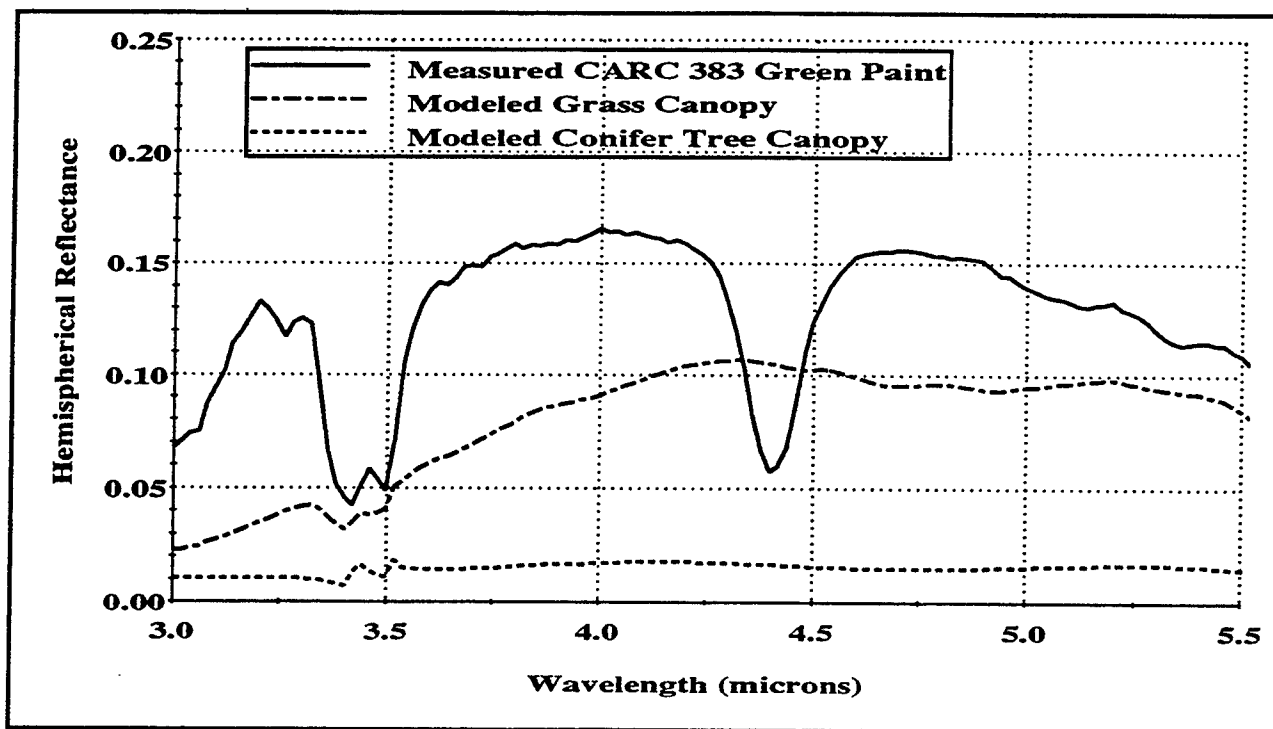
- θ_i = polar angle of incidence,
- ϕ_i = azimuth angle of incidence,
- θ_r = polar angle of receiver,
- ϕ_r = azimuth angle of receiver,
- λ = wavelength,
- $L(\theta_i, \phi_i, \lambda)$ = incident radiance from θ_i, ϕ_i ,
- $\rho(\theta_i, \phi_i, \theta_r, \phi_r, \lambda)$ = BRDF for source and receiver at $\theta_i, \phi_i, \theta_r, \phi_r$ at wavelength λ ,
- $d\Omega_i$ = element of solid angle from θ_i, ϕ_i ,
- $\varepsilon(\theta_r, \lambda)$ = emittance at angle θ_r at wavelength λ ,
- $L_{bb}(T, \lambda)$ = blackbody radiance at temperature T at wavelength λ ,
- $L_p(R, \lambda)$ = path radiance between the target and receiver at range R , and
- $\tau(R, \lambda)$ = transmission between the target and receiver at range R .

The above radiative transfer equation includes illumination from the entire hemisphere above the flat plate, which includes radiance from the sky and from the ground as a function of the panel orientation. The bidirectional characteristics of the reflectance and the angular dependence of the emittance are included as well as path transmission and path radiance from the path between the target and the sensor. The model is an approximation in that it does not, for example, include multiple reflections between the target and adjacent background nor does it (as described above) include any polarization characteristics of the BRDF.

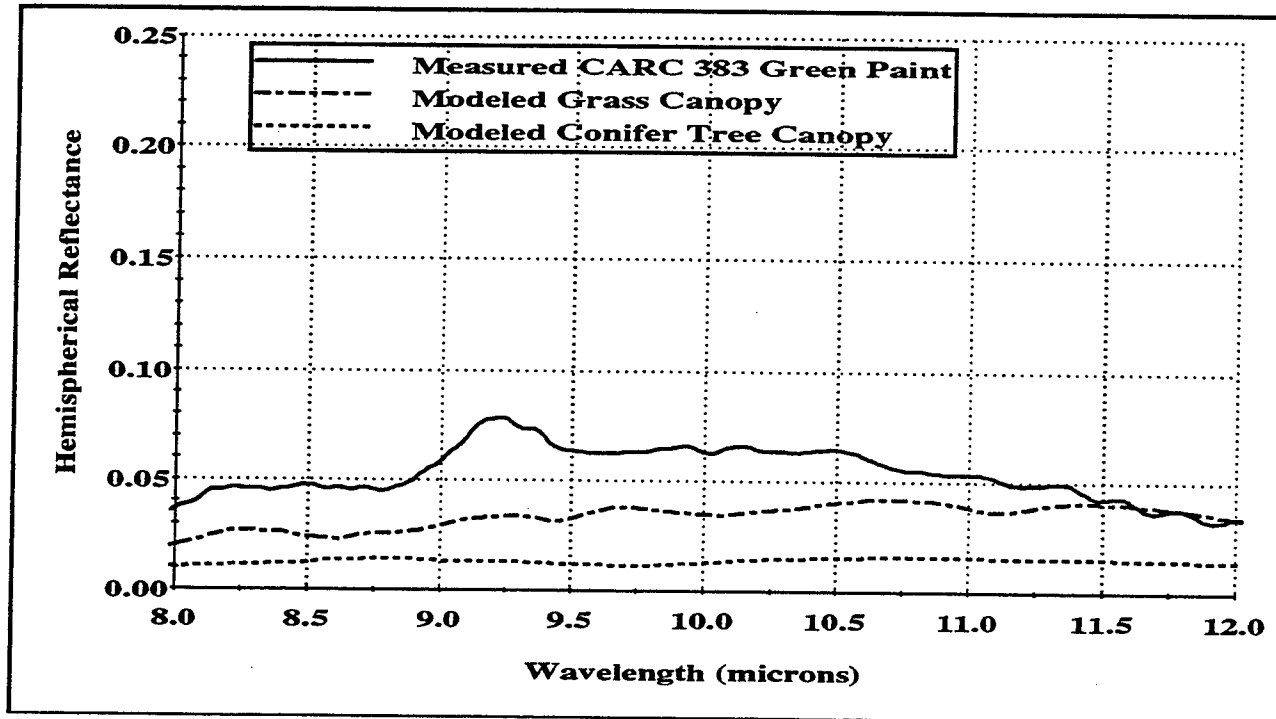
The inputs to the flat plate model are the spectral bidirectional reflectance and angular dependent emittance properties of the flat plate. For purposes of illustration the ERIM BRDF model is used with a spectrally nonselective rough surface component and a spectrally dependent diffuse component derived from the spectral directional reflectance data. All of the environment radiance and atmospheric transmission and path radiance input are modeled using MODTRAN.

The model has been compared with spectral radiance measurements taken with a BOMEM FTS. Measurements and modeling were done with 8 cm-1 spectral resolution in the 3-14 μ m spectral band (the modeling and measurements were obtained as part of the Joint Multispectral Program).

Figure 5-1 shows the hemispherical spectral reflectances for a CARC 383 green panel and for a grass and conifer background. These data were used as inputs to the flat plate model. A comparison of actual and modeled spectral radiances for the CARC 383 green panel target and a conifer background are shown in Figure 5-2, and for a CARC 383 green panel target and grass in Figure 5-3 (Schwartz, C.R., T.J. Rogne, and J.N. Cederquist 1994). Model predictions are shown to accurately predict the spectral features in the measured data.

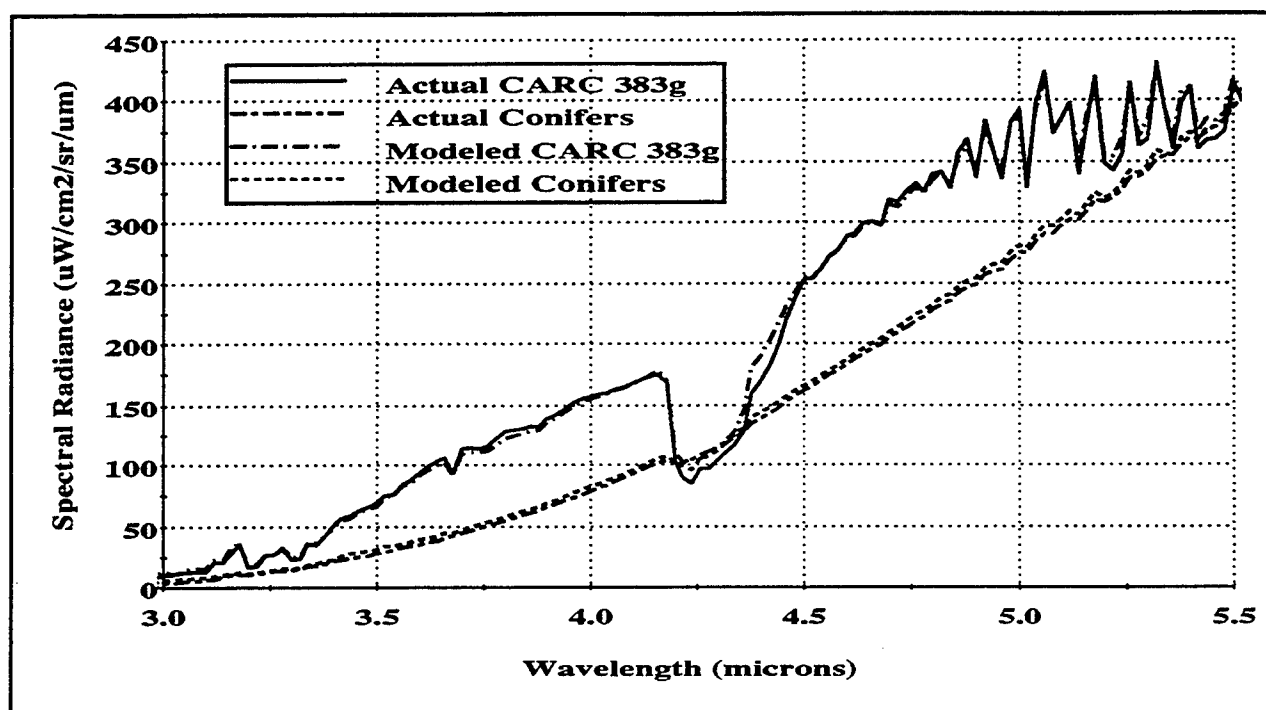


(a)

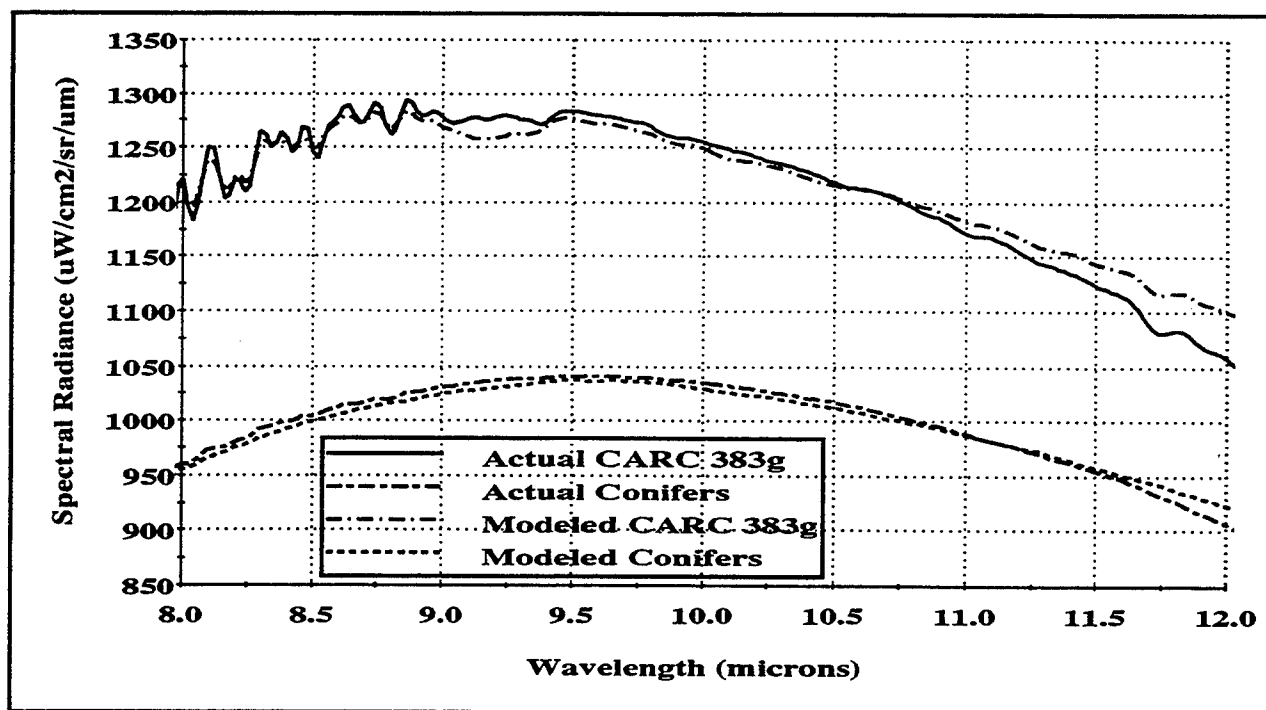


(b)

Figure 5-1. Target/Background Hemispherical Spectral Reflectances. a) In the MWIR (8cm^{-1} Spectral Resolution) and b) in the LWIR (8cm^{-1} Spectral Resolution).

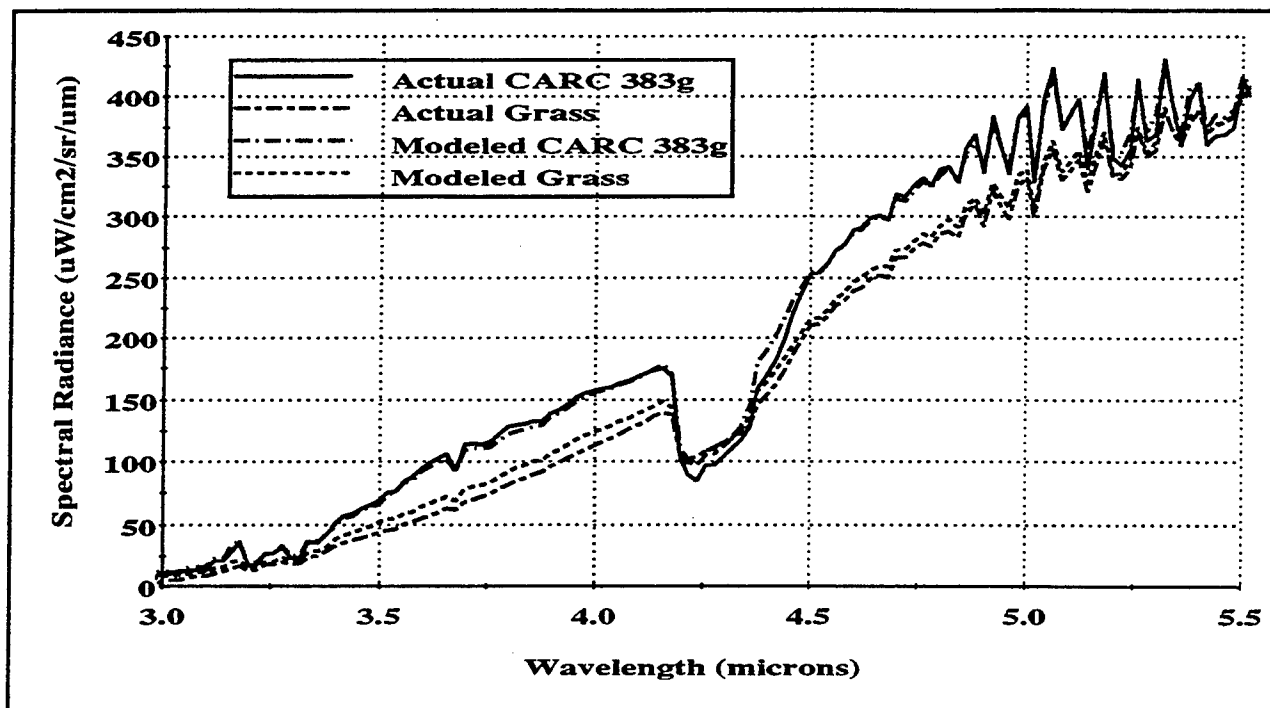


(a)

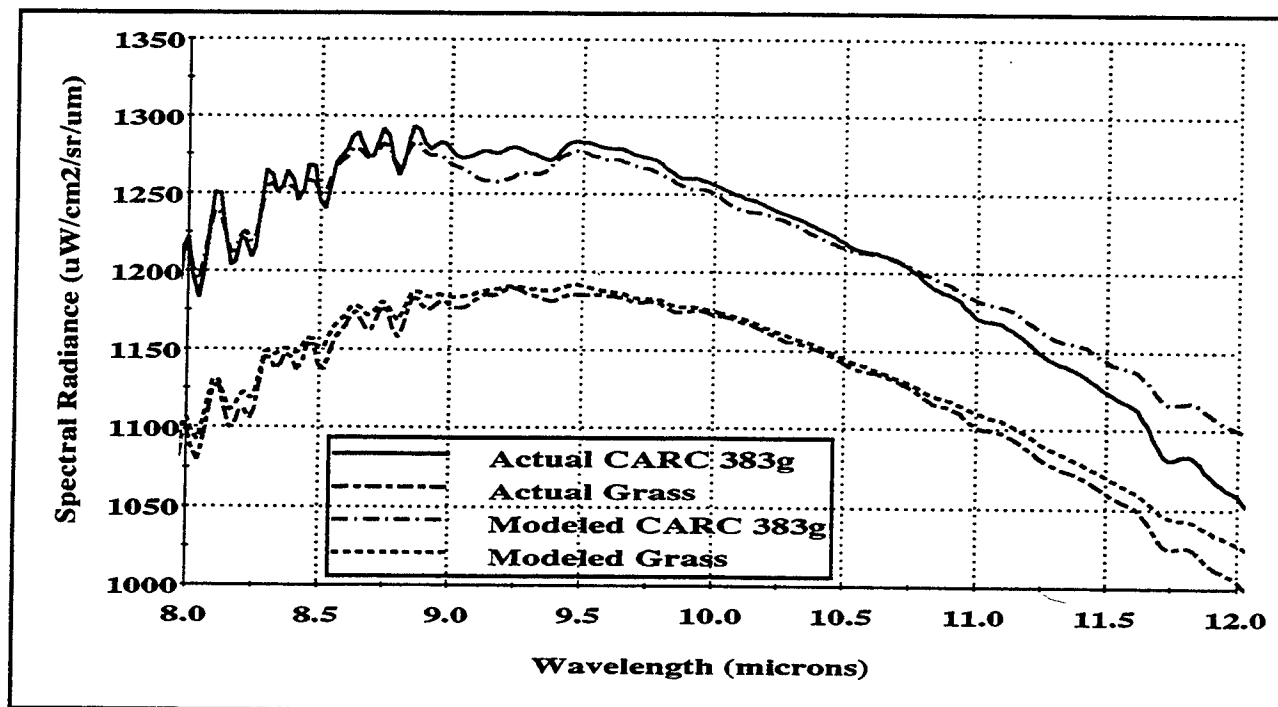


(b)

Figure 5-2. Actual and Modeled Target and Conifer Background Signatures. a) In the MWIR and b) in the LWIR.



(a)



(b)

Figure 5-3. Actual and Modeled Target and Grass Background Signatures. a) In the MWIR and b) in the LWIR.

5.6 BIBLIOGRAPHY

- Blakeslee, L. and L. Rodriguez, "Technical Reference Guide for TCMZ," Interim Report WL/AARI-3, Wright-Patterson AFB, Ohio, 1993.
- Keweenaw Research Center, *PRISM Users Manual*, Michigan Technological University, Houghton, MI.
- Robertson, D.C., "Aircraft Contrast Signatures in the Infrared Spectral Region," Sensing Design Using Computer Tools, SPIE, Vol. 327, 1982.
- Schwartz, C.R., T.J. Rogne, and J.N. Cederquist, *Infrared Multispectral Sensor Program, Phase 2: Field Measurements, Analysis and Modeling, Vol. 5: Hyperspectral Modeling With Comparison to Field Measurements*, ERIM Report No. 253840-1-F (V5), Environmental Research Institute of Michigan, Ann Arbor, May 1994.

6.0 SPECTRAL ALGORITHMS

In single broadband reflective or thermal data, target detection is usually based on target contrast with spatial resolution used to exploit spatial features that distinguish the target from other target-like contrast elements in the scene (background clutter). Tone, texture, spatial extent, and context are used to detect the target and to distinguish between various background elements.

The purposes of multispectral sensing are to detect targets and to discriminate between various target and background types on the basis of differences in their spectral characteristics. The advantages are automated signal processing and lower spatial resolution requirements. In many instances the target signal-to-clutter ratio (SCR) is low in all spectral bands so that no single band system will perform adequately in terms of probability of detection and probability of false alarm. However, multispectral sensing can frequently increase the target signal-to-clutter ratio using two or more bands simultaneously. Further, automatic processing has the potential for reducing the amount of raw data transmitted to the user and for reducing the time required to accomplish time sensitive missions.

The main purpose of multispectral signal processing is to increase the target SCR. More generally there may be several classes of targets, and the function is to detect all of them and discriminate among them.

6.1 SINGLE SPECTRAL-BAND PROCESSING

The radiance at a remote sensor from the target will be denoted by L_T and from the background by L_B . Consider initially the radiances in a single spectral band. The target-background irradiance difference at the sensor aperture, ΔH_T , is

$$\Delta H_T = \frac{(L_T - L_B) A_{\text{IFOV}} \tau}{R^2}, \quad (6-1)$$

where A_{IFOV} is the area of the IFOV of the sensor projected onto the scene, τ the atmospheric transmission, and R the range to the scene. The target is assumed to be larger than the IFOV. Extension of the analysis for unresolved targets is straightforward.

The signal-to-noise ratio (SNR) is

$$\text{SNR} = \frac{\Delta H_T}{\text{NEI}}, \quad (6-2)$$

where NEI is the noise equivalent irradiance of the sensor. The SNR defines the best performance for this sensor in detecting a target with radiance L_T against a background with radiance L_B .

Performance is, however, generally limited by background clutter. Background clutter describes all of the radiance variations in the scene that appear in the sensor output. For the

single band sensor, background clutter is the spatial variation in the radiance from the background.

The target SCR is the ratio of the mean target background radiance difference and the background radiance standard deviation

$$SCR = \frac{L_T - L_B}{\sigma_B}, \quad (6-3)$$

where σ_B is the spatial standard deviation file background radiance.

For the single band system, spatial filtering is generally used to take advantage of the differences in the spatial frequency content of the target and background to increase the target SCR.

The increase in performance with signal processing is frequently expressed in terms of a clutter suppression ratio (CSR), defined as the ratio of the standard deviation of the clutter before processing, $\sigma_{unprocessed}$, to the background standard deviation after processing, $\sigma_{processed}$

$$CSR = \frac{\sigma_{unprocessed}}{\sigma_{processed}}. \quad (6-4)$$

The CSR only includes the effect of the signal processing on the background.

The signal processing gain, G, includes the effect of signal processing on the target signal and background clutter and is generally a more appropriate performance metric. G is defined as the ratio of the SCR after processing, $SCR_{processed}$, to the SCR before processing, $SCR_{unprocessed}$

$$G = \frac{SCR_{processed}}{SCR_{unprocessed}}. \quad (6-5)$$

The above definitions of SNR, SCR, CSR, and G are defined in terms of radiances (or irradiances) at the sensor aperture. In the signal processing literature these parameters are generally expressed in dB, for example

$$G(\text{dB}) = 20 \log_{10} \frac{SCR_{processed}}{SCR_{unprocessed}}. \quad (6-6)$$

The above discussion provides a basis for describing the target signal and the target SCR for a single band sensor in terms of target radiances (or irradiances) at the sensor aperture. Probability of detection, P_D , and probability of false alarm, P_{FA} , can be determined from the SCR at the output of the signal processor if the background clutter at the output of the signal processor is zero mean and Gaussian. Under these conditions the P_D versus P_{FA} receiver operating characteristic (ROC) curve can be determined from standard tables such as shown in Figure 6-1 with P_D versus SNR for various P_{FA} .

The above discussion can be extended to multiband, multispectral, and hyperspectral data. This extension and insight into the design of a multispectral processor is outlined in the next section.

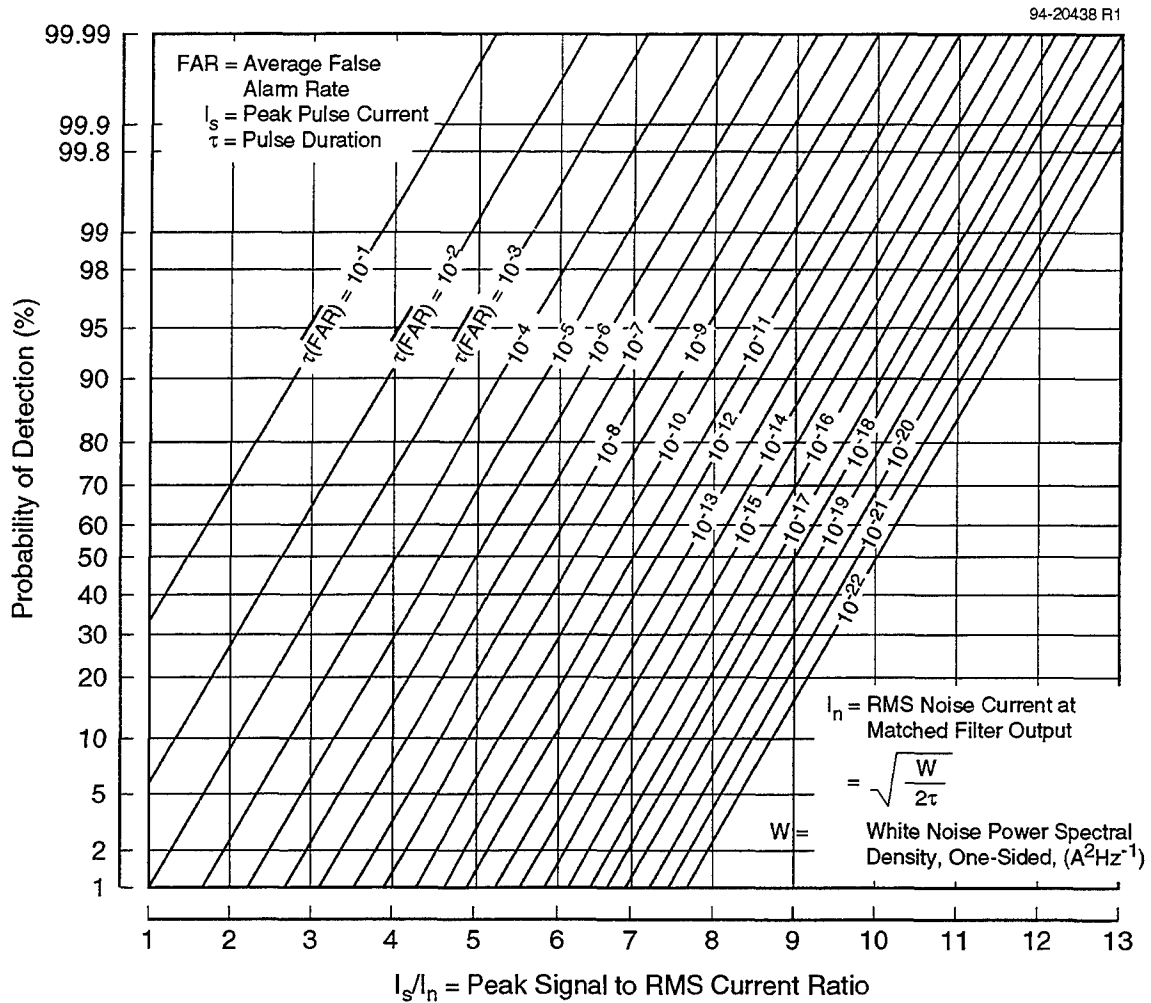


Figure 6-1. Probability of Detection vs. Peak Signal to RMS Noise Ratio

6.2 LOG LIKELIHOOD RATIO DETECTOR

Most targets and backgrounds have variable radiance characteristics so that it is necessary to describe them statistically. Some of the more common statistical measures used to characterize targets and backgrounds in a single spectral band are the mean radiance level, standard deviation, power spectral density, and scale length.

Additional characteristics describing multispectral data include spectral covariances, spectral correlation coefficients, and spatial and spectral coherence functions. Temporal changes in the target or background signal may also be an important component of the signature. These may be due to target motion or to other changes that may occur between data collections. Temporal characterization of the data can be included formally in a straight forward way by increasing the dimensionality of the data. The development that follows is based on the assumption that a target/background decision is made for every pixel. An extended target can be included in the analysis by extending the analysis to multipixel targets.

The mathematical description for a Gaussian image, of which \underline{X} is one realization, is given by the probability density function $p(\underline{X})$, as follows

$$p(\underline{X}) = \frac{1}{(2\pi)^{N/2} |\underline{R}|^{1/2}} e^{-\frac{1}{2}(\underline{X}-\underline{\mu})^T \underline{R}^{-1} (\underline{X}-\underline{\mu})}, \quad (6-7)$$

where $\underline{\mu}$ is the mean image vector and \underline{R} is the image covariance matrix. The image \underline{X} is a column vector of spectral pixel radiances taken from the image \underline{X} in a raster scan format, one pixel after another along rows, one row after another, and T represents the transpose. The data vector \underline{X} of a multispectral image is represented as

$$\underline{X} = [(x_{11}^{\lambda_1}, \dots, x_{11}^{\lambda_L}), \dots, (x_{MN}^{\lambda_1}, \dots, x_{MN}^{\lambda_L})]^T. \quad (6-8)$$

This data vector contains all of the data and is of size $M*N*L$ where M is the number of rows, N the number of columns, and L the number of wavelengths. The elements of the mean image vector and the covariance matrix for an ensemble of multispectral images are

$$\begin{aligned} \underline{\mu} &= E\{\underline{X}\} \\ \underline{R} &= E\{(\underline{X} - \underline{\mu})(\underline{X} - \underline{\mu})^T\}, \end{aligned} \quad (6-9)$$

where E is the expectation operator over an ensemble of images.

The diagonal elements of the covariance matrix are the pixel variances and the off-diagonal elements the covariances. The full covariance matrix is a square matrix with dimensions $(M*N*L)$ by $(M*N*L)$.

The assumption that multispectral images are Gaussian provides an elegant formalism for evaluating various signal processing techniques designed to increase the target signal-to-background clutter ratio. Formal developments can be found in a number of standard textbooks and in the literature. The likelihood ratio detector is the optimal detector for selecting between two hypotheses,

$$\begin{aligned} H_0 &: \text{background} \\ H_1 &: \text{target} \end{aligned} \quad , \quad (6-10)$$

in that it provides the best probability of detection for any probability of false alarm. In the most general case the likelihood ratio detector takes the form

$$\frac{P(\underline{X}|H_1)}{P(\underline{X}|H_0)} > \Lambda \quad \text{for} \quad \begin{array}{l} \text{target} \\ \text{background} \end{array} \quad (6-11)$$

The log likelihood ratio for Gaussian data reduces to

$$(\underline{X} - \underline{\mu}_B)^T \underline{R}_B^{-1}(\underline{X} - \underline{\mu}_B) - (\underline{X} - \underline{\mu}_T)^T \underline{R}_T^{-1}(\underline{X} - \underline{\mu}_T) > \Lambda \quad \text{for} \quad \begin{array}{l} \text{target} \\ \text{background} \end{array} \quad (6-12)$$

with various constants not dependent on \underline{X} absorbed into the constant Λ .

The Gaussian log likelihood ratio detector is quadratic in the data. In general the Gaussian log likelihood ratio detector depends on both the target and background covariances.

When the target and background covariance matrices are the same, as for example when the target is an unresolved additive point target, the Gaussian log likelihood ratio detector reduces to a linear test of the form

$$(\underline{X} - \underline{\mu}_B)^T \underline{R}_B^{-1}(\underline{\mu}_T - \underline{\mu}_B) > \Lambda \quad \text{for} \quad \begin{array}{l} \text{target} \\ \text{background} \end{array} \quad (6-13)$$

with the additional terms not depending on \underline{X} absorbed into the constant Λ .

The log likelihood ratio test for Gaussian probability density functions is itself a one-dimensional Gaussian probability density function. Hence the probability of detection, P_D , and probability of false alarm, P_{FA} , can be determined from a knowledge of the target mean, the background mean and covariance, and the log likelihood ratio threshold by referring to Figure 6-1.

It is necessary to specify the image mean vector and the image covariance matrix in order to formally implement the log likelihood ratio detector. If the statistical characteristics of the

target and background are not completely known or if they are incorrectly specified, the performance will be less than that of the optimal maximum likelihood ratio detector.

A priori statistics characterizing the target and background are seldom available and usually have to be estimated from the data. Use of maximum likelihood estimates for the unknown statistical parameters leads to the generalized log likelihood ratio detector. For the Gaussian case, the generalized log likelihood ratio detector is

$$(\underline{X} - \hat{\underline{\mu}}_B)^T \hat{\underline{R}}_B^{-1} (\underline{X} - \hat{\underline{\mu}}_B) - (\underline{X} - \hat{\underline{\mu}}_T)^T \hat{\underline{R}}_T^{-1} (\underline{X} - \hat{\underline{\mu}}_T) \begin{matrix} > \Lambda & \text{for target} \\ < \Lambda & \text{for background} \end{matrix} \quad (6-14)$$

where the hat (^) represents the maximum likelihood estimate for the parameter. Maximum likelihood estimates can be made from local averages of means and covariances of the data.

The statistics of the target and background clutter are almost always assumed to be Gaussian. Over small homogeneous regions in the imagery this is a reasonable assumption. Departures from Gaussian statistics can cause significant departures from estimates assuming Gaussian statistics. For example there may be significant losses along the boundaries between different homogeneous regions in the imagery.

The generalized log likelihood ratio detector represents the optimum detector for Gaussian statistics and hence represents an important baseline for evaluating the performance characteristics of any other detector.

An anomaly detector for detecting nonbackground-like objects (potential targets) can be formulated using only estimates of the statistical properties of the backgrounds in the local neighborhood of the pixel under test. An adaptive threshold can then be adjusted to maintain a predetermined false alarm rate. The form for a multispectral anomaly detector is

$$P(\underline{X}|H_0) \begin{matrix} > \Lambda & \text{for background} \\ < \Lambda & \text{for non-background} \end{matrix} \quad (6-15)$$

which for Gaussian data is

$$(\underline{X} - \hat{\underline{\mu}}_B)^T \hat{\underline{R}}_B^{-1} (\underline{X} - \hat{\underline{\mu}}_B) \begin{matrix} < \Lambda & \text{for background} \\ > \Lambda & \text{for non-background} \end{matrix} \quad (6-16)$$

This is a quadratic detector which does not depend on a priori knowledge of the target signal. The term on the left is a weighted square of the distance from the mean background distribution. If the distance is larger than some threshold then it is a nonbackground. This detection can be shown to have constant false alarm rate (CFAR) properties.

6.3 TWO BAND LOG LIKELIHOOD RATIO DETECTOR

It is convenient to consider the multispectral data as components of a vector in an N-dimensional space. A two band example will be presented in this section to provide geometrical insight and make it easier to extend the concepts to N-dimensions.

Let \underline{X} represent the two spectral radiances of a point in a two-dimensional spectral space. Denote the two dimensions of the spectral space by x and y . Each image pixel occupies a point in this two-dimensional space. The mean spectral radiance for each point, $\underline{\mu}$, is represented by the following two component vector

$$\underline{\mu} = \begin{bmatrix} \mu_x \\ \mu_y \end{bmatrix}, \quad (6-17)$$

and the covariance, \underline{R} , by the following 2 by 2 matrix

$$\underline{R} = \begin{bmatrix} \sigma_{xx} & \sigma_{xy} \\ \sigma_{yx} & \sigma_{yy} \end{bmatrix} = \begin{bmatrix} \sigma_x^2 & \rho \sigma_x \sigma_y \\ \rho \sigma_x \sigma_y & \sigma_y^2 \end{bmatrix}. \quad (6-18)$$

Estimates of the variances of the pixel radiance in spectral bands x and y , σ_{xx} and σ_{yy} and the covariances, $\sigma_{xy} = \sigma_{yx}$, can be obtained by averaging over nearby pixels,

$$\sigma_{xx} = \frac{1}{N} \sum_i (x_i - \mu_x)(x_i - \mu_x) \quad \sigma_{yy} = \frac{1}{N} \sum_i (y_i - \mu_y)(y_i - \mu_y), \quad (6-19)$$

$$\sigma_{xy} = \sigma_{yx} = \frac{1}{N} \sum_i (x_i - \mu_x)(y_i - \mu_y), \quad (6-20)$$

$$\mu_x = \frac{1}{N} \sum_i x_i \quad \mu_y = \frac{1}{N} \sum_i y_i. \quad (6-21)$$

The standard deviations in bands x and y , σ_x and σ_y , are

$$\sigma_x = \sqrt{\sigma_{xx}} \quad \sigma_y = \sqrt{\sigma_{yy}}. \quad (6-22)$$

Contours of equal probability are quadratic curves obtained by setting the quadratic term in the exponent of the multivariate probability density function equal to a constant

$$(\underline{x} - \underline{\mu})^T \underline{R}^{-1} (\underline{x} - \underline{\mu}) = \text{constant}. \quad (6-23)$$

This is an ellipse in two dimensions, shown in Figure 6-2, and a hyperellipsoid in N dimensions.

The equal probability contours in two dimensions are ellipses that can be characterized by a major axis, σ_{\max} , minor axis, σ_{\min} , the angle the major axis makes with the x axis θ , and the center of the ellipse at μ_x and μ_y . The direction of the major axis θ can be determined from the eigenvectors of the covariance matrix. The variances along these directions are given by

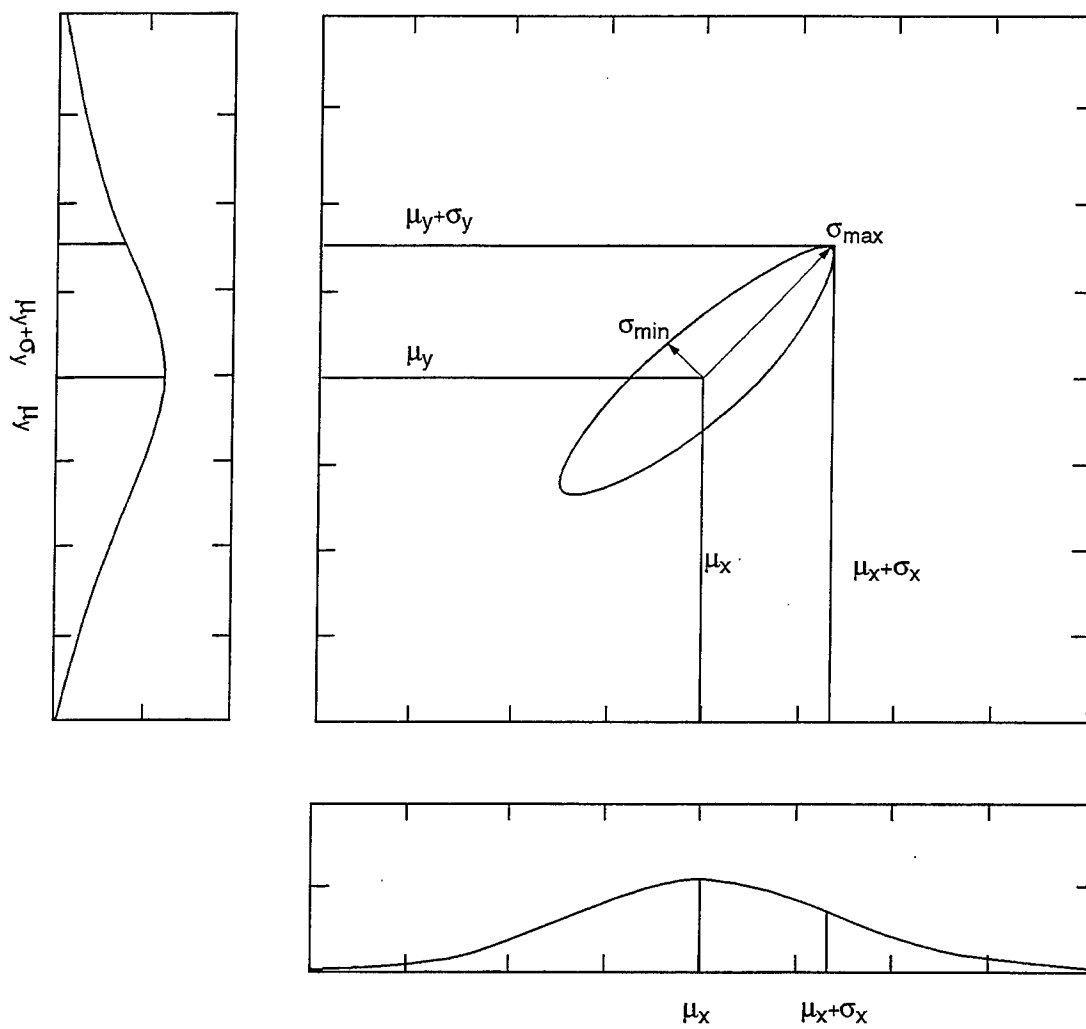


Figure 6-2. Single Band and Two Band Mean and Variance

the eigenvalues of the covariance matrix. An important parameter related to the variances and covariances is the correlation coefficient, ρ , given by

$$\rho = \frac{\sigma_{xy}}{\sqrt{\sigma_{xx}\sigma_{yy}}} . \quad (6-24)$$

The correlation coefficient is limited to the range $-1 \leq \rho \leq 1$.

The SCR in a single band is given by the expression

$$\text{SCR} = \frac{\mu_T - \mu_B}{\sigma_B} . \quad (6-25)$$

For a two-spectral-band system, when the covariance matrices for the target and background are the same, the SCR is the projection of the mean target minus background difference vector along the eigenvector associated with the minimum eigenvalue divided by the variance along the eigenvector associated with the minimum eigenvalue. This is shown graphically in Figure 6-3.

The optimal processor is a linear processor when the covariance matrices for the target and background are the same, namely

$$(\underline{X}_T - \underline{\mu}_B)^T \underline{R}^{-1}(\underline{\mu}_T - \underline{\mu}_B) > \gamma \quad \begin{matrix} \text{Target} \\ \text{Background} \end{matrix} . \quad (6-26)$$

Multispectral processing may provide a significant performance gain if there are mean color differences and if the radiances are highly correlated. When there is a mean color difference between target and background, and when the covariances for the target band background data are the same, the optimal processor defines the optimum linear combination of spectral bands upon which to decide target or background.

When the target and background covariances are the same, the two-band multispectral gain, G , for the optimal multispectral processor, that is, the ratio of the signal-to-clutter power at the output of the processor to that at the input, can be shown to be

$$G = \frac{(1 - 2\rho c + c^2)}{1 - \rho^2} . \quad (6-27)$$

The target background color difference, c , is defined to be

$$c = \frac{\text{SCR}_{\min}^2}{\text{SCR}_{\max}^2} \quad \text{with} \quad -1 \leq c \leq 1 , \quad (6-28)$$

where SCR_{\min} is the smaller and SCR_{\max} the larger single band SCR. The color is negative when the target radiance is smaller in one band and larger in the other. When the target radiance is larger (or smaller) in both bands the color is positive.

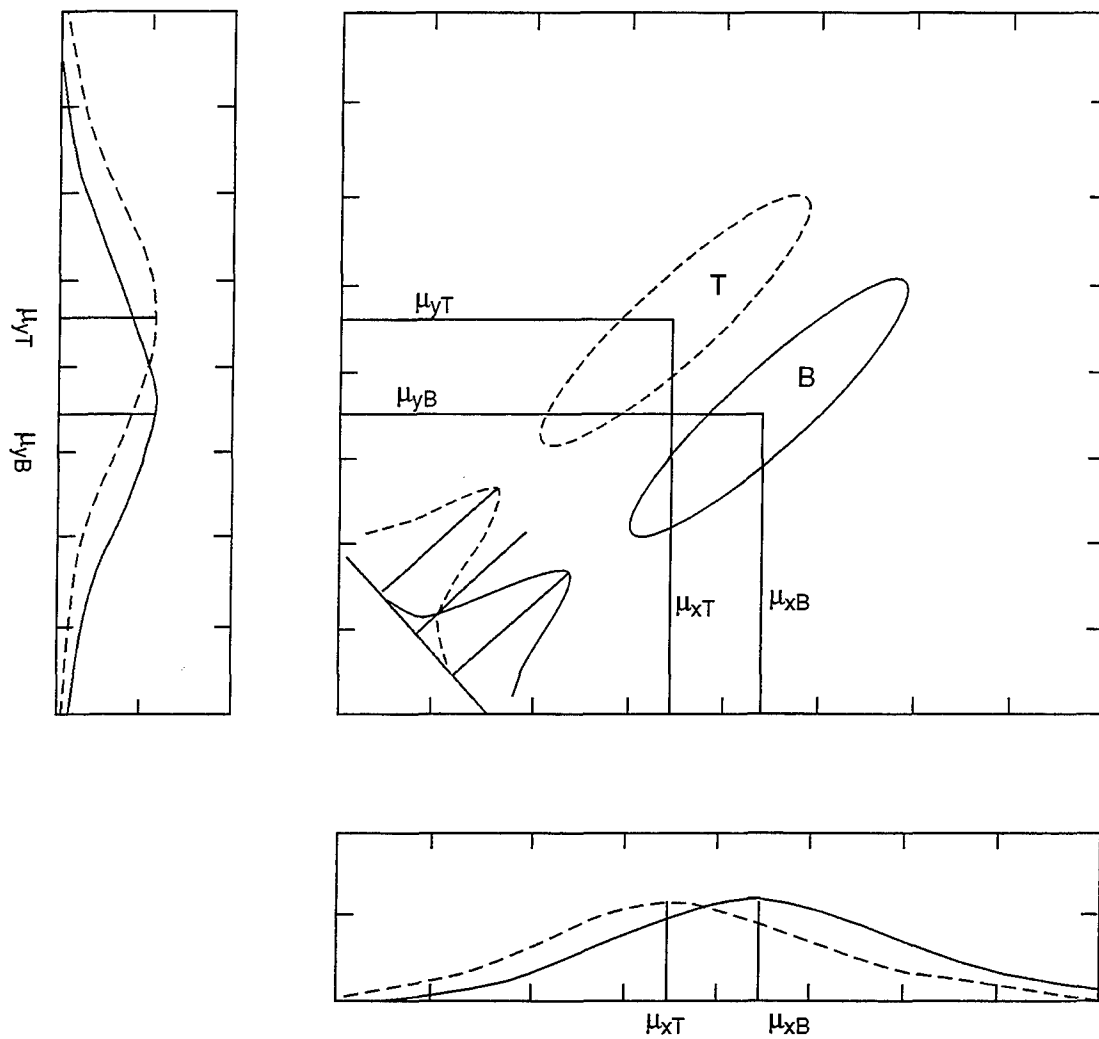


Figure 6-3. Single Band and Two Band Mean and Variance Differences for Target/Background Discrimination

The gain expressed in dB is $10 \log(G)$ when the signal-to-clutter ratios are power ratios (as defined above). When G is expressed in terms of radiance signal-to-clutter ratios, the gain in dB is $20 \log(G)$.

The optimal processor gain is shown as a function of color, C , and background correlation coefficient, ρ , and is shown in Figure 6-4. The gain is large with $c = -1$ for data with a high positive correlation coefficient. This corresponds to discrimination on the basis of the mean spectral emissivity difference. The gain is also large with $c = +1$ for data with a high negative correlation coefficient. This represents discrimination on the basis of brightness, illumination, or temperature. Discrimination with negative values of color and high positive spectral correlation coefficient are of high practical interest in detecting low contrast targets.

The practical use of multispectral processing needs to be evaluated in terms of multispectral gain and the improved SCR after processing. This depends not only on the statistical characteristics of the background, for example as represented by the two-dimensional scatter plot in Figure 6-2, but on the mean spectral emissivity and radiance differences between the target and background as shown in Figure 6-3.

6.4 MULTISPECTRAL CHANGE DETECTION

6.4.1 General Discussion

The regularity of repeat coverage by satellite multispectral imaging systems make them very amenable to the detection of changes in the landscape being observed. Upon spatially registering two images, a comparison can show areas of change between the two dates. Changes will appear as a brightening or darkening of the affected scene elements from the first date to the second and thereby be detectable. A variety of ways can be used to make such comparisons, and use of color is an effective approach. For instance, by properly normalizing (balancing) the signals and then displaying those from the first date in cyan and those from the second date in red, areas of no change will appear gray. Areas that are brighter on the second date will appear in red tones and those that are darker on the second date will appear in cyan tones. Change images typically are analyzed by human image interpreters in hardcopy photographic form (prints or transparencies) or in softcopy form (on digital displays). In digital form they also are amenable to more automated techniques of information extraction, subject to some complicating factors (discussed later).

A change image can be constructed from a pair of single-spectral-band or panchromatic images. However, the availability of multiple spectral bands offers four advantages. The first is the capability to combine band signals in a way that emphasizes selected kinds of changes in the change image, such as clearing of forests or vegetated areas during new construction. The second is the capability to differentiate between different kinds of change, based on the spectral observation vectors. The third advantage is that the spectral properties can be used to identify and mask confounding factors, such as clouds and cloud shadows. They also can be used to identify and mask scene classes of little interest to a given detection problem, such as water bodies on both dates or vegetation on the second date (e.g., when new construction is of interest). The fourth advantage is that spectral analysis can be used to detect the presence of atmospheric haze and help compensate for its confounding effects on change images.

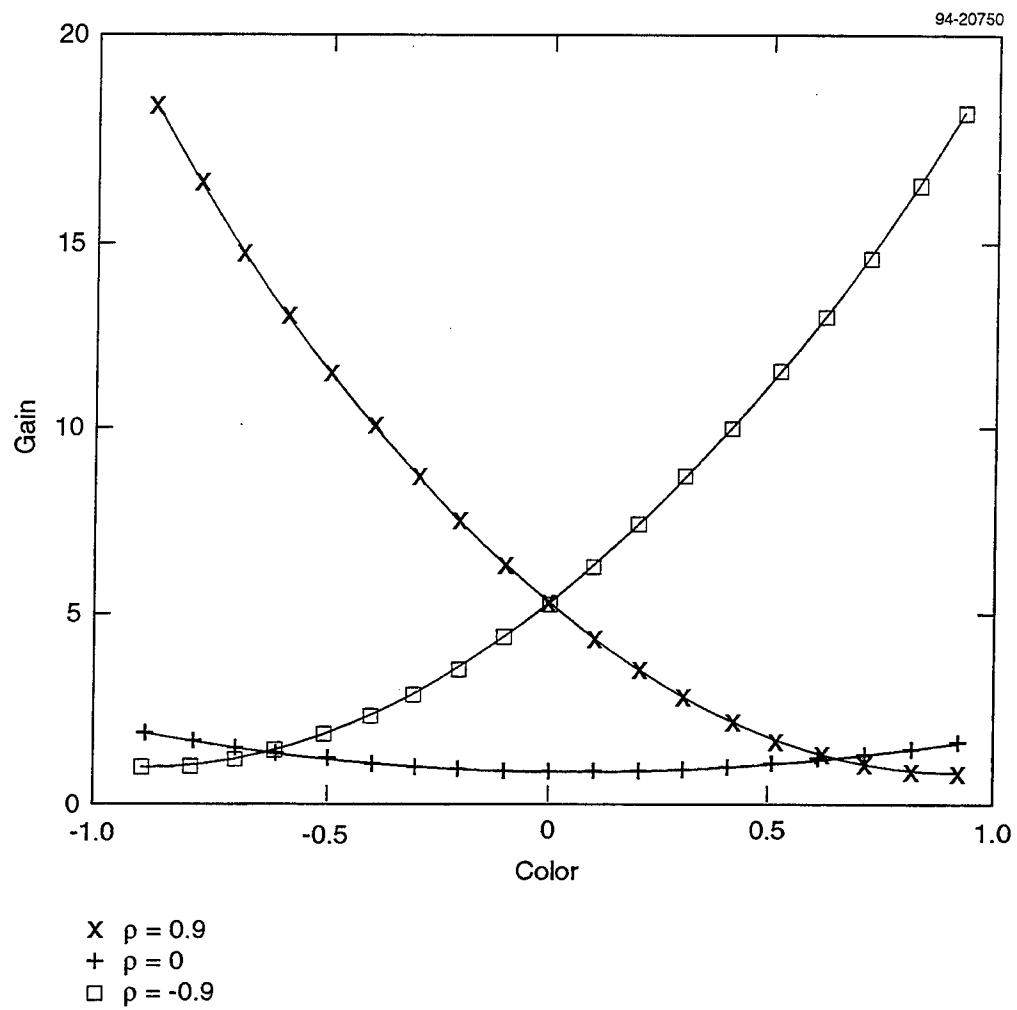


Figure 6-4. Optimal Multispectral Processor Gain vs. Target/Background Color

While the concept of change images for change detection is simple, there are complicating factors, some of which have just been alluded to. Complications arise when changes are present in the data that are not related to the changes on the ground that are of interest; these can produce false indications of change, or perhaps mask changes of interest, unless taken into account. First, there can be changes in sensor calibration from one date to the next; although the satellite sensors tend to be quite stable, long-term degradation trends in responses have been observed. Also, if two different sensors are being used for the change pair, their differences must be taken into account. Second, although the sensors tend to be in sun-synchronous orbits, there will be differences in the sun elevation and azimuth angles if the images are not acquired on the same day of the year (i.e., on anniversary dates); such differences affect the magnitude of solar irradiance. Third, clouds on either date will cause false indications of change. Fourth, there can be differences in the atmospheric conditions present on the two dates; of particular concern are spatially varying differences. (Refer to Section 6.5 on preprocessing techniques for a discussion of how to mitigate the above types of change.)

Other complications or confusion factors are related to nonrelevant changes on the ground. First, seasonal and year-to-year changes in vegetation growth patterns and plant vigor can occur, but these changes may not be of interest; year-to-year changes in agricultural field patterns can be particularly troublesome. Second, there can be changes in the weather-related conditions, such as rainfall just before one of the acquisitions which will darken areas of exposed soil.

The majority of change analysis that has been accomplished to date has relied on human analysts for interpretation. Human analysts have the capability to take into account many of the above-mentioned complicating factors when they are analyzing images, especially if some compensation techniques are employed in the production of the change image products being analyzed.

Automated analysis techniques are under research and development. With them, it is more important to account for as many of the complicating factors as possible to the best of one's ability. It is likely that the human analyst will be required "in the loop" for some time yet, to confirm and validate detections obtained by automated procedures.

6.4.2 Example Change Detection Procedures

Two change detection procedures are briefly described here to illustrate approaches that have been taken to implement change analysis of satellite multispectral data. Example products are presented in Section 8.

The first procedure is called PISCES (Production Image Screening and Change Editing System). It has been one of the capabilities in the Multispectral Imagery Materials Exploitation System (MIMES) processing system at SPACECOM (see Section 7.3.1.1) since 1988 and also recently was ported to the Multisensor Automatic Target Recognition With Interactive Exploitation (MATRIX) system (see Section 7.3.1.3). The PISCES procedure was designed for analysis of full (100 x 100 nmi) frames of Landsat TM data. It employs image-to-image registration as a first step in the procedure. Then, a screening analysis is used to detect clouds, which can be masked in the final product, since they cause false indications

of change. Any linear combination of the six TM bands can be used as the spectral change variable used to produce the change image product. A spectral feature designed to detect removal of forest vegetation, for example, has proven useful for detection of construction activities. The radiometric values of the two registered scenes are normalized or balanced so that unchanged areas have the same digital values and changed areas have larger or smaller values in the second-date image. By color coding the first date in cyan and the second date in red, the composite change image shows unchanged areas in gray tones, brightened areas in red tones, and darkened areas in cyan tones. Cloudy areas can be coded in white and, optionally, areas that are vegetated on the second date can be masked and tinted green (when changes in such areas are deemed to be of no interest, e.g., in agricultural fields). Geographic coordinates and grid markings based on satellite ephemeris also can be applied. More accurate location and geocorrection can optionally be performed using a few ground control points.

The second example procedure is called CVA (Change Vector Analysis). In this case, multiple spectral variables are analyzed and used to detect pixels that have changed from the first to the second date. Each spectral vector of change has both a magnitude and an angular orientation. Decisions about whether or not changes are of interest can be made by requiring both the change magnitude to be above a specifiable threshold and the angles of change to be in a given direction or sector. All the previously discussed masking and normalization operations are pertinent here as well.

To summarize, it is noted that, while panchromatic data also can be used to detect changes in scene content, multispectral characteristics offer the user the opportunity to differentiate between different types of change and to emphasize changes of particular interest. Although several parts of procedures have been automated, human analyst inputs have been required for the final use and application of change products, with higher degrees of automation being a subject of research and development.

6.5 PREPROCESSING OR SIGNAL CONDITIONING TECHNIQUES

Artifacts and features that are related to the sensor system and to the conditions of observation, rather than to characteristics of the scene surfaces being observed, can exist in remotely sensed data. When present, they detract from the quality of data exploitation processing and analysis results. User preprocessing or signal-conditioning procedures are designed to remove or reduce such effects before data exploitation techniques are applied. These effects may be either systematic or random, or both. Systematic effects are more easily characterized and corrected. The sections that follow discuss preprocessing corrections for sensor radiometry, scene conditions and atmospheric haze, and sensor geometry. Also, screening of data for the presence of clouds, and so forth, is discussed.

6.5.1 Corrections for Sensor Radiometric Effects

Systematic sensor-related effects include relative and absolute radiometric calibrations, stability of response, and scan-angle-dependent effects.

Two types of relative radiometric calibration are within-band equalization and between-band calibration.

Within-band equalization becomes an issue when multiple detectors are used for sensing within individual spectral bands in multispectral or hyperspectral systems. (For example, the Landsat Thematic Mapper scans 16 detectors for each spectral band, while SPOT uses thousands of detectors in a linear pushbroom array. Airborne line scanners, on the other hand, typically use only one detector per band.) Ideally, data from the within-band detector channels would be equalized by the time they reached the output of the sensor and ground processing system, so that the user need not worry about any such differences in the distributed data. However, when that is not the case, individual gains and offsets may have to be adjusted during user preprocessing operations to equalize the responses. This has been done by various organizations using several variants of histogram equalization, based on statistical analyses conducted over substantial portions of the scene or scenes, for example, equalization of means and matching of percentiles or standard deviations or matching of cumulative distribution functions.

Laboratory calibration procedures are used by sensor system developers as a step in accomplishing within-band equalization of multiple detectors. By having the individual detectors view reference sources and then adjusting their system outputs, equalization can be accomplished under the laboratory conditions. If channel responses would remain constant under operational conditions, the outputs would remain equalized. However, this constancy cannot always be relied upon, so additional reference sources typically are added by system designers, when it is feasible to do so. For instance, line scanners can be designed so they view reference sources in conjunction with each scan of the detectors over the scene, creating a continuous frame of reference for channel equalization.

Between-band calibration procedures also can make use of such reference sources. Stable relative calibration between spectral bands is important to the successful exploitation of certain spectral features of scenes and data sets. There are circumstances wherein band-to-band relationships may change from data set to data set. For instance, an airborne scanner system, with independent gain switches for each spectral band, may have different combinations of settings from collection to collection, when they are acquired under varied conditions. Such gain flexibility is desirable since it permits tailoring of collection parameters to optimum settings for a wide range of acquisition conditions. Satellite systems, on the other hand, tend to allow less flexibility in parameter settings. Nevertheless, parameters can change from sensor to sensor within a series of sensors of a given type (such as the Landsat TM series or the SPOT series) or gains among similar spectral bands can differ between sensor types (e.g., the visible and near-IR bands of Landsat versus SPOT). One must refer to absolute spectral radiance calibration coefficients in order to account for such differences.

Absolute spectral radiometric calibration information usually is delivered in the data tape headers, when available to the system operators. This information allows the user to convert digital counts on the data tapes to quantitative measures of spectral radiance or in-band radiance. These values generally can be referred back to well-established standards, such as National Institute of Science and Technology (NIST) standards or derivatives thereof. However, the calibration uncertainties typically may be 5 to 10 percent.

It is important to note that absolute radiometric calibration of data signals, while desirable, is not crucial to many exploitation applications. Those applications may either use training

data extracted directly from the data sets being analyzed or rely solely on the relative calibration between bands. Absolute calibration can be important for procedures that rely on spectral signature databases, for atmospheric corrections procedures that rely on model calculations, and/or for scientific investigations.

Stability of system response is crucial for maintaining calibration, both relative and absolute. When there is a tendency to drift, clamping of signals to stable signal sources (such as a dark level or a calibration source) can be employed. Clamping is required when the detector outputs are d-c coupled to the preamplifier circuitry, such in thermal systems.

Scan-angle effects can result when the sensor system has nonuniformities in the optical paths traversed by signals at different scan angles. This introduces systematic scan-angle-dependent effects which should be removed or reduced during user preprocessing. Even the sensor's signal-handling electronics can introduce scan-angle-dependent effects (e.g., signal droop effects observed in Landsat TM data).

Random noise effects also are present in multispectral and hyperspectral data. In addition to conventional random noise sources, describable by Gaussian or other statistical distributions, there may be other, more systematic noise sources. At times, interference from other electrical systems may introduce coherent noise at particular frequencies. In such instances, filtering techniques based on Fourier transforms have been used to reduce the noise effects. With Landsat TM, another type of artifact was observed, namely minor level shifts of predictable magnitudes that occurred at random, but post-facto identifiable, times. For applications where these effects would cause serious problems, preprocessing procedures could be designed to mitigate them.

6.5.2 Corrections for Scene Observation Conditions and Atmospheric Haze Effects

Both systematic and spatially varying effects can be introduced into multispectral and hyperspectral data by the conditions of observation. Recently, in June 1993, the Defense Landsat Program Office (DLPO) sponsored a Workshop on Atmospheric Haze Correction. During that meeting, a variety of algorithms and procedures were described and discussed. The reader is referred to those proceedings for details. Some general comments are given below.

Systematic effects related to conditions of observation include the effects of sun elevation angle at the time of collection and the effects of uniform atmospheric haze. Atmospheric haze can affect signals in two ways, by adding path radiance and by introducing multiplicative path transmittance effects. The observed path radiance depends on the illumination geometry and its relationship to the observation geometry (i.e., on solar elevation and solar azimuth angles relative to the directions of view or scan). For instance, the amount of observed path radiance typically increases as the view direction moves toward and away from the sun, and is least when the view direction is nearer to nadir (although the minimum is not necessarily at nadir). By flying directly toward or away from the sun, the sun-related component can be minimized.

The scan-angle effects observed in scanner data also can have a component that is scene-related. This is due to the fact that the bidirectional reflectance properties of many scene materials are not uniform as a function of view angle. Just as for atmospheric haze effects,

these bidirectional reflectance effects depend on both the illumination and view geometries and their relationships to each other.

Airborne scanners typically have larger scan angle ranges and greater scan angle effects than satellite systems. Active scan angle ranges often are as large as + and -45 degrees from nadir for airborne systems. Landsat TM, on the other hand, scans only + and -7.6 degrees from nadir.

Sun angle corrections recognize the fact that, when sunlight illuminates a flat surface, the irradiance (or radiant power per unit area) depends on the cosine of the angle between the surface normal and the direction of the sunlight. Thus, when the sunlight is normal to the surface, the irradiance is a maximum. For horizontal ground surfaces, this would occur with the sun directly overhead (zenith angle = 0). For other sun zenith angles, the irradiance would vary as the cosine of the angle. When two or more data sets are acquired at different sun angles, a useful approach has been to normalize them to a common sun-angle condition. Rather than picking the overhead position, it has been found convenient to select some intermediate sun-angle reference position.

The simple cosine correction for sun angle differences is often a reasonable approximation to the real situation, which is that there is some interaction between the sun-angle effect and the amount of atmospheric haze present. Ideally, corrections would take both factors into account.

Corrections for spatially uniform atmospheric haze have been made using several different procedures. Most rely on knowing or assuming something about the character of the haze parameters and using one of the available atmospheric models to estimate the atmospheric effects. Another method relies on there being some dark objects (such as water bodies) within the scene with which to estimate path radiance and transmittance effects; if there is a range of view angles represented in the data, there should be a good distribution of dark objects throughout the scene for best results. A different approach for correcting Landsat data (developed at ERIM) uses spectral haze diagnostics extracted from the data themselves to generate correction coefficients.

Spatially varying haze correction is a practical need for many data processing and exploitation operations, especially when large areas are being considered. Frequently, atmospheric haze and other such effects are not uniform and do vary as a function of position within the scene. Unless mitigated, they can degrade the performance of exploitation algorithms. Very few correction procedures have addressed this problem of spatially varying haze, instead concentrating on point locations or small areas. One approach would be to resort to haze-based scene stratification and to use different sets of haze correction parameters in the different strata.

An approach that has directly addressed the problem of spatially varying haze correction uses haze diagnostic spectral features extracted from the scene data themselves. Thus, it is able to estimate the variable amounts of haze present throughout the scene and adjust correction coefficients accordingly. This technique is still in development.

6.5.3 Corrections for Sensor Geometric Effects

Three aspects of geometric processing of multispectral/hyperspectral image data are: removing image-formation distortions, performing georeferencing and/or geocoding, and creating image mosaics. The level of geometric processing required by users depends on requirements of the particular applications of the data.

Geometric distortions can reduce the utility or ease of use of image data if they are not corrected, at least partially. Geometric distortions are observed in airborne line scanner data when they are reproduced directly into an image format. IFOVs are defined by angular dimensions and usually are scanned perpendicular to the flight direction. Therefore, the ground resolution element that is observed at nadir has the smallest pixel dimensions, while those at off-axis angles are progressively larger. Aircraft roll, pitch, and yaw, along with the scanning pattern and aircraft motion along track, introduce other types of distortions. Satellite sensors have their own types of scan distortions, be they line scanners or pushbroom arrays.

It is common for airborne line scanners to employ only a roll correction procedure on the raw data that are recorded. Therefore, if necessary, any other scan distortions have to be corrected during post-collection or pre-exploitation processing operations. In order to do this, use is made of on-board inertial navigation data and, more recently, Global Positioning System (GPS) data.

The Landsat TM system on the other hand has a complicated bi-directional scanning pattern so the ground-processing system usually performs a first level of geometric correction on TM data before they are distributed to users.

Georeferencing and geocoding involve higher levels of geometric processing. The increasing use of geographic information systems and image-based mapping has made them more important for image data applications. In georeferencing, selected image data points are matched to ground-control reference points, and geographic coordinates can be computed for each pixel. Geocoding usually refers to a resampling of the image data so as to conform to a selected geographic coordinate projection grid. This can be used, for example, to rotate images to a north-south orientation and permit overlays of map information.

An even higher level of correction is orthorectification, which takes into account image distortions caused by varying terrain elevation relief and different viewing perspectives. The corrected pixel are located on a horizontal ground projection, as though the sensor had been directly overhead when viewing each of them. DTED are required in the orthorectification process.

Orthorectification of airborne scanner data is more of a challenge than spaceborne scanner data, due to the greater amounts of platform motion caused by air turbulence. Only recently have procedures been implemented to do this on an operational basis. For instance, ERIM's M-7 Mapper now can record and use differential GPS measurements to supplement inertial navigation signals and produce orthorectified and geocoded image data [Rice 1994].

Mosaicking is used to create larger image databases from two or more smaller images that are contiguous or overlapping. Typically mosaicking is done with geocoded data. Use of orthorectified images in the mosaicking process produces the most accurate results.

6.5.4 Data Screening and Masking Procedures

All pixels are not necessarily useful for the exploitation of spectral data. For example, clouds can interfere with views of the ground, and their shadows can confuse spectral algorithms. Also, bad data values may exist, such as due to data dropouts, saturation, and so forth. Procedures that detect and flag such pixels are called data screening procedures. These procedures employ spectral decision rules and knowledge of the expected distributions of valid spectral data. The screening information usually is captured in the form of image masks which can be applied during data exploitation.

Image masks also can be developed to select pixels based on other attributes, such as their ground-cover class, for selective use in data exploitation. For example, a user might wish to detect and flag all pixels having vegetated ground cover or those covered by surface water. Again, spectral or spectral-spatial decision rules are used as the basis for mask generation.

6.6 TERRAIN CATEGORIZATION

The availability and use of spectral differences for categorizing various terrain classes is a major advantage of multispectral image data over single-band (e.g., panchromatic) data. While image tone and texture have use as single-band discriminants, it is the spectral dimension that leads to greater discrimination possibilities, both in terms of class separability and the number of classes that can be distinguished. Note that in addition to "categorization", this function also is called "classification."

Two major classes of categorization techniques are discussed in the literature, supervised and unsupervised techniques. The "supervision" distinction refers to the use of analyst-designated training data in establishing the decision-rule parameters or decision boundaries for the particular categorization task, that is, a supervised technique could require the analyst to select and label a representative set of training data, within the data set being analyzed.

An unsupervised technique on the other hand, would be expected to operate independently on the data and come up with an appropriate categorization.

Most image processing packages have a selection of categorization rules which can be employed. The following sections discuss the general characteristics of many of those techniques.

6.6.1 Supervised Techniques

Categorization techniques usually partition the data space into regions with assigned labels. Each pixel is assigned the label of the region into which it falls. Training data are used to establish the partitions, using descriptors that are appropriate to the decision rule being employed. The descriptors typically are statistical in nature.

Paralleliped decision rules are one of the simplest supervised spectral categorization techniques. Each training set is characterized by the range of its data values in each variable. Using these limits to establish decision boundaries and paralleliped cells, pixels are tested and assigned the label of the cell they fall in. If the cells overlap, a precedence rule is invoked.

For maximum-likelihood decision rules, training data are described statistically by their mean vectors and variance-covariance matrices; these at times are referred to as training

signatures. The corresponding decision partitions are multidimensional quadratic surfaces. The procedure computes the quadratic distance of each pixel from each of the signature means, inversely weighted by the variance-covariance in the corresponding direction. The closest category is selected. If desired, a test can be made to insure that the pixel distance exceeds a specified threshold; if not, the pixel is assigned to the "Unclassified" category. Different weights can be assigned to target and background categories, to implement Bayesian decision rules.

Quadratic decision rules are optimum, when the data are in multivariate Gaussian (normal) distributions about their respective means. In actuality, the data usually are not perfectly normally distributed, but the assumption is often made for ease of computation and analysis.

Maximum likelihood calculations are more intensive than parallelopiped calculations. Before general-purpose computers had present-day computational speeds, at least two different approaches were taken toward solution of this problem for large data sets. ERIM, for instance, developed special-purpose computer hardware that implemented a quadratic decision rule and, for a software solution, made best-linear approximations to the quadratic decision rules.

As the number of spectral bands increases, the dimensionality of the variance-covariance matrix increases accordingly, and the number of training samples required to obtain well conditioned matrices goes up by the square of the number of bands. Sometimes, with small targets, it is not possible to get enough samples to properly train a maximum-likelihood decision rule. In such cases, a K-nearest-neighbor rule can be employed. Rather than computing distances from ill-defined statistical distributions of the training classes, distances are computed from individual training pixels in the categories of interest. The most common category found among the K nearest training pixels is assigned to the pixel in question.

6.6.2 Unsupervised Techniques

Clustering is often referred to as an unsupervised technique, in that such techniques can operate autonomously on data and determine localized groupings or clusters within the spectral, spectral-spatial, spectral-temporal, or spectral-spatial-temporal data space. The number of clusters is a function of algorithm parameter selections and the underlying data structure.

Spectral clustering is the most common form of clustering used with multispectral data. The distance metrics are based solely on the spectral observation vectors. Another form is spectral-spatial clustering, which segments images into contiguous groups of pixels with homogeneous spectral characteristics (within the variance parameters used in the procedure). Spectral-temporal clustering can be used simply by combining two data sets acquired on different dates into a set with twice the dimensionality and then applying regular spectral clustering procedures.

A problem with clustering approaches is that the clusters usually do not have automatically assigned labels that identify them as belonging to specific terrain categories. Some categories of interest may have multiple clusters, while others may have only one. Also, there is the possibility that some spectral clusters may contain more than one cover class of interest. Tree-structured approaches may be helpful in organizing the results for analysis and labeling.

In order to go from a spectral clustering to a terrain categorization product, analyst input usually is required to assign labels to the various spectral classes that have been identified. If the entire data set had been clustered, then the labeling step would complete the categorization process. If only a sample of data had been clustered, then the labeled clusters could be used to establish data-space partitions for categorization of the remaining data set pixels. Any of the techniques previously discussed for supervised categorization could then be employed.

Automated cluster labeling could be a possibility, if proper attention were paid to normalization of the data sets to reduce or remove effects caused by different conditions of observation. The labeling process would most likely concentrate on spectral characteristics of the data, with less emphasis on spatial properties. Such automation presently is more in the realm of research and development than operational practice.

Neural networks have some similarities to clustering techniques. In this case, labeled training data are provided to the processor which analyzes them and establishes decision patterns to be applied to new or unknown data samples. A key requirement is that the training data be representative of the data sets to be analyzed. Without adequate preprocessing and normalization, this could be a daunting requirement, with operation in a truly unsupervised mode more hope than reality. Again, neural network procedures for multispectral categorization are primarily in the research and development stage.

6.6.3 Target Detection

Automatic target recognition is a goal of many systems. As with terrain categorization, the spectral dimension can add considerable discrimination power to image data. When target properties are unique or distinctly different from their backgrounds, use of automated procedures become feasible, but complete automation is an elusive goal. Section 8.xyz presents one example of multispectral discrimination of camouflaged targets, using spectral rules combined with spatial processing and proximity calculations.

Since targets of interest often are small, the discussion in Section 6.6.1 on training and K-nearest-neighbor techniques is important. Also, robustness will be an issue since there can be many observation variables (such as sun angle, terrain slope, vegetation shadows, and vegetation and terrain variability) affecting the spectral signals received by an imaging sensor. This highlights the need for normalization or some form of compensation for the variability. Ratios are sometimes used to cancel multiplicative effects.

6.7 SUBPIXEL SPECTRAL MIXTURE ESTIMATION

Individual pixel observations by multispectral and hyperspectral sensing and imaging systems frequently contain mixtures of two or more classes of materials, such as a target and its surrounding background or two or more different land cover classes (at boundaries). Furthermore, the material classes themselves can be composed of more than one spectral subclass and these subclasses, in turn, can be subjected to different illumination and shadowing conditions, such as in a vegetation canopy or a complex target. Finally, even the materials of the spectral subclasses themselves can contain multiple components that contribute distinctive spectral characteristics, such as the biochemical components of a leaf or the minerals in a rock.

Techniques to assay spectrally the composition of individual pixels or observations have been described or referred to by several different names. Among these are proportion estimation, convex mixtures analysis, sub-pixel analysis, and spectral unmixing.

6.7.1 Background

Early sub-pixel proportion estimation techniques were developed and applied to Landsat Multispectral Scanner (MSS) data by ERIM investigators. The 80-meter spatial resolution of MSS caused crop inventory accuracy problems on boundary pixels that contained mixtures of different crops. Therefore, techniques were designed to improve the accuracies of crop area inventories (Horwitz, et al., 1971 and 1975; Nalepka and Hyde, 1972). These techniques also were applied to improve surface-water area determinations for lakes and ponds, which also suffered from effects of mixed (water/land) pixels (Work, et al., 1973; Malila and Nalepka, 1973). Another innovation by Horwitz, et al., 1975, called LIMMIX (standing for limited mixtures) increased computational efficiency. In effect, it found boundary pixels, determined for each one which major crop class was on each side of the boundary, and then computed the mixture ratio between those crops.

Richardson, et al., 1975, investigated regression relationships for describing proportions of plant, soil, and shadow reflectances in row crops. All the above were primarily limited to research applications.

A number of astronomers and planetary geologists made use of sub-pixel techniques for interpreting imaging spectrometer images from geological sites and planetary probes (Marsh, et al., 1980; Pieters, et al., 1985; Kruse, et al., 1990). The term "spectral endmember" was adopted to describe the fundamental components which could comprise a pixel. Some have found it helpful to include a shade category (or shade "spectral endmember") to reduce uncertainties or variations induced by terrain slope and aspect effects.

The end-member approach also was applied to Landsat data of naturally vegetated scenes (Adams and Adams, 1984; Adams, et al., 1990) with definition of generic spectral endmembers, such as green leaves, stems, and bare soil. These, along with the shade endmember, were used to describe vegetation canopies. Alternatively, by first estimating and then removing the vegetation component(s) from their analysis, some investigators have claimed improved performance in geologic mapping applications.

A sub-pixel estimation procedure for detecting the presence of roads in Landsat Thematic Mapper multispectral data was developed by Rice (1989).

A subpixel approach was applied by Dozier (1981) and Mattson and Dozier (1981) to estimate temperature and size of subpixel-sized sources in two-band thermal data from the AVHRR satellite (1,100-meter resolution).

Gillespie, et al., 1990, applied the spectral unmixing approach to multiband thermal data, to capitalize on differences in spectral emittance. Temperature is a confounding factor. Instead of adding a shade endmember spectrum, as was done for analyses of reflected data, they defined a "virtual cold" endmember.

Recently, NASA sponsored investigators to look at remote sensing methods for determining foliar chemistry of forests and other types of vegetation, in support of the HIRIS

(High Resolution Imaging Spectrometer) system, which had been planned for the EOS. However, HIRIS has been eliminated from the baseline EOS sensor configuration.

6.7.2 Discussion of Approaches

The various technical approaches that have been taken toward solving the spectral sub-pixel estimation or unmixing problem are characterized by: (a) their underlying models, (b) their data domains, and (c) their computational procedures.

6.7.2.1 Mixing Models

Linear models are preferred for formulation of spectral unmixing algorithms, because of their mathematical tractability. In all three types of sub-pixel estimation problems, linear models usually have been employed, sometimes through the use of linearization transformations, approximations, and assumptions.

In their initial formulation of the spectral mixtures problem (for initial application to agricultural crop inventory), Horwitz, et al. (1971) derived a multivariate-normal model in which signals from each component class were described by a mean vector and a variance-covariance matrix. Their linear model of a mixture pixel's mean vector was a simple weighted average of the component-class mean vectors. Similarly, their mixture covariance matrix was modeled as a simple weighted average of the component covariance matrices. This linear approach appears to be reasonable for Type I problems, despite the complexities of individual canopy reflectances which actually are nonlinear functions of components.

Individual rock types are nonlinear (sometimes called "intimate") mixtures of small mineral grains of various types; that is, their reflectance spectra are nonlinear functions of the pure-constituent spectra. Nevertheless, linear treatment of mixture spectra has been found to be an acceptable approximation for geological remote sensing applications.

A common formulation of the problem expresses each pixel's signal as a linear combination of "end-member" spectra and a residual term:

$$S_i = \sum_k f_k M_{ki} + e_i \quad (6-29)$$

where S_i is the observed signal in spectral band i ,
 M_{ki} is the i^{th} spectral component of endmember k ,
 f_k is the fraction of endmember k , and
 e_i is the residual error for spectral band i .

The spectral unmixing solution then becomes one of finding appropriate end-member spectra and doing an inversion for each observation S to determine the corresponding fraction coefficients f_k which best fit the observation, that is, in vector/matrix form:

$$F = M^{-1}S + E \quad (6-30)$$

6.7.2.2 Data Domain of Analysis

Remote sensors detect spectral radiances emanating from scenes. Information about objects and materials being observed via reflected radiation is introduced through their bidirectional spectral reflectance and transmittance characteristics; physical properties and structures; and orientations with respect to illumination sources. However, the intervening atmosphere confounds the problem of analysis, through the introduction of both additive path radiance and path transmittance losses.

Spectral unmixing analyses have been conducted in radiance data space, in reflectance data space, and in $\log(1/\text{reflectance})$ space.

Radiance-Space Analysis

The most direct approach to spectral mixtures analysis and spectral unmixing deals directly with the observed radiances. If examples of pure endmembers, or pure targets, can be extracted from the image data, then the unmixing calculations can proceed.

For some unmixing procedures, a shade endmember is needed. Analysts would prefer it to be from a dark material that is shadowed. When this is difficult to find, an approximation is made by selecting the darkest pixel in the scene (Gillespie, et al., 1990). Recently, it has been realized that "shade" can have a spectral character. For example, shadows cast by leaves are dark in the visible region, but brighter in the near-IR, since near-IR leaf transmittance is about 50 percent, versus 5 to 15 percent in the visible.

In the case of multiband thermal data, observed radiances are functions of both the temperatures and spectral emittances of constituent materials. In linearizing the model, Gillespie, et al. (1990) assumed that each pixel was made up of spectral components at the same temperature, although the temperature could vary from pixel to pixel. This simple model results in errors when the assumptions are not met, which is the case when rocks and vegetation are mixed. Other ramifications and considerations are discussed by those authors in their paper.

Reflectance-Space Analysis

As an integral part of their analysis and interpretation of data, especially hyperspectral data, many investigators are interested in referring to a reference library of reflectance spectra. This means that some method must be employed to account for atmospheric and illumination effects in the data and put them into reflectance terms.

Perhaps the ideal way would be to have co-incident ground-based spectral-reflectance measurements of scene materials at several locations within the scene. The selection would provide at least one low-reflectance and one high-reflectance measurement at each wavelength. If the atmospheric conditions are uniform, the image data can then be calibrated into reflectance throughout the scene and reference reflectance libraries can be used in analyses.

In the absence of co-incident ground-based measurements, some investigators make assumptions about what types of materials are at some locations and assign reflectance spectra to them from a spectral library. Then the analysis proceeds as it would in a ground-calibration case.

When atmospheric conditions vary spatially (e.g., spatial distribution or terrain elevation differences), only addressed once or twice in the literature, the solution has been to perform multiple calibrations to reflectance, each for a different segment of the scene.

Log(1/R)-Space Analysis

In laboratory reflectance spectroscopy, it has been found that the reflected radiance spectra depend on the absorption spectra of the constituent materials of the sample. Since absorption is an exponential function of concentration, a good approximation has been found to be that concentration, c , is proportional to the negative logarithm of reflectance (R), that is,

$$C \propto -\log(R) = \log(1/R) . \quad (6-31)$$

Therefore, in $\log(1/R)$ space, the unmixing problem is treated as a linear combination of absorbing material concentrations.

6.7.2.3 Computational Procedures

Continuum Versus Band Residuals

Outside of atmospheric (and solar) absorption bands, the solar irradiance spectral distribution is smooth and has a blackbody shape. The spectral characteristics of materials being observed influence the received radiation; dips occur where there are absorptions. Some investigators have found it helpful to consider each measured spectrum to consist of a continuum, which describes the general background shape, and a residual, which contains spectral contributions from unusual scene constituents and nonlinear effects, especially concentrated in narrow absorption bands.

After selecting a set of endmember spectra to model the continuum domain, each individual pixel vector is analyzed and decomposed into the best fitting mixture of the endmember spectra. If the fit is not perfect, there is a residual error. The errors may appear only at certain wavelengths, such as in narrow absorption bands that are not represented in the endmember spectra. After analysis, new endmembers may then be added and the procedure repeated. The sequence then continues until the residuals reach an acceptable minimum level or cannot be improved. Typically four to eight endmembers are selected in an analysis, even when hyperspectral data are analyzed.

Comments from some other investigators have been to the effect that the emphasis on residual analysis reflects a deficiency of the procedure for selecting the endmember spectra. A key need is for an optimum procedure to select or determine appropriate endmembers for each pixel.

To display results of a spectral unmixing analysis, several "fraction images" often are created, each one showing the fraction of a given class that is detected at (or estimated for) each pixel. These fraction images can be analyzed during the analysis process, as well as at the end of the procedure.

Analysis-Driven Selection of Endmembers

Especially when reflectance calibration of the data is possible, knowledge about the scene and its characteristics can be used to select spectral endmembers from a spectral library or

from ground-based measurements. In theory, one can have one more endmember than the number of bands available, but the high degree of correlation among hyperspectral bands drastically reduces the number of distinct endmembers that can be employed. Noise and scene variability also have effects.

Log Residuals Analysis

Australian researchers, Green and Craig, 1985, developed a ratio-like method of converting raw data to apparent reflectance, without having to rely on field measurements to convert to absolute reflectance. The method approximately removes multiplicative effects due to the atmosphere, solar illumination, instrument gains, and also irradiance differences due to surface geometry variations. On the other hand, it is sensitive to noise in the data and to the uniformity of distribution of materials and presence of outlier spectra (clouds, shadows, water, etc.) in the scene.

Expert Systems

Expert system approaches to analysis of hyperspectral data have been under development for geological mapping by Kruse (1988). Rubin (1989) describes a knowledge-based approach to automated mapping of mineralogy, using multispectral data.

Categorization

Categorization of data sets can be based on the estimated sub-pixel components. For instance, Lavreau and Tréfois (1988) used spectral mixing models for soil classification of Landsat TM data. Also, Adams, et al. (1990) applied the approach to categorization of Landsat data of the Amazon forests, finding that different combinations of green, bare-wood components, bare soil, and shadow components permitted definition of distinct classes.

Atmospheric Water Vapor Estimation

Several investigators have analyzed spectral dips in radiance within the 940 nanometer water vapor absorption band to estimate the total precipitable water vapor in the atmospheric column (Gao and Goetz, 1990; and Green, et al., 1991). Claims of being able to detect small enough differences in precipitable water vapor to measure terrain elevation differences (under the assumption of uniform atmosphere) have been made (Green, et al., 1991).

Leaf Moisture Estimation

Gao and Goetz (1990), went one step farther in water vapor estimation, analyzing the possibilities of differentiating between atmospheric water vapor absorption and absorption by liquid water in green leaves. They are exploiting spectral differences in these two absorption phenomena, that is, an offset of about 50 nanometers in the absorption band centers.

Spectrum Matching

With the large number of spectral bands, it becomes computationally involved to conduct spectrum matching operations. At least two procedures have been developed for making these calculations, the Hamming Distance Metric and Spectral Angle Metric (SAM). These measure the similarity between vectors without regard for their relative magnitudes (brightness).

6.8 UNIQUE ASPECTS OF SPECTRAL PROCESSING IN THE THERMAL INFRARED

The multispectral signal processing principles are the same in the reflective and emissive portions of the spectrum. However, the interactions with the environment are different so that the target-background contrasts, signal-to-clutter levels, and background statistics are different in the two regimes of the spectrum.

Spectral reflectance differences between classes of materials in the reflective portion of the spectrum between 0.4 and 2.5 μm are frequently large and pronounced. These arise because of differences in chemical composition and corresponding differences in electronic structure. This might suggest that multispectral discrimination should be easy. However, there are large natural variations in the reflectances of samples from the same class. This leads to the requirement for a statistical characterization of the reflectance properties of materials in terms of the mean spectral reflectances, variances and spectral correlations. Even more spectral variability is introduced by illumination from the sun, sky, clouds, and surrounding background, by the viewing geometry, and by the atmosphere. Despite the statistical variations, there are many examples of the application of multispectral target detection and target/background discrimination demonstrated for both military and civilian applications. Some of these will be detailed in Section 8.

Spectral emittance variations in the thermal infrared, between 3 and 14 μm , tend to be smaller than the corresponding spectral reflectance variations in the reflective portion of the spectrum between 0.4 and 2.5 μm . Many target and background materials, for example, many paints, water, soil, road materials, and vegetation have spectral emissivities between 0.8 and 0.95 between 8 and 14 μm and between 0.5 and 0.9 between 3 and 5.5 μm . Although there are spectral emissivity differences between different materials, they are less pronounced than in the reflective portion of the spectrum. In the MWIR between 3 and 4.2 μm , both solar reflection and thermal emission contribute to the spectral radiance. Spectral signature analysis in this portion of the MWIR is difficult to analyze during the daytime because an increase in reflectivity causes an increase in the reflected radiance; at the same time the decrease in emittance ($\epsilon = 1 - \rho$ by Kirchhoff's law) causes a decrease in the emitted radiance. These competing effects cause the signature effect of either alone to be reduced.

Radiance in the thermal infrared is determined by emittance and temperature. Variations in temperature can cause large variations in the radiance at a remote sensor (analogous to variations in the intensity of solar input in the visible). Temperature variations can also cause spectral variations (Planck's law). It is not possible, by remote sensing alone, to measure the temperature and spectral emissivity separately. This causes additional variability in the statistics of targets and backgrounds that makes target/background discrimination more difficult.

Multispectral sensing may be able to utilize bands in the reflective and emissive portions of the spectrum effectively for both day and night operation or as a means of discrimination on phenomena of different origin, for example, electronic transitions in the visible and near infrared and molecular vibrational transitions in the thermal infrared.

This section presents a discussion of two thermal multispectral applications that are significantly different and potentially important for military applications. The first is

emissivity mapping, the second is spectrally correlated background clutter suppression. Thermal multispectral target detection and target/background discrimination is currently the subject of intensive investigation. Suppression of spectrally correlated backgrounds as a means of enhancing target contrast for target detection is one example of multispectral target detection in the thermal infrared.

6.8.1 Emissivity Mapping

The radiance in the thermal infrared at a remote sensor $L(T, \lambda)$, includes both emitted and reflected radiance and is given by the following expression

$$L(T, \lambda) = \tau_p(\lambda)[\varepsilon(\lambda)L_{bb}(T, \lambda) + (1 - \varepsilon(\lambda))L_{env}(\lambda)] + L_p(\lambda) , \quad (6-32)$$

where $L_{bb}(T, \lambda)$ is the Planck blackbody radiance,
 $L_{env}(\lambda)$ is the radiance from the environment,
 $\varepsilon(\lambda)$ is the spectral emittance,
 $1 - \varepsilon(\lambda)$ is the spectral reflectance,
 $\tau_p(\lambda)$ is the atmospheric transmission, and
 $L_p(\lambda)$ is the path radiance.

It is not possible to measure both the temperature and the spectral emissivity by means of spectral radiance measurements alone. N spectral band measurements cannot unambiguously determine N spectral emissivities and a temperature. However, there are a number of factors that permit a practical separation of the spectral emissivity and temperature. The simplest of the emissivity mapping techniques is based on a principal component analysis. Under conditions when radiance variations are dominated by thermal variations in the scene, for example, with solar loading during the day, most of the variation caused by temperature is contained in the principal component image corresponding to the largest eigenvalue. Variations in the other principal component images correspond to spectral emissivity variations. If the dimensionality of the space is reduced by one, from N to $N - 1$, by projecting out the dimension of the principal component containing the temperature variations, the result is N images containing only variations due to spectral emissivity variations.

Other methods have been developed for emissivity mapping and for viewing thermal multispectral thermal data. These include band ratioing and normalization of the data by the data in a broad band channel. The results using these other techniques are similar.

There are significant potential applications for emissivity mapping to terrain categorization, trafficability, moisture content, new construction, and temporal changes in the terrain as part of the military requirements for mission planning and intelligent battlefield preparation. Several examples of emissivity mapping in the thermal infrared will be given in Section 8.

6.8.2 Spectrally Correlated Background Clutter Suppression

Emissivities for most materials vary between 0.8 and 0.95 in the 8 to 14 μm thermal infrared. Thermal emission is generally the dominant term with variations caused by spectral emittance variations small by comparison. The signal to clutter ratio is frequently less than one in any one single band in the thermal infrared.

Variations in the radiance in the thermal infrared are due largely to variations in temperature. Recent work by ERIM, Space Computer Corp., and SAIC for the Air Force Wright Laboratories, sponsored by ARPA, has discovered that the radiance correlations between spectral bands in the thermal infrared is very high. For example, the spectral correlations within the window region between 8 and 12 μm is frequently 0.99 to 0.9999 for vegetation or partially vegetated desert backgrounds. Correlations are smaller at thermal crossover when thermal variations are smaller. Correlations are also high between band pairs in the 4.2 to 5.5 μm MWIR, and between bands in the 4.2 to 5.5 μm MWIR and 8 to 12 μm LWIR. This is very significant because it suggests that the variability in the spectral emissivity for these backgrounds is very small.

Differences in the mean spectral emissivities of targets and backgrounds have also been found to exist. The significance is that even when the SCR is low in a single infrared band, multispectral processing can significantly suppress the clutter because of the high spectral correlation in the thermal infrared. This results in a significant increase in the SCR.

Multispectral and hyperspectral sensing has been shown to have significant potential in the thermal infrared for detecting low contrast targets with possible application to camouflaged and partially obscured targets. An example is shown in Section 8.

6.9 BIBLIOGRAPHY

- Adams, J.B., V. Kapos, M.O. Smith, R.A. Filho, A.R. Gillespie, and D.A. Roberts, "A New Landsat View of Land Use in Amazonia." In *Proceedings of International Symposium on Primary Data Acquisition '90*, ISPRS, pp. 177-185, 1990.
- Adams, J.B., M.O. Smith, and P.E. Johnson, "Spectral Mixture Modeling: A New Analysis of Rock and Soil Types at the Viking Lander 1 Site." *Journal of Geophysical Research*, Vol. 91, No. B8, pp. 8098-8112, 1986.
- Boardman, J.W., "Inversion of Imaging Spectrometry Data Using Singular Value Decomposition." In *Proceedings of IGARSS '89*, pp. 2069-2072, 1989.
- Carmer, D.C., R. Horvath, D.P. Rice, and J.W. Sisak, "M-7 Mapper Multispectral Testbed." In *Proceedings of the Second Thematic Conference on Remote Sensing for Marine and Coastal Environments*, New Orleans, LA, 1994.
- Clark, R.N., A.J. Gallaher, and G.A. Swayze, "Material Absorption Band Depth Mapping of Imaging Spectrometer Data Using a Complete Band Shape Least-Squares Fit With Library Reference Spectra." In *Proceedings of Second AVIRIS Workshop*, pp. 76-186, 1990.
- Clark, R.N., T.V.V. King, and N.S. Gorelick, "Automatic Continuum Analysis of Reflectance Spectra." In *Proceedings of Third AIS Workshop*, pp. 138-142, 1987.

- Colwell, J.E. and F.P. Weber, "Forest Change Detection," in the *Proceedings of the Fifteenth International Symposium on Remote Sensing of Environment*, Ann Arbor, MI, pp. 839-852, 1981.
- Crist, E.P. and R.C. Cicone, "A Physically-Based Transformation of Thematic Mapper Data--The TM Tasseled Cap", *IEEE Transactions on Geoscience and Remote Sensing*, Vol. GE22, No. 3, pp. 256-263, 1984.
- Crist, E.P., "A Spectral Haze Diagnostic Feature for Normalizing Landsat Thematic Mapper Data." In *Proceedings of Eighteenth International Symposium on Remote Sensing of Environment*, Paris, France, pp. 735-744, 1984.
- Defense Landsat Program Office, *Proceedings of the Workshop on Atmospheric Correction of Landsat Imagery*, Geodynamics Corp., Torrance, CA, June 1993.
- Dozier, J., "A Method for Satellite Identification of Surface Temperature Fields of Subpixel Resolution," *Remote Sensing of Environment*, Vol. 11, pp. 221-229, 1981.
- Gao, B.C., and A. Goetz, "Column Atmospheric Water Vapor and Vegetation Liquid Water Retrievals From Airborne Imaging Spectrometer Data." In *Journal of Geophysical Research*, Vol. 95, No. D4, pp. 3549-3564, 1990.
- Gillespie, A., M. Smith, J. Adams, and S. Willis, "Spectral Mixture Analysis of Multispectral Thermal Infrared Images." In *Proceedings of 2nd Thermal Infrared Multispectral Scanner (TIMS) Workshop*, JPL Publication 90-55, pp. 57-74, 1990.
- Gillespie, A., M. Smith, J. Adams, S. Willis, A. Fischer III, and D. Sabol, "Interpretation of Residual Images: Spectral Mixture Analysis of AVIRIS Images, Owens Valley, CA." In *Proceedings of Second AVIRIS Workshop*, pp. 243-270, 1990.
- Goetz, A.F.H. and J.W. Boardman, "Quantitative Determination of Imaging Spectrometer Specifications Based on Spectral Mixing Models." In *Proceedings of IGARSS '89*, pp. 1036-1039, 1989.
- Goetz, A.F.H., G. Vane, J. Solomon, and B. Rock, "Imaging Spectrometry for Earth Remote Sensing," *Science* V228, Vol. 4704, pp. 1147-1153, 1983.
- Green, R., J. Conel, J. Margolis, C. Bruegge, and G. Hoover, "An Inversion Algorithm for Retrieval of Atmospheric and Leaf Water Absorption From AVIRIS Radiance With Compensation for Atmospheric Scattering." In *Proceedings of Third AVIRIS Workshop*, JPL Publication Vol. 91, No. 28, pp. 51-61, 1991.

- Green, A.A., and M.D. Craig, "Analysis of Aircraft Spectrometer Data With Logarithmic Residuals." In *Proceedings of First Airborne Imaging Spectrometer Data Analysis Workshop*, April 1985, JPL Publication, pp. 86-35, 1985.
- Horwitz, H., J. Lewis, and A. Pentland, "Estimating Proportions of Objects From Multispectral Scanner Data," ERIM Report No. 109600-13-F, Environmental Research Institute of Michigan, Ann Arbor, p. 108, 1975.
- Horwitz, H., R. Nalepka, P. Hyde, and J. Morgenstern, "Estimating the Proportions of Objects Within a Single Resolution Element of a Multispectral Scanner." In *Proceedings of the Seventh International Symposium on Remote Sensing of Environment*, pp. 1307-1320, 1971.
- Kauth, R.J. and G.S. Thomas, "Tasselled Cap—A Graphic Description of the Spectral-Temporal Development of Agricultural Crops Seen by Landsat." In *Proceedings of Symposium Machine Processing of Remotely Sensed Data*, Purdue University, W. Lafayette, IN, 1976.
- Kruse, F.A., W.M. Calvin, and O. Sez nec, "Automated Extraction of Absorption Features From AVIRIS and GERIS Data." In *Proceedings of First AVIRIS Workshop*, pp. 62-75, 1988.
- Kruse, F.A., K.S. Kierein-Young, and J.W. Boardman, "Mineral Mapping at Cuprite, Nevada With a 63-Channel Imaging Spectrometer," *Photogrammetric Engineering and Remote Sensing*, Vol. 56, No. 1, pp. 83-92, 1990.
- Kruse, F.A., "Use of Airborne Imaging Spectrometer Data to Map Minerals Associated With Hydrothermally Altered Rocks in North Grapevine Mountains in Nevada and California," *Remote Sensing of Environment*, Vol. 24, pp. 31-51, 1988.
- Lambeck, P., R. Kauth, and G. Thomas, "Data Screening and Preprocessing for Landsat MSS Data." In *Proceedings of Twelfth International Symposium on Remote Sensing of Environment*, Manila, Philippines, pp. 999-1008, 1978.
- Lavreau, J. and P. Trefois, "The Use of Spectral Mixing Models for Soil Classification on the Basis of Landsat TM and HRS Field Data." In *Proceedings of IGARSS '88*, p. 1053, 1988.
- Lyzenga, D.R., "Passive Remote Sensing Technique for Mapping Water Depth and Bottom Features," *Applied Optics*, Vol. 17, No. 3, pp. 379-383.
- Malila, W.A. and R.F. Nalepka, "Advanced Processing and Information Extraction Techniques Applied to ERTS-1 MSS Data." In *Proceedings of the Third ERTS-1 Symposium*, NASA SP-351, pp. 1743-1772, 1973.

- Malila, W.A., "Change Vector Analysis: An Approach For Detecting Forest Changes with Landsat." In *Proceedings of the 6th Annual Symposium on Machine Processing of Remotely Sensed Data*, Purdue University Press, West Lafayette, IN, pp. 326-335, 1980.
- Malila, W.A., J.B. Odenweller, and D.P. Rice, "Atmospheric Correction of Landsat Data: An AgRISTARS Legacy and Beyond." In *Proceedings of Workshop on Atmospheric Corrections of Landsat Imagery*, Torrance, CA, 1993.
- Markham, B.L. and J.L. Barker, Guest Editors, *Landsat Image Data Quality Analysis (LIDQA)*, Special Issue of *Final Symposium on Photogrammetric Engineering and Remote Sensing*, Vol. 51, No. 9, pp. 1315-1330, September 1985.
- Mattson, M. and J. Dozier, "Identification of Subresolution High Temperature Sources Using a Thermal IR Sensor," *Photogrammetric Engineering and Remote Sensing*, Vol. 479, pp. 1311-1318, 1985.
- Metzler, M.D. and R.C. Cicone, "Assessment of Technologies for Classification of Mixed Pixels." In *Proceedings of 17th International Symposium on Remote Sensing Environment*, pp. 1015-1021, 1983.
- Mustard, J.F. and C.M. Pieters, "Quantitative Abundance Estimates From Bidirectional Reflectance Measurements," *Journal of Geophysical Research*, Vol. 92, No. B4, pp. E617-E626, 1987.
- Mustard, J.F. and C.M. Pieters, "Abundance and Distribution of Mineral Components Associated With Moses Rock (Kimberlite) Diatreme." In *Proceedings of Second AIS Data Analysis Workshop*, pp. 81-85, 1986.
- Mustard, J.F. and C.M. Pieters, "Abundance and Distribution of Ultramafic Microbreccia in Moses Rock Dike: Quantitative Application of Mapping Spectroscopy," *Journal of Geophysical Research*, Vol. 92, No. B10, pp. 10376-10390, 1987.
- Nalepka, R.F. and P.D. Hyde, "Classifying Unresolved Objects From Simulated Space Data." In *Proceedings of Eighth International Symposium on Remote Sensing of Environment*, pp. 935-949, 1972.
- Odenweller, J.B. and D.P. Rice, "Thematic Mapper Data Screening and External Effects Correction." In *Proceedings of Twenty-first International Symposium on Remote Sensing of Environment*, Ann Arbor, MI, 1987.
- Rice, D.P. and J.B. Odenweller, "External Effects Correction of Landsat TM Data," *ISPRS Journal of Photogrammetry and Remote Sensing*, Vol. 44, pp. 533-568, 1990.

- Richardson, A., C. Wiegand, H. Gausman, J. Cuellar, and A. Gerbermann, "Plant, Soil and Shadow Reflectance Components of Row Crops," *Photogrammetric Engineering and Remote Sensing*, Vol. 41, pp. 1410-1407, 1975.
- Rogne, T.J., D.P. Rice, W.A. Malila, K.W. Gunderson, and J.B. Odenweller, "Spectral Diagnostics for Spatially Varying Haze Corrections of Landsat TM Data." In *Proceedings of Workshop on Atmospheric Correction of Landsat Imagery*, 1993.
- Rubin, T.D., "Automated Spectral Recognition of Alteration Mineralogy in Imaging Data Using a Knowledge-Based Expert System." In *Proceedings of IGARSS '89*, pp. 2065-2068, 1989.
- Singh, A., "Digital Change Detection Techniques Using Remotely-Sensed Data," *International Journal of Remote Sensing*, Vol. 10, pp. 989-1003, 1989.
- Townshend, J.R., C.O. Justice, and V. Kalb, "Characterization and Classification of South American Land Cover Types Using Satellite Data," *International Journal of Remote Sensing*, Vol. 8, pp. 1189-1207, 1987.
- Tucker, C.J., B.N. Holben, and T.E. Goff, "Intensive Forest Clearing in Rondonia, Brazil, As Detected By Satellite Remote Sensing," *Remote Sensing of Environment*, Vol. 15, pp. 255-261, 1984.
- Tucker, C.J., J.R. Townshend, and T.E. Goff, "African Land-Cover Classification Using Satellite Data," *Science*, Vol. 227, pp. 369-375, 1985.
- Virag, L.A. and J.E. Colwell, "An Improved Procedure For Analysis of Change in Thematic Mapper Image-Pairs." In *Proceedings of the 21st International Symposium on Remote Sensing of Environment*, Environmental Research Institute of Michigan, Ann Arbor, pp. 1101-1109, 1987.
- Work, E.A. Jr., D.S. Gilmer, and A.T. Klett, "Utility of ERTS for Monitoring the Breeding Habitat of Migratory Waterfowl." In *Proceedings of the Third ERTS-1 Symposium*, NASA SP-351, pp. 1671-1685, 1973.

7.0 POTENTIAL DEFENSE APPLICATIONS OF MULTISPECTRAL AND HYPERSPECTRAL TECHNIQUES

7.1 CLASSES OF APPLICATIONS

For purposes of this report, potential defense applications of multispectral and hyperspectral data are considered to be in one of two categories, strategic or tactical.

7.1.1 Strategic

The class of strategic applications includes those which are amenable to use of data from satellite multispectral sensors, in that they typically are not time-sensitive and can use synoptic broad-area coverage with modest spatial resolution. For instance, they can use the 10- to 30-meter resolution of Landsat and SPOT data with their two- to four-week nadir revisit times.

7.1.2 Tactical

The class of tactical applications may require better timeliness and finer spatial resolution, while being able to get by with more limited spatial coverage. Such requirements might be better met with data from airborne sensors.

7.2 DEFENSE APPLICATIONS AND ASSOCIATED SENSOR REQUIREMENTS

Multispectral and hyperspectral data have potential applicability for many different defense related problems and tasks. For any given task, the critical factors that determine how useful the spectral data can be include the phenomena that can be observed, the sensor parameters that determine how well the scene characteristics can be sampled and defined and, finally, the amount of relevant information that can be extracted from the remotely sensed data.

To help establish requirements for new systems or define the applicability of existing systems, studies have been or can be made of the relevant factors and information elements and requirements. For instance, the DLPO recently conducted a definition study and survey for an Advanced Land Remote Sensing System (ALRSS), as a possible follow-on to the Landsat series of multispectral satellites (see bibliographical reference). They identified defense applications and organized them into the eleven major categories shown in Table 7-1. Since the information needs of any military crisis or other crisis with military implications, will vary and depend on the particular circumstances, it is difficult to make a single prioritization of a list of applications such as presented here.

Each of the eleven categories was further detailed into application tasks and subtasks. To better indicate the extent of utility, we have also included the task-level entries in Table 7-1.

Table 7-1. Illustrative Defense Applications of Multispectral Sensors (To the Task Level)

1. Mapping, Charting, and Geodesy
 - Image mapping
 - Terrain characterization analysis
 - Feature extraction and analysis
 - Elevation data extraction
 - Map creation
 - Change detection
2. Broad Area Search
 - Automated change detection
 - Cueing support
3. Disaster Support
 - Natural disaster assessment
 - Man-made disaster assessment
4. Strategic Industry and Resource
 - Monitoring
 - Natural resource exploration/mining
 - POL facilities
 - Industrial material process flow
 - Seaport usage
 - Power supply
 - Underground facilities
 - CW/BW production
5. Contingency Planning Support
 - Intelligence preparation of the battlefield
 - Landing zone/drop analysis
 - Amphibious operations planning
 - Airfield analysis
 - Noncombatant evacuation operations
 - Environmental hazards
6. Mission Planning and Rehearsal
 - Large area orientation
 - Operations planning
 - Mission rehearsal fly-through
 - Mission assessment
7. Current Operations Support
 - Theater surveillance
 - Order of battle analyses (naval, ground, air/air-defense, missile, CW/BW)
8. Targeting Support
 - Target detection
 - Target identification and tracking
 - Target vulnerability characterization
 - Advanced target materials
 - Target penetration analysis
 - Bomb damage assessment
 - Cruise missile targeting
9. Counternarcotics
 - Support counternarcotics operations
 - Narcotics transshipment
 - Narcotics processing
 - Growing activity
10. Treaty Monitoring
 - START
 - CW/BW
 - Conventional Forces Europe (CFE)
 - Environmental treaty monitoring
 - Nuclear weapons proliferation
11. Counterterrorism
 - Support counterterrorism operations

For each subtask under these tasks, the pertinent observables were listed, along with estimates of which spectral bands would be most useful and what ranges of other sensor parameters would be required, such as spatial resolution, revisit interval, and stereo coverage, to provide the desired information. Also, the value of the multispectral imagery (MSI) contribution was estimated as being major, significant, added value, or no contribution.

One finds that every spectral region, from panchromatic and spectral visible, through near infrared and short-wave infrared, to the mid-wave and long-wave thermal infrared regions has pertinence for some defense application. Usually, the applications will benefit from use of more than one band or spectral region, as in multispectral, hyperspectral, or ultraspectral sensing, although a few may be specialized to a single spectral region or constrained from using others.

7.3 IMPLEMENTATION CONSIDERATIONS

In order to use multispectral and hyperspectral data for defense purposes, one must have data collection sources, data dissemination resources, and data exploitation capabilities. Collection capabilities have already been discussed in Section 4. Some of the other issues are discussed below.

7.3.1 Existing Software/Hardware Systems and Facilities

Both capable hardware and efficient software implementations of effective algorithms are needed in order to exploit multispectral and hyperspectral data in a timely and effective manner. Research and development activities generally precede operational capabilities. Government-sponsored developments by contractors and government personnel have produced operational data exploitation capabilities at a few defense establishments. Expansion of the user base and exploitation capabilities are proceeding, as the technology matures. In recent years, commercial off-the-shelf software and hardware have gained capability and have more potential for meeting the needs of military users.

7.3.1.1 MIMES

Units of United States Air Force (USAF) Space Command (SPACECOM) [formerly under STRATCOM and Strategic Air Command (SAC)] have had access to a multispectral data processing and production system called MIMES since 1988. The system uses a VAX mainframe computer, with peripherals such as an array processor and specialized hardware processors for rapid geometric correction and maximum-likelihood categorization processing of the Landsat data.

The software is configured in such a way that a number of multispectrally based products can be produced routinely by military personnel. Products using standard TM data inputs include TM analysis images (to provide scene overviews) and change images and associated single-date reference images (to provide change products for interpretation and cueing and made using the PISCES procedure described in Section 6.4.2).

Provisions also exist for geocoding the image data (i.e., rotating and resampling to a controlled north-south-oriented coordinate grid in a projection of the user's choosing) and then producing a number of products with accurate geolocation. Among these are TM image

graphics (with coordinate markings), terrain-categorized image products, multiscene image mosaics (hundreds of miles square), perspective views (draping TM data over digital terrain elevation data), and other specialized or custom image products.

ERIM developed and installed the system and continues to maintain the software and special-purpose hardware and to periodically train the operational personnel. For additional information, contact Capt. Ronald Senger, SPACECOM, (402) 294-7784.

7.3.1.2 DAIRS/SPECTRA

The Defense Intelligence Agency (DIA) has capabilities to produce customized image products from civilian multispectral satellite data, using a collection of hardware and software called DAIRS (DIA Advanced Imagery Reproduction System). Standardized Production Environment for the Classification of Terrain and Resource Analysis (SPECTRA) is another capability for UNIX workstations, intended to provide capabilities similar to MIMES, and has been under development for some time. For information about DIA systems, contact Mr. Wayne Hallada of DIA, (202) 373-2086.

7.3.1.3 MATRIX/MAGISTIC

MATRIX and MAGISTIC are other workstation-based data exploitation systems under development, with capabilities for multispectral data exploitation. MATRIX was developed initially to process other data types, but has been adding capabilities for multispectral image processing and information extraction. MAGISTIC (MATRIX Geographic Information System and Turnkey Imagery Capability) is a more inclusive concept which is to include MATRIX. For information, contact Capt. Joseph Brickey of the Defense Landsat Program Office, (703) 267-4496.

7.3.1.4 HYDICE Exploitation Toolkit

In anticipation of the operational availability of HYDICE hyperspectral data, the HYDICE Program Office has developed and made available a software toolkit which can provide an initial starting point for interested users. It includes basic capabilities for handling and manipulating hyperspectral data. It is based around the Spectral Image Processing System (SIPS) from the University of Colorado and requires use of a commercial software package called IDL, from Research Systems, Inc., for its underlying functionality. For information, contact Comdr. Mark Andersen, NRL, (202) 279-2349.

7.3.1.5 Aircraft Mission Planning

The Air Force presently has deployed the Mission Support System-II (MSS-II) and will be deploying the advanced Air Force Mission Support System (AFMSS). These provides users with image-based and other tools needed for planning missions, including route analysis, threat analysis, preview, image backdrop, geolocation, and perspective viewing. They presently use only panchromatic image data, such as provided by SPOT, but could possibly have enhanced capability through future use of multispectral data for natural color and/or other types of image displays. For information, contact Maj. Robert Ekstrom, HQACC, Langley AFB, VA, (804) 764-3311.

Another example system is the Tactical Aircraft Mission Planning System (TAMPS) which utilizes Landsat, SPOT, and Arc Digital Raster (ADRI) imagery for route planning. The system is used to view the image data and to manipulate them over other data sets for three-dimensional perspective viewing. Hosted on Navy standard hardware, the current version of software is TAMPS V6.0. For additional information, contact Lt. Comdr. Zdenka Willis at (703) 604-3379, Ext. 8818.

7.3.1.6 Commercial Software Packages

A number of commercial firms have developed software packages that can be used to exploit multispectral and hyperspectral image data. These packages tend to have increased capability with each release.

Typically, no package has all the functionality or ease of use that is needed or desired by a particular user. Many are best suited to analysis and operational or demonstration processing on smaller-sized data sets, having less facility for handling larger full scenes and multiscene mosaics.

A partial list of vendors is presented in Table 7-2. Apologies to any vendors who are not included, but should be.

7.3.2 Tactical-Unit Availability

7.3.2.1 Issues Concerning Multispectral Data Use in Tactical Scenarios

Timeliness is a key issue in the use of multispectral or hyperspectral image data in tactical scenarios. For intelligence preparation of the battlefield (IPB) and other planning operations, use can be made of satellite multispectral data collected months or even years before, in some scenarios. However, for others, there likely will be requirements for up-to-date information in rapidly changing conditions. This requires improvements in the "pipelines" for image product preparation, production, and dissemination.

7.3.2.2 XVIII Airborne Corps

A few tactical groups have explored the use of multispectral data in operational planning and training activities. One example is the XVIII Airborne Corps, Ft. Bragg, NC, which has an imagery dissemination network to provide MSI support to selected elements of its command, along with commercial image processing software.

7.3.2.3 Eagle Vision

Eagle Vision is a 14-month demonstration project that recently began in Europe (*Aviation Week & Space Technology*, May 16, 1994). Project officials indicated that Eagle Vision will provide forces in the field with a capability to directly receive 10-meter SPOT panchromatic data, without encountering multiweek delays such as occurred during Persian Gulf War operations.

Table 7-2. Representative Commercial Image Processing Software Products

Product Name	Developer/Vendor	Platforms		Comments	Telephone No. Fax No.
		UNIX Workstation	IBM-PC and Compatibles		
IMAGINE	ERDAS, Inc. 2801 Buford Hwy., Ste. 300 Atlanta, GA 30029	X	X	Multispectral Image Processing	404-248-9000 404-248-9400
ARC/INFO	ESRI 380 New York St. Redlands, CA 29373	X	X	Geographic Information System	909-793-2853 909-793-4801 or 793-5953
SPECTRA	Intergraph Corp. One Madison Industrial Park Huntsville, AL 35894-0001	X (Special hardware may be required)		Multispectral Image Processing	205-730-2000 205-730-6750
EASI/PACE	PCI Remote Sensing Corp. 1925 N. Lynn St., Ste. 803 Arlington, VA 22209	X	X	Multispectral Image Processing	703-243-3700 703-243-3705
ENVI (Includes IDL)	Research Systems, Inc. 2995 Wilderness Place Boulder, CO 80301	X	X	Multispectral and Hyperspectral Image Processing	303-786-9900 303-786-9909
GenIsis	WTJ Software Services 809 Lawrence Road San Mateo, CA 94401		X	Multispectral and Hyperspectral Image Processing	415-344-6771 415-344-2491

The Eagle Vision system has two major components, a French-built (Matra Cap Systems) portable ground station to receive the downlinked data and a companion U.S.-built (ERIM) data processing, data integration, and data exploitation system.

The full system involves individual truck-mounted shelters for the data acquisition and data integration segments and a small trailer-mounted antenna. All can be transported in a single Lockheed C-130 aircraft.

The Eagle Vision system reportedly will permit images to be received and distributed within the theater within hours and updated daily with multiple satellite passes in range of the station. Products include orthorectified image maps in ADRI format.

7.4 BIBLIOGRAPHY

Covault, C., "Eagle Vision Trails Readied," *Aviation Week and Space Technology*, p. 56, May 16, 1994.

Defense Landsat Program Office, "Advanced Land Remote Sensing System (ALRSS): Concept Definition Studies, Applications and Performance Goals, Annex D: Remote Sensing System Applications Document, Version 3," 1 September 1993.

Neer, M.M., "Multispectral Imagery in Support of Low Intensity Conflict," U.S. Army War College, Carlisle Barracks, PA, 1990.

8.0 EXAMPLE DATA PRODUCTS FOR DEFENSE APPLICATIONS OF SPECTRAL PHENOMENA

Multispectral data have been available from both airborne and commercial satellite sensors for use in defense applications and applications research and development. The derived data products presented in this section were selected to illustrate pertinence to a variety of potential defense applications. Beginning with finer-spatial-resolution airborne data products, the section ends with Landsat and SPOT satellite data products.

Section 8.1 shows uses of multispectral reflective data collected in spectral bands between 0.45 and 2.34 μm . Examples of terrain categorization and target detection are included. Section 8.2 shows examples of the potential for terrain categorization and target detection with multiband thermal data collected in six spectral bands between 8 and 12 μm .

Section 8.3 gives an example of emissivity mapping with multispectral data in the LWIR with classification of terrain on the basis of soil content. Section 8.4 presents results of low noise hyperspectral measurements in the MWIR and LWIR with potential application for clutter suppression and detection of low contrast, partially obscured, and camouflaged targets obtained by ERIM under the ARPA/Air Force (AF)/Navy/Army Joint Multispectral Program. Section 8.5 shows several additional examples of multispectral and hyperspectral sensing in the MWIR developed as part of the Airborne Instrument Program. Section 8.6 shows results using the MUSIC sensor in the LWIR to detect ethyl ether vapor on the basis of vapor cloud absorption between 8 and 9 μm .

Finally, Section 8.7 presents applications examples making use of commercially available, multispectral satellite data. The examples include image mapping, various types of feature extraction and mapping, and visualization and image fusion.

8.1 TARGET DETECTION IN THE VISIBLE AND REFLECTIVE IR

There is a wide diversity amongst the spectral reflectance characteristics of target and background materials in the visible and reflective infrared regions. Figure 8-1 shows a categorization image developed with M-7 data collected over Griffiss Air Force Base (AFB). This example illustrates the potential for using multispectral data in the visible and short wavelength infrared for materials discrimination and/or identification.

Figure 8-2 illustrates vehicle detection through spectral contrast enhancement and machine processing of multispectral data. Figure 8-2a shows a natural color image from TMS data over Ft. Chaffee (with blue 0.46-0.52, green 0.53-0.60, and red 0.63-0.69 μm). Several targets in this image are very hard to detect against their backgrounds. (Most target locations are identified by computer-generated circles in Figure 8-2d.) Figure 8-2b shows an enhanced image generated by using three non-visible bands to produce a false-color (SWIR-composite) image (blue 0.77-0.90, green 1.53-1.73, and red 2.06-2.33 μm). The color contrast between targets and backgrounds in this false-color image is increased because of the pronounced spectral reflectance differences between the targets and backgrounds in the shortwave infrared (IR) spectral region. Figure 8-2c shows a fully processed terrain classification and target detection image based on all six TM spectral bands.

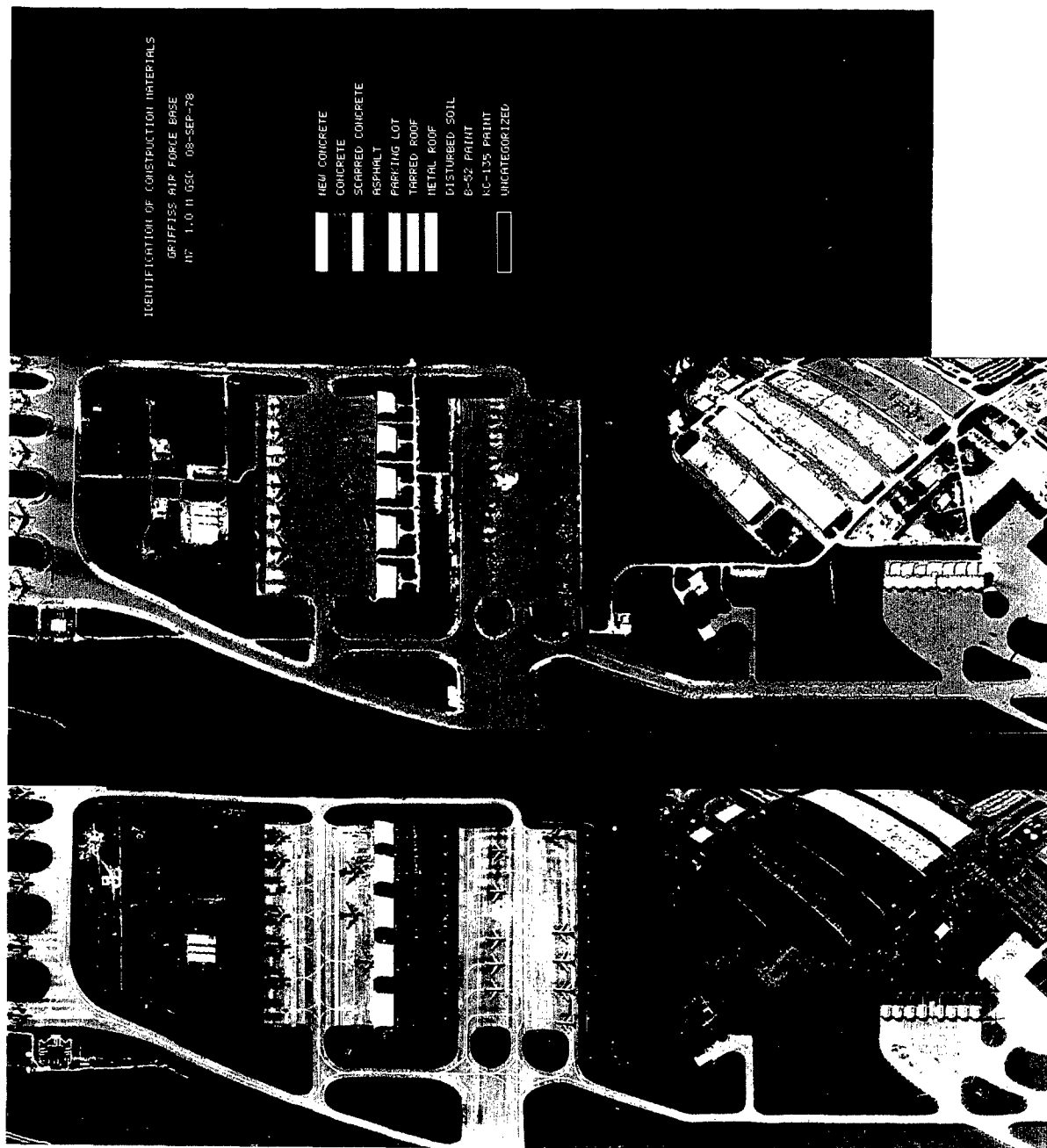


Figure 8-1. Multispectral Discrimination of Construction Materials. (1-m GSD M-7 data at Giffiss AFB, NY, 8 Sep 78.)
 This image was provided by ERIM.



Blue .46-.52 Green .53-.60 Red .63-.69 um

a) Natural-color image



Blue .77-.90 Green 1.53-1.73 Red 2.06-2.33 um

b) Enhanced contrast on SWIR composite image

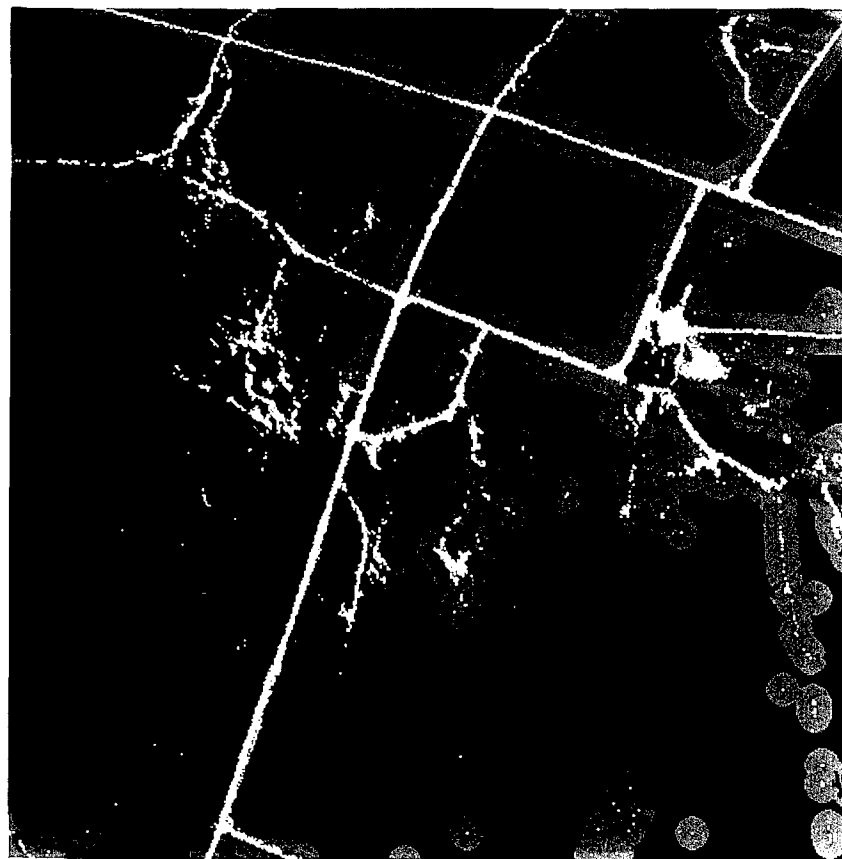
Figure 8-2. Multispectral Detection of Vehicular Targets. 2.5 m GSD TMS data at Ft. Chaffee, AK, 28 Apr 86. This image was provided by ERIM.



Target	Road	
Open	Water	Shadow
Uncategorized		

c) Target detection and terrain categorization map
(computer-generated circles of detections)

Figure 8-2. Multispectral Detection of Vehicular Targets. 2.5 m GSD TMS data at Ft. Chaffee, AK, 28 Apr 86. This image was provided by ERIM. (Continued)



d) Spatial processing results for detecting targets
near roads

Figure 8-2d shows results of spatial processing of the results in Figure 8-2c to detect targets near roads.

The above examples show the potential for using the reflective IR to help in classifying terrain and building materials and in detecting targets having low visible contrast with their backgrounds.

8.2 MATERIALS CLASSIFICATION IN THE LWIR

The spectral emissivities in the thermal IR are generally high, and the spectral variations in spectral emissivity are smaller than the corresponding variations in reflectance in the visible and reflective IR. Nonetheless, significant spectral emissivity differences exist in the thermal IR that provide the potential for target contrast enhancement, terrain categorization, and materials classification.

Figure 8-3 shows a false color image using three of the six bands of LWIR spectral data obtained with the TIMS sensor at Griffiss AFB. The average level of the return in each of the three bands has been adjusted so that much of the background is gray with gray levels representing variations in temperature. Some parts of the scene, particularly the road, runway, and asphalt taxiways, are pink. These are backgrounds having a spectral variation in the LWIR. Specifically, the coloring in this imagery is mainly due to the SiO_2 reststrahlen feature in these materials.

Figure 8-4 shows alternative views of the same data. Images of the ratio of two different band pairs are shown on the left. The band ratio 3/5 is the ratio of the 9-9.4 and 10.3-11.7 μm bands, and the band ratio 4/6 is the ratio of the 9.6-10.2 and 10.3-11.1 μm bands. Color-coded level-sliced ratios are shown on the right. Surfaces with a reststrahlen feature are shown in color, with blue the weakest feature and red the strongest.

These examples show the potential for spectral data in the thermal region to provide information for terrain categorization, materials classification, and potentially for target detection and classification.

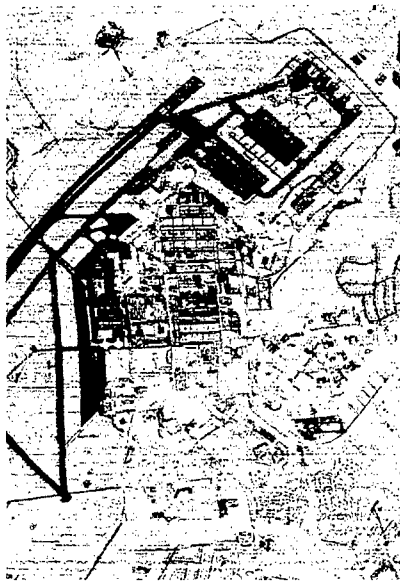
8.3 EMISSIVITY MAPPING IN THE LWIR

An example of emissivity mapping is shown in Figures 8-5 and 8-6. Figures 8-5a and 8-5b show imagery of an Adelaide scene collected with the TIMS 6-band LWIR thermal infrared sensor in two of the six spectral bands, namely Bands 3 and 6. The images in all six spectral bands appear very much alike. Figures 8-5c and 8-5d show the principal component images corresponding to the largest and next largest eigenvalue. The image with the largest eigenvalue, Figure 8-5c, contains almost all of the variability. Almost all of this variability is due to temperature, and the image is very similar to any of the original images. Figure 8-5d is the image corresponding to the next largest eigenvalue and contains most of the variation caused by variations in spectral emissivity.

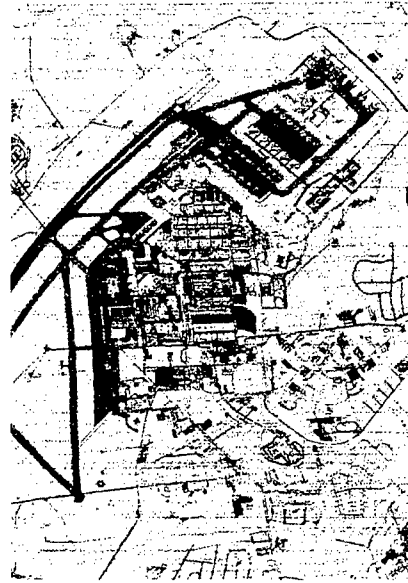
Figures 8-6a and 8-6b show the imagery in Bands 3 and 6 after the temperature variations, contained in the first principal component image, have been projected out. It should be noted that the emissivity of the roads in the imagery are low in Band 3 and high in Band 6. Figure 8-6c shows the spectral emissivity variations from road and vegetation areas in the imagery from all six TIMS bands after having projected out the temperature. The reststrahlen band at approximately 9.2 μm due to SiO_2 is readily apparent. Finally, Figure 8-6d shows the sensor NEAT requirement for detecting emissivity changes in the thermal infrared. It is seen that the TIMS sensor, with an NEAT of 0.2 K is limited to detecting emissivity changes of 0.5 to 1 percent with a SNR of one. Detection of emissivity changes of 0.5 to 1 percent will generally require sensors with NEATs of better than 50 mK.



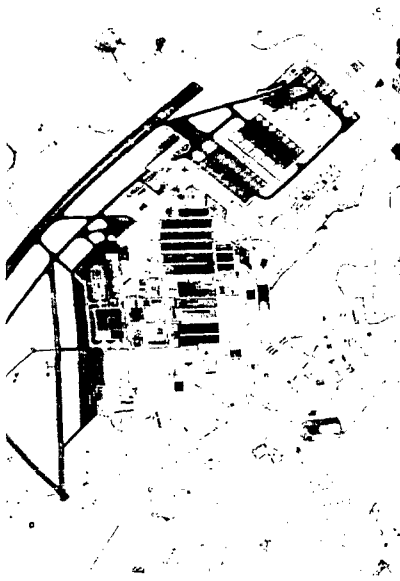
Figure 8-3. Illustration of LWIR Spectral Diversity. Three bands of 5 m GSD TIMS data at Griffiss AFB, NY, 2 Sep 83. This image was provided by ERIM.



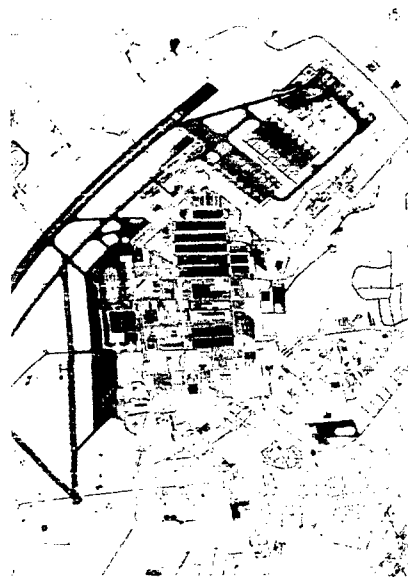
Color Sliced
Emissivity Ratio



Color Sliced
Emissivity Ratio



Bands 3/5
Emissivity Ratio

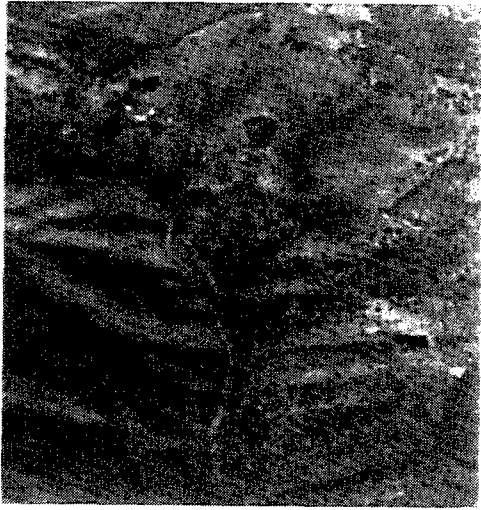


Bands 2/4
Emissivity Ratio

Figure 8-4. Use of LWIR Spectral Emissivity Differences to Discriminate Among Construction Materials. 5 m GSD TIMS data at Griffiss AFB, NY, 2 Sep 83. This image was provided by ERIM.



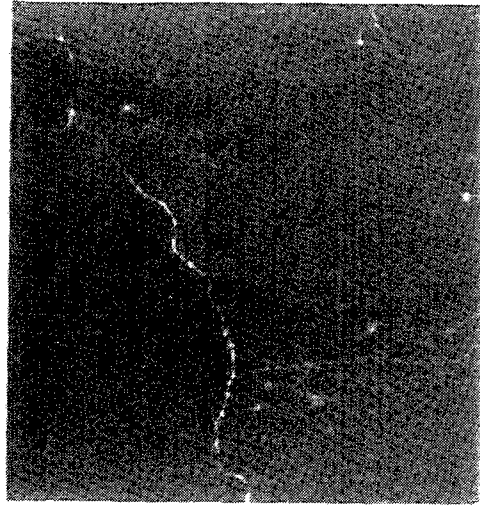
a) Band 3



b) Band 6



c) Largest principal component image (temperature)

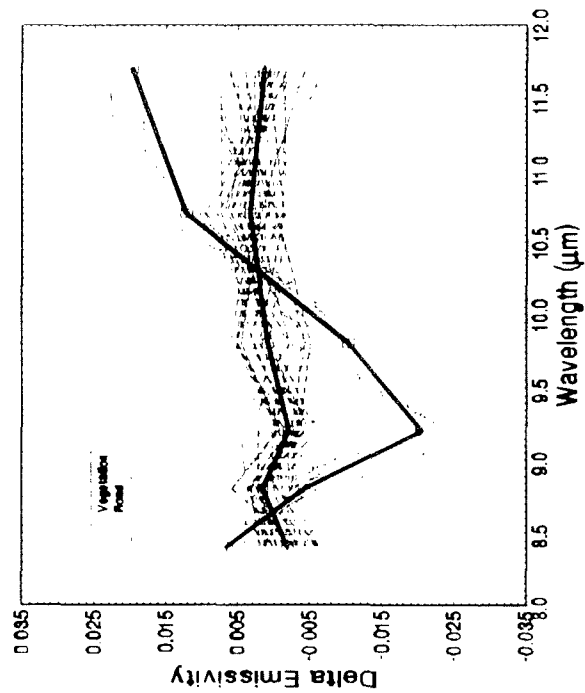


d) Next largest principal component image (emissivity)

Figure 8-5. TIMS Imagery of Adelaide Scene.



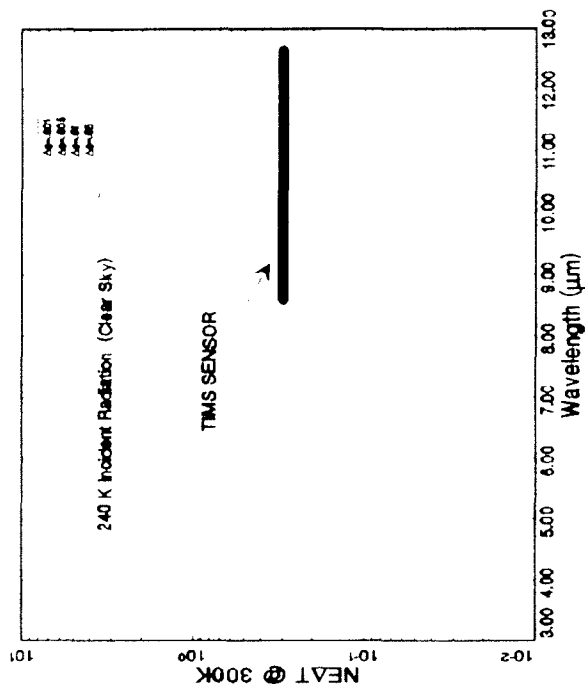
a) Emissivity map for band 3



c) Emissivity of vegetation and roads in all 6 bands



b) Emissivity map for band 6



d) NEAT required to detect emissivity differences of .05, .01, .005 and .001 in the thermal infrared

Figure 8-6. TMS Imagery of Adelaide Scene

This shows the capability of emissivity mapping in the LWIR to detect roads. Emissivity mapping also has the potential for terrain categorization, trafficability and route planning.

8.4 SPECTRALLY CORRELATED BACKGROUND CLUTTER SUPPRESSION IN THE MWIR AND LWIR

Temperature variations are the primary source of clutter in the thermal IR. Spatial filtering frequently cannot provide enough gain in the SCR for adequately high probability of detection and low probability of false alarm. However, recent measurements with high sensitivity hyperspectral radiometers have shown that the spectral correlation within the window regions of the LWIR and MWIR, as well as between the LWIR and MWIR, can be very high. This high correlation is the key to detecting low contrast, partially obscured, and camouflaged targets in the thermal IR using multispectral and hyperspectral techniques.

Figures 8-7a and 8-7b show a photograph and a broadband LWIR thermal image of a truck target partially obscured by a vegetative canopy. Figure 8-7c shows the spectral apparent temperature contrast between the target and the background. Figure 8-7d shows a scatter plot of pixel radiances from the vegetative background and from the partially obscured truck in two MWIR spectral bands. These data were obtained by ERIM as a part of the ARPA/AF/Navy/Army Joint Multispectral Program; Dr. Larry Stotts, ARPA Program Manager; and Capt. Robert Esquire, Wright Laboratory (WL) Program Manager. The background correlation is 0.99917 in these data. The SCR is much less than one in either the broadband image or narrow spectral band alone. However, due to the high background spectral correlation and the mean spectral (emissivity) difference between the target and the background, the target SCR can be improved by nearly 18.31 dB ($SCR = 8.23$) using two spectral bands together.

Multispectral and hyperspectral imaging in the MWIR and LWIR has significant potential for detecting low contrast and partially resolved targets with high probability of detection and low probability of false alarm. It is anticipated that these sensors will have to have NEATs of 50 mK or less to take full advantage of the high spectral correlations observed in the thermal IR.

8.5 HYPERSPECTRAL IMAGING IN THE MWIR

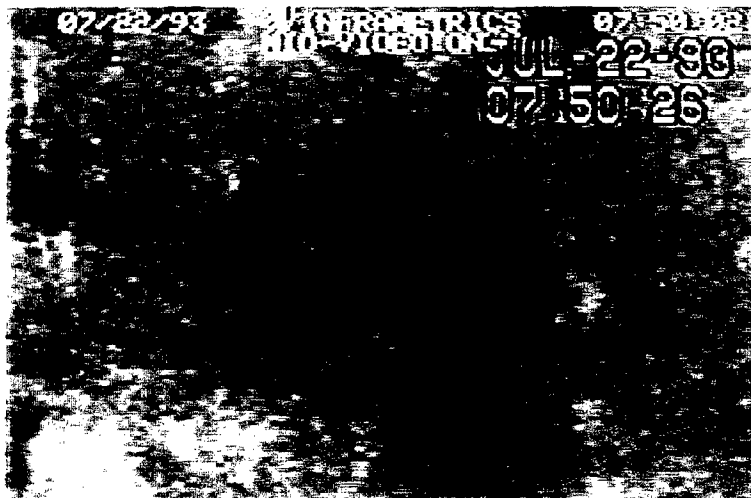
The material in this section was provided by Capt. Larry Adair, the Airborne Instrument Program (AIP) Program Manager. Images were taken from the AIP Sensor Capabilities report.

Multispectral and hyperspectral sensors in the MWIR have a number of potential applications. Several examples are presented in this section of the report developed with data collected using the AIP sensor. This sensor is similar to the HICAMP-II and MUSIC sensors. It operates in the MWIR in either a staring mode or pushbroom mode. The sensor has a 45×90 Si:In focal plane array. The IFOV is 1.165 mrad. It is typically flown on the WB-57F aircraft operated by the NASA Johnson Space Center. With the aircraft at 60,000 feet, the ground resolution is approximately 20 m.

The instrument can be operated in a staring mode in four spectral bands using a four-position filter wheel, or the instrument can be operated with a MgO/Ge prism as a pushbroom spectrometer. The four spectral filters are centered at 2.232, 2.844, 3.783, and 4.479 μm . The imaging spectrometer covers the spectral range 2.0-6.3 μm with 75 bands with a spectral range varying from 0.02 to 0.07 μm . Table 8-1 summarizes the instrument characteristics.

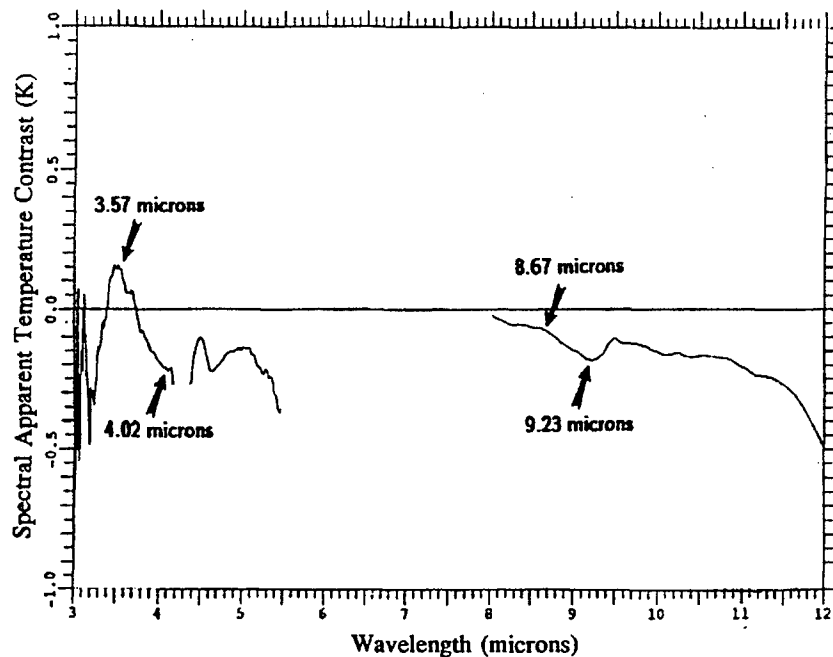


a) Visible image of truck in trees

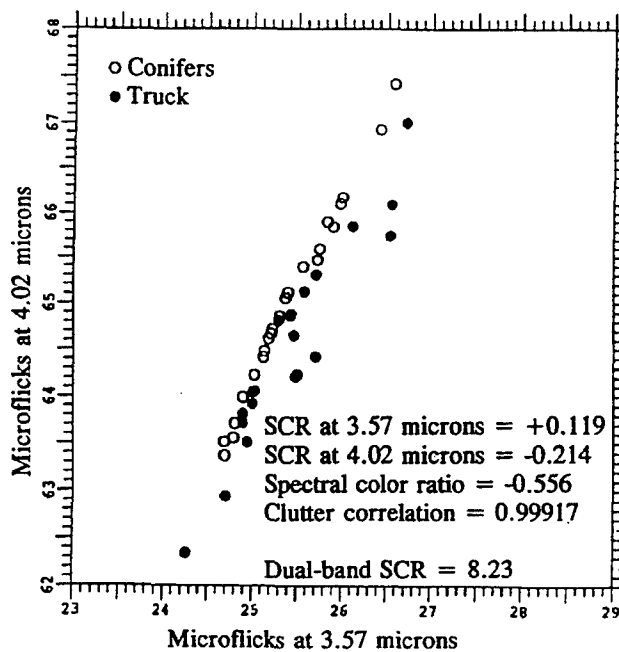


b) MW FLIR image of truck

Figure 8-7. Low Contrast Target Detection With Spectral Correlation Sensor



c) Spectral contrast of truck with trees



d) Dual band scatter plot showing good dual band detectability of truck

Figure 8-7. Low Contrast Target Detection With Spectral Correlation Sensor (Continued)

Table 8-1. Airborne Instrument Program (AIP) Sensor Characteristics

Parameter	Value
Aircraft	WB-57F, NASA 928
Maximum altitude	~60,000 feet (load dependent)
True air speed	125 - 390 kt (altitude dependent)
Maximum mission duration/range	6 hours/2300 nm
Instrument	
Modes of operation	Staring Radiometer Imaging Spectrometer
Focal Plane	Mosaic 45 x 90 pixels, CCD (Si:In)
Frame Rates (nominal)	10, 20, 40, 80 Hz
Integration Times, @	
81.38 Hz	12.29 msec
40.69 Hz	24.58 msec
20.35 Hz	49.14 msec
10.17 Hz	98.33 msec
A/D	12 Bit
Radiometer	
Single Detector Field of View	1.120 mrad square
Pixel Pitch	1.165 mrad
Sensor Field of View	52.43 mrad square
Spectral Filters (Ctr)	LBE - UBE (1/2 Power)
2.232 μm	2.205-2.259 μm
2.844 μm	2.716-2.972 μm
3.783 μm	3.723-3.843 μm
4.479 μm	4.406-4.553 μm
Imaging Spectrometer	
Spectral Coverage	2.0 to 6.3 μm
Spectral Resolution	0.02-0.07 μm (20 - 70 nm)
Number of Bands	75
Slit IFOV	52.43 mrad by 300 μrad
Spatial Resolution (pushbroom)	1.165 mrad cross track, down-track determined by frame rate and forward velocity/scan rate.

In the shorter wavelength bands, from 2.0 to about 3.5 μm , the dominant signal in the daytime is reflected sunlight, allowing identification of narrow-band spectral (reflectance/absorption) features. This capability may be used in defense, for example in the characterization of false alarm sources by spectral/temporal characteristics (solar reflections, lightning, explosions); in law enforcement, for example in the detection of illicit drug processing by detection of narrowband absorption features of solvents; and in a variety of economic areas such as geology and mining, agriculture and forestry, hydrology, and environmental monitoring and cleanup.

In the longer wavelengths (from about 3 to 6 μm) thermal emission dominates. This has utility in the determination of subtle temperature differences around ambient. Applications include industrial capacity, geology, and environmental studies.

In many cases, band differencing between the shorter (reflective) and longer (thermal) bands highlights cultural features such as road networks and enhancement of narrowband absorption or reflectance features.

The following sections illustrate the applications of multispectral and hyperspectral sensing in the MWIR along with one example of results obtained with the MUSIC sensor in the LWIR.

Industrial Activity

Figure 8-8 shows an image over the AT&SF Railroad near Kingman, Arizona. This image is the result of using the 3.8 and 4.5 μm bands. Considerable cultural detail is shown along with the presence of several diesel locomotives (upper right) evident by the exhaust stack radiance.

False Alarm Sources

Figure 8-9 shows an off-nadir image of solar reflections from high-altitude lakes at 2.2 μm . The upper image is scaled to show reflections from partially melted lake surfaces. The lower image is scaled to bring out lake boundaries.

Material Spectral Features

Figure 8-10 shows an "image cube" of 45 of the 75 available spectral images obtained using the AIP sensor in the imaging spectrometer mode. The front image is at 2.3 μm ; a total of 45 images is shown.

Figure 8-11 shows two images of Oahu, Hawaii. The upper image is a 2.2 μm image in which clouds appear bright due to solar reflections. They are dark in the lower image at 4.5 μm due to their colder temperature. City features (buildings, streets) in the right portion of the image are brighter.

Figure 8-12 shows the result of wide band differencing to enhance contrasts based on spectrally dependent features. In the upper 2.3 μm band image, streets and roads to the east of Diamond Head and within the crater disappear into the general clutter. In the middle 5 μm image they can be distinguished, but the contrast is greatly enhanced when the longwave image is subtracted from the shortwave image shown in the lower figure.

Figure 8-13 shows another example of wide band image differencing. In the upper image, two aircraft parked on the (dark colored) ramp at Hickam AFB are readily discerned at 5 μm . In the middle 2.3 μm image, the first two disappear but three others are evident. When the two images are differenced, all five become apparent (circled).

8.6 HYPERSPECTRAL DETECTION OF ETHYL ETHER VAPOR IN THE LWIR

Figure 8-14 shows data obtained with the MUSIC sensor (very similar to the AIP sensor except operating in the LWIR). The two upper figures are images at 8.85 and 8.94 μm . A cloud of ethyl ether vapor has been released but is not apparent in either image alone. The lower images are difference images in which the ether cloud is readily apparent (especially in the lower filtered image).

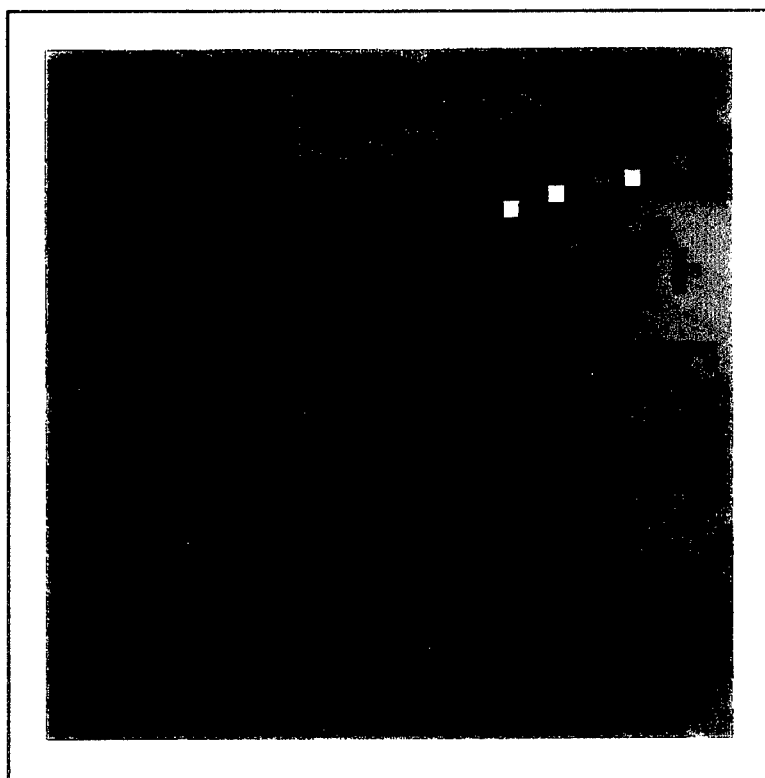


Figure 8-8. AT&SF Railroad at Kingman AZ. Diesel locomotives (upper right) evident by exhaust stack radiance utilizing the $3.8\ \mu\text{m}$ and $4.5\ \mu\text{m}$ bands.

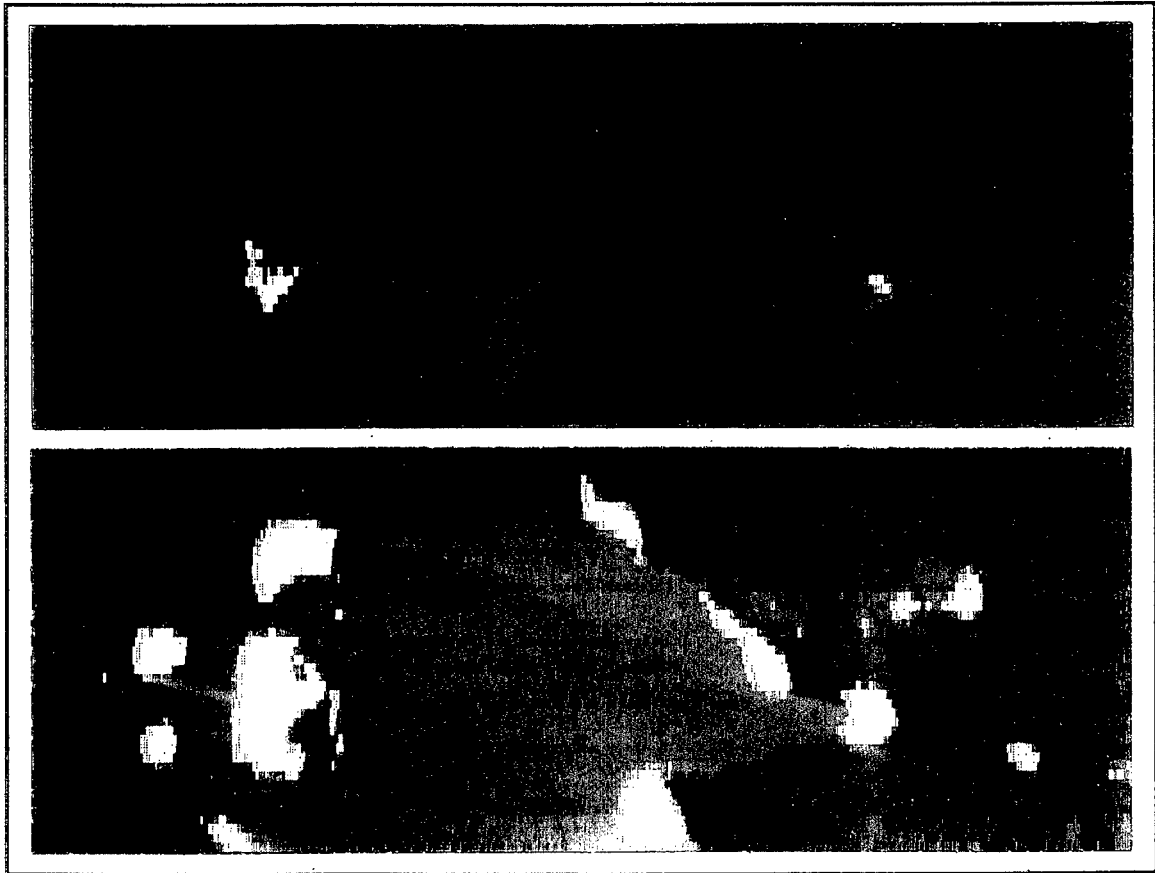


Figure 8-9. Off-Nadir Images of Solar Reflections From High-Altitude ($\sim 12,000$ ft) Lakes at $2.2\ \mu\text{m}$. Upper image scaled to show reflections off partially-melted pools on frozen lake surface. Lower image scaled to bring out lake boundary vs. land.

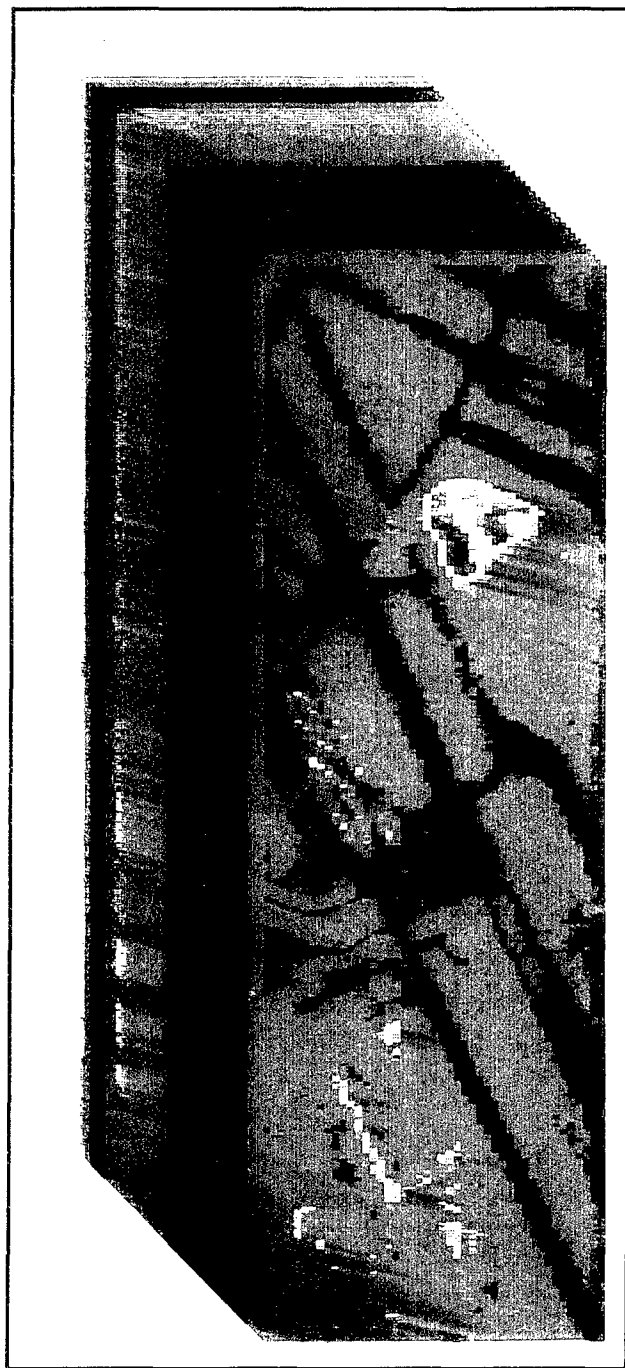


Figure 8-10. Graphic Depiction of a Multispectral Image. The "front" image is formed at the shortest wavelength processed (in this case $2.3 \mu\text{m}$). Stacked behind it are up to 74 additional simultaneous images - each formed at progressively longer wavelengths (not all bands may be of interest, in the example, 45 total bands are shown).

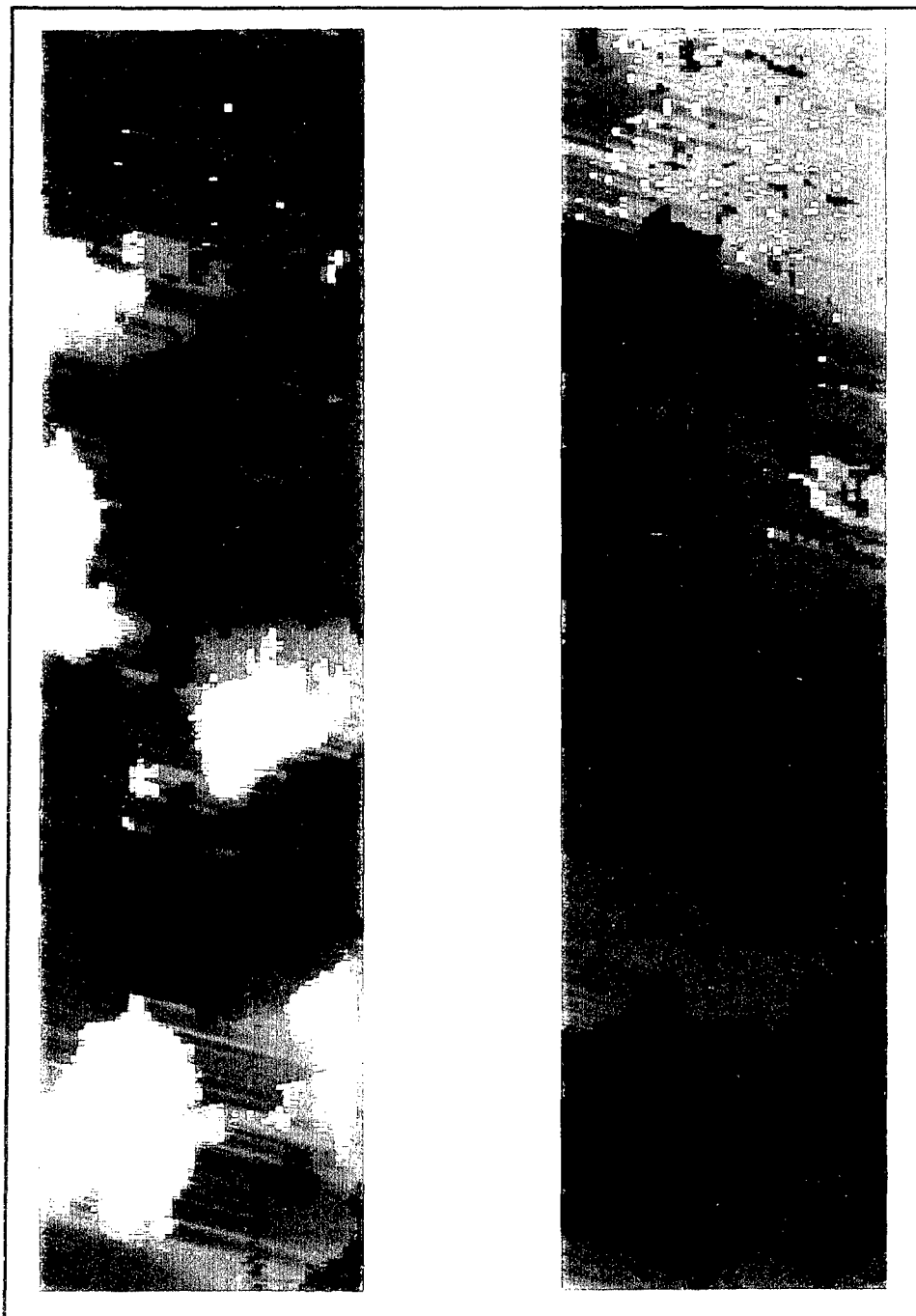


Figure 8-11. Simultaneous Multispectral Images of Oahu. Upper image at 2.2 μm , lower at 4.5 μm . Clouds appear bright at 2.2 due to reflected sunlight, and are dark at 4.5 due to relative coolness. city features (buildings, streets, right side) are brighter at the longer wavelength.

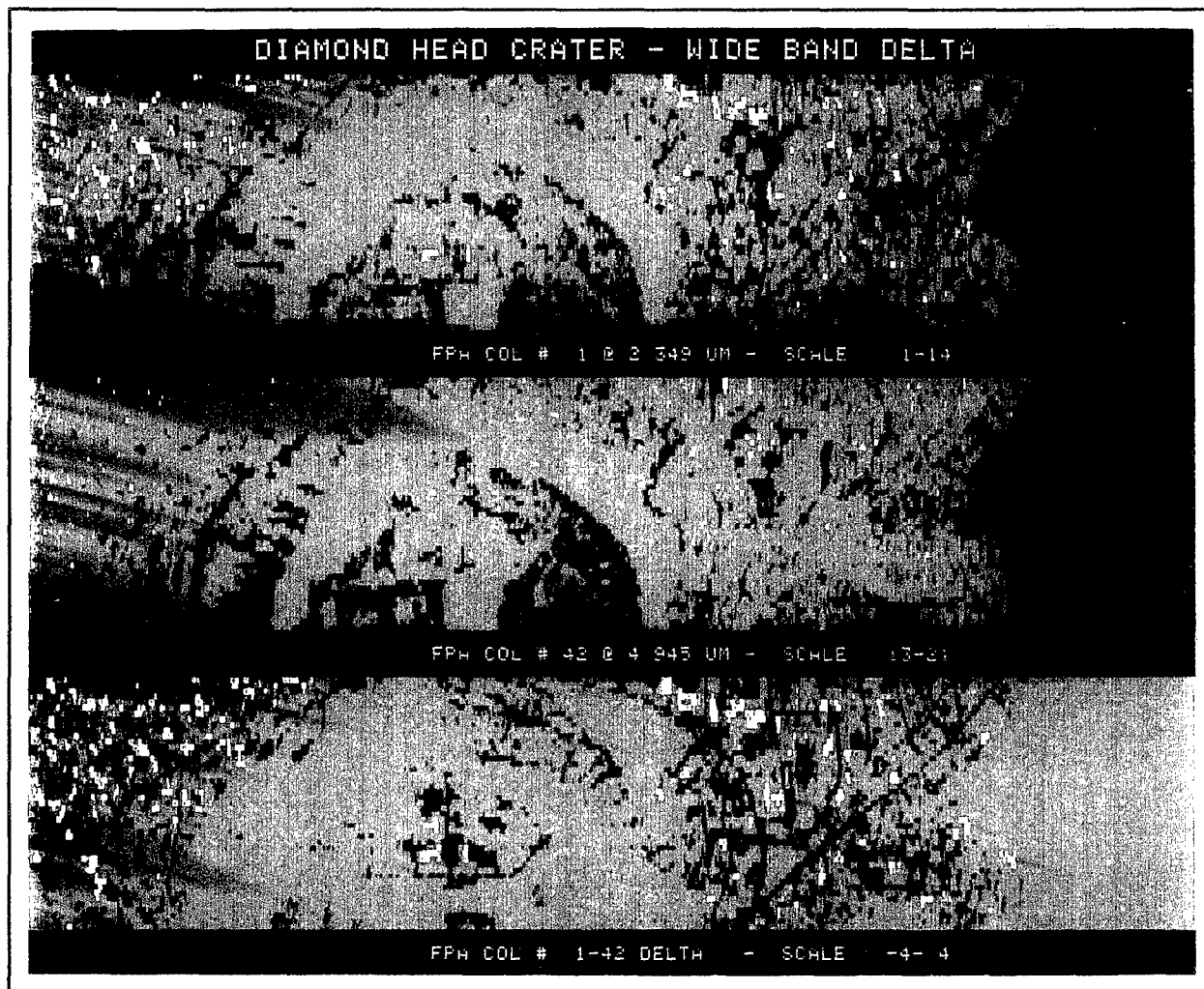


Figure 8-12. An Example of Wide-Band Differencing. In the upper $2.3 \mu\text{m}$ image, streets and roads to the east of Diamond Head and within the crater disappear into the general clutter. In the lower $5 \mu\text{m}$ image, they can be distinguished, but the contrast is greatly enhanced if the longwave image is subtracted from the shortwave.

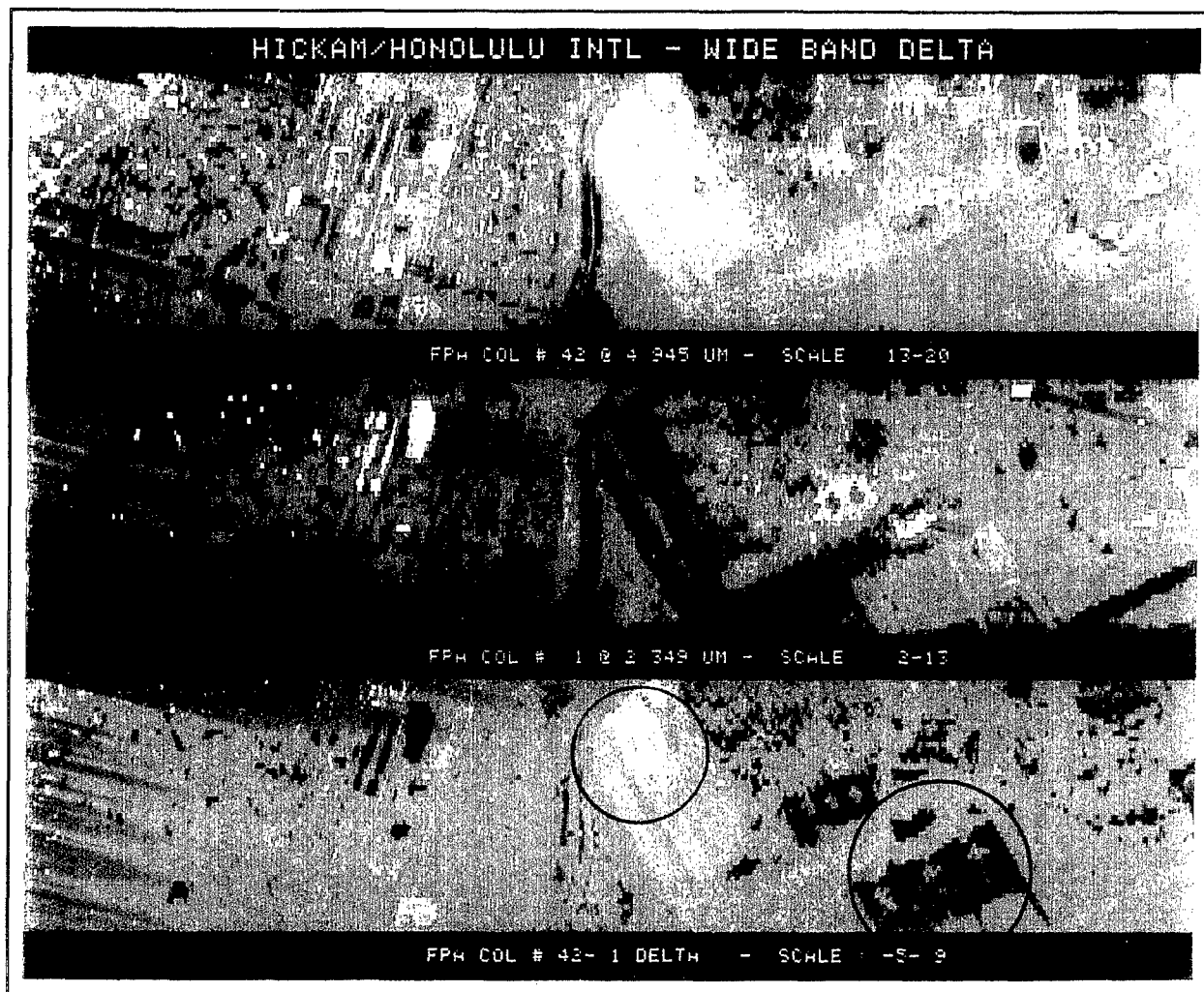


Figure 8-13. A Second Example of Wide-Band Differencing. In the upper image, two aircraft parked on the (dark-colored) ramp at Hickam AFB may readily be discerned at $5\ \mu\text{m}$ (upper center). In the $2.3\ \mu\text{m}$ shortwave image below, the first two disappear, but three others are evident (lower right). When the two are differenced, all five become apparent (circled).

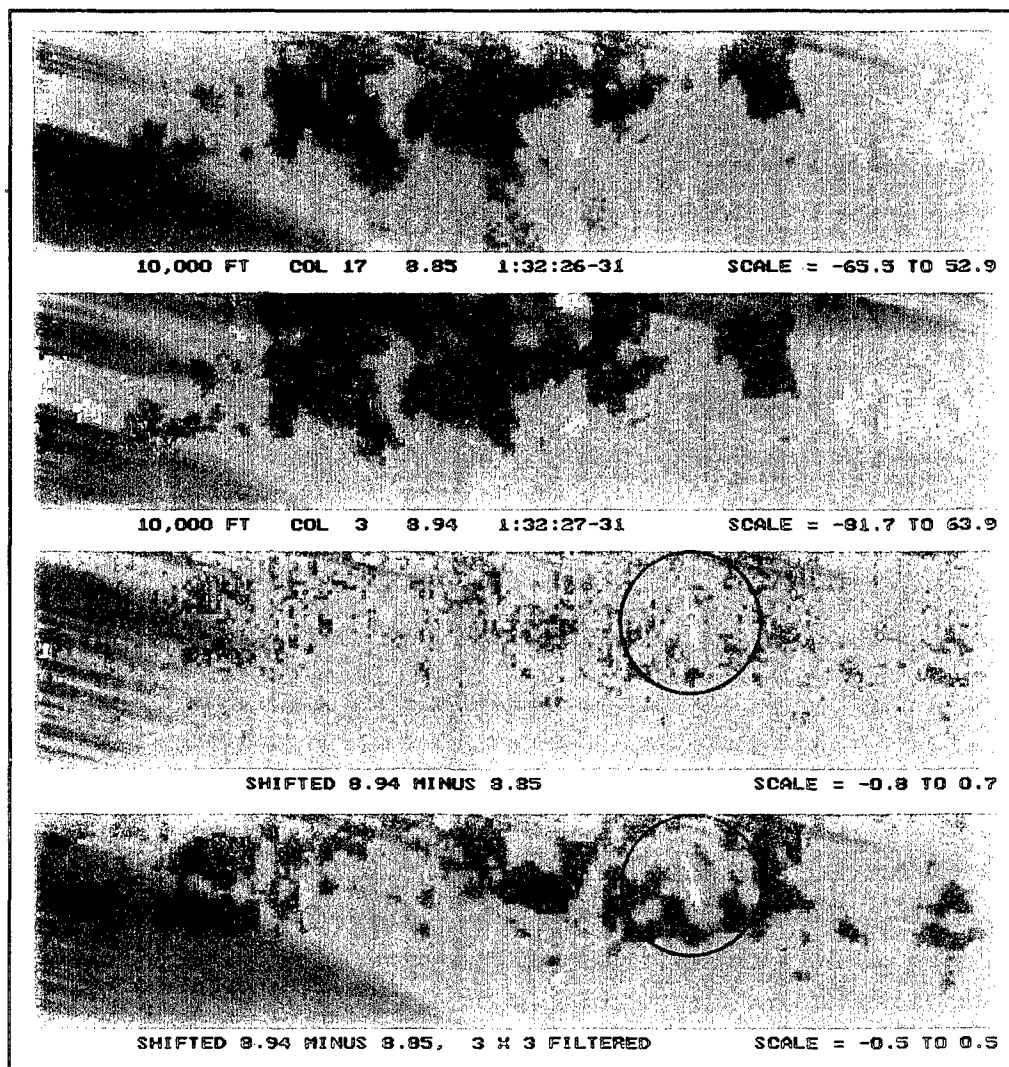


Figure 8-14. A Second Example of Narrow-Band Differencing. In both the upper images ($8.85\ \mu\text{m}$ and $8.94\ \mu\text{m}$ - data from the MUltiSpectral Ir Camera (MUSIC)) a cloud of ethyl ether vapor has been released, but is not apparent. In the differenced third image, the gas plume is easily detected.

8.7 PRODUCTS FROM COMMERCIALLY AVAILABLE SATELLITE DATA

Satellite-collected multispectral data (Landsat) have been available for commercial or civilian purchase for more than twenty years, beginning in 1972 with Landsat 1. Since the launch of the Landsat 4 TM in 1982, the usage of satellite remote sensing has grown for development of products to support DoD applications. Today, satellite data from TM, SPOT, and other sensors are accepted for usage in various projects to support defense applications. These applications vary from support to Desert Shield and Desert Storm to determination of poppy cultivation in Afghanistan.

Satellite data have several unique properties that make them useful for such applications, such as:

- Their wide field of coverage is especially useful for broad area coverage applications. Even with coarse resolution, trackage, new construction, and other intelligence indicators can be very apparent and useful for cueing other, higher resolution data sources.
- Their high radiometric quality across multiple bands allows discrimination of vegetation and terrain classes useful in area limitation and trafficability analyses.
- These data are readily available and unclassified, facilitating usage and distribution to allies during joint campaigns or exercises. Techniques to geocode the data precisely allow up-to-date maps of even remote regions of the Earth to be developed quickly, for example, to accompany troops during exercises and campaigns.
- The coverage is repetitive and suitable for change detection, and some systems are pointable to allow more frequent coverage of selected areas.
- The data are digital, allowing access to a large suite of automatic and automated algorithms for feature extraction. Techniques have been clearly demonstrated to extract land cover, bathymetry, elevation, and line of communication (LOC) information directly from the data. This also facilitates fusion of the extracted and original data with image or vector data for incorporation into GIS, use in mission planning systems, and warping into perspective views for mission planning or rehearsal.

As noted earlier, DoD organizations, such as SPACECOM and DIA, are now creating products and data graphics from satellite data on a regular basis. These products typically draw on the automatic, automated, and interactive algorithms available in the individual systems also noted earlier. Various levels of capabilities support the individual requirements of the users of the systems.

Probably the most important capability of each system is the ability to geocode (including orthorectification of) the data. This very necessary precision preprocessing step ensures the maximum utility of the data at any later processing step. Many of the examples presented herein are much more useful with the geocoding process, because it allows integration with other types of image data or direct integration into a GIS. This section illustrates the charting, feature extraction, and visualization and data fusion capabilities demonstrated with satellite imagery.

8.7.1 Types of Color Composite Images

Color is used to present MSI data and hyperspectral data for interpretation and viewing. Many different combinations are possible in terms of spectral bands assigned to the red, green, and blue components of an image, be they on hardcopy film or a softcopy computer display. Table 8-2 presents a few of the more common combinations and associated product names.

Table 8-2. Band Combinations for Common Color Composite Images

Color Composite Name	Color Assigned to Spectral Band					Appearance of:		
	Vis Blue	Vis Green	Vis Red	Near IR	SW IR	Veg	Bare Soil	Water
Natural Color	B	G	R			Green	Brown	Dark Blue
False-Color IR		B	G	R		Red	Cyan	Black
SWIR			B	G	R	Green	Mag	Dark

8.7.2 Image Mapping

A good example of precision correction is the image map illustrated in Figure 8-15. This image map was produced from Landsat TM data and geocoded using the available 1:50,000-scale chart source for the area. By precisely correcting the data, one can readily use the Defense Mapping Agency (DMA) chart data as a backdrop for the image data or vice versa. Comparison with the chart then allows the data to become even more useful as an intelligence tool. Since the image is more recent than the chart, it provides an update to the DMA chart.

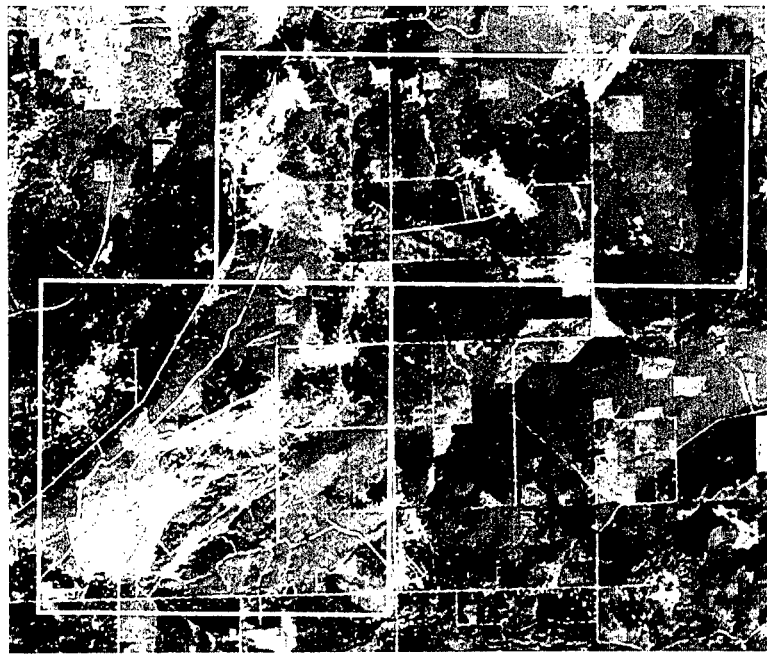
Interpretation of the image data with the chart now very clearly shows changes to the area since the DMA chart was produced. New clearings and new road construction indicate the usage of the area for licit or possibly illicit crop production. Chart information, such as location of villages, towns and power lines in proximity to the new construction, add additional levels of useful intelligence information.

This comparison of the newer TM data with the DMA chart data also shows clearly the ability to use TM data to directly update the chart or to indicate charts with enough change and intelligence priority to warrant update. An important asset then becomes the ability to use the new MSI data in conjunction with already available and excellent cartographic information from DMA or other sources to prioritize and complete charting projects.

8.7.3 Feature Extraction

8.7.3.1 Land Use Mapping

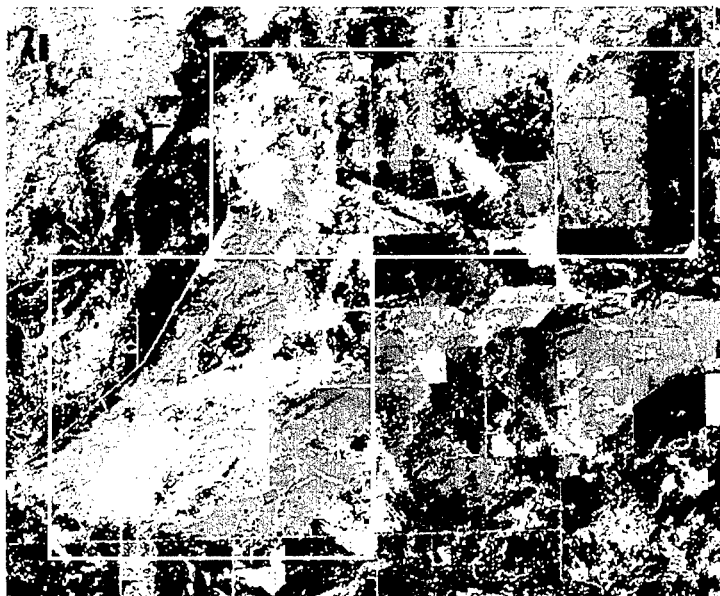
Information can also be extracted directly from geocoded satellite data, as shown in the previous example, or even from uncorrected data. Figure 8-16a shows a false-color-infrared composite image of a Landsat TM subscene acquired at Camp Grayling in Michigan. This geocoded false-color image



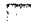




Scene ID: 51293-15484 Path/Row 21/29
 Scene Date: 15 September 1987
 Projection: UTM, Clark 1866 Spheroid
 TM Band 4=red, 3=green, 2=blue



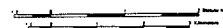
a) False-color infrared composite image



KEY

-  Deciduous Forest
-  Coniferous Forest
-  Shrub
-  Bare
-  Surface Water

Scene ID: 51293-15484 Path/Row 21/29
 Scene Date: 15 September 1987
 Projection: UTM, Clark 1866 Spheroid
 Categorized TM Data



b) Terrain categorization map

Figure 8-16. Landsat-Based Terrain Categorization, Camp Grayling, MI. This image was provided by ERIM.

provides useful information, but further processing with spectral categorization algorithms allows extraction of the ground cover classes within the camp, as shown in 8-16b. This then allows an accurate and up-to-date presentation of the land cover within the camp.

The geocoded land cover data also can be input into a GIS and combined with other data types, such as elevation data and outputs related to trafficability. For example, the land cover data and elevation data could be combined very effectively to allow accurate estimation of runoff characteristics in a watershed. In addition, some of the features such as forests and water bodies can be used individually in mapping and charting projects to quickly isolate changes and update the chart data.

Accurate up-to-date land cover information is not available for most of the world. Satellite multispectral data are readily usable to fill this void, because of their digital nature and broad area coverage.

8.7.3.2 Ice Type Mapping

Other types of feature extraction have also been accomplished using satellite data. Figure 8-17 illustrates the extraction of ice types in Saginaw Bay, Michigan, using the same spectral categorization techniques that were used for land cover extraction. This type of information becomes useful in mission planning exercises related to ship usage or missions involving underwater activities.

8.7.3.3 Water Temperature Mapping

In addition to use of the reflective spectral bands for extraction of land cover features, the thermal band in Landsat TM has proven useful for extraction of thermal features, as illustrated in Figure 8-18. This is an image of a power plant with hot water discharging into Par Pond at the Savannah River facility in Georgia. The temperature of the water effluent indicates whether the plant is operational and also provides valuable insight on the capacity of the plant.

Interpretation and analysis of thermal effects can be facilitated by fusion of the lower spatial resolution (120-meter) thermal data with higher resolution data or features extracted from the other Landsat bands or other sensors. Using spectral rules, the pixels associated with water were isolated from their surroundings and their color-coded temperatures are displayed in this figure in the context of one of the finer-resolution reflective TM bands.

8.7.3.4. Change Detection

Another type of multispectral feature extraction that has shown very high, possibly the highest, potential is change detection. These techniques have advanced from simple single-band comparison techniques to more complex and automated techniques that can be selective about the kinds of changes that are detected.

Detected changes can be compared to a database or target list to determine if they are of interest. By using spatial analysis techniques, the change can also be qualified and quantified and reported to a database or used as output to an intelligence report.

Road construction and road improvement are important items that can have military implications. Figure 8-19 shows a Landsat change image for an area near Kazan in the former USSR. This image very clearly shows (in red) major construction or improvement of a road leading to an existing dam over the Volga River. The improvements would facilitate traffic and deployment of weapon systems in this region.

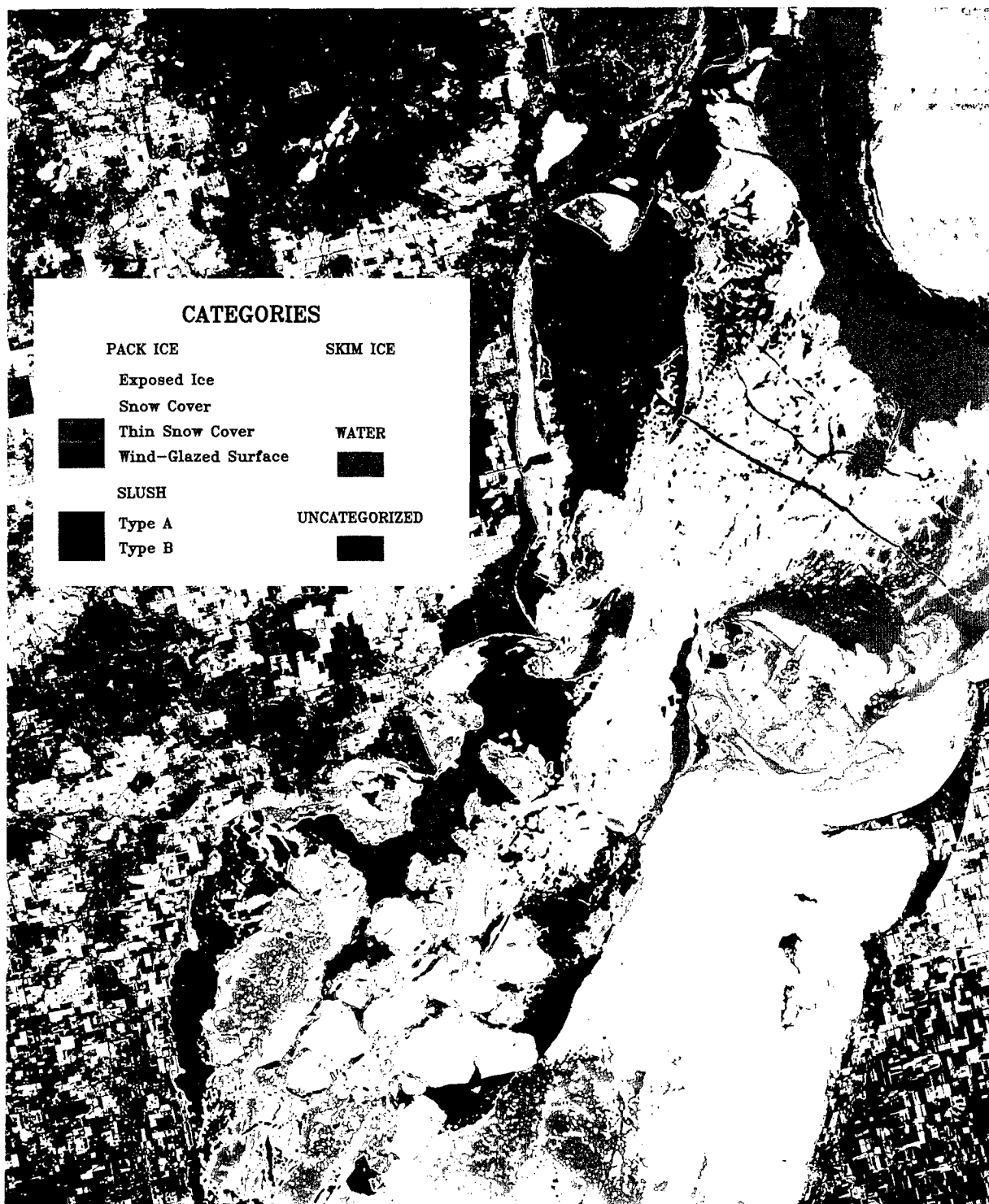


Figure 8-17. Examples of TM-Based Categorization of Ice Types (Saginaw Bay of Lake Huron, near Tawas City, MI). This image was provided by ERIM.

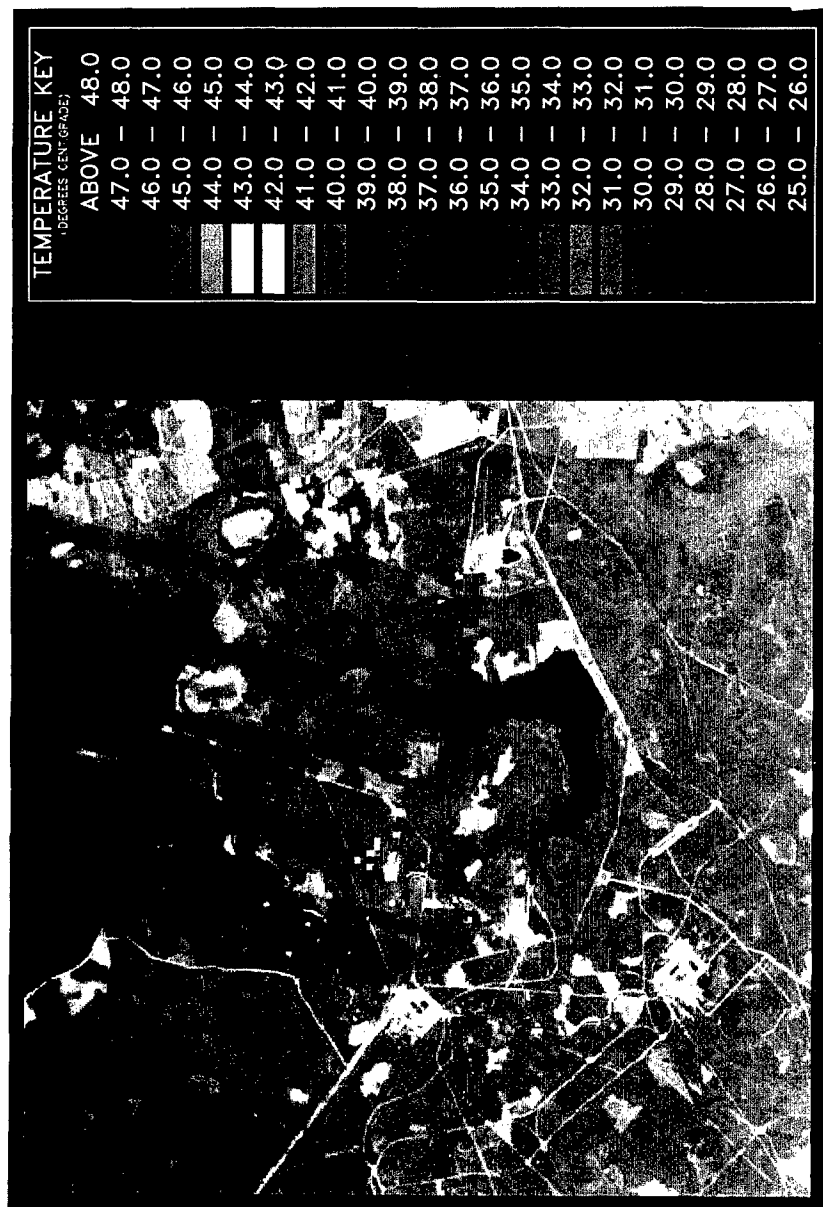


Figure 8-18. Water Temperature Map Derived From Landsat TM Data. (Par Pond, Savannah River Plant, Landsat-5 TM, 15 Oct 85.) This image was provided by ERIM.

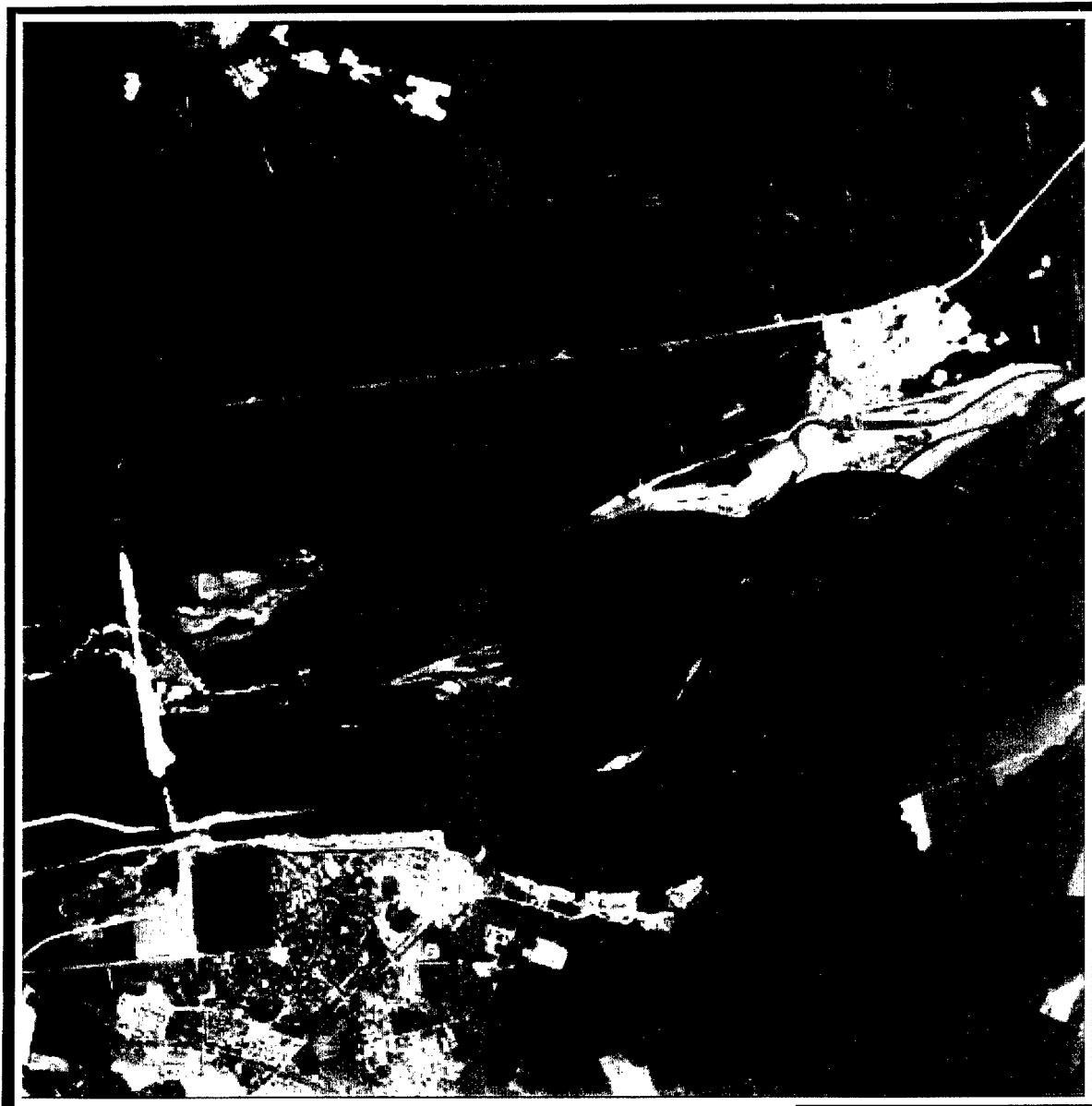


Figure 8-19. Landsat TM Change Image Near Kazan, Russia, 31 May 85 to 2 May 86.
Changes appear in red and cyan tones.

Because of high spectral contrast between construction activity and natural features, these types of changes are easily discernible in TM data with their 30-meter spatial resolution. The broad area coverage (100 x 100 nautical miles) of Landsat can provide opportunities for detection of construction and development that could be missed by systems with higher resolution and smaller coverage areas.

Figure 8-20 shows a change image generated for a storage area in Iraq. The change image clearly shows smoke over the recently struck known part of the facility. Also visible to the southwest is another large storage area created between the collection of the first and second image that does not appear to be damaged.

Satellite multispectral systems also can detect occurrences related to trafficability and natural disaster, such as flooding. Figure 8-21 is a change image set developed for an area near St. Louis, Missouri, that shows the extent of the flooding during summer 1993. The image is also geocoded and annotated with coordinate information that allows exact areas of flooding to be extracted and measured, as well as potentially being combined with other information in a GIS.

The excellent spectral coverage and the broad area coverage characteristics of satellite data ensure their usefulness for detecting and measuring changes. Many changes of small areal extent can be detected by these multispectral systems and, even though their type cannot be identified, they can have utility for keying other higher-resolution sensor systems for closer analysis and coding of changes. Pointability is important for being able to monitor areas more frequently than the nominal repeat cycle of the satellite orbit [e.g., SPOT and the once-planned High Resolution Multispectral Imagery (HRMSI) sensor for Landsat 7].

8.7.3.5 Bathymetric Analysis and Mapping

Water depth or bathymetric information is often included on charts. Satellite multispectral data have shown excellent utility as a source for bathymetric information. Water depths have been mapped to 30 meters in clear water. Water-depth calculation algorithms make use of differences in the absorption coefficient of water for radiation detected by the different multispectral bands.

Figure 8-22 presents an example of bathymetric information extracted from satellite data collected by the Landsat Thematic Mapper over the Bahamas. Water depth was computed and quantized into depth intervals. These intervals were then color-coded for display of the bathymetric information.

Figure 8-23 shows the same water depth information after it has been converted to vector form and plotted as contour lines over a false-color rendition of the original TM data. The vector information represents a more compact form of storage that is better oriented toward GIS.

The above types of data can be valuable in development of planning information for underwater missions, anchorage analysis, and as tools for planning ship or landing craft exercises.

8.7.3.6 Lines of Communication Mapping

Landsat and SPOT data have also proven useful in the extraction of LOC information. Nearly every mission planning and trafficability application requires as input roads, rails, canals, power lines, and so forth. These data are useful to determine the types of threats that might be found for aircraft mission planning exercises or the best corridors to navigate in determining the fastest/safest route to a target. LOCs are also some of the most rapidly changing information and are therefore outdated quickly on available map sheets. The satellite data provide an accurate and up-to-date source of information that is available for virtually anyplace in the world.

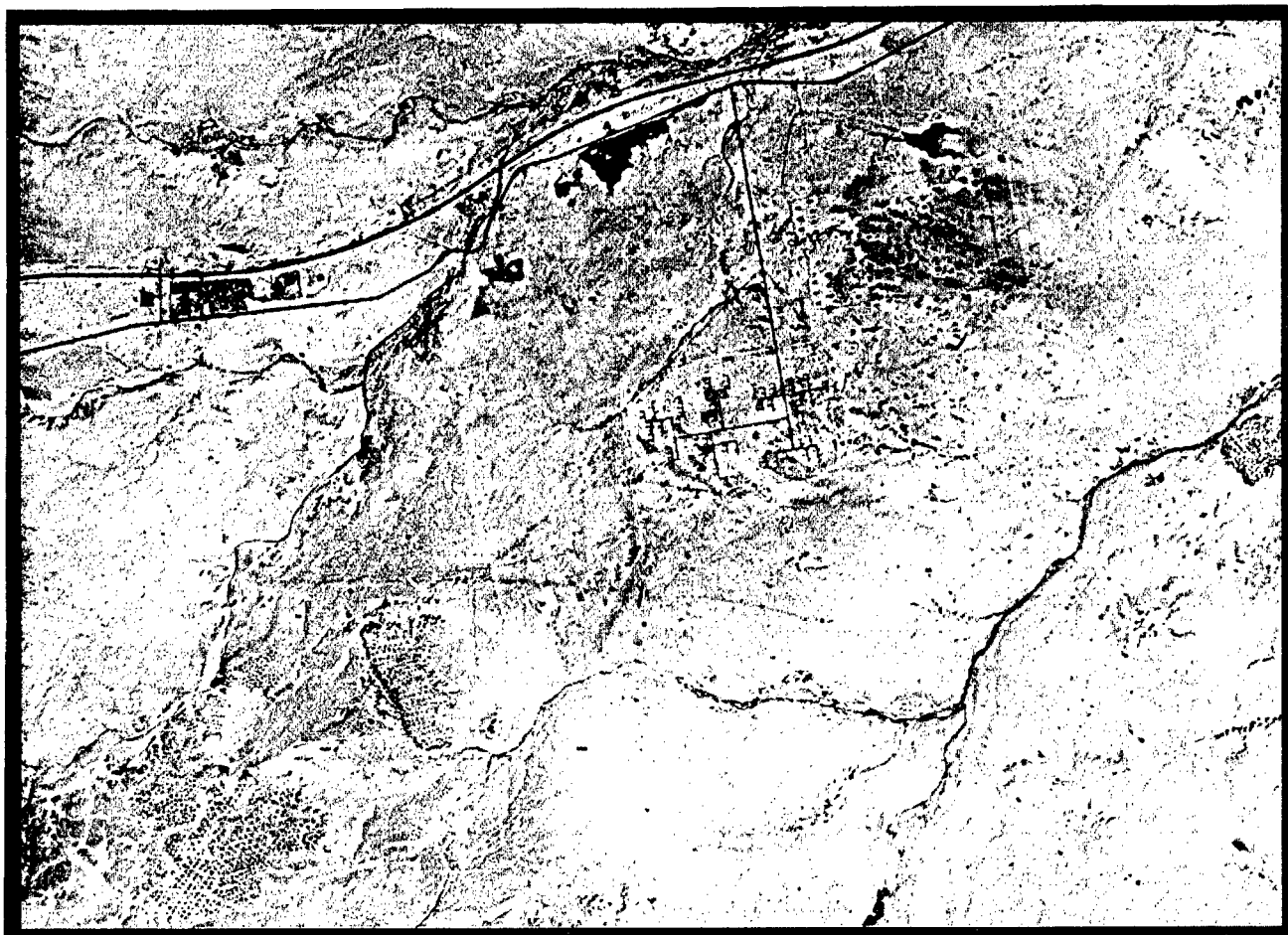


Figure 8-20. TM-Based Change Detection of Storage Areas in Iraq. Cyan represents new construction (lower left) and smoke/damage plumes (upper right). This image was provided by ERIM.



Landsat Satellite Thematic Mapper (TM) Change Image

Scene Dates: 15 July 86 Band 5 (Water Mask - Light Blue)
 18 July 93 Bands 2, 4, 7 (Background Image)

0 10 Miles

This Thematic Mapper change image of the St. Louis, Missouri area indicates the dramatic effects of flooding along the Mississippi, Missouri and Illinois Rivers during the summer of 1993. TM data (bands 7, 4 and 2) from July 18, 1993 were geometrically corrected using **ERIM's Restoration** resampling technique to create the background image which shows flooded areas as dark blue. A water mask (light blue), created using TM band 5 data from July 15, 1986 and which identifies the rivers' boundaries during a year of average rainfall, was superimposed onto the background image.

Figure 8-21. Change Detection Mapping of Flooded Area (St. Louis, MO). This image was provided ERIM.

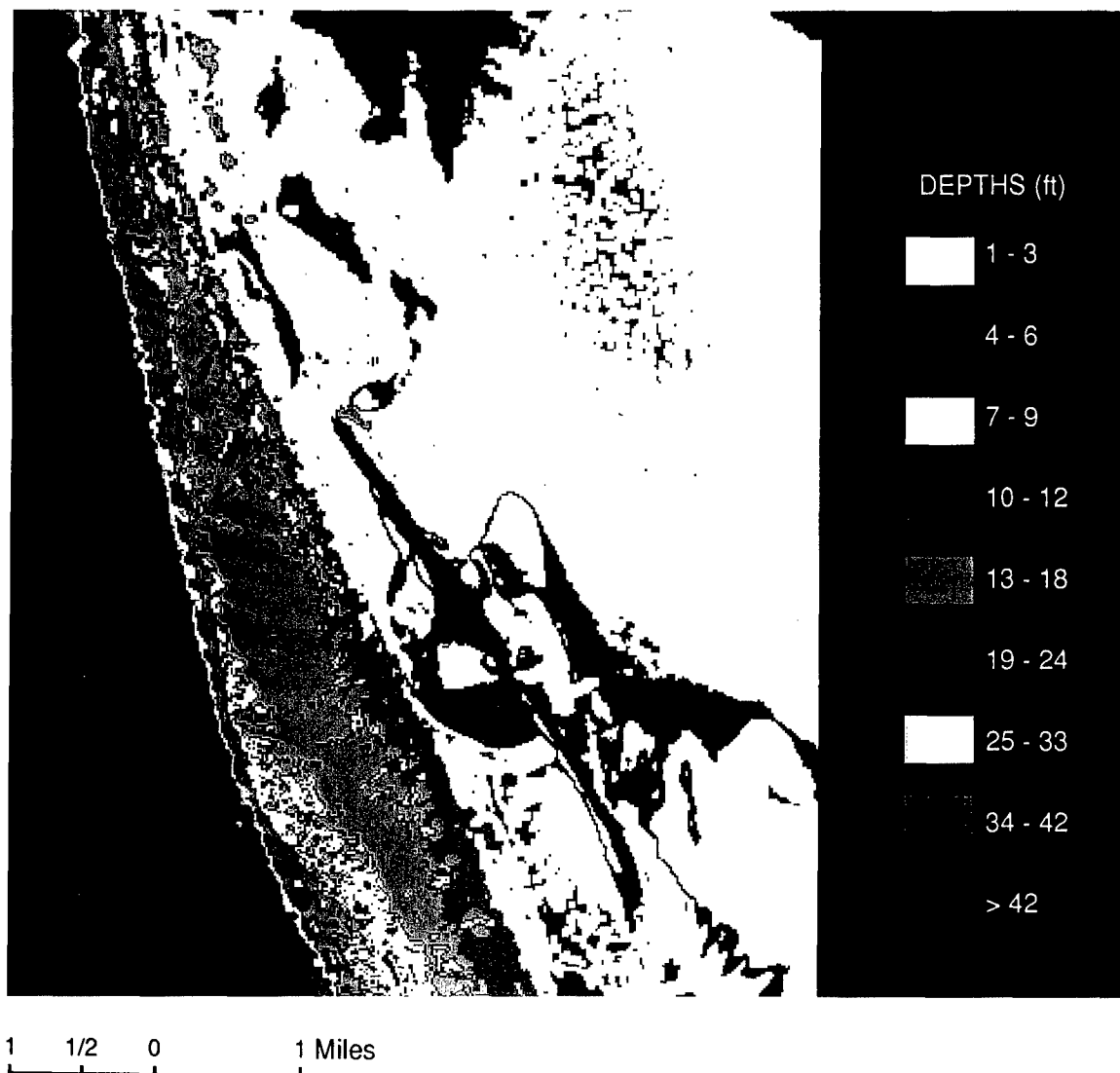


Figure 8-22. Landsat-Based Bathymetric Image (North Cat Cay, Bahamas, 30 Jun 86, Mercator Projection). This image was provided by ERIM.

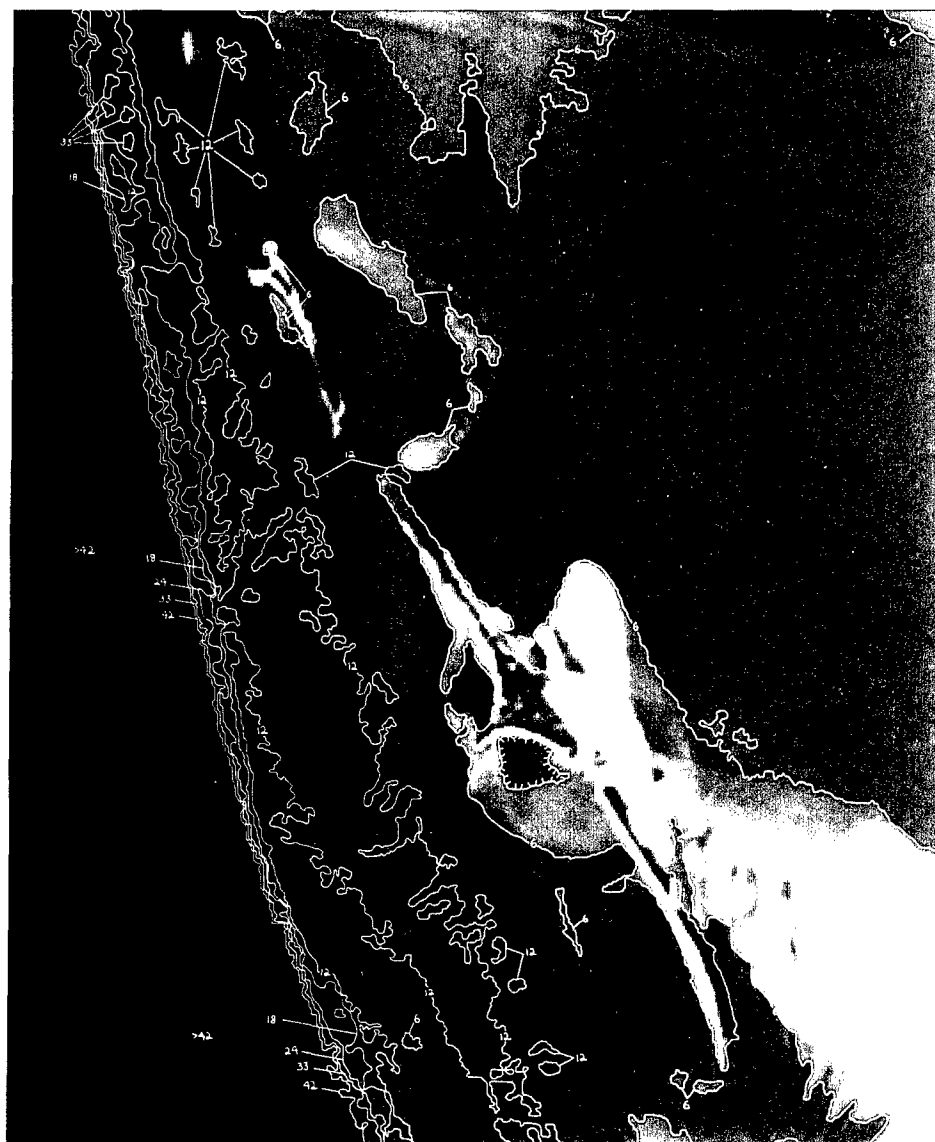


Figure 8-23. Contoured Version of Landsat-Based Depth Image (North Cat Cay, Bahamas, 30 Jan 86). Depths in feet; average error for extracted depths = 1.77 ft.; maximum depth calculated = 42 ft.; maximum depth of field data available for accuracy assessment = 32 ft. This image was provided by ERIM.

Figure 8-24a shows an example of automatically extracted LOC information from TM data for an area in North Carolina. It clearly shows the ability to extract much of the LOC network.

Figure 8-24b shows the same data after manual interpretation of the satellite data to connect the LOC feature information. An additional step would be to attribute the feature information to include LOC type, composition, purpose, bridges, and so forth. After completion of these steps an excellent LOC database suitable for direct input into a GIS is complete and suitable for use in mission planning and trafficability analysis. Higher resolution data such as SPOT or the planned 5- and 1-meter systems will allow development of algorithms and techniques to improve this application significantly, but even the low-resolution database can suffice when only little or dated information exists for an area. This could also be considered a first step in development of a database that can be updated in the future with higher-resolution data sources.

8.7.3.7 Elevation Data Extraction

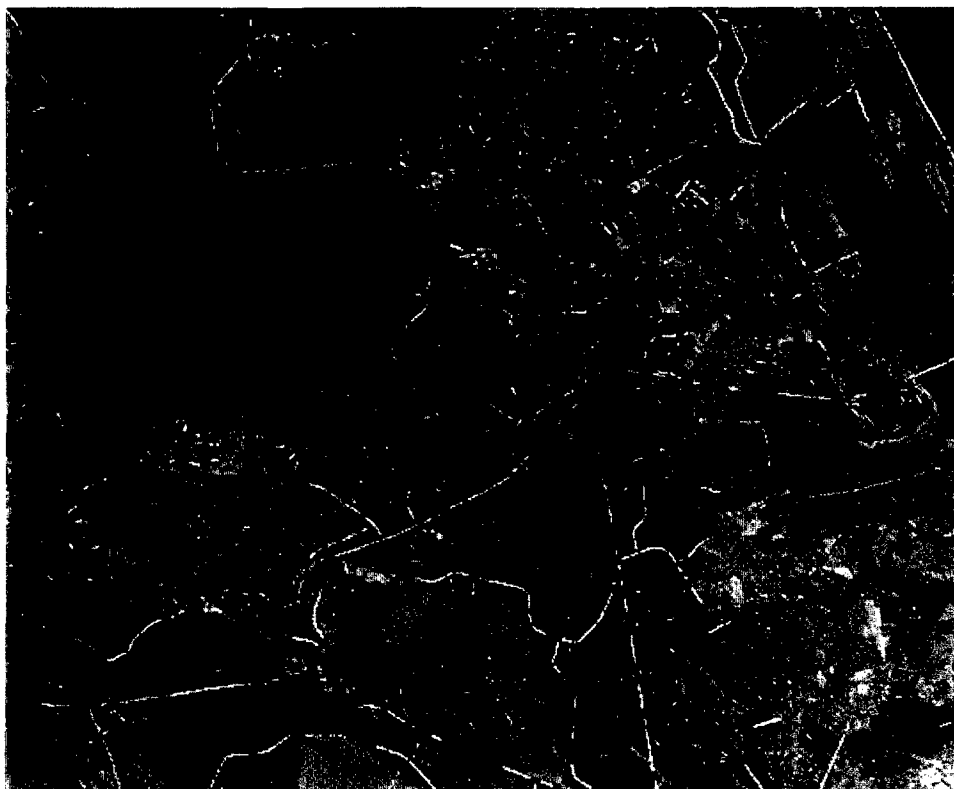
Figure 8-25a shows elevation data extracted from two SPOT scenes. For comparison Figure 8-25b is an image of U.S. Geological Survey (USGS) 3-arc-second digital elevation data of the same area. The area is located near Rapid City, South Dakota. The elevation data were extracted by stereographic processing of data from two SPOT scenes viewing the ground from different off-nadir perspectives. These data have been found to correlate extremely well with elevation information digitized from the USGS quad sheet of the same area. The figure thus illustrates that stereo coverage can be processed to accurately extract elevation information over remote areas of the world at 10-meter resolution.

Strictly speaking, one does not need multispectral data to extract elevation data. In fact, data from the 10-meter panchromatic band of SPOT were used to create the above example. Nevertheless, the example is included here, because multispectral sensors are being equipped with higher spatial resolution panchromatic bands to provide such capabilities, for example, SPOT and the initially planned HRMSI for Landsat 7. As satellite sensors become more sophisticated, with higher spatial resolution and off-nadir pointing capabilities, both the accuracy of extracted elevation data and requirements on precision of elevation data for the most accurate geocorrection and exploitation will increase dramatically. Elevation extraction from satellite data themselves may become a critical tool to support exploitation of data from these systems.

8.7.4 Visualization and Image Fusion

Landsat and SPOT data have proven of great utility in applications requiring visualization of terrain, such as in mission planning and rehearsal projects or in the fusion of different types of sensor data to extract the maximum information available in each sensor. The ADRI program, first mentioned in Section 7.3.1.5, supplies high quality image information to be used in mission planning exercises on a production basis. While present systems do not have capability to use color images, they could be a source of improvement in the future.

SPACECOM's MIMES facility has been supplying perspective views and image maps to bomber crews for several years and has created a large demand for these types of products in the intelligence community. Nearly all these products require the fusion of DMA DTED data with image data; this is necessary in order to produce image maps using off-nadir SPOT images or TM scenes collected in high terrain areas.

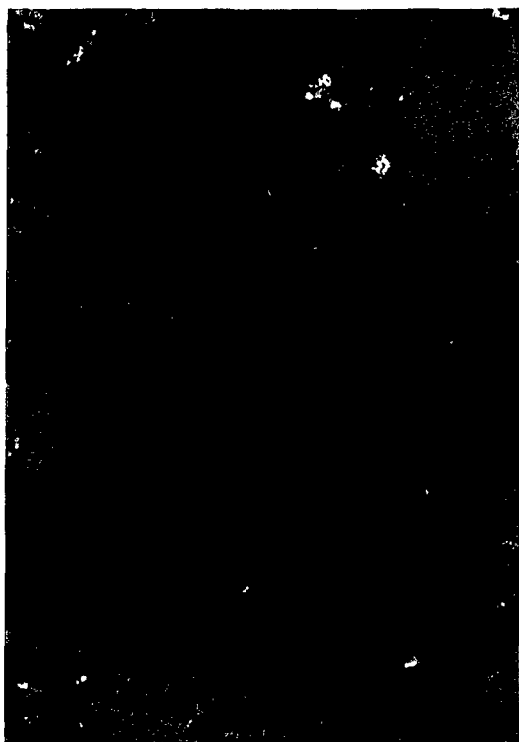


a) Automatically extracted segments (in red).



b) Combined manual and automated product.

Figure 8-24. LOC Extraction From Landsat TM Data.



a) SPOT-derived elevation map



b) Level II USGS DEM (3 arc seconds)

Figure 8-25. Comparison Between SPOT-Derived Terrain Elevation Data and USGS DEM Data. This image was provided by ERIM.

Figure 8-26 presents a perspective view image created near Las Vegas, Nevada, looking toward Lake Mead. The data combine DMA DTED for elevation information with image data from three separate sensor systems to achieve a very high quality, accurate representation of the terrain. High-resolution SPOT data were used in the foreground, Landsat TM data in the mid-ground, and AVHRR data in the background. This is an advantage over systems that only use one input data type to create a perspective view, since in them each individual output pixel may require anywhere from less than one to many input data cells. By using data at three different resolutions, the appropriate data type was used to create the best spatial and spectral resolution for each output cell. In addition to creation of single perspective views, these techniques have also been used to produce spectacular terrain fly-throughs that give the sense of flying over the terrain in whatever aircraft is being simulated.

Figure 8-27 illustrates a data fusion application that combines most of the products and techniques noted above. A database was created in a GIS that contained the 1 degree x 1 degree ADRI product for this area near Eglin AFB in Florida. TM data were processed and land cover information extracted, as shown in the upper right. LOC information was obtained for the area. The GIS was then used to process each of the layers to produce products related to mobility impedance (upper left) and relative travel time from two possible landing spots on the beach (lower left). Finally least-cost paths were computed from those points to several different locations on the base (paths are shown in red on the lower right image), against the backdrop of an ADRI image. These calculations can be modified to adjust for using different vehicles or different parameters of operation. Additionally, the ADRI 10-meter panchromatic data were fused with the TM data to produce a natural color 10-meter image simulation (not shown). This simulation was then used to produce perspective views with various aircraft operating parameters over the region.

Commercial multispectral satellite data's major drawbacks are typically weather, revisit time, and spatial resolution. These are offset by their advantages of broad area coverage, spectral diversity, low cost, historical coverage, and diversity of applications, which make them tools that should be considered for most intelligence problems and many defense applications now and in the future.



Location: N 115.0752 W 36.2672
Elevation: 3200 m HDG: 120

Depression Angle: 5 degrees

Figure 8-26. Multisensor Perspective View, Using Data From SPOT, Landsat TM, and AVHRR Sensors (Lake Mead, NV). This image was provided by ERIM.

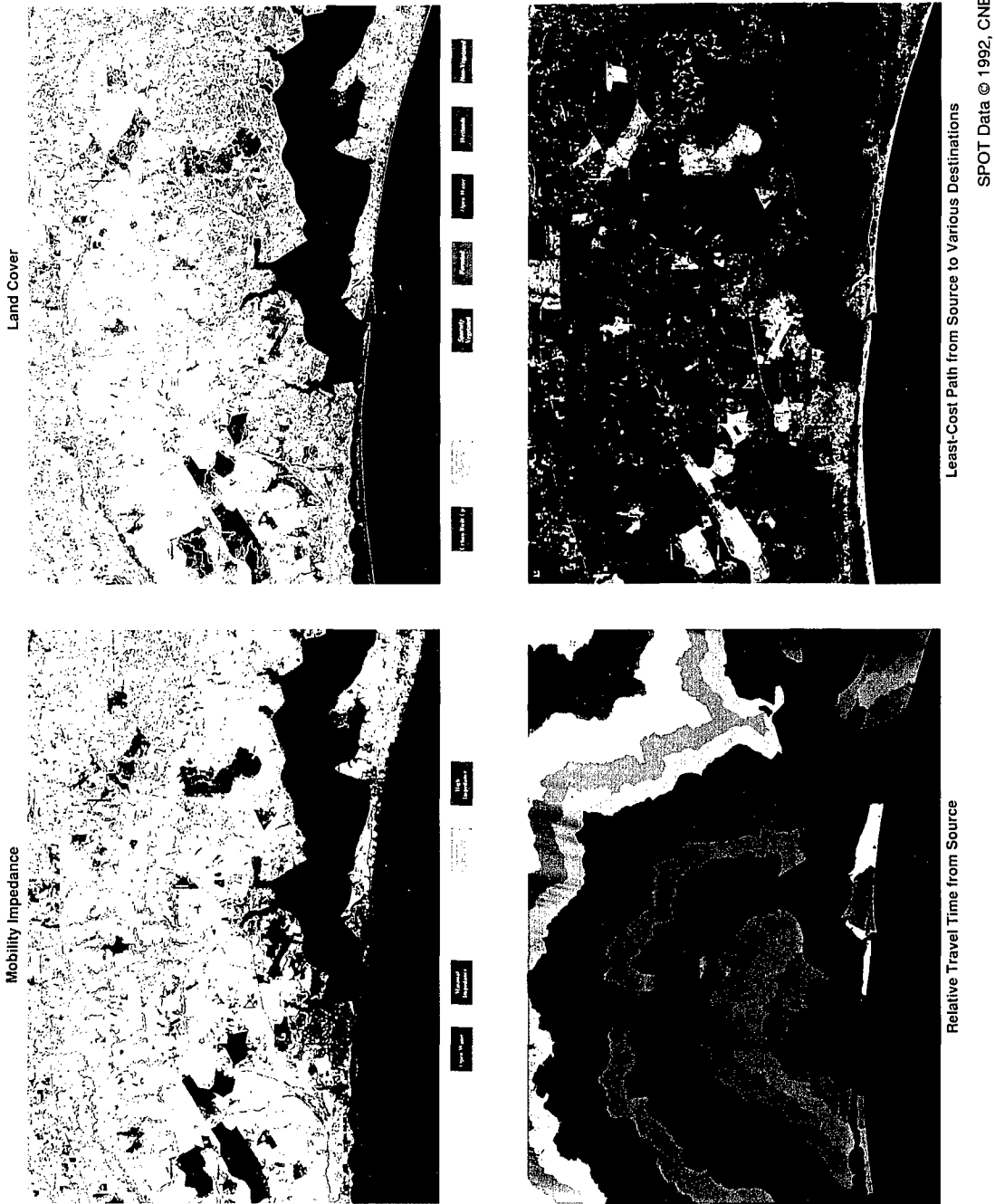


Figure 8-27. Mobility and Routing Analysis Using Multispectral Inputs. This image was provided by ERIM.

Appendix A: Materials Phenomenology

A.1 Purpose

A variety of applications have long shown the usefulness of multispectral techniques at the visible through shortwave infrared wavelengths (0.4 to 2.5 μm). More recent needs have prompted an interest in the applicability of multispectral techniques to the thermal infrared (2.5 to 14.0 μm). Unfortunately, the physical phenomenology of materials in the thermal infrared is not well understood. This appendix is a first step in deepening our understanding of the sources of spectral features in the thermal infrared. It begins with a brief review of the physics describing the optical properties of materials and is concludes with a series of short sections providing brief spectral analyses of several interesting materials like soils, road materials, vegetation, camouflage nets, and paints.

A.2 Background Material

The following section is a short review of some quantities important in describing the optical properties of materials. It is not intended to be a thorough treatment of optical wave theory but instead is presented to quickly reacquaint the reader with some important aspects of the subject.

A.2.1 Complex Index of Refraction

Probably the most fundamental quantity commonly used to describe the optical properties of a material is the complex index of refraction. For a homogeneous medium devoid of solutes the complex index of refraction is all that is needed to specify the material's reflectance, transmittance, and absorptance. The complex index of refraction also describes the material's spectral characteristics since it is a function of frequency. Of particular interest are the special resonant frequencies of a material where the index of refraction undergoes dramatic changes.

In electro-magnetic wave theory, the time harmonic form of Maxwell's equations can be written:

$$\nabla \times \vec{E} = -j\omega\mu\vec{H} \quad (\text{A-1})$$

$$\nabla \times \vec{H} = (\sigma + j\omega\epsilon)\vec{E} = j\omega\epsilon_r\epsilon_o\vec{E} \quad (\text{A-2})$$

where

\vec{E} = the electric field vector

\vec{H} = the magnetic field vector

ω = frequency

$$\begin{aligned}
\mu &= \text{the magnetic permeability of the medium} \\
\epsilon &= \text{the electric permittivity of the medium} \\
\sigma &= \text{the conductivity of the medium} \\
\epsilon_o &= \text{the permittivity of free space} \\
\epsilon_r \equiv \epsilon' - j\epsilon'' &= \text{the complex relative permittivity (complex dielectric constant)} \\
\epsilon' = \frac{\epsilon}{\epsilon_o} &= \text{the real part of the complex relative permittivity} \\
\epsilon'' = \frac{\sigma}{\omega\epsilon_o} &= \text{the imaginary part of the complex relative permittivity.}
\end{aligned}$$

These equations have been written for an isotropic homogeneous medium with the scalar quantities μ , ϵ_o and ϵ_r . An extension to anisotropic materials can be made by making these scalar quantities into tensors.

We can relate the complex dielectric constant, ϵ_r , to the complex index of refraction, N , by:

$$\epsilon_r = N^2 \quad (\text{A-3})$$

where

$$\begin{aligned}
N &= n - j\kappa \\
n &= \text{the real or dispersive part} \\
\kappa &= \text{the imaginary or absorptive part.}
\end{aligned}$$

The real and imaginary parts of the dielectric constant are related to the index of refraction by:

$$\epsilon' = n^2 - \kappa^2 \quad (\text{A-4})$$

$$\epsilon'' = 2n\kappa. \quad (\text{A-5})$$

From the absorptive term (κ) comes a very useful result called the absorption coefficient. We can derive the absorption coefficient by writing the complex propagation constant ($\tilde{k} = Nk_o$) as (where $k_o = \frac{\omega}{c_o}$ is the propagation constant of free space and c_o is the speed of light)

$$\tilde{k} \equiv k - j\frac{\alpha}{2} \quad (\text{A-6})$$

and, since by definition $\tilde{k} = \frac{\omega N}{c_o}$, we can write:

$$k - j\frac{\alpha}{2} = \frac{\omega}{c_o} (n - j\kappa) \quad (\text{A-7})$$

where

$$\alpha = \frac{2\omega\kappa}{c_o} = \frac{4\pi\kappa}{\lambda_o} = \text{the absorption coefficient.}$$

A more physical understanding of the absorption coefficient can be found in the derivation of Beer's law. We can write the scalar electric field as:

$$E = E_o e^{j(\omega t - \tilde{k}z)} \quad (\text{A-8})$$

and using our definition of the propagation constant \tilde{k} we can write:

$$E = E_o e^{-\frac{\alpha}{2}z} e^{j(\omega t - kz)} \quad (\text{A-9})$$

The irradiance of the optical wave is related to the electric field strength by:

$$I = \frac{1}{2} \epsilon c |E|^2 \quad (\text{A-10})$$

giving:

$$I = \frac{1}{2} \epsilon c E_o^2 e^{-\alpha z} \quad (\text{A-11})$$

and defining

$$I_o = \frac{1}{2} \epsilon c E_o^2 \quad (\text{A-12})$$

we arrive at Beer's law with:

$$I = I_o e^{-\alpha z} \quad (\text{A-13})$$

The exponential term in Beer's law is actually just the transmittance of the material after propagating a distance z through it. Thus we see that the absorption coefficient provides a quantitative description of the rate at which energy is absorbed in the medium.

A.2.2 The Lorentz Model

The complex index of refraction is a function of frequency and it undergoes rather dramatic changes near certain resonant frequencies characteristic of the medium. These resonances are due to electronic, vibrational, and rotational quantum transitions within the medium. The physical reasons for these transitions will be discussed later. It would take a full quantum mechanical approach to rigorously model the full optical behavior of materials near resonance. Fortunately, there is a classical oscillator model, the Lorentz model, which accurately predicts both the dispersive and absorptive properties of the index of refraction near resonance. In this section we will briefly describe this model since it will help us to better understand the observed optical properties of some materials.

The presence of an electric field in a medium forces the electrons in that field to oscillate. Since the electric field is an AC field, these oscillations will be seen as an alternating induced polarization in the medium. Under such conditions the electrons behave as a system of coherent oscillating dipoles which reradiate the incident energy.

We can write the equation of motion for a forced, damped harmonic oscillator as:

$$m\ddot{x} = -eE(t) - m\gamma\dot{x} - Kx \quad (\text{A-14})$$

where m is the electron mass, e is the electronic charge, γ is the damping coefficient necessary to make the Lorentz model accurately predict absorption, and K is a restoring force spring constant needed to model the bound nature of electrons and atom-to-atom bonds. The resonant frequency of such a classical oscillator is given as:

$$\omega_o = \sqrt{\frac{K}{m}} \quad (\text{A-15})$$

This permits us to write the differential force equation as:

$$\ddot{x} + \gamma\dot{x} + \omega_o^2 x = -\frac{e}{m} E_o e^{j\omega t} \quad (\text{A-16})$$

with the solution of this equation given as:

$$x(t) = x_o e^{j\omega t} = \left[\frac{-\left(\frac{eE_o}{m}\right)}{\omega_o^2 - \omega^2 + j\omega\gamma} \right] e^{j\omega t}. \quad (\text{A-17})$$

Now if we briefly return to classical EM theory we know that the relationship between the electric displacement vector \vec{D} , the electric field \vec{E} , and the polarization \vec{P} , is given as:

$$\vec{D} = \epsilon_o \vec{E} + \vec{P} = \epsilon \vec{E} \quad (\text{A-18})$$

In addition, we can write the polarization as:

$$\vec{P} = \epsilon_o \tilde{\chi} \vec{E} \quad (\text{A-19})$$

where $\tilde{\chi}$ is the complex electric susceptibility given as $\tilde{\chi} = \chi' - j\chi''$. This permits us to write the electric displacement as:

$$\vec{D} = \epsilon_o [1 + \tilde{\chi}] \vec{E} = \epsilon \vec{E}. \quad (\text{A-20})$$

The relative complex dielectric constant becomes:

$$\epsilon_r = 1 + \tilde{\chi} \quad (\text{A-21})$$

giving:

$$\epsilon' = n^2 - \kappa^2 = 1 + \chi' \quad (\text{A-22})$$

$$\epsilon'' = 2n\kappa = \chi''. \quad (\text{A-23})$$

Now if we return to our solution to the classical oscillating dipole model we find that the dipole moment for an individual oscillator is:

$$p(t) = -ex(t). \quad (\text{A-24})$$

The material's macroscopic polarization is:

$$P(t) = Mp(t) = -Mex(t) \quad (\text{A-25})$$

where M is the number of oscillators per unit volume. Analogously, we can equate the electric field polarization with the classical macroscopic polarization, giving:

$$-Mex(t) = \epsilon_o \tilde{\chi} E_o e^{j\omega t} \quad (\text{A-26})$$

Using Equation (B-17), we can now write the electric susceptibility as:

$$\tilde{\chi} = \frac{\left(\frac{Me^2}{m\epsilon_o} \right)}{\left(\omega_o^2 - \omega^2 \right) + j\omega\gamma} = \frac{\omega_p^2}{\left(\omega_o^2 - \omega^2 \right) + j\omega\gamma} \quad (\text{A-27})$$

where ω_p is the plasma frequency of the medium, the significance of which will be described shortly.

What we really want to know though is how the complex index of refraction behaves near resonance. One can show that for frequencies close to the resonant frequency ω_o , i.e., for $|\omega_o - \omega| \ll \omega_o$, we can write:

$$n(\omega) \approx 1 + \frac{1}{2}\chi' \approx 1 + \frac{\left[\frac{\omega_p^2 (\omega_o - \omega)}{4\omega_o} \right]}{(\omega_o - \omega)^2 + \left(\frac{\gamma}{2} \right)^2} \quad (\text{A-28})$$

$$\kappa(\omega) \approx \frac{1}{2}\chi'' \approx \frac{\left[\frac{\omega_p^2 \gamma}{8\omega_o} \right]}{(\omega_o - \omega)^2 + \left(\frac{\gamma}{2} \right)^2} \quad (\text{A-29})$$

where $n(\omega)$ describes the dispersive characteristics of the medium near resonance and $\kappa(\omega)$ describes the absorptive characteristics near resonance. An illustration of these quantities can be found in Figure A-1. The two most important things to note here are the enormous increase in the absorptive term near resonance and the large rate of change of the real part of the index of refraction near resonance.

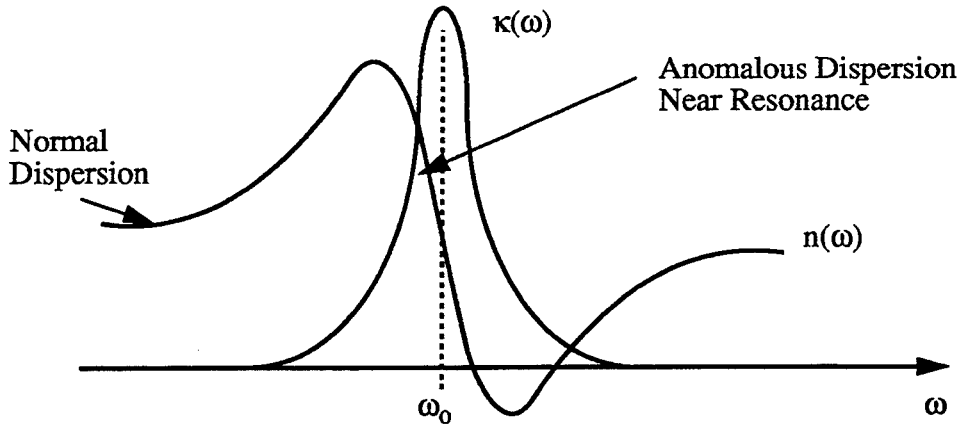


Figure A-1: The Lorentz Model of the Complex Index of Refraction at Resonance.

We have just derived a model which describes the behavior of the complex index of refraction near resonance. Almost all materials have more than one resonant frequency though. Many materials will have several fundamental resonances and each fundamental reso-

nance may be accompanied by a series of overtone resonances. We can write a relation for a material with M resonances (absorption bands) as:

$$\epsilon_r = N^2 = 1 + \omega_p^2 \sum_{i=1}^M \left(\frac{f_i}{(\omega_{oi}^2 - \omega^2) - j\omega\gamma_i} \right) \quad (\text{A-30})$$

where f_i is the oscillator strength of the i th transition resonance with $0 \leq f_i \leq 1$ and

$$\sum_{i=1}^M f_i = 1. \quad (\text{A-31})$$

Thus we now have a mathematical model, the Lorentz model, which can describe the optical properties of even highly complex multi-resonant materials. Unfortunately, this version of the Lorentz model works only for non-conducting dielectrics.

A.2.3 An Extension of the Lorentz Model for Metals

The original Lorentz model was derived for non-conducting dielectrics. In dielectrics the energy band gap between the valence band and the conduction band is large enough to restrict the vast majority of electrons to their atom-to-atom bonding sites. As an optical wave strikes the dielectric, the electrons will oscillate but are not free to roam the material.

Conducting metals are different in that they have essentially no energy band gap between the valence and conduction bands. Thus the electrons are free to roam the metal's crystal lattice. This accounts for the large conductivity of metals.

To extend the Lorentz model to conductors we will need to drop the restoring force term in the oscillator equation of motion, i.e., $\omega_o = 0$. This is done because the electrons are free and there is no restoring force constraining the electrons to their bonding sites. In addition, we also need to define a relaxation time τ of the conducting metal as:

$$\tau = \frac{1}{\gamma}. \quad (\text{A-32})$$

The relaxation time describes how long the transient current induced by the electric field remains. Thus the relaxation time is related to the current density \hat{J} by:

$$\hat{J}(t) = \hat{J}_o e^{-\frac{t}{\tau}}. \quad (\text{A-33})$$

Typical relaxation times for metals are on the order of 10^{-13} seconds.

To convert the electric susceptibility for dielectrics to one for metals, all we need to do is set ω_o equal to zero and replace γ with $\frac{1}{\tau}$. This gives the electric susceptibility for metals as:

$$\tilde{\chi} = \frac{\omega_p^2}{-\omega^2 + j\frac{\omega}{\tau}} \quad (\text{A-34})$$

with the real and imaginary parts of the dielectric constant as:

$$\epsilon'(\omega) = n^2(\omega) - \kappa^2(\omega) = 1 - \frac{\omega_p^2 \tau^2}{1 + \omega^2 \tau^2} \quad (\text{A-35})$$

and

$$\epsilon''(\omega) = 2n(\omega)\kappa(\omega) = \frac{\frac{\omega_p^2 \tau}{\omega}}{1 + \omega^2 \tau^2} \quad (\text{A-36})$$

We can now see the significance of the plasma frequency ω_p . At the plasma frequency, i.e. at $\omega = \omega_p$, the real part of the dielectric constant for metals is nearly zero and this means that the dispersive and absorptive terms of the index of refraction are equal ($n(\omega) = \kappa(\omega)$). For frequencies above ω_p the metal becomes transparent because the frequency is too high for the metal to respond to it and therefore there is no resonance. For frequencies below the plasma frequency (longer wavelengths), the real part of the dielectric constant becomes very small and the absorptive term κ dominates over n . In this regime metals are highly attenuating, i.e., the transmittance is zero, and as a consequence they are also highly reflecting. The frequencies of interest to us are all below the plasma frequency. So for our purposes metals are always highly absorptive and highly reflective.

A.2.4 Resonant Absorptions

The absorption features of solids and liquids in the 0.4-14.0 μm wavelength range are all due to electronic and/or vibrational energy transitions at resonant frequencies. Rotational energy transitions do not play an important part until the millimeter wavelength and microwave frequency regimes. Spectral absorption features in the wavelength range of 0.4-2.5 μm are due to electronic energy transitions. At longer wavelengths the photon energies are too low to excite electronic transitions so vibrational transitions dominate the 2.5-14.0 μm absorption features. There is some overlap however and in particular many overtones and combinations of strong fundamental vibrational resonances occur below 2.5 μm . We will mainly concentrate on the causes and types of vibrational absorption resonances since we are primarily interested in spectral features above 2.5 μm .

The vibrational molecular bonds within a material can couple with an incident optical wave if the following two conditions are met: 1) the vibrations of the molecule must produce

an oscillating net dipole moment so there can be an electrical interaction between the molecule and the field, and 2) the frequency of vibration of the molecule must match that of the optical wave. Homonuclear diatomic molecules, like H_2 , N_2 , and O_2 can not meet the first requirement since they all have a zero dipole moment for any bond length. For this reason this type of diatomic molecule can never interact with an optical wave to create spectral absorption features. Condition two is not usually met at a broad continuum of wavelengths due to the quantum nature of the vibrational energy transitions. The successful coupling of the molecular vibrations and the optical wave results in a dramatic attenuation of the wave. A large portion of the optical wave's energy is transferred directly to the molecule in the form of heat or subsequent re-emission.

The molecular complexity of materials plays a very large part in the number of absorption features seen. Simple pure, elemental materials, like intrinsic silicon, tend to exhibit a single, but very strong, fundamental vibrational resonance. The perfect homogeneous nature of the atom-to-atom bonds limits the material to a single fundamental resonance. This fundamental resonance may however have overtones which provide additional, but weaker, absorption features. The introduction of impurities or imperfections in the crystal lattice changes the nature of bonds within the material and allows for more fundamental resonances with subsequent overtone and combinational resonances. Complex giant molecular materials, like polymers, can possess dozens of fundamental, overtone, and combinational resonances due to the large diversity of bond types within the material.

A.2.5 Atmospheric Absorption Bands

Care must be used when trying to uncover the cause of spectral features in remotely sensed radiance data. The intervening atmosphere will impart its own spectral signature which is independent of the desired target surface properties. The atmospheric absorption bands are well known and Figure A-2 provides plots showing the absorption band locations and the molecules causing them.

For the wavelength range of 2.5-14.0 μm , water has important absorption bands at 3 μm and 5-8 μm . In the 3 to 5 μm atmospheric transmission window there are spectral absorption features due to CO_2 , O_3 , N_2O , CH_4 , and CO . In the 8.0 to 14 μm atmospheric transmission window there are spectral absorption features due to CO_2 and a larger feature due to O_3 . The presence of these absorption features should always be kept in mind when dealing with remotely sensed data.

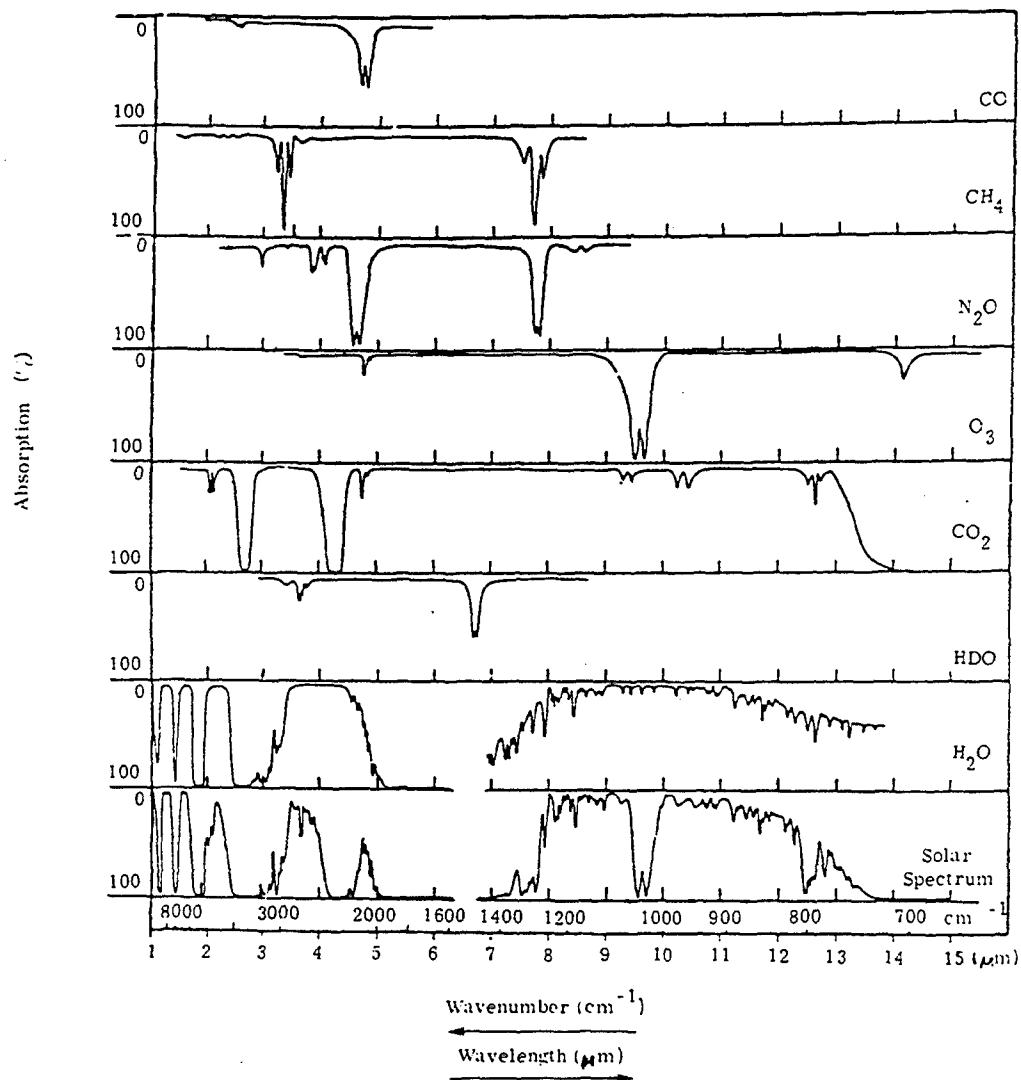


Figure A-2: The Atmospheric Absorption Spectral of Several Molecular Species [A.18].

A.3 Homogeneous Solids and Liquids

A.3.1 Crystalline Materials

Essentially all metals, a major fraction of ceramic materials, and certain polymers possess a crystalline atomic structure when in solid form. A crystal is any material possessing a basic atomic structure, called a crystal unit cell, which is exactly replicated in 3-dimensional space. Crystals are thus highly periodic and exhibit long range order.

The fundamental unit cell structure takes on different geometries depending on the material type. The interconnected sum of many unit cell structures builds up what is called the crystal lattice. It is the crystal lattice geometry and the internal atomic bonds which determines the strength, and spectral wavelength location, of resonant absorption features in crystals.

Resonant absorptions can be very strong in crystalline materials. This is because of the highly periodic and uniform nature of pure crystalline materials. A resonant absorption which can occur because of atom to atom bonds in any single unit cell will also occur in all other unit cells. Thus the whole crystal, not just an isolated portion, experiences the same electronic or vibrational transitions at resonant frequencies. The introduction of impurity atoms or defects in the crystal lattice will tend to reduce the strength of fundamental resonances, but also may introduce new resonant absorption features.

Crystalline solids possess two chief sources of absorption in the visible to infrared: 1) lattice vibrations, and 2) electronic transitions. For most materials there is a wide spectral window that exists between the limits of strong electronic absorption and strong vibrational absorption. In this window many pure solids are transparent.

There can however be residual absorption features in this transmissive window due to: 1) defects and impurities in the material, 2) multiphonon vibrational processes which induce overtones and combinations of the fundamental vibrational resonances, and 3) vibrational phonon assisted electronic transitions which occur close to the long wavelength side of the strong electronic absorption region.

In this section we will concentrate on the optical properties of some relatively simple materials. This will permit us to build an understanding which will aid in the later examination of more complex inhomogeneous materials.

A.3.1.1 Metals

Uncoated metals are of interest to us since they often constitute the basic structural material of targets. The lattice unit cell configurations for metals differ based on the type of metal. Aluminum for instance has a face centered cubic (FCC) unit cell arrangement and titanium has a hexagonal close-packed (HCP) structure. The unit cell geometry and density, and the atom to atom bond strengths, determine the spectral location of the metal's plasma frequency and absorption features. At wavelengths above the plasma wavelength, metals are highly absorptive and thus are also highly reflective. Below the plasma wavelength metals become transparent.

Figure A-3 displays the complex index of refraction of aluminum as a function of frequency [A.12]. There is an absorption feature at $0.8\ \mu\text{m}$ which leads to a pronounced drop in the reflectance of the crystalline aluminum. This feature is a strong interband transition due to the transition of electrons from a previously occupied conduction sub-band to another unoccupied conduction sub-band. Notice that at the infrared wavelengths the absorptive term is between 5 to 10 times as large as is the dispersive term. The high absorption of metals in gen-

eral makes them very opaque and highly reflective at the infrared wavelengths. The reflectance is solely due to first surface reflections because the transmittance is essentially zero.

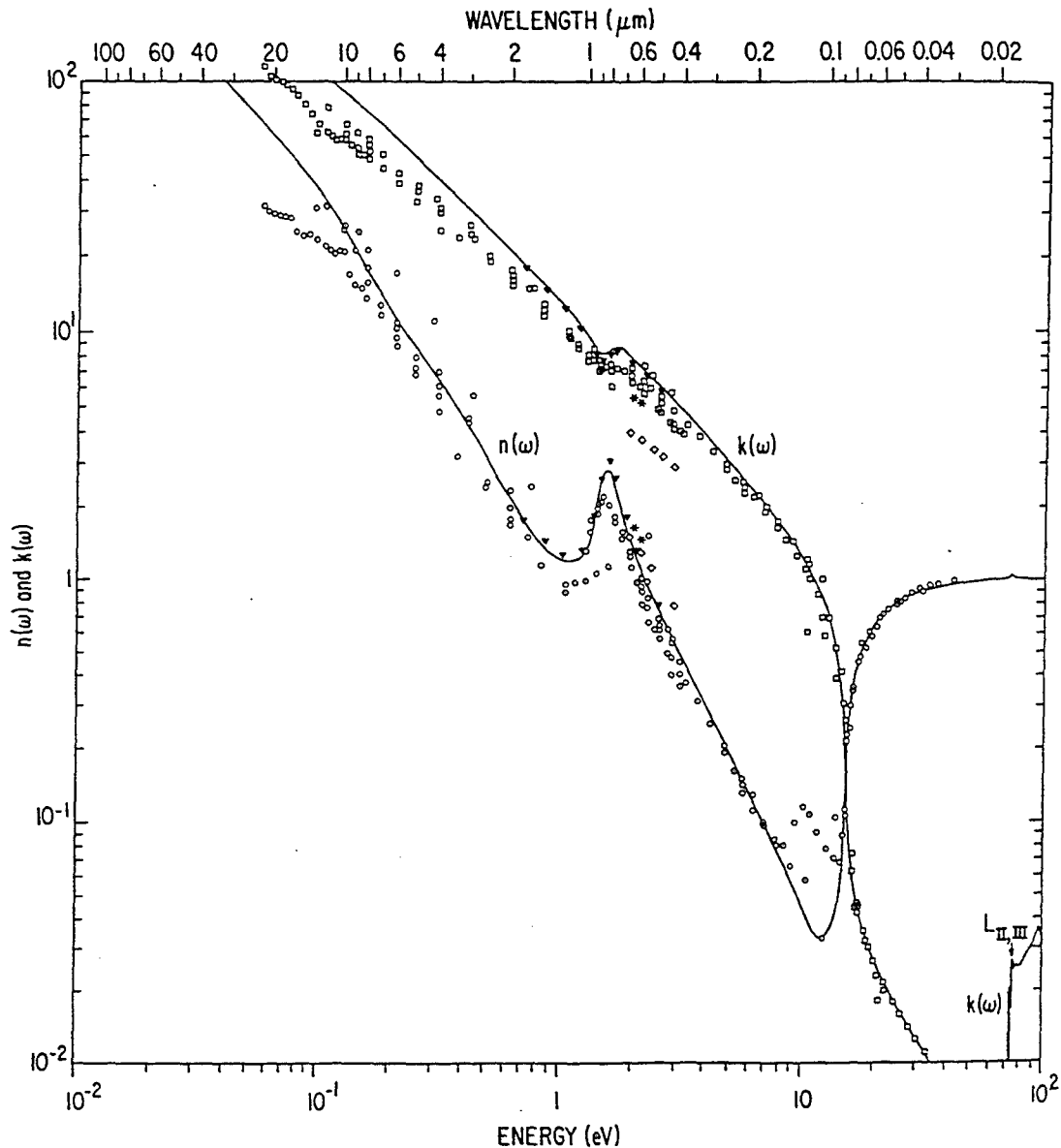


Figure A-3: The Complex Refraction Index of Crystalline Aluminum [A.12].

Figure A-4 provides directional hemispherical reflectance measurements of some metal samples. These measurements have been taken from the SAL database of spectral reflectances. The reflectance scale of this figure has been broken in order to display multiple materials with comparable reflectances on the same plot. The sample labeled 0014UUUALM is a piece of oxidized aluminum. Sample 0112UUUMTL is presumed to be a clean aluminum plate. And sample 0332UUUMTL is an unpolished block of gray metal of unknown type. In all three cases the absorption features seen at 3, 6, 7, and 9 μm are either due to surface con-

taminants, impurities in the metal lattice, or moisture. A surface oxide layer (Al_2O_3) is not expected to cause any of the features below $6\mu\text{m}$ since the oxide of aluminum is highly transparent from 0.18 to $6\mu\text{m}$ [A.12]. The strong features at $3\mu\text{m}$ and $6\mu\text{m}$ are presumably due to water absorption resonances from moisture trapped at the metal's surface. The overall lower reflectance of the unpolished gray metal block is due to a reduction in the first surface reflectance. The roughness of an unpolished surface leads to surface scattering and increased absorption by the metal.

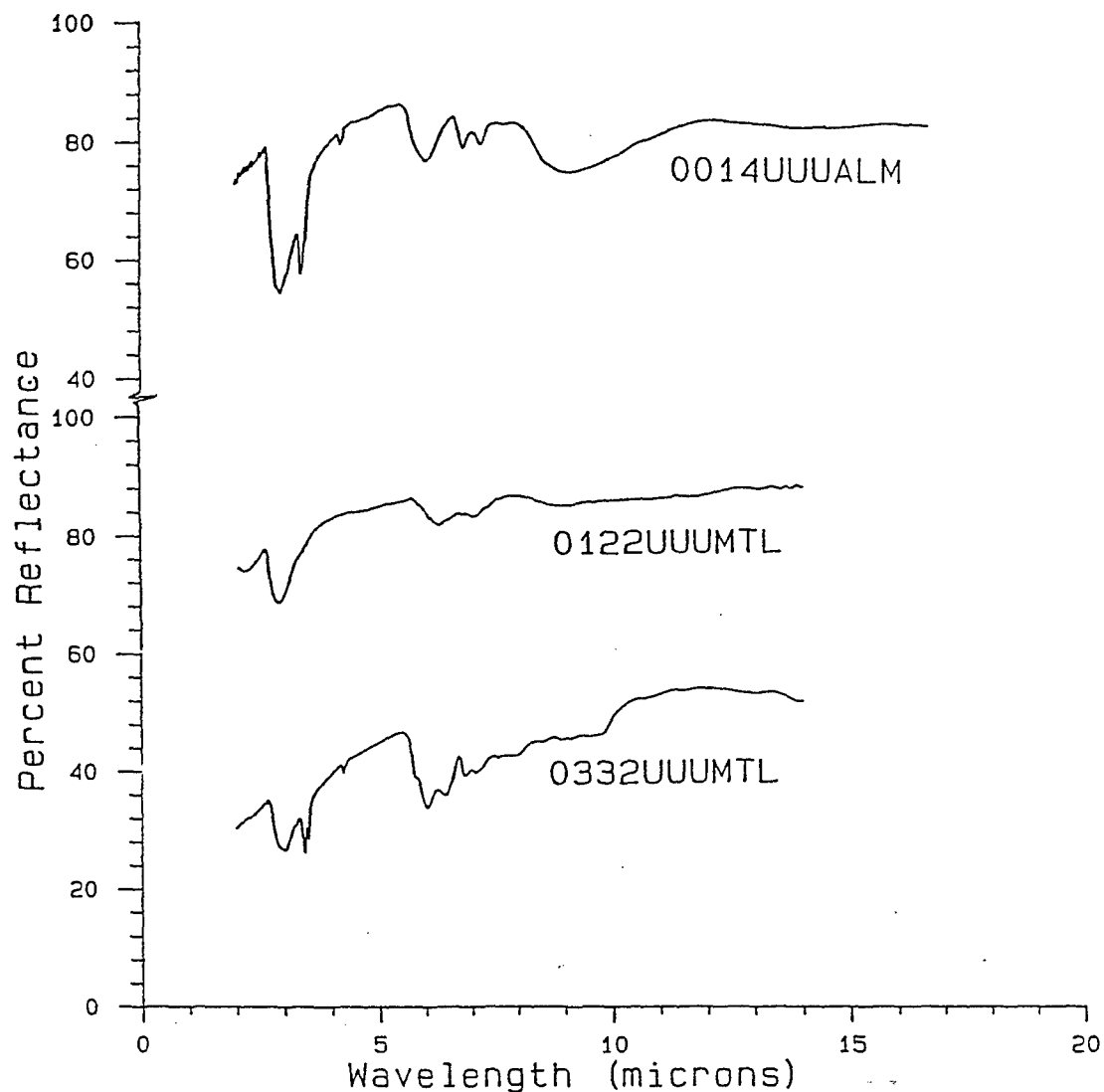


Figure A-4: The Hemispherical Spectral Reflectance of Three Metal Samples*.

Sample 0014UUUALM — oxidized aluminum

Sample 0122UUUMTL — a clean polished aluminum plate

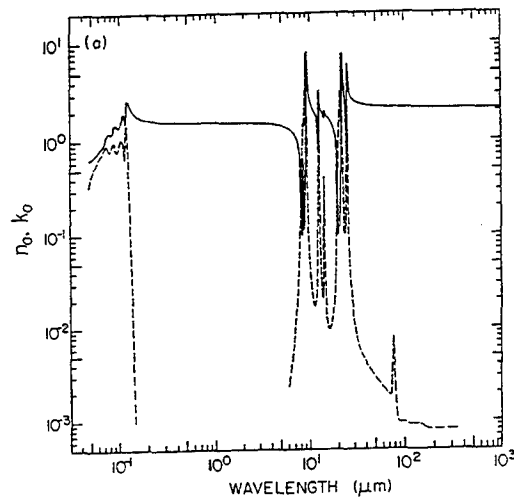
Sample 0332UUUMTL — an unpolished block of steel.

*[Taken from the SAL spectral database]

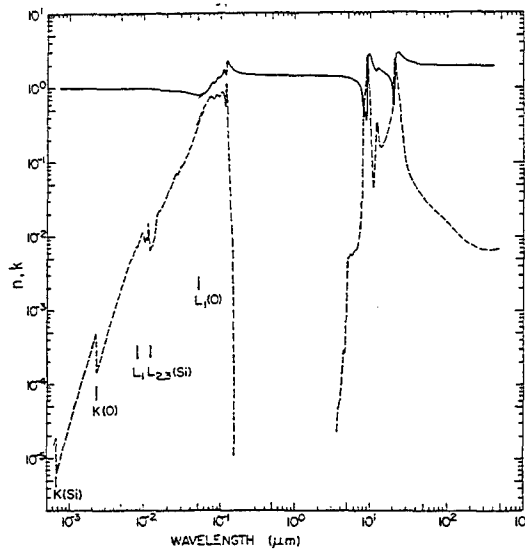
A.3.1.2 Ceramic Crystals

Ceramic crystals are of interest since many naturally occurring rocks and minerals contain large concentrations of ceramic crystals, like quartz (SiO_2) and other silicates. Also, there is interest in producing new paints with ground ceramic crystals, like gallium arsenide (GaAs), as solutes with which to tailor the paint's spectral properties in the infrared.

Figure A-5 shows the complex index of refraction for crystalline (type alpha) silicon dioxide (SiO_2) [A.12]. The very strong absorption at about $9\text{ }\mu\text{m}$ is due to the asymmetric stretches of O-Si-O and Si-O-Si bonds within the SiO_2 crystal lattice. The somewhat weaker absorption band at about $13\text{ }\mu\text{m}$ is due to the symmetric stretches of the Si-O-Si bonds. Finally, there is a second symmetric Si-O-Si stretch at about $21\text{ }\mu\text{m}$.



a)



b)

Figure A-5: The Complex Index of Refraction of SiO_2 . a) Type alpha crystalline silicon dioxide (SiO_2) and b) Amorphous silicon dioxide (SiO_2) (Glass) [A.12].

All of these spectral features will result in large first surface reflections and a peak in the spectral reflectance at resonance. This is because at each resonance the absorption increases as much as three orders of magnitude making the SiO_2 material opaque. The bulk reflectance term is zero because of this total loss of transmittance. At the same time the dispersive part of the refractive index is undergoing a very dramatic change itself, creating a large index mismatch between the crystal and air. This mismatch, coupled with high absorption, leads to a large increase in the first surface reflectance. This reflectance feature is often called the reststrahlen band.

Many ceramic crystals can also be found in an amorphous glass state. Glasses are non-crystalline because they lack the repetitive structure and long range order of crystals. Commercial glasses are commonly silicates (SiO_4).

The glass form of many materials is interesting because it has different spectral qualities than its crystalline counterpart. Figure A-5 also shows the complex index of refraction for amorphous quartz (SiO_2) [A.12]. Amorphous glasses have their absorption features centered at the same wavelengths as their crystalline cousins. However, the peak absorption in amorphous form is typically more than an order of magnitude less than the crystal's. On the other hand, glasses have much broader absorption spectra than do crystals. Figure A-6 shows the absorption coefficient for both crystalline and amorphous SiC. It is interesting to note that the total area under the absorption spectra for amorphous and crystalline materials are almost the same [Palik, 1985]. The reason for absorption band widening is because in the less ordered amorphous state of glass the selection rules for the allowed quantum transitions are relaxed.

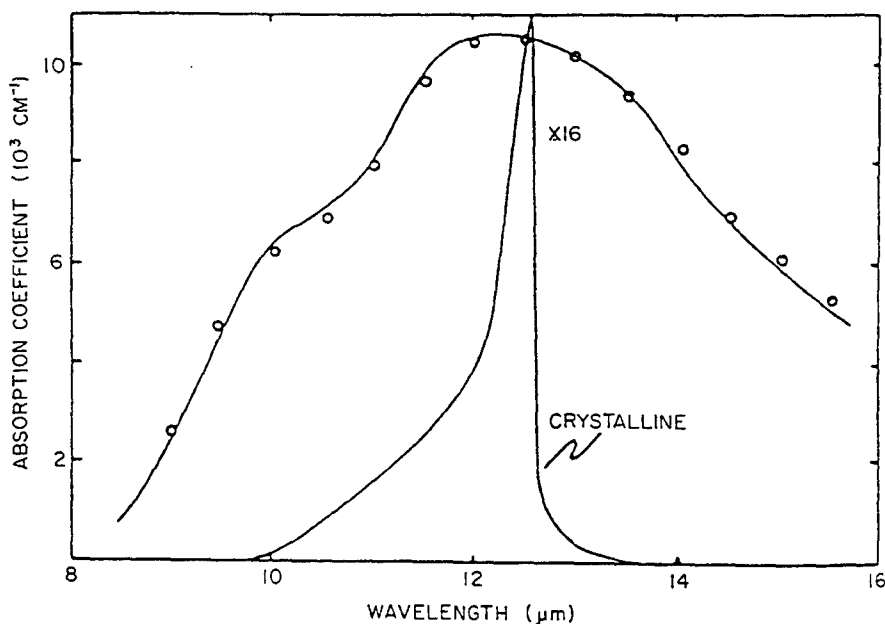


Figure A-6: The Weakening and Broadening of an Absorption Resonance in Amorphous SiC [A.12].

The introduction of defects and impurities into the crystal lattice strains the lattice and affects the absorption spectra. The introduction of defects and impurities creates new atom to atom bonds, new lattice vibrational resonances, and thus completely new absorption features. Defects and impurities also weaken and broaden previously existing fundamental resonances due to another relaxation in the transition selection rules.

A.3.2 Liquid Water

Water is a major component of any plant. Typical green leaves are between 50% and 75% water by weight [A.4]. Even dry woody plant material is usually 5% to 10% water by weight. Thus, in order to understand the spectral properties of plants, it is imperative to understand the spectral properties of water.

Water is extremely transmissive (non-absorptive) between 0.4 to 0.8 μm . Figure A-7 shows the absorption coefficient of pure water in the wavelength range 0.32-2.50 μm [A.18]. Absorption bands in liquid water are caused by transitions of vibrational states of water molecules in the thermal infrared. There are 3 fundamental vibrational resonances that occur in liquid water between 0.4 to 14.0 μm . The fundamental resonances occur because of vibrational stretches of the H-O-H molecular bonds. The fundamental resonance with lowest frequency occurs at 2.9 μm . The other two fundamental resonances occur at 3.11 and 6.08 μm and can be seen in the infrared hemispherical reflectance of water plotted in Figure A-8. The absorption bands near 1.88, 1.38, 1.14, and 0.94 μm are all overtones and combinations of these fundamental vibrational resonances [A.2]. These overtones and combinations have lower transition probabilities and therefore successively weaker absorption bands than the fundamental.

Water is essentially opaque to IR radiation longer than 2.5 μm . In fact, few liquids have absorption coefficients of the same order of magnitude. Consequently, a water layer as thin as 0.1mm is enough to completely absorb any radiation in the wavelength range of 3.0-14.0 μm . In this range, and for such a thin layer, there is no significant difference in the absorptive properties of pure distilled water and sea water [A.18]. Figures B-9 through B-11 show the transmittance, index of refraction, reflectance, and absorption coefficient all as functions of wavelength for sea water. Note the anomalous dispersion characteristics, predicted by the Lorentz model, in the index of refraction and reflectance curves.

The high absorption coefficient of water at the thermal infrared wavelengths means that even the thinnest layer of moisture on a material can dramatically alter the spectral reflectance or emissivity of that material. Figure A-11 suggests that an absorption coefficient of 300 cm^{-1} is a reasonable estimate for wavelengths above 3.0 μm . Using this absorption coefficient we find that a very thin moisture layer of 10 μm provides a one way transmittance of 74% and a two way transmittance of 55%. Thus a 10 μm thick moisture layer is enough to reduce the measured reflectance of the material by a factor of two. In addition, the spectral properties of the moisture covered material would be altered by the spectral properties of water. A 100 μm thick layer is enough to reduce the measured reflectance by a factor of 400. Actually the pres-

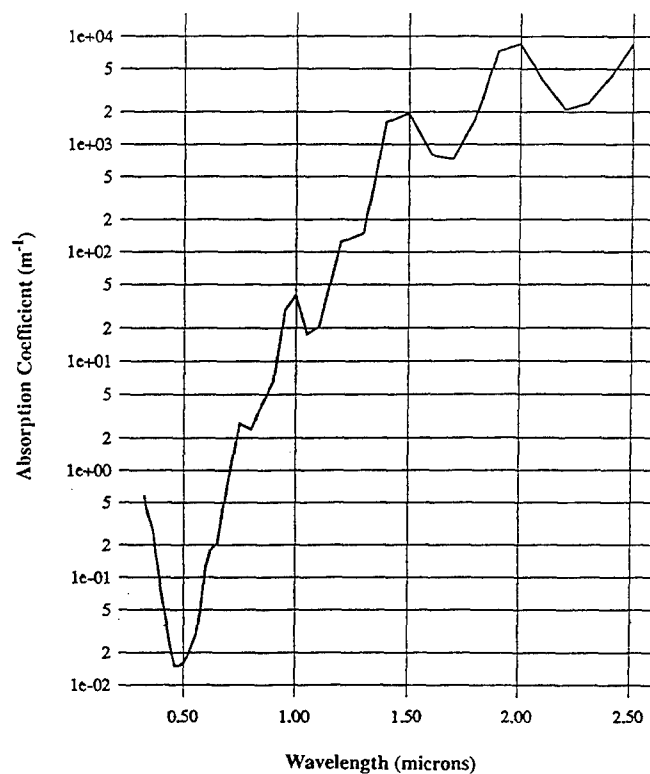


Figure A-7: The Absorption Coefficient of Pure Water [A.18].

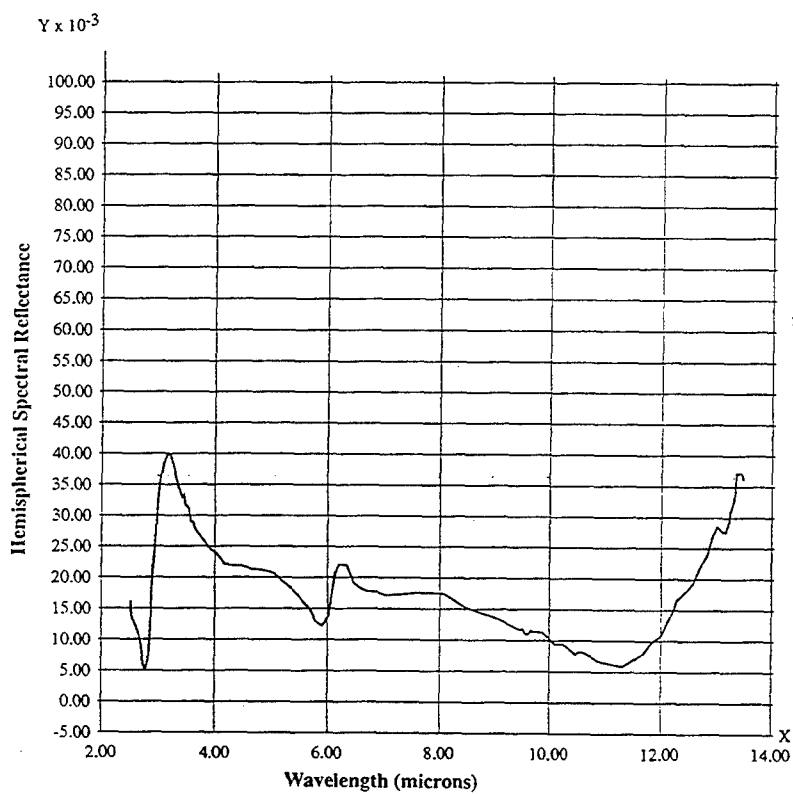


Figure A-8: Hemispherical Spectral Reflectance of Water [A.14].

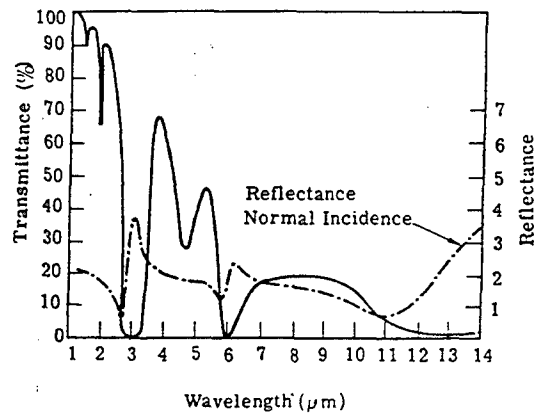


Figure A-9: Transmittance and Reflectance of 0.002 cm of Sea Water [A.18].

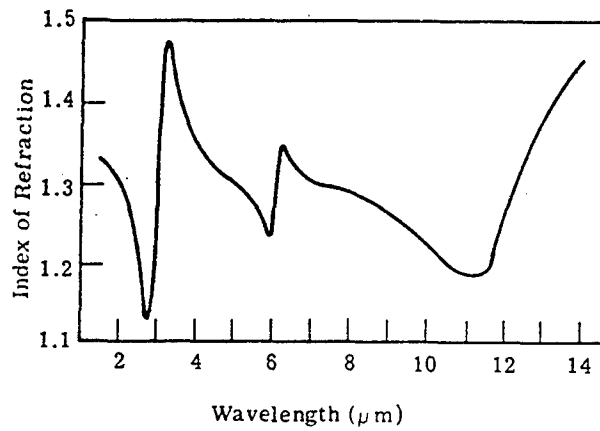


Figure A-10: The Index of Refraction of Sea Water Calculated from the Reflectivity Data of Figure A-9 [A.18].

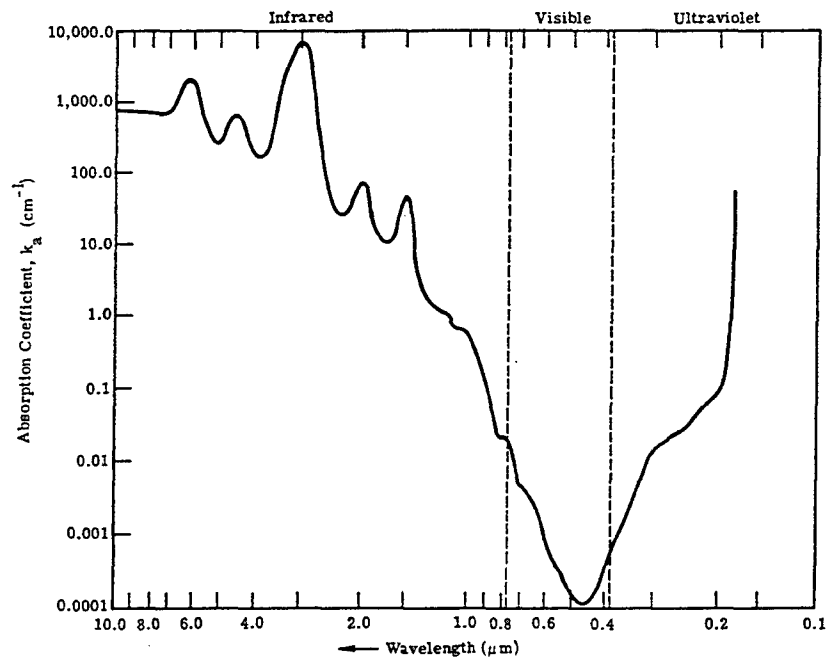


Figure A-11: The Absorption Coefficient of Sea Water [A.18].

ence of a 100 μm thick moisture layer means that we would be effectively measuring the surface reflectance of only the water. Fortunately low concentrations of water, like dew, tend to accumulate on natural materials in small droplets. In this case the measured reflectance would be a mixture of the opaque water and the exposed material surfaces.

In summary, we see that water is highly transparent (non-absorptive) in the visible and contains strong absorption bands due to fundamental resonances at 2.9, 3.11, and 6.08 μm . These resonances have overtones and combinations that create the weaker absorption bands at 0.94, 1.14, 1.38, and 1.88 μm . The absorption coefficient of water for wavelengths above 2.5 μm is so high that the water is essentially opaque and the directional hemispherical reflectance varies only between about 0.5% to 4.0%. No volume scattering occurs in water at wavelengths above 2.5 μm , even in the presence of heavy solutes, because of this extreme absorption.

A.4 Complex Inhomogeneous Solids and Liquids

A.4.1 Minerals

Minerals are by far the best understood materials for the physical basis of their absorption characteristics in the thermal infrared. For a quarter century, scientists have understood the usefulness of remote sensing for the location and classification of minerals.

The absorptive characteristics of minerals are due again to electronic and vibrational resonant transitions. The electronic transitions occur purely below 2.5 μm . Electronic transitions can potentially provide information useful in detecting the presence and nature of particular ions and in detecting defects in specific crystal lattice locations. Unfortunately, the interatomic bonds of the most common constituents in rocks and minerals, Si, Al, and O, do not contribute to electronic absorption features. Most features in this wavelength range are due to the hydroxyl ion and carbonates. The hydroxyl ion provides absorption bands at 1.4 and 2.77 μm , with additional bands at 2.2 μm , when combined with aluminum, and 2.3 μm when combined with magnesium. The carbonates produce multiple absorption bands at 1.9, 2.0, 2.16, 2.35, and 2.55 μm . There is an additional lattice overtone feature at 1.6 μm due to the bond stretching of layered silicates like clay and micas. Figure A-12 summarizes the location and cause of absorption features seen in this wavelength region.

The spectral features of minerals in the mid-infrared (2.5-5.0 μm) is less understood. This is because technology has found it more difficult to provide sufficient SNR in this spectral region and signature analysis is complicated by the additional solar reflected radiation. Thus this wavelength region has received less attention.

In the mid-infrared (2.5-5.0 μm) most minerals are significantly transmissive. This means that a bulk reflectance component exists and absorption features manifest themselves as reflectance minima. The spectral features present in this wavelength range are useful in the detection of carbonates, sulfates, and nitrates. Figure A-13 provides spectral reflectances for calcium carbonate, hydrous calcium sulfate, sodium nitrate, and silica sand [A.10]. Carbon-

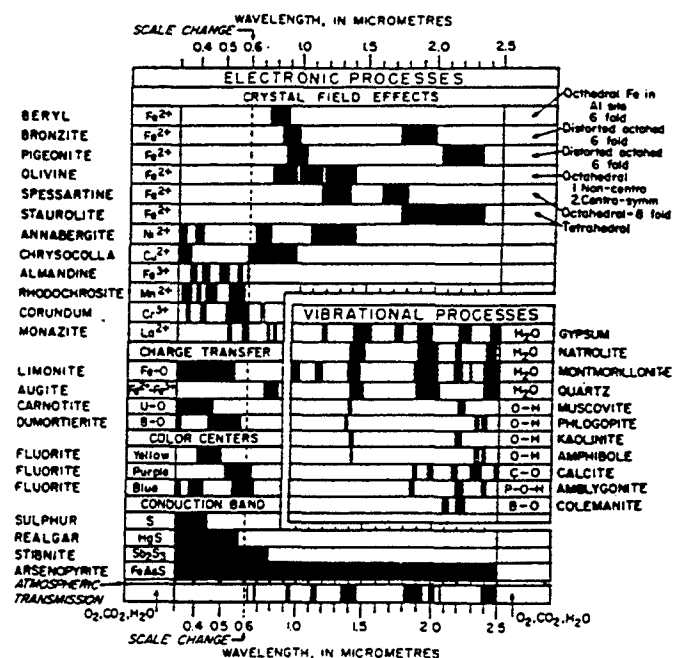
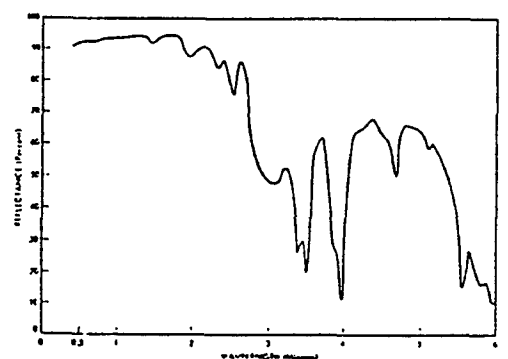
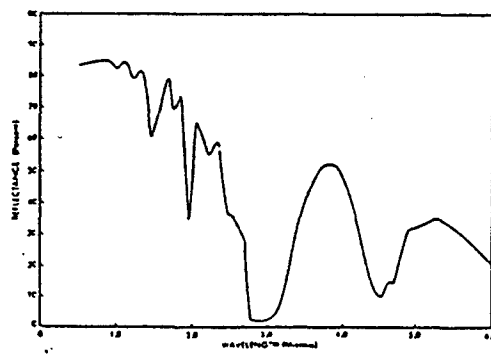


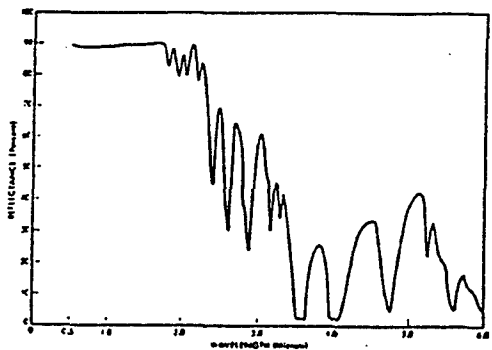
Figure A-12: The Location of Mineral Spectral Features From 0.4 to 2.5 μm [A.3].



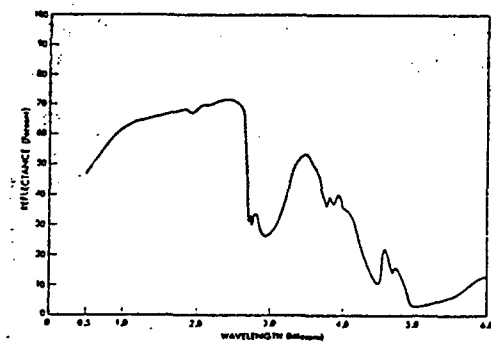
Spectral reflectance of calcium carbonate.



Spectral reflectance of hydrous calcium sulfate.



Spectral reflectance of sodium nitrate.



Spectral reflectance of silica sand.

Figure A-13: The Spectral Reflectance of Some Minerals From 0.5 to 6.0 μm [A.10].

ates display important absorption features at 3.5, 4.0, and 4.7 μm . The 3.5 and 4.0 μm features are thought to be overtones of a strong C-O fundamental stretch. Sulfates produce absorption

bands at 3.0 and 4.5 μm . The 3.0 μm absorption band of hydrous calcium sulfate is primarily water absorption. Nitrates are normally found in arid regions and possess absorption features near 3.6, 4.0, 4.8, 5.3, and 5.7 μm . Silica has a very prominent absorption feature near 4.7 μm which is probably an overtone to the well known reststrahlen absorption at about 9 μm . Even with these examples, most mineral spectral in this wavelength range are quite featureless [A.13].

The spectral features found in minerals at the longwave infrared (8-14 μm) are some of the most dramatic known. Spectral features in this wavelength region are the result of vibrational (bending & stretching) molecular motions, with the most intense spectral features resulting from the excitation of fundamental resonant modes.

Silicates are the most abundant of the fundamental building blocks that form rocks. The nature of the Si-O bonds in silicate minerals causes the fundamental vibrational absorption resonances, called the reststrahlen bands, that dominate the spectral features of geologic materials past 8.0 μm . Actually the reststrahlen band is an overlap of multiple allowed asymmetric O-Si-O, Si-O-Si, and $\text{O}^-\text{Si-O}^-$ stretches and symmetric $\text{O}^-\text{Si-O}^-$ stretches. At the reststrahlen resonances the absorption is so high that the silicates become opaque and the reflectance is purely first surface. For this reason the reststrahlen resonances are seen as reflectance peaks and emissivity minima.

Silicate minerals divide themselves into 6 categories base on their Si-O bonds between adjacent SiO_4 tetrahedra. The tectosilicate class experience bonding between all 4 oxygens in the tetrahedra. Examples of tectosilicates are quartz (SiO_2) and feldspars. The phyllosilicates share 3 oxygens between tetrahedra in a sheet structure with the mineral muscovite being an example. Inosilicates are seen as chains formed by the sharing of 2 or 3 oxygens between tetrahedra. Cylosilicates share 2 oxygens in a ring structure. Sorosilicates possess a double tetrahedra structure created by sharing one oxygen between tetrahedra. Finally olivine and garnets are examples of nesosilicates which are composed of isolated tetrahedra having no shared oxygen atoms. Figure A-14 shows examples of these various silicate structures with the effect they have on absorption band location and strength.

The reststrahlen band shifts its spectral location based on the percentage of silicate contained in the material. Figure A-15 shows the spectral emissivity of various minerals. The reststrahlen band emissivity minima (or reflectance maxima) moves from lower to longer wavelengths (approximately 9 to 10.5 μm) with decreasing silicate content. This can be a useful feature in the classification of mineral types.

Other features that can be seen at these wavelengths are the Christiansen peaks and an H-O-Al fundamental resonance which occurs near 11 μm . Figure A-16 summarizes all the sources of resonant absorptions from 8 to 14 μm and beyond.

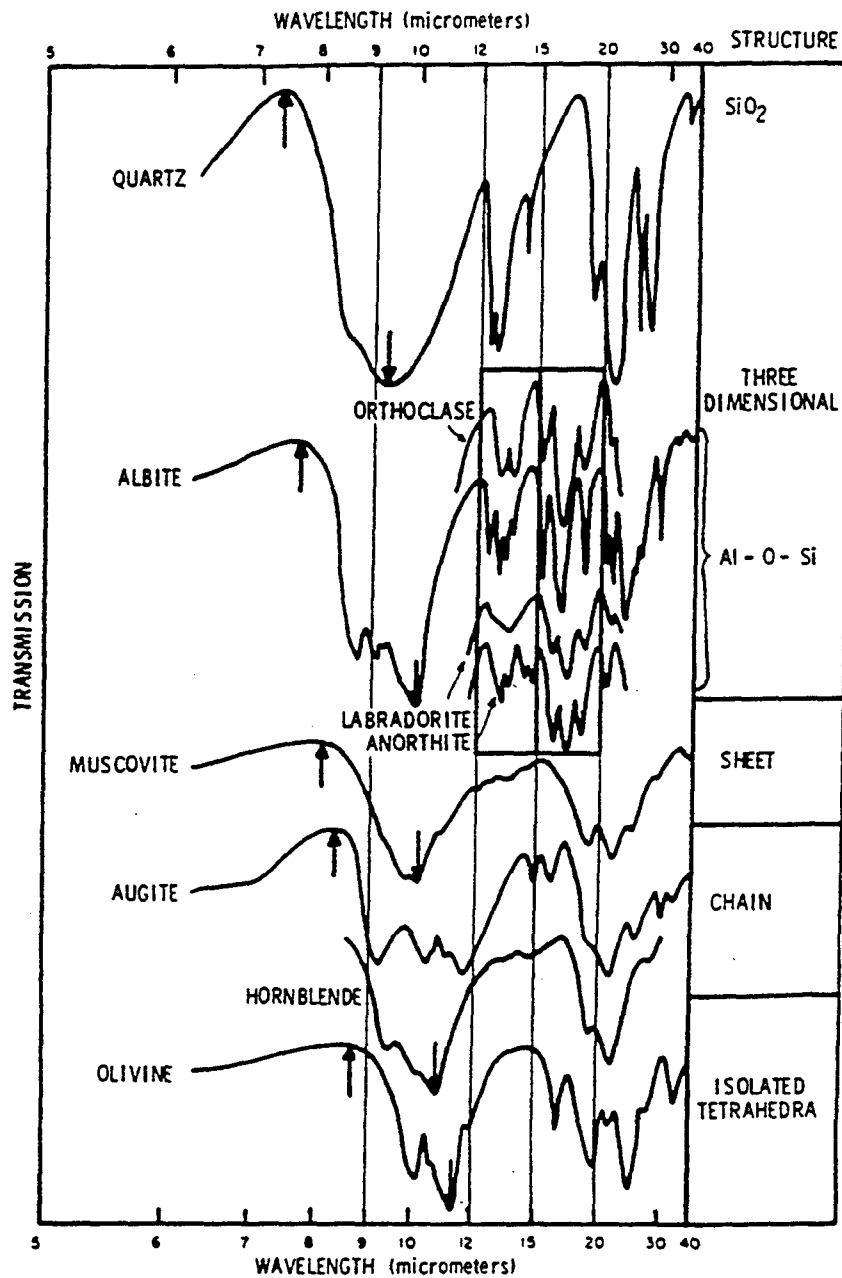


Figure A-14: The Transmission of Various Silicates Showing the Dependence of the Reststrahlen Band Location and Strength on Silicate Structure [A.16].

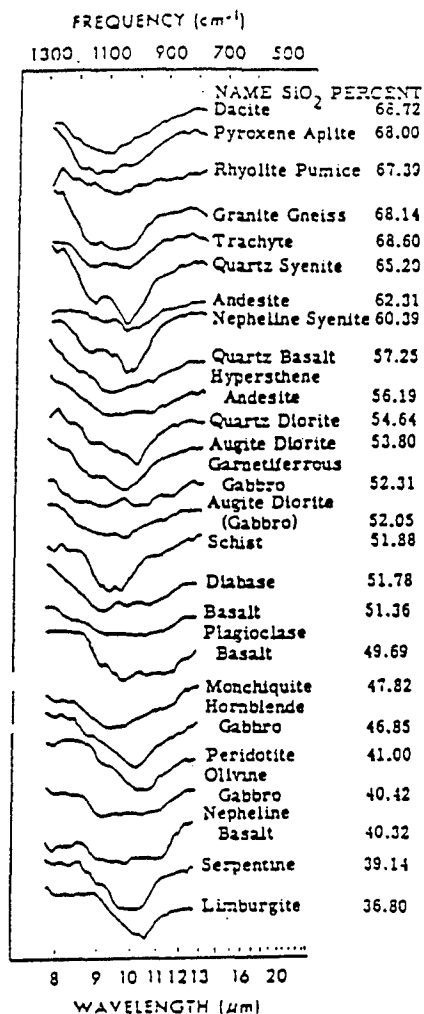


Figure A-15: The Spectral Emissivity of Minerals in the Vicinity of the SiO₂ Reststrahlen Band [A.18].

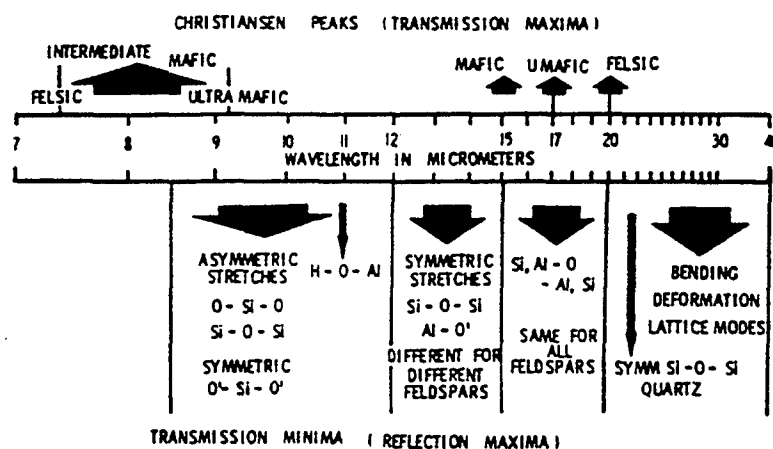


Figure A-16: Summary of Physical Reasons for Spectral Features in Minerals for Wavelengths above 7.0 μm [A.16].

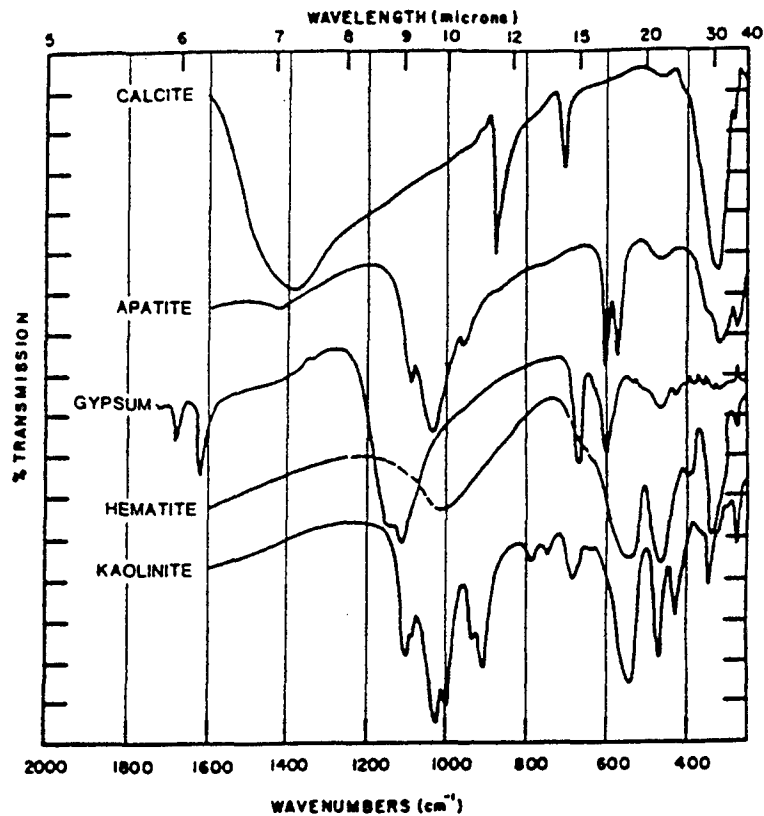


Figure A-17: Spectral Transmission for Some Common Nonsilicate Minerals [A.16].

The Christiansen peak is an increase in transmittance of the material due to a near equal match in the index of refraction for both the material and air. Its effect is made more pronounced by the fact that it occurs just before the strong reststrahlen absorption. Figure A-14 has up arrows pointing to the Christiansen peak transmissions.

Nonsilicate minerals also exhibit spectral features in the 8-14 μm . region, although these features are less dramatic than the reststrahlen silicate feature. Figure A-17 displays transmission spectra which show the absorption features of some nonsilicate minerals. As examples, calcite has 3 absorption features at 7, 11.5, and 14 μm which come from internal vibrations of the carbonate ion, and kaolinite has an H-O-Al bending resonance near 11 μm .

It should be noted that the atmosphere provides absorption bands at 4.3 μm (CO_2), 4.7 μm (N_2O), and 9.6 μm (O_3) which will interfere with the material's spectral features. This must always be remembered when working with remotely sensed reflected or emitted radiation.

A.4.2 Soils

It is important to understand the spectral properties of soils because they are a major component of any natural background. This section will discuss the physical basis for spectral

features of soils in the thermal infrared. Much of the spectral analysis and all of the soil examples and accompanying mineral analyses have been extracted from the SAL spectral database.

Loams are soils consisting of varying proportions of clay, silt, and sand. Clay is composed mainly of fine particles of hydrous aluminum silicates and other minerals. Silt, which is sediment from rivers and lakes, is composed of very fine grain minerals and is usually rich in organic materials. Sand is usually primarily quartz, however some sand, like the sand found at White Sands, New Mexico, is almost pure gypsum.

Many different soils share common spectral features from common constituents like water, hydrocarbons, carbonates, and silicates. The strength of these features depends on the varying concentration of each constituent. Most spectral absorption features in the 3 to 5 μm wavelength region show up as reflectance minima due to the presence of a large bulk reflectance component in most soils. Absorption features in the 8 to 14 μm wavelength region usually show up as reststrahlen reflectance maxima due to the lack of bulk reflectance in most soils.

One common feature seen in all soil types is the strong water absorption band at 3 μm . In addition many soils contain varying amounts of hydrocarbons from organic materials. Hydrocarbons contribute absorption features at 3.42 and 3.5 μm due to the stretching of the C-H molecular bonds. The presence of minerals like kaolinite, muscovite, and smectite lead to distinguishable hydroxyl features near 2.71 and 2.76 μm . Calcite contributes to various absorption features at 3.36, 3.47, 3.98, 4.68, and 5.57 μm . Finally, the silicate quartz, which is found in almost all sand bearing soils, produces various spectral features from 4 to 14 μm . Combination and overtone features of the strong fundamental quartz reststrahlen bands located from 8 to 12 μm show up as numerous reflectance minima features from 4.5 to 6.0 μm . The strong reststrahlen features themselves show up as a doublet at 8.3 and 9.0 μm , often seen primarily by the dip between peaks, and a doublet located at about 12.6 μm which has been called the alpha quartz doublet.

Table A-1 provides the loamic composition of several soil samples for which hemispherical spectral reflectances exist in the SAL spectral database. These samples were selected to display the diversity of spectral features of soils in the SAL database.

Table A-1: The Loamic Composition of Selected Soils from the SAL Spectral Database

Database ID	Sample Location	Percentage of			Soil Description
		Clay	Silt	Sand	
0146UUUSOL	Smith Co, TX	2.3	19.9	77.8	Brown sandy loam
0227UUUSOL	Yancey Co, NC	9.9	14.2	75.9	Brown sandy loam
0138UUUSOL	Klickitat Co, WA	2.7	29	68.3	Brown gravelly fine sandy loam
0127UUUSOL	Kenai-Cook Inlet, AK	NA	NA	NA	Organic rich reddish silty loam
0213UUUSOL	Nez Perce Co, ID	30.3	63.4	6.3	Grayish brown silty loam
0148UUUSOL	Dona Ana Co, NM	18.4	71.9	9.7	Reddish tan silty loam
0226UUUSOL	Howard Co, MD	25.7	30.7	43.6	Dark brown micaceous loam
0429UUUSOL	NA	NA	NA	NA	Light brown indurated clay soil
0149UUUSOL	White Sands, NM	0	0	100	White gypsum sand

Figure A-18 shows the hemispherical thermal reflectance of some sandy loam soils. Sample 0146UUUSOL is a light brown sandy loam taken from Smith County, Texas. The silt and sand mineralogy for this sample was measured as 94% quartz, 4% aggregate (gravels), and 2% K-feldspar. The high silicate content produces a very strong quartz reststrahlen doublet at 8.3 and 9.0 μm , a strong alpha quartz doublet at 12.6 μm , and various reststrahlen overtones and combinations from 4.5 to 6.0 μm . The silicate features seen in this sample are among the strongest spectral features seen in any material in the thermal infrared. In addition, the C-H bond stretching of hydrocarbons contributes to minor features seen at 3.42 and 3.5 μm . There is a strong 2.76 μm hydroxyl band that probably indicates the presence of muscovite or kaolinite in the aggregate.

Sample 0227UUUSOL is also shown in Figure A-18. This sample is a brown sandy loam taken from Yancey County, North Carolina. The clay mineralogy was determined to be mica, vermiculite, kaolinite, and goethite. The silt and sand mineralogy was determined to be 50% quartz, 24% muscovite, 17% biotite, and 7% other. The presence of muscovite accounts

for a hydroxyl band at 2.76 μm . Hydrocarbon C-H absorption features due to clay can be seen at 3.42 and 3.5 μm . The quartz features are significantly subdued compared to the previous sample 0146UUUSOL. This is because of its lower quartz content. A third reststrahlen feature is present below 10 μm . This feature is at 9.62 μm and is due to the mineral muscovite.

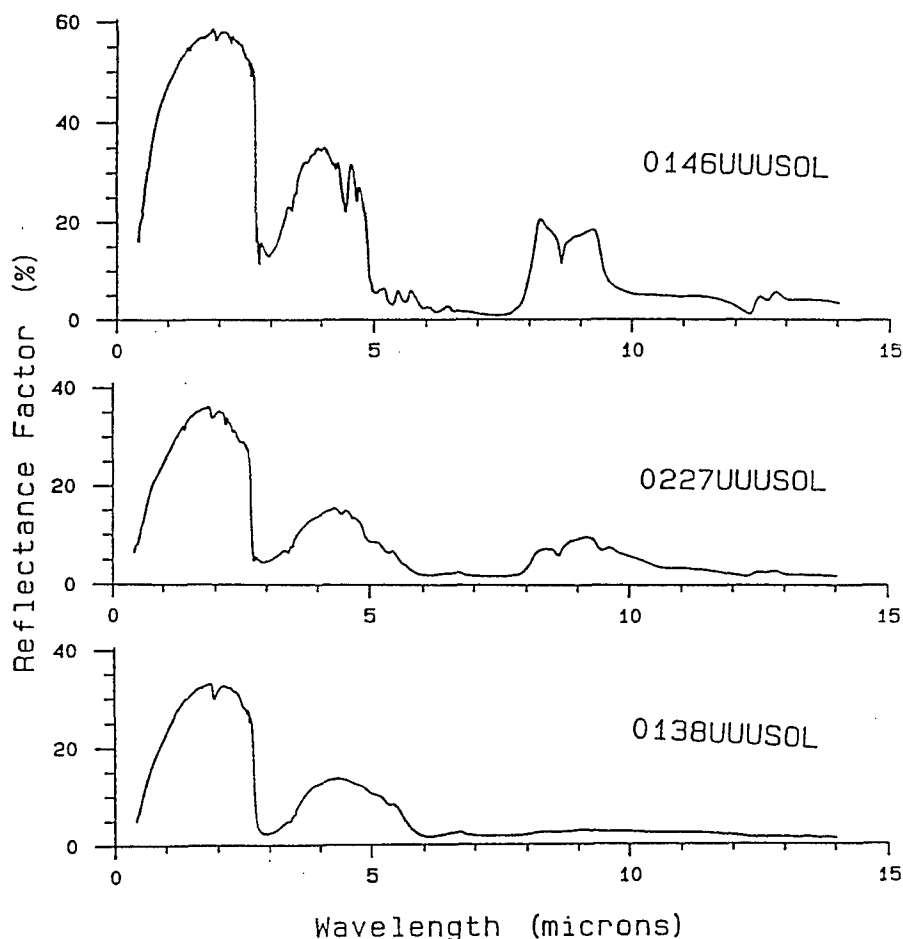


Figure A-18: The Hemispherical Spectral Reflectance of Some Brown Sandy Loam Soils.
[Taken from the SAL spectral database.]

Finally, Figure A-18 also shows a brown gravelly fine sandy loam soil titled sample 0138UUUSOL. This loam was collected in Klickitat County, Washington and has a measure silt and sand mineralogy of 40% weathered aggregates, 24% glass coated grains, 19% glass aggregate, 10% quartz, 7% plagioclase, and 1% tourmaline. The high amorphous glass content and the corresponding low crystal silicate content serve to almost completely erase all reststrahlen features beyond 5 μm . Only faint overtones and a very weak reststrahlen doublet at 8.3 and 9.0 μm can be seen. Organic matter in the silt contributes to the C-H bands seen at 3.4 and 3.5 μm . The low clay content is responsible for the missing hydroxyl band at 2.76 μm . In summary, Figure A-18 shows the great diversity in spectral content that can be seen even in a single class of soils such as sandy loams.

Figure A-19 shows the hemispherical reflectance of some silty loam soils. Sample 0127UUUSOL is a reddish brown organically rich silty loam taken from Alaska. Clay mineralogy measurements show the clay mineral content to be non-crystalline. The silt and sand mineralogy measurements show the silt and sand mineral content to be 87% glass and 13%

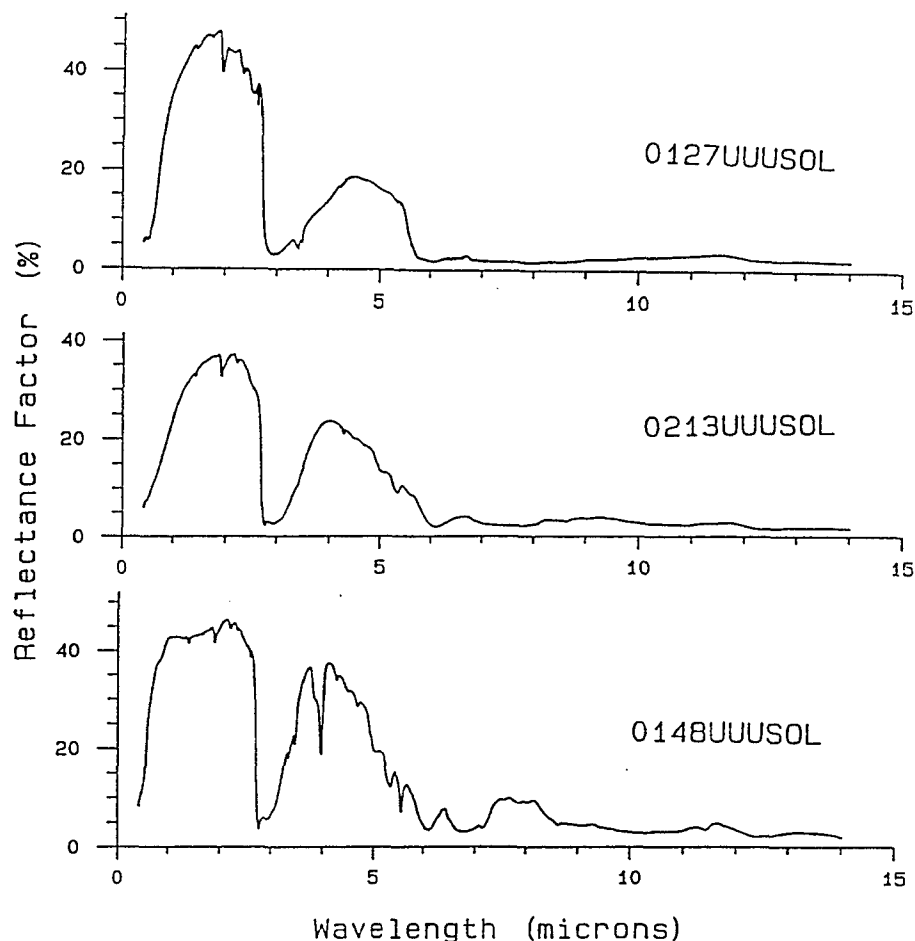


Figure A-19: The Hemispherical Spectral Reflectance of Some Silty Loam Soils.
[Taken from the SAL spectral database.]

quartz. The large organic content produces very strong hydrocarbon (C-H) features at 3.42 and 3.5 μm . The organic material is probably also contributing to a small but broad reflectance peak at 11.7 μm . This reflectance peak is most likely due to modest volume scattering within the organic material leading to a correspondingly modest bulk reflectance. There are no visible silicate reststrahlen features due to the high glass and low crystalline quartz content.

Sample 0213UUUSOL is a grayish brown silty loam collected at Nez Perce County, Idaho. The high clay content produces a hydroxyl feature at 2.76 μm typical of montmorillonite and kaolinite. The silt and sand mineralogy measurements show that 38% of the mineral content is quartz. This higher quartz content over the previous silt loam sample (0127UUU-

SOL) accounts for the increased reststrahlen doublet at 8.3 and 9.0 μm . The reemergent quartz combination and overtone absorption features from 4.5 to 6.0 μm leads to the changed shape of the long wavelength side of the 3.0 to 6.0 μm bulk reflectance hump from the previous sample. There are two small additional reststrahlen bands due to K-feldspar and muscovite centered at the wavelengths of 9.27 and 9.58 μm respectively.

Figure A-19 is concluded by sample 0148UUUSOL which is a reddish tan silty loam collected at Dona Ana County, New Mexico. Mineralogy measurements show a mineral composition of 20% kaolinite, 19.3% smectite, 19.8% calcite, 18.8% quartz, 15.2% mica, and 2.7% Fe-oxyhydrides. The kaolinite and smectite are believed to contribute to the 2.76 μm hydroxyl feature. The large concentration of calcite is responsible for the weak absorption bands at 3.35 and 3.48 μm and the very strong features at 3.98 and 5.56 μm . The distinctive 3.98 μm absorption feature is due to an asymmetrical stretching vibration in calcite. Quartz contributes to the various combination and overtone features seen from 4.5 to 5.5 μm and the weak reststrahlen doublet at 8.3 and 9.0 μm . This doublet has been severely altered by the large reflectance peak spanning 7.7 to 8.6 μm which is due to a combination of quartz, calcite, and Fe-oxyhydrides. Finally, a reflectance minima feature can be seen at 11.42 μm which is due to a fundamental bending vibration of carbonate. This feature is seen as a minima because it occurs in the midst of a small but broad bulk reflectance peak. In general, silty loams appear to possess less dramatic spectral features than do sandy loams in the 8 to 14 μm wavelength region.

In Figure A-20 we have three more soils that do not fit the general sandy or silty loam categories shown in Figures B-18 and B-19. Sample 0226UUUSOL is a brown micaceous loam collected at Howard County, Maryland. It has significant mineral content with the clay containing kaolinite, mica, vermiculite, and goethite. The silt and sand mineralogy measurements for this sample shows a break down in mineral content as 67% biotite, 17% muscovite, 10% quartz, 3% goethite, 2% K-feldspar, and 2% other. The kaolinite contributes to two strong hydroxyl features at 2.71 and 2.76 μm with muscovite adding a weak feature at 2.9 μm in the midst of the water absorption band. Other notable features include the quartz combination and overtone absorption features from 4.5 to 6.0 μm and the quartz reststrahlen doublet at 8.3 and 9.0 μm . Here the quartz doublet is overshadowed by two additional reststrahlen features due to muscovite at 9.28 and 9.58 μm . There is a reststrahlen feature due to biotite at 9.90 μm .

Sample 0429UUUSOL also shown in Figure A-20 is a brown indurated clay soil of unknown locational origin. The composition of this soil sample was not measured but some interesting features reveal possible mineral content. The very sharp and distinctive absorption feature at 4.0 μm indicates that this clay soil contains considerable calcium carbonate. Another calcium carbonate band overlaps the common hydrocarbon features at 3.5 μm . Hydrocarbon features in this sample indicate the presence of organic materials which are expected. Quartz, calcite, and mica are the minerals most likely contributing to the broad reflectance features between 7.3 to 8.5 μm and 9 to 10 μm .

Finally, one of the more interesting samples is the pure gypsum sand sample 0149UUUSOL also shown in Figure A-20. This sample was taken from White Sands, New Mexico and is typical of many soils found in the western US [A.10]. Gypsum is mainly calcium sulfate (CaSO_4) and the spectral reflectance of this sample looks much like the hydrous calcium sulfate shown in Figure A-13. One difference is that the gypsum sand exhibits much lower reflectance from 3 to 5 μm and this is probably due to the larger grain size of the gypsum sand. The very large reststrahlen reflectance peak at 8.9 μm is due to stretching vibrations

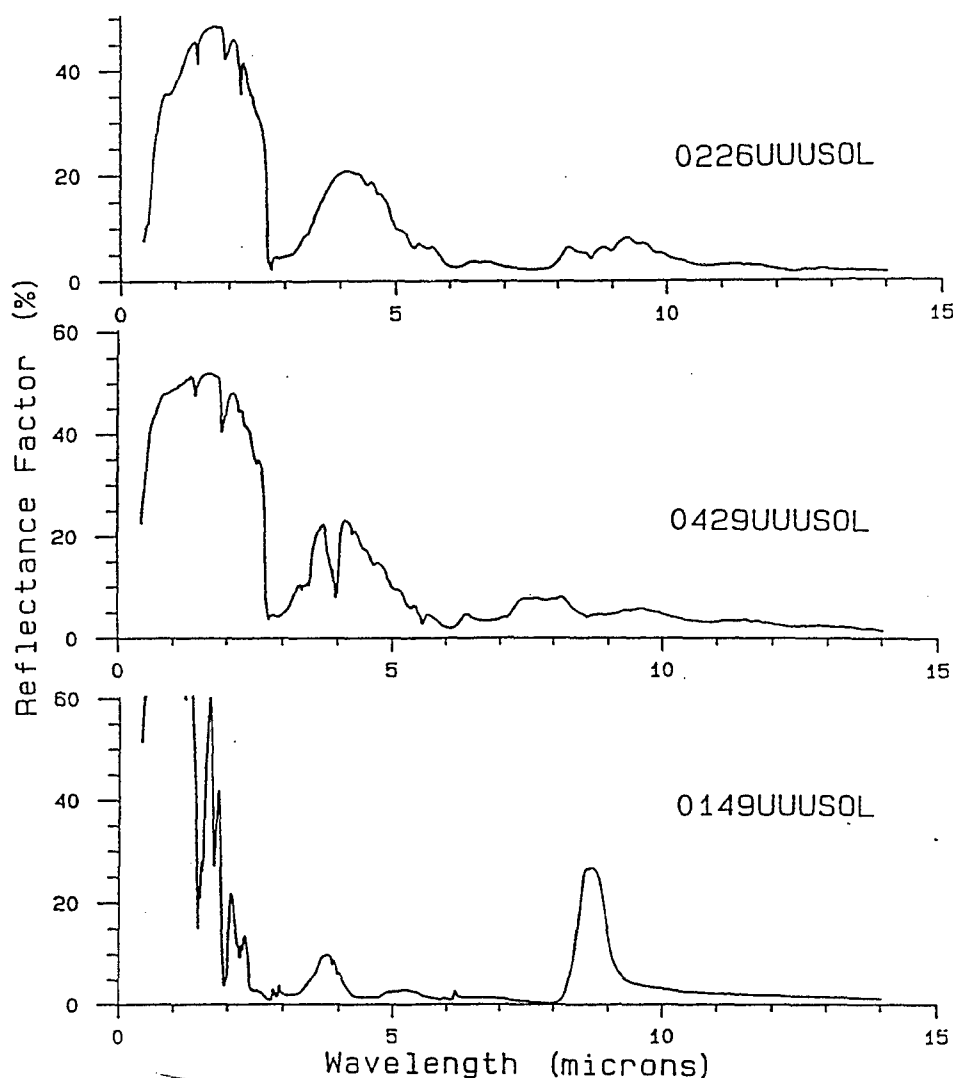


Figure A-20: The Hemispherical Spectral Reflectance of Various Soils.

Sample 0226UUUSOL — a micaceous loam

Sample 0429UUUSOL — an indurated clay soil

Sample 0149UUUSOL — gypsum sand

[Taken from the SAL spectral database].

of SO_4 . These vibrations also are the source of the doublet features at 2.8 and 2.9 μm in the midst of the water absorption band.

A.4.3 Road Materials

Road materials are of special interest because potential targets often times are found on or near them. Indirect target detection can sometimes be done through the direct detection of lines of communication and transportation. It is also important to be able to spectrally discriminate targets from roads.

Most road materials consist of gravel, concrete, or asphalt. Gravel and concrete possess spectral features much like minerals. Asphalt is generally featureless except when it is mixed with an aggregate like gravel and sand.

Concrete is a mixture of cement and aggregates like gravel (crushed rock) and sand. The cement is the main solvent in which the gravel and sand is suspended. The most common cement, Portland cement, includes raw materials like calcined clay, limestone, or their derivatives. Portland cement is actually a mixture of calcium silicates (Ca_3SiO_5 or Ca_2SiO_4) and calcium aluminate ($\text{Ca}_3\text{Al}_2\text{O}_6$) that hydrate in the presence of water.

Figure A-21 shows the hemispherical reflectance of three concrete examples. Sample 0399UUUCNC is a measurement of the weather exposed interior surface of a variegated concrete pillar. The pillar was cut across in order to expose embedded aggregate rock and sand. The spectral reflectance of this sample shows the prominent reststrahlen feature of the concrete's quartz content at 8.3 and 9.0 μm , and a doublet at 12.6 μm . There are weaker bands at 4.2, 6.7, and 11.5 μm which are due to the presence of limestone (calcite). The large falloff in reflectance from the near-infrared is caused by the strong water absorption band near 2.9 μm .

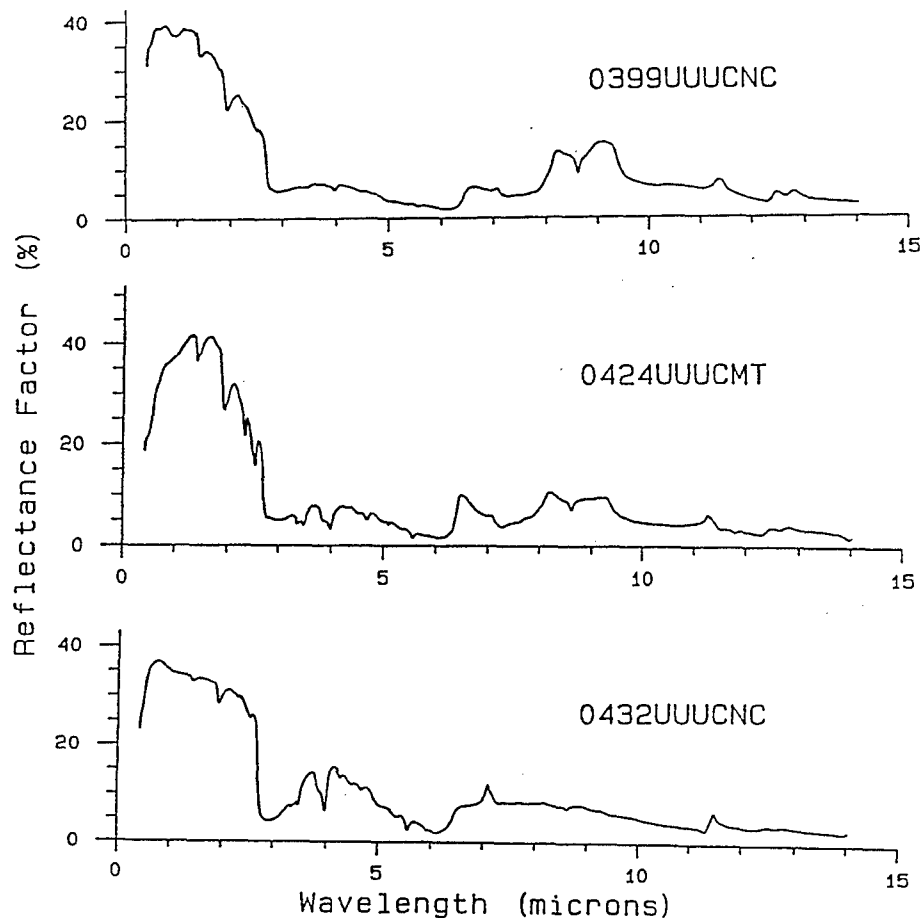


Figure A-21: The Hemispherical Spectral Reflectance of Some Concrete Samples.
 [Taken from the SAL spectral database.]

Sample 0424UUUCMT is a measurement of two large pieces of chunked concrete. This specimen has as much limestone (calcite) content in the aggregate as quartz. Because of this the overtone and combinational absorption bands of limestone dominate the spectrum out to 7.5 μm . These include calcite features at 2.6, 3.5, 4.2, 4.7, 5.2, 5.6, and 6.6 μm . These calcite features manifest themselves as reflectance minima due to the bulk reflectance of limestone. The limestone contributes a weaker reststrahlen band near 11.3 μm . The quartz content contributes large reststrahlen reflectance peaks at 8.3 and 9.0 μm with a weaker doublet between 12.5 and 13.0 μm . Quartz also contributes some combinational tone bands that overlap the limestone bands near 4.7 and 5.6 μm . The broad band near 2.9 μm is a water band from water trapped in inclusions of the quartz.

Sample 0432UUUCNC is a measurement of a concrete block fragment. This concrete sample is unusual in that it contains more limestone than quartz. This means that the calcite carbonate limestone dominates most of the spectral features up to about 6 μm . The limestone exhibits a bulk reflectance below 6 μm so the limestone features at 2.6, 3.5, 4.0, and 5.6 μm

all show up as reflectance minima. The limestone also provides weaker absorption bands which overlap with quartz absorption bands between 4.0 and 5.6 μm . The large reflectance peaks at 7.2 and 11.6 μm are due to the vibrational bond bends of limestone. Both of these reflectance peaks are unusual. The strong peak at 7.2 μm is usually seen as a broader reflectance peak from 6.3 to 6.6 μm and the reflectance peak at 11.6 has been shifted from about 11.3 μm due to unusual carbonate composition.

The quartz content again contributes broad reflectance peaks at 8.3 and 9.0 μm , but here they can only be separated by a slight dip between them. The quartz contributes some combination bands which overlap those of limestone near 4.7 and 5.6 μm in addition to a doublet between 12.5 and 13.0 μm . In all three concrete samples we see the dominance of the mineral features.

Asphalt is an oil by-product called a petroleum bitumen. Like tar, it is the residue that remains after distillation removes the gaseous and fluid fractions. Asphalt does not have a specific composition, but rather is a mixture of many naturally occurring linear polymers dominated by hydrocarbons.

Figure A-22 shows three asphalt samples from the SAL database. Sample 0099UUUTAR is black tar which has uniformly low reflectance across the spectrum. The tar has weak hydrocarbon bands (H-C stretching vibrations) at 3.5 and 5.5 to 8.0 μm . Sample 0416UUUASP is a reflectance measurement of a fresh black asphalt core. This sample contains aggregate material not contained in the pure tar sample. From the quartz content of the aggregate we can see the reststrahlen doublet between 8 and 9.5 μm , except that the reflectance peak closer to 9 μm has been reduced due to absorption by a clay coating on the quartz grains. This characteristic is often seen in clay soils. Unlike the concrete aggregate, the asphalt also provides an hydroxyl feature near 2.7 μm , characteristic of clays, and a strong C-H stretch near 3.5 μm . This sample's reflectance is probably fairly typical of most asphalt roads.

Finally, sample 0425UUUASP is a chunk of pebbled asphalt which contains a large amount of aggregate material. This asphalt material displays a reflectance much like the reflectance of concrete sample 0424UUUCMT. This is because the features due to the aggregates are very similar. In addition to these aggregate features, the asphalt also contributes a strong C-H stretch at 3.5 μm due to tar. It is interesting to note that for some reason the asphalt sample 0425UUUASP has higher bulk reflectance from 3 to 5 μm than does the concrete sample 042UUUCMT. This seems odd due to the low continuum reflectance of the tar content of asphalt.

In summary, road materials are dominated by the spectral characteristics of their mineral content. Asphalt looks much like concrete when the internal aggregate materials are exposed. However, typical asphalt roads probably look more like tar than concrete.

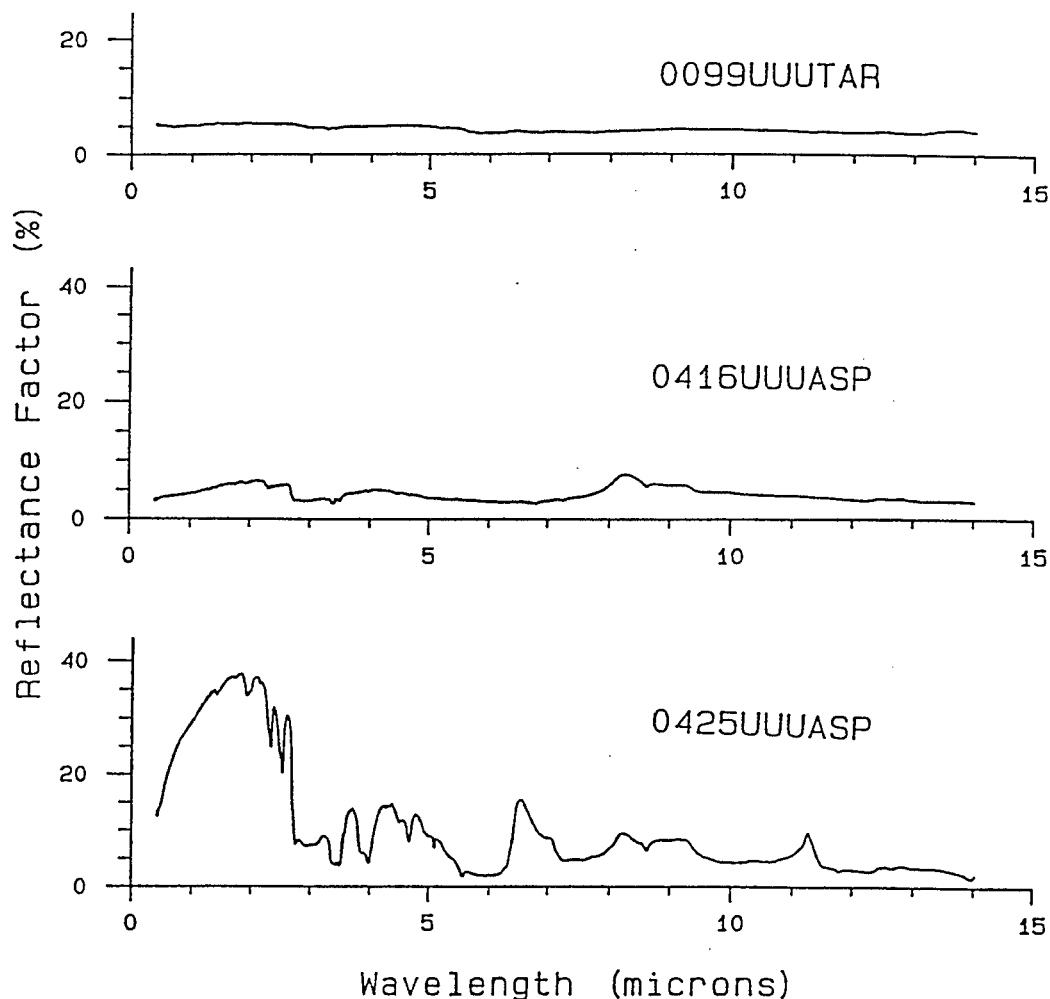


Figure A-22: The Hemispherical Reflectance of Some Asphalt Samples. [Taken from the SAL spectral database]

A.4.4 Vegetation

A.4.4.1 Early Infrared Measurements

Early spectral measurements of leaves in the thermal infrared indicated that vegetation displayed near-blackbody qualities, with little if any spectral information. Gates and Tantraporn [A.8] made specular reflectance measurements of leaves for approximately two dozen plant species. These measurements were made at incidence angles of 20 and 65 degrees and at wavelengths of 3.0, 5.0, 7.5, 10.0, and 15.0 μm . Gates and Tantraporn found in general that green leaves possess small reflectances, typically less than 5% reflectance at the 20 degree specular angle and less than 10% reflectance at the 65 degree specular angle. They also found that the leaves exhibited very little spectral variation. Only a slight reflectance peak at 10.0 μm was detected.

Wong and Blevin [A.19] measured the directional hemispherical reflectance of some tropical plant leaves. These measurements were made with 0.3 μm wide bands centered at the wavelengths of 8.0, 9.0, 10.0, 11.0, and 12.0 μm . They found that the average maximum reflectance was only 4% and that a reflectance peak at 9.0 μm was found to be common among all the leaf samples measured. Wong and Blevin concluded from their analysis that leaves are near blackbody radiators with very little spectral character. They also believed that all plants would exhibit nearly the same spectral characteristics.

Faulkner et al. [A.5] measured the spectral radiance of grass over the wavelength range 3.3-14.0 μm . From the inversion of the Planck function they were able to compute and plot the spectral apparent temperature of grass. For any single wavelength, the apparent temperature is the temperature of an equivalent blackbody emitting the same radiance as the grass. Thus by definition, any spectral differences in emissivity should also be seen as spectral differences in spectral apparent temperature. Their research showed potential spectral features in the mid-infrared (3.3-5.5 μm). However, in the far-infrared (8.0-14.0 μm) the grass exhibited near featureless blackbody characteristics.

The consistent results shown in these early works might be considered sufficient if it were not for the following problem. Unfortunately some potential target materials, like painted metals and camouflage nets, also tend to act like spectrally flat blackbodies over the wavelength range of 8.0-14.0 μm . A thermally suppressed near blackbody target hiding in a near blackbody forest, or grassy pasture, could potentially be impossible to detect using broad band multispectral methods. It could be however that a state of the art infrared multispectral sensor may be sensitive enough to detect very small narrow band spectral differences between targets and vegetated backgrounds, that is, if these differences exist. These early infrared measurements were not of sufficient quality or depth to unquestionably conclude that vegetation is spectrally featureless. This section will discuss some physical basis for thermal infrared multispectral vegetation signatures and will also survey two new sets of thermal measurements by Elvidge [A.4] and Salisbury [A.14].

A.4.4.2 Leaf Cellular Structure

The optical properties of leaves are strongly influenced by leaf chemistry and cellular structure. This section will briefly discuss this cellular structure. The cross section of a typical leaf can be found in Figure A-23. The middle layer, called the mesophyll, contains the palisade parenchyma cells which are filled with cell protoplasm. Suspended in this protoplasm are the chloroplasts which are small cellular sacks containing the important chlorophyll pigments. The chloroplasts are generally found in higher concentrations towards the leaf's upper surface where the sun's radiation is more intense. Towards the leaf's lower surface are contained the spongier palisade parenchyma cells which contain less dense concentrations of chloroplasts. Spread throughout the mesophyll are large intercellular spaces containing moisture-saturated air which are called the stomatal cavities. Above and below the mesophyll lies a layer of palisade parenchyma cells constituting the leaf's upper and lower epidermal layers. Above the upper epidermis is located a thin waxy cuticle layer.

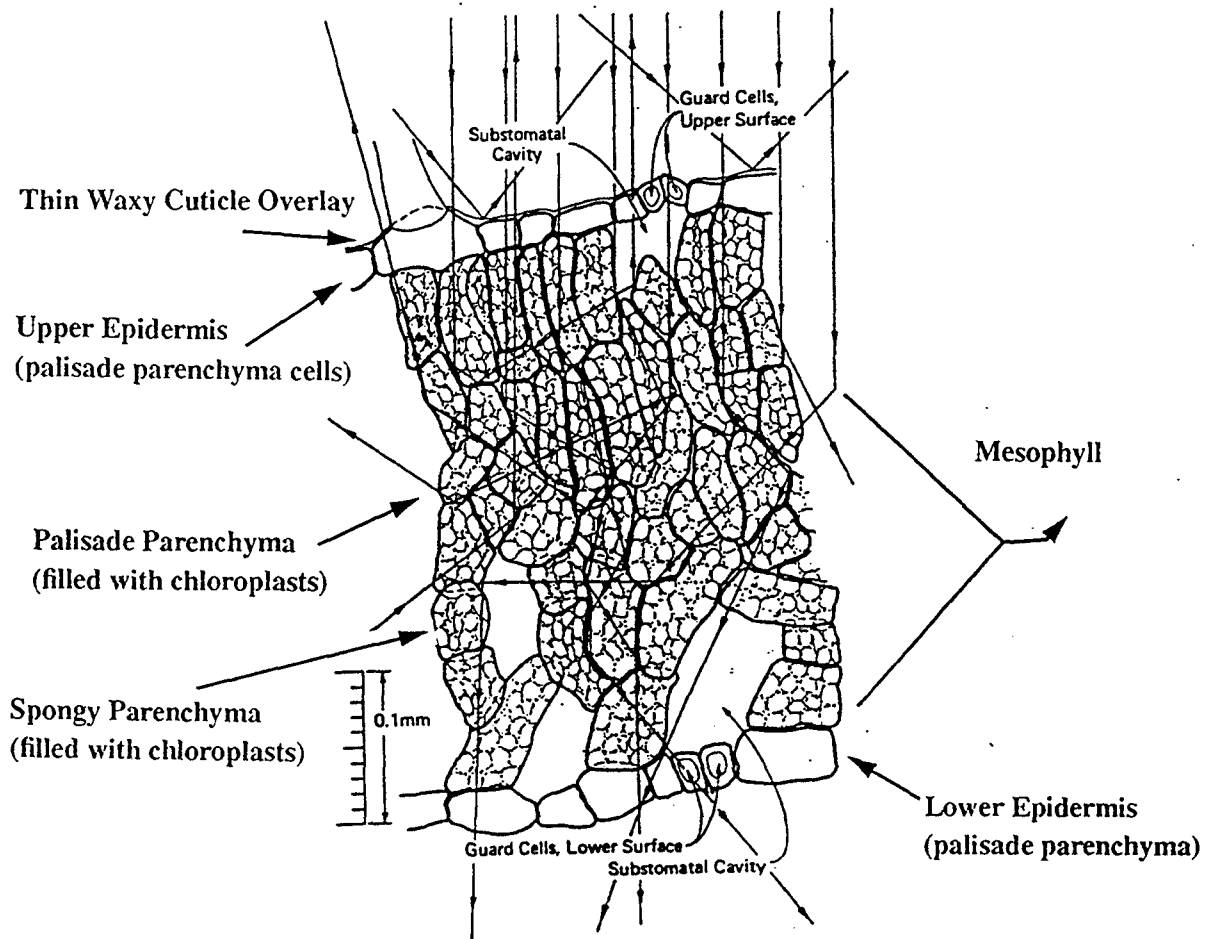


Figure A-23: The Cross-Section of a Typical Green Leaf [A.6].

The cellular structure of a leaf is large compared to the wavelengths of visible light and comparable to wavelengths in the far IR. Some typical cell dimensions are given in Table A-2.

Table A-2: Typical Cell Dimension of Leaves

Cell Type	Typical Size (μm)	Purpose
Palisade Parenchyma	15x15x60	Houses Chloroplasts
Spongy Parenchyma	15x15x20	Houses Chloroplasts
Epidermal Parenchyma	15x15x20	Protective Layer
Waxy Cuticle	3 to 5 μm Thick	Protective Layer
Chloroplasts	5 to 8 μm Dia. by 1 μm wide	Houses Grana
Grana	0.05 μm Dia. by 0.5 μm long	Houses Chlorophyll

A.4.4.3 Spectral Properties of Leaves

Plants are well adapted to the radiation environment they live in. Figure A-24 [A.6] shows the spectral distribution of direct sunlight, sunlight diffusely scattered through clouds, diffusely scattered skylight, and light diffusing through forest vegetation. Figure A-25 [A.6] shows measured spectral reflectance, transmittance, and absorptance typical for a leaf, in this case *nerium oleander*. Inspection of both figures will quickly show that the leaf's high absorptance at the visible wavelengths permits the efficient capture of radiation for photosynthesis. The simultaneous decrease of the leaf's absorptance and increase of the leaf's reflectance and transmittance near $0.7\ \mu\text{m}$ keeps the leaf from absorbing the bulk of the sun's energy which protects the leaf from overheating, drying out, and sustaining irreparable protein damage. Gates [A.7] has reported that leaves typically reach temperatures as high as 50 degrees C and are usually 10 to 20 degrees C above air temperature. The absorption of the sun's radiation above $0.7\ \mu\text{m}$ would lead to leaf temperatures far above 50 degrees C which is close to the denaturation temperature for most plant proteins. In the infrared the leaf's absorptance once again rises, the reflectance falls very low, typically about 5%, and the transmittance becomes essentially zero. This high leaf absorptance in the infrared is no longer a weakness since the solar irradiance, which can be modeled approximately by a 5900 K blackbody, is too low to harm the plant at wavelengths longer than $3\ \mu\text{m}$. High infrared absorptance means the leaf is a good emitter and this quality permits the leaf to cool itself down by efficient reradiation.

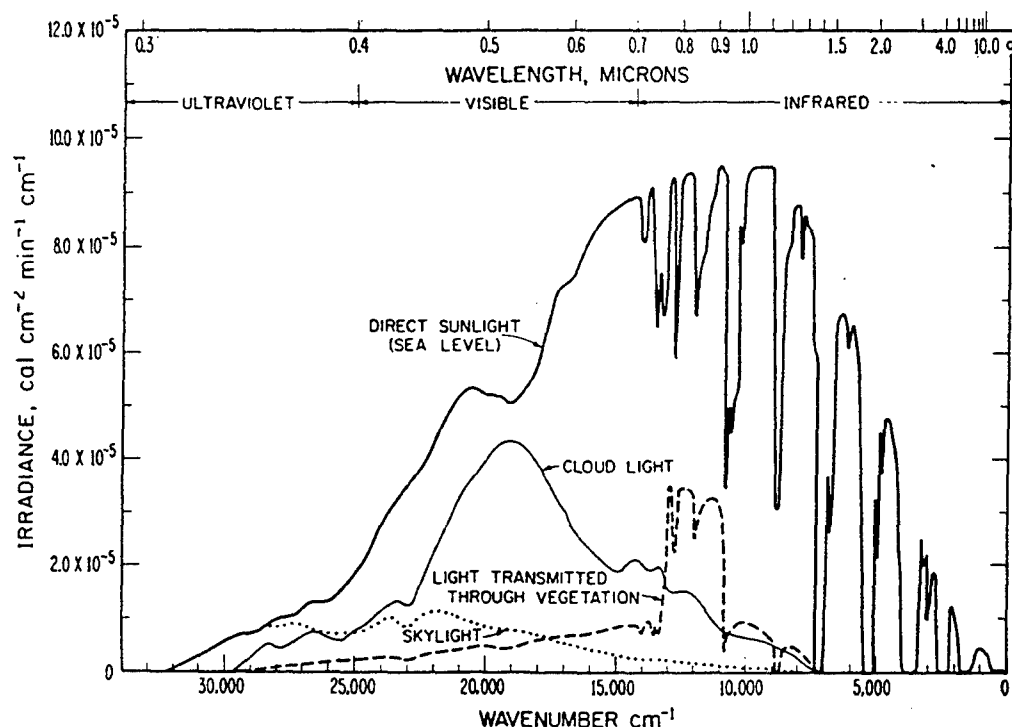


Figure A-24: The Spectral Distribution of Radiant Sources in Vegetation Canopies [A.6].

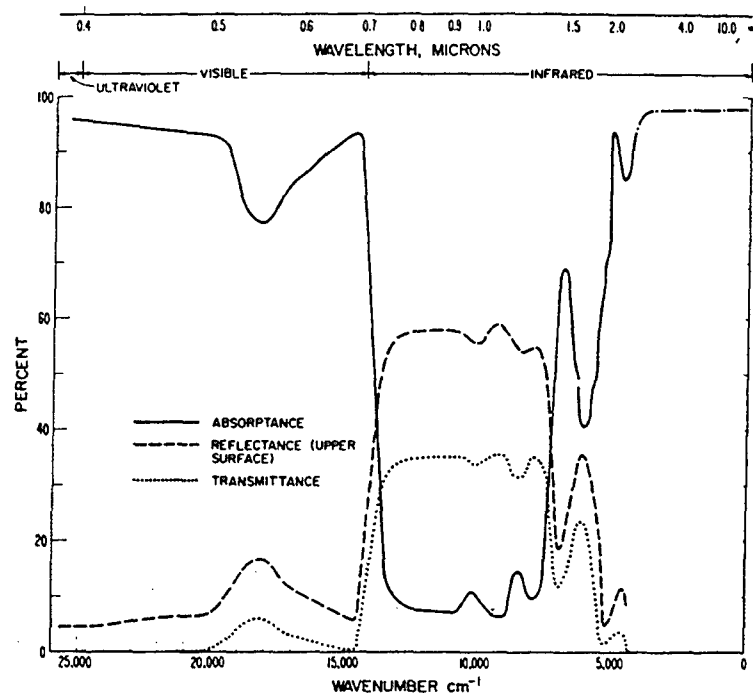


Figure A-25: The Spectral Reflectance, Transmittance, and Absorptance for *nerium oleander* [A.6].

One might naturally assume that the tailoring of these spectral characteristics to the sun's radiation must have occurred over eons of evolution, but this is apparently not the case. Aquatic vegetation usually receives very little direct solar radiation, yet its spectral characteristics are essentially identical to non-aquatic vegetation [A.6].

Figure A-23 shows how light may enter and scatter within a leaf. Any first surface reflections will occur at the boundary between the waxy cuticle, or upper epidermis, and the air. If the cuticle and upper epidermis are relatively transmissive, then the light will diffuse and scatter through the cuticle and epidermis into the leaf's volume, the mesophyll. This internal scattering will contribute a bulk reflectance component.

As the light enters the mesophyll it will begin scattering off cell to cell boundaries and the intercellular air spaces between parenchyma cells. Scattering can also occur off cellular structures whose size is of the order of the wavelength of light. This particle, or Mie, scattering is not wavelength dependent except for the possible resonances due to wavelength and particle size matches. This scattered light will then experience absorption by the internal leaf pigments of other cellular material like cellulose, lignin, or water. Any light that is not absorbed will continue to scatter throughout the mesophyll until it is finally absorbed or exits through the upper or lower epidermis. This bulk reflectance could potentially be an important feature in discriminating between plant species or between vegetation and potential target materials.

Figure A-26 [A.14] shows directional hemispherical reflectances of some common leaves [A.14]. The waxy cuticle and the upper and lower epidermis are relatively transmissive in the wavelength ranges of 2.5-2.8 μm , and 4.0-5.6 μm . This suggests that a large bulk reflectance should be seen at these wavelengths. Unfortunately, the high water content of leaves tends to diminish this bulk reflectance.

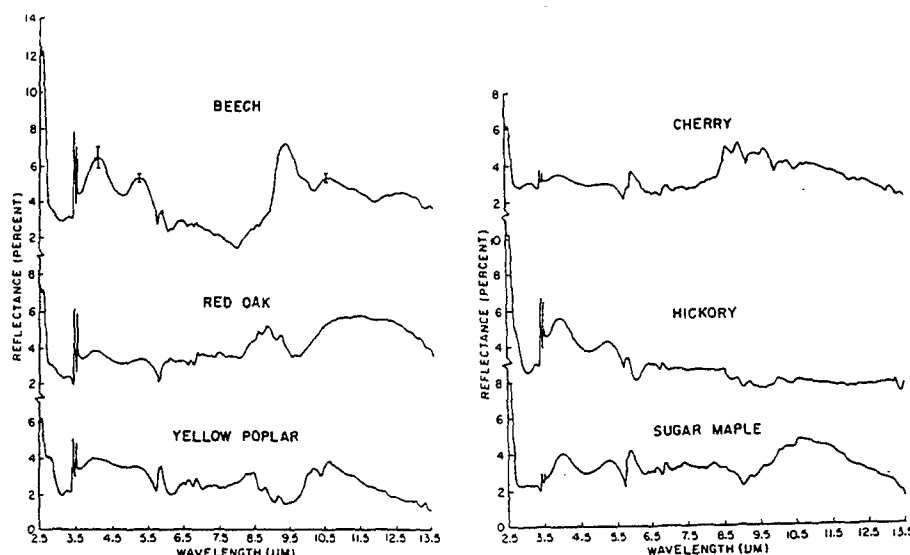


Figure A-26: The Hemispherical Spectral Reflectance of Some Common Leaves [A.14].

The presence of liquid water in leaves has been believed to cause the overall low reflectance continuum beyond 2.5 μm [A.15]. Healthy green leaves are typically between 50% and 75% water by weight [A.4]. Because of this high water content the spectral characteristics of green leaves are dominated by water absorption. Figure A-27 shows the effects of water content on the visible and near infrared spectral reflectance of a bean leaf. Notice the strong overtone water absorption resonances at 1.38 and 1.88 μm .

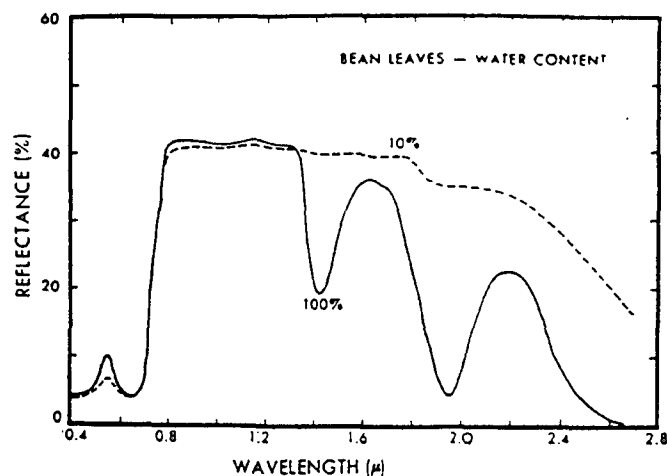


Figure A-27: Effects of Water Content on the Spectral Reflectance of Bean Leaves [A.11].

The effects of water in the thermal far-infrared are just as pronounced. Figure A-28 shows the directional hemispherical reflectance of water, a green cherry leaf, and a cherry leaf dried from 48 hours of exposure to a stream of very dry air. In Figure A-28 it is readily apparent how water absorption within the green leaf has quenched the bulk reflectances otherwise seen at 2.6 and 5.0 μm .

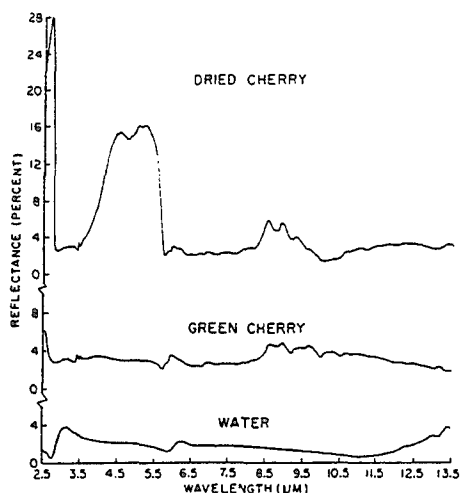


Figure A-28: The Hemispherical Spectral Reflectance of a Dried Cherry Leaf [A.14].

Figure A-29 shows how the presence of water can reduce bulk reflectance even at wavelengths where water is transparent. Water is very transparent from the visible out to about 1.3 μm , except for a very weak overtone resonance at 0.94 μm . The leaf's cuticle and epidermis are also quite transmissive at these wavelengths. This results in the high bulk reflectance seen in the normal bean leaf of Figure A-28. The low reflectance below 0.8 μm is due to inter-

nal chlorophyll pigment absorption. The second curve shown in Figure A-28 is of a bean leaf that has been saturated with water. This saturation has caused the previously air-filled stomatal cavities and intercellular air spaces to become filled with water. As the air cavities saturate the leaf becomes a continuous liquid phase medium. This eliminates many refractive index changes between cell boundaries and increases the leaf's direct transmittance at the expense of scattering and bulk reflectance. Thus we seen how water can affect a leaf's spectral properties by both absorption and transmission.

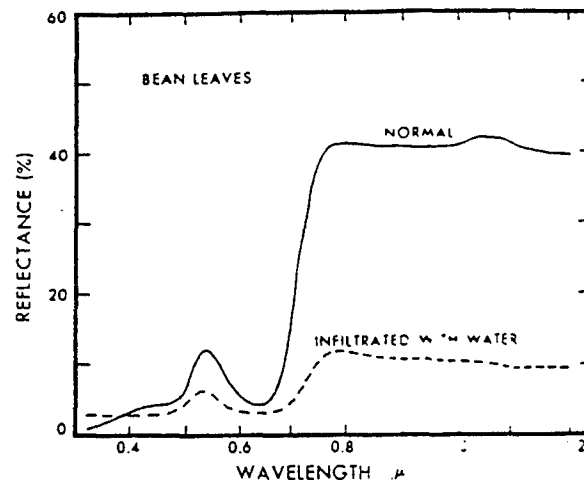


Figure A-29: Effects of Water Saturation on the Spectral Reflectance of Bean Leaves [A.11].

The effects of leaf water content is also seen in leaf senescence. As leaves undergo senescence in the autumn they begin to dehydrate. Dehydration leads to a decrease in the leaf's volume because of the absence of water. Dehydration also causes the number of cell to cell interfaces within the mesophyll to increase. This is because the microcavities between palisade cells remain but as the cells dry they split apart and living cell material begins to pull away from the internal cell walls. All of these dehydration effects lead to an increase in bulk reflectance below 6.0 μm . Salisbury [A.15] showed that dehydration due to senescence had little effect on the reflectance of leaves for wavelengths greater than 7 μm . As senescence reaches it final stages the bulk reflectance actually decreases as the cell walls continue to break down.

The increase in bulk reflectance at 2.6 and 5 μm , due to dehydration, may make it possible to detect targets indirectly by the damage they do to vegetation or by the target being covered by cut branches. Leaves begin to experience water stress soon after a branch has been severed.

The presence of other leaf materials such as cellulose and lignin also affect the spectral properties of leaves. Cellulose is a major component of leaf cell walls and typically constitutes one third to one half of the dry weight of most plants [A.4]. Lignin is a complex polymer

which encrusts cellular fibrils. The quantity of lignin in plant materials ranges from 10 to 35% of the dry weight [A.4]. Figure A-30 shows the biconical spectral reflectance of cellulose and lignin. Tables A-3 and A-4 provide the physical basis for absorption features in cellulose and lignin.

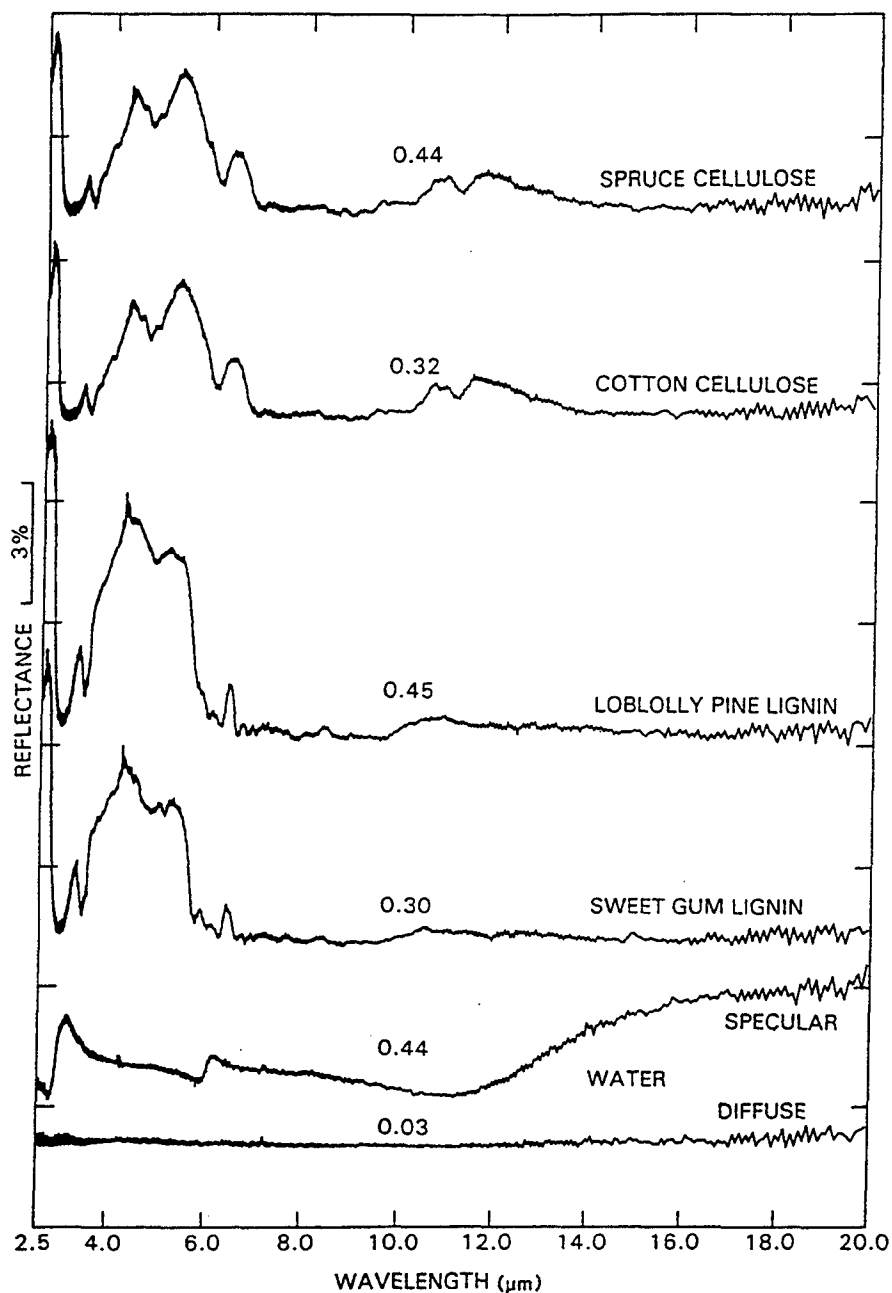


Figure A-30: Biconical Spectral Reflectance of Dry Plant Cellulose and Lignin [A.4].

Table A-3: Cellulose Absorption Features [A.4]

Wavelength (μm)	Identification
2.90	OH stretching
3.03	same
3.15	same
3.37	C-H stretching
3.38	same
3.41	CH ₂ asymmetric stretching
3.44	C-H stretching
3.46	same
3.48	same
3.51	CH ₂ symmetric stretching
6.12	absorbed water
6.80	OH in-plane bending
6.94	
7.06	CH ₂ symmetric bending
7.27	C-H bending
7.33	same
7.49	OH in-plane bending
7.60	CH ₂ wagging
7.83	C-H bending
7.96	
8.16	
8.33	OH in-plane bending
8.66	asymmetric bridge C-O-C stretching
9.03	asymmetric in-phase ring stretching
9.28	skeletal vibrations involving C-O stretching
9.43	same
9.66	same
9.80	same
9.95	same
10.04	same
10.36	same
11.21	asymmetric out-of-phase stretching
12.50	ring breathing
13.16	CH ₂ rocking
14.29	OH out-of-phase bending
15.38	same

Table A-4: Lignin Absorption Features [A.4]

Wavelength (μm)	Identification
2.92	OH stretching
3.42	C-H stretching in methyl and methylene groups
3.48	same
3.55	same
5.76	C=O stretching in unconjugated acids and esters
5.81	C=O stretching in unconjugated ketone and carboxyl groups
6.02	C=O stretching in para substituted aryl ketones
6.23	aromatic skeletal vibrations
6.62	same
6.80	C-H deformations from methyl and methylene groups
6.85	same
6.99	aromatic skeletal
7.30	C-H symmetric deformation
7.52	syringyl ring breathing with C-O stretching
7.87	guaiacyl ring breathing with C-O stretching
8.13	syringyl and guaiacyl ring breathing with C-O stretching
8.77	aromatic C-H in-plane deformation, guaiacyl type
8.85	aromatic C-H in-plane deformation, syringyl type
9.22	C-O deformation in secondary alcohols and aliphatic ethers
9.66	aromatic C-H in-plane deformation, guaiacyl type and C-O deformation in primary alcohols
10.31	=CH out-of-plane deformations
11.80	same
12.27	same
13.00	same

The most prominent absorption features of cellulose is the OH stretch at 2.9 μm , a reflectance peak at 3.28 μm due to C-H stretching, a reflectance minima at 6.08 μm due to water absorption, and a reflectance minima at 11.11 μm due to asymmetric out of phase bond stretching. There is a very prominent reflectance minima at 4.66 μm which seems to be characteristic of cellulose but whose origin is unknown. Lignin provides the same set of prominent spectral features excluding the 11.11 μm stretch.

Salisbury [A.14] has identified some physical reasons for the spectral characteristics of plants beyond those we've already identified. The spectral features in the 8.0-14.0 μm range are thought to be specular first surface reflections off the waxy cuticle. The absorption due to water is too great to permit bulk reflectance in this wavelength region. These spectral features are seen as reflectance peaks analogous to the reststrahlen reflectance peaks of minerals. Strong vibrations of hydrocarbon in the waxy cuticle are probably responsible for these reflec-

tance peaks. In addition, the sharp reflectance peaks near $3.4\text{ }\mu\text{m}$ are first surface reflectances due to C-H fundamental stretching vibrations.

Another material important in determining the leaf's optical properties are the pigments within the chloroplasts. The pigments most generally found in the chloroplasts are chlorophyll, carotenes, and xanthophylls, where chlorophyll is the most abundant pigment. Visible radiation is absorbed by the chlorophyll pigments and converted into heat or photochemically converted into stored energy through photosynthesis. The absorption spectra of some leaf pigments and liquid water is shown in Figure A-31. This figure shows that radiant absorption is dominated by pigment absorption at the visible wavelengths and dominated by water absorption at the infrared wavelengths. The visible wavelength pigment absorption band ranging over $0.4\text{--}0.6\text{ }\mu\text{m}$ is called the chlorophyll absorption band. Pigment absorption at the visible wavelengths is due to electronic transitions within the pigment's molecular bonds. Leaf pigments fail to provide any meaningful absorption features beyond $2.5\text{ }\mu\text{m}$.

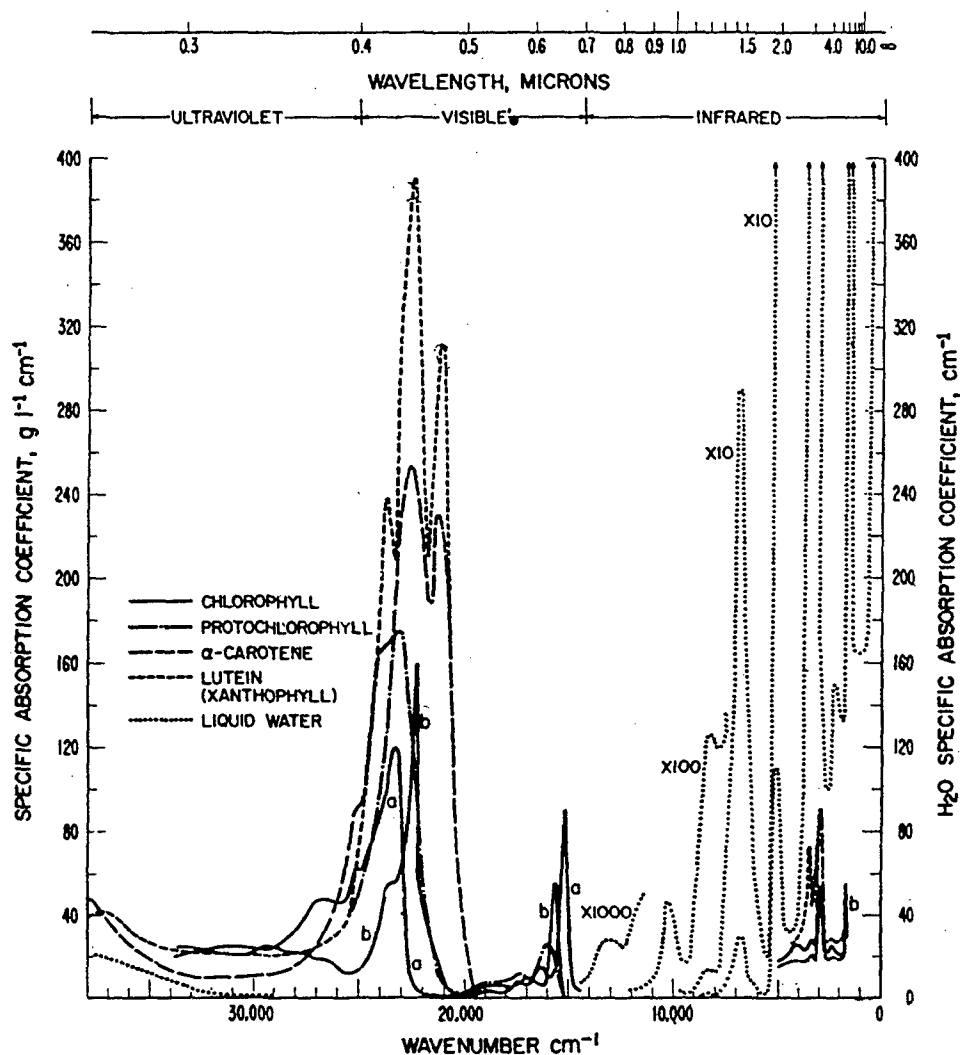


Figure A-31: The Spectral Absorption Coefficient for Plant Pigments and Water [A.6].

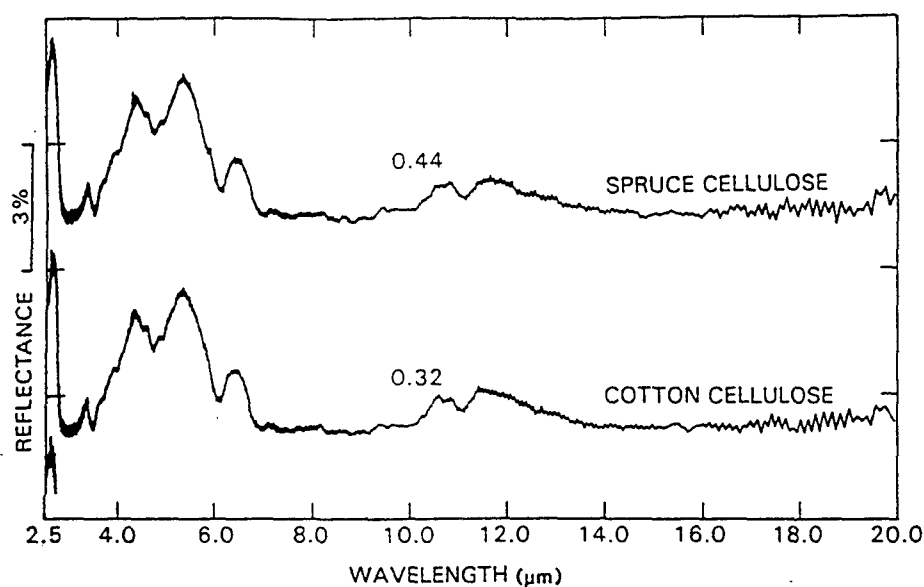
A.4.4.4 Spectral Effects of Vegetation Canopy Geometry

Salisbury [A.14] found that the average spectral contrast of green leaf spectra was generally only 3 to 4 percent in reflectance, and he speculated that this contrast would be reduced by at least a factor of two when the leaves are placed in a multiple scattering vegetation canopy environment. The reason for this spectral contrast reduction is due to the multiple emissions and reflections that occur within a canopy. Individual leaves may have characteristic spectral emissivities that are defined by various dips and humps in the spectral curve due to reflection, transmission, and absorption characteristics specific to that type of leaf. Unfortunately the spectral reflectance of that same leaf has dips where the emissivity had humps and humps where the emissivity had dips. Thus for a collection of leaves at about the same physical temperature, the characteristic spectral emission of a single leaf will be washed out by the subsequent reflections off and emissions from adjacent leaves. The presence of spectrally different stems, bark, and litter further alters the emission spectra. The end result is that all vegetation canopies, whether they be simple canopy structures like grass or more complicated forest structures, make rather good blackbody cavities. Unfortunately the amount of spectral contrast reduction incurred or the level to which vegetation canopies can truly be modeled as blackbodies is not really known. In addition, it is not well understood how other canopy components, such as stems, bark, litter, and soil, affect the canopies spectral signature in the thermal infrared.

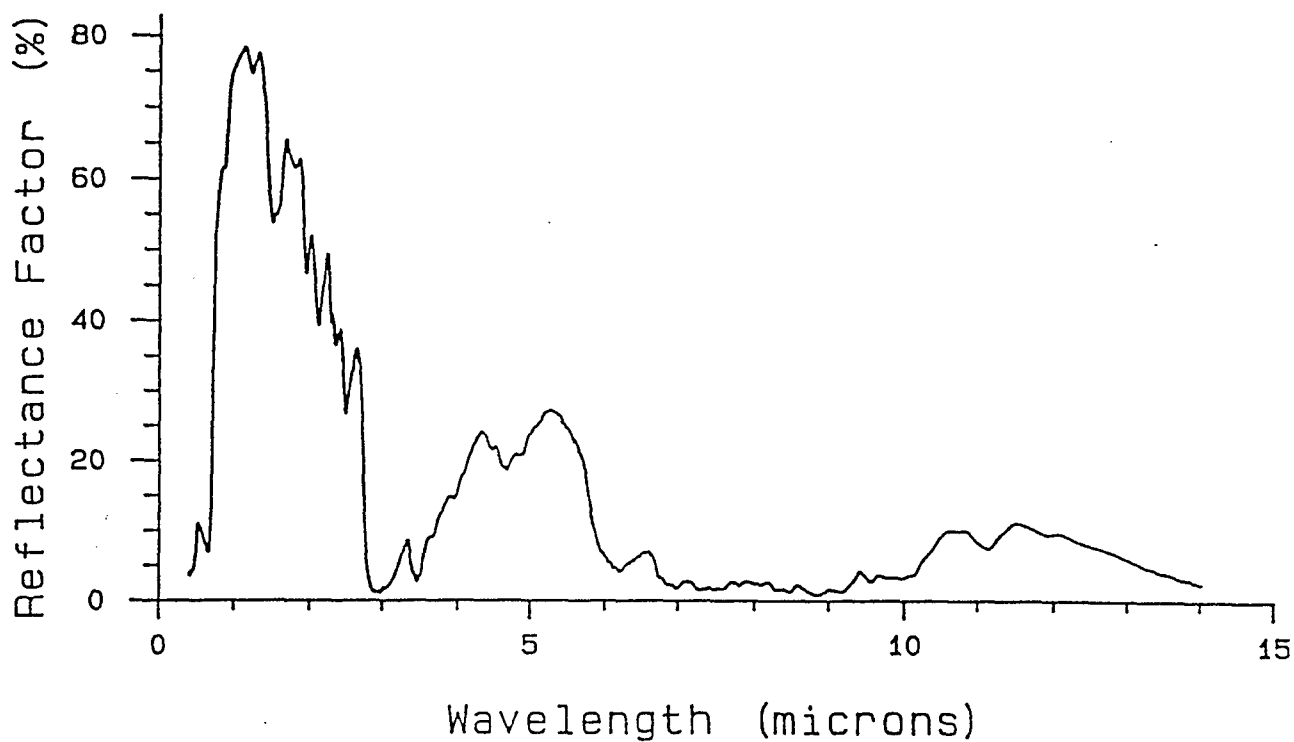
A.4.5 Camouflage Materials

Camouflage materials are important since they alter the visual and thermal signature of the potential targets they are intending to hide. Camouflage materials range in nature from natural fiber canvases and clothes to plastic polymeric materials. This memo will only concentrate on those camouflage materials which have been measured and included in the SAL spectral database.

Camouflage materials made from natural fiber clothes and canvases display the spectral features of the natural fiber. Figure A-32 show the spectral reflectance of cotton cellulose and the hemispherical spectral reflectance of a green woven cloth camouflage net (sample 0032UUUCNT). Notice that the spectral features for both are almost identical in shape and spectral location over the wavelength range of 2.5 to 14.0 μm . The previous section on vegetation describes the physical origin of the spectral features in cotton cellulose. The magnitude of reflectance can not be directly compared between Figures A-32 (a) and A-32 (b) since the cellulose measurements are biconical spectral reflectance [A.4] and the camouflage net material is hemispherical spectral reflectance. Figure A-33 (a) shows the hemispherical spectral reflectance of a dark green heavy canvas cloth (sample 0001UUUCAN). The primary natural fiber of this canvas is presumed to be cotton. The spectral reflectance shows a water absorption band at 3.0 μm and a strong hydrocarbon (C-H) stretch near 3.5 μm . A bulk reflectance plateau is seen between 3.0 and 6.0 μm but many of the characteristic features of cotton cellulose seen in Figure A-32 are absent. It is believe that this sample has been impregnated with a large amount of organic material used as water proofing and that the presence of this material dominates the spectrum of this sample.



(a)



(b)

Figure A-32: Spectral Reflectance of Natural Fibers. a) The biconical spectral reflectance of cellulose [A.4] and b) the hemispherical spectral reflectance of a green woven cloth camouflage net material [Sample 0032UUUCNT — SAL Database].

Plastic or nylon camouflage net materials are composed of polymers with numerous hydrocarbon (C-H) molecular bonds. The presence of these bonds can be seen in the strong hydrocarbon absorption feature at $3.5\text{ }\mu\text{m}$. All of the plastic or nylon camouflage nets in the SAL database exhibit this strong feature. Figure A-33 (b) shows the hemispherical spectral reflectance of a white winter camouflage net (sample 0020UUUCAM). This net was made of a fabric of nylon mesh impregnated with a white chalky substance giving the net its white visual appearance. Three very distinct features are seen below $6.0\text{ }\mu\text{m}$. In the midst of the 3.0 to $6.0\text{ }\mu\text{m}$ bulk reflectance plateau is a very strong C-H stretch at $3.5\text{ }\mu\text{m}$, an absorption feature due to nitrite at $4.5\text{ }\mu\text{m}$ (apparently from the white chalky substance), and a very strong carbonyl band at $5.7\text{ }\mu\text{m}$. In addition the various smaller spectral features superimposed on the 3.0 to $6.0\text{ }\mu\text{m}$ bulk reflectance are primarily hydrocarbon features and the features from 5.7 to $7.5\text{ }\mu\text{m}$ are a combination of hydrocarbon and carbonyl features.

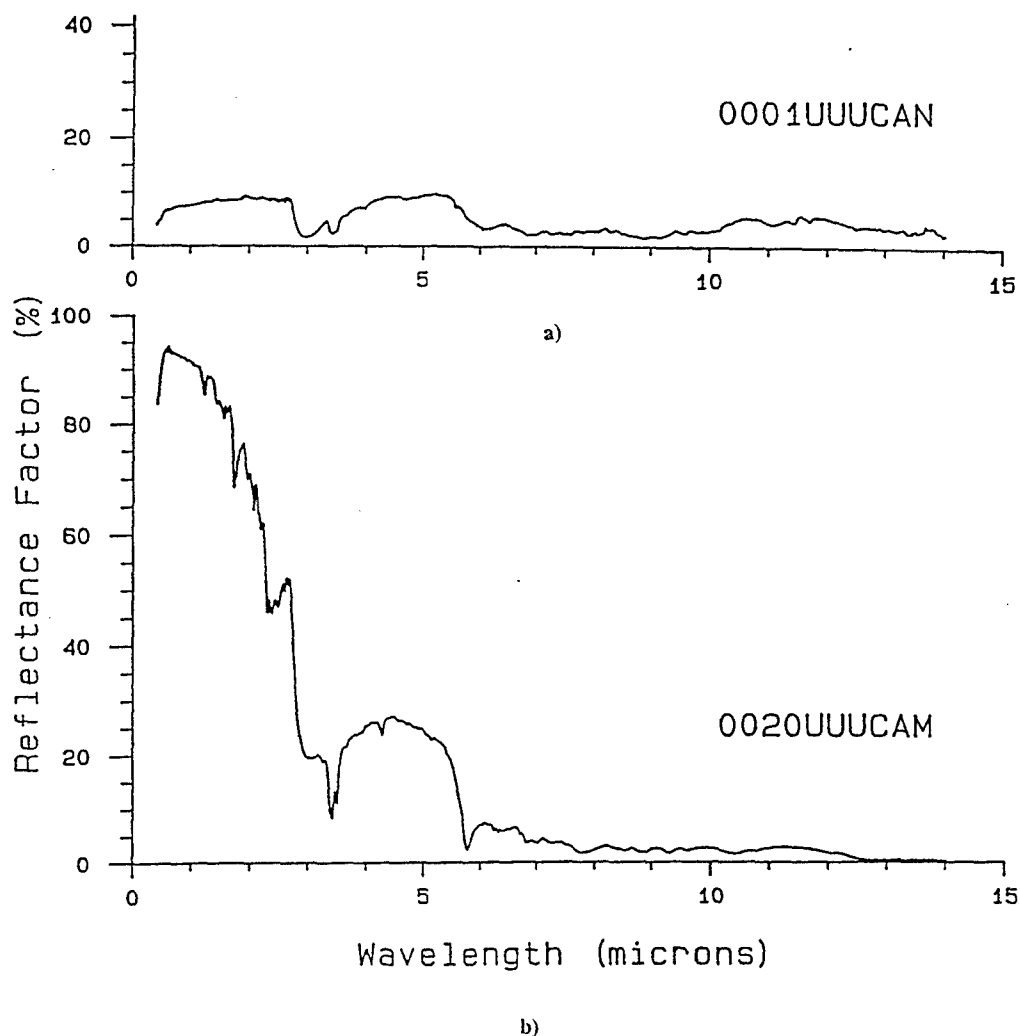


Figure A-33: Spectral Reflectance of Man-Made Fibers. a) The hemispherical spectral reflectance of dark green canvas [Sample 0001UUUCAN — SAL database] and b) the hemispherical spectral reflectance of a white winter camouflage net [Sample 0020UUUCAM — SAL database].

All of the plastic camouflage nets in the SAL database are relatively thin sheets of plasticized or rubberized fabric. The woodland spring or summer camouflage nets have two different visual colors of brown and green on opposite sides of the sheet. The plastic sheets are then contour cut and folded to provide a two color net with both colors showing on both sides. The green and brown sides of the polymeric material show little spectral difference in the thermal infrared. Figure A-34 displays the hemispherical spectral reflectance of both the green (sample 0019UUUCAMg) and brown (sample 0019UUUCAMb) components of a plasticized fabric camouflage net. The pigments which provide the nets visual signature does not appreciably alter the thermal infrared reflectance of the net. The only visible difference from 2.5 to 14 μm is the strength of the water band at 3.0 μm and the strength of the carbonyl and hydrocarbon features from 5.7 to 7.5 μm . From this point on only the brown component of woodland camouflage nets will be shown.

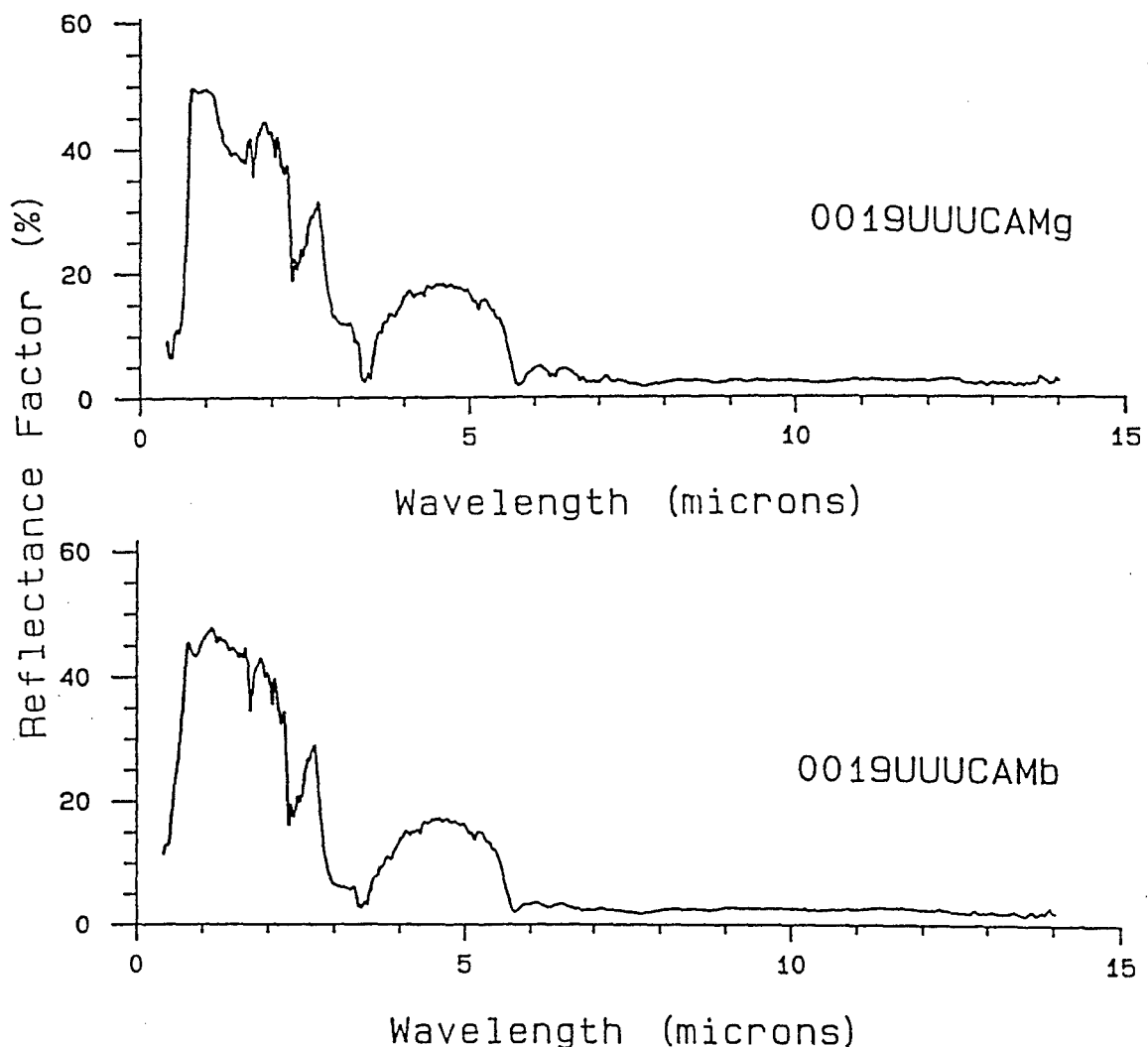


Figure A-34: The Hemispherical Spectral Reflectance of the Green (0019UUUCAMg) and Brown (0019UUUCAMb) Components of a Plasticized Fabric Camouflage Net. [Taken from the SAL spectral database.]

Figure A-35 shows the hemispherical spectral reflectance of the brown component of three different camouflage nets. These particular nets have been chosen to display a spectral diversity in polymeric camouflage net materials. Sample 0443UUUCAMb is a fairly opaque single layer of rubberized camouflage net material. This material shows the already familiar features of a water absorption band at 3.0 μm , a very prominent C-H stretch absorption band at 3.5 μm , a strong carbonyl band at 5.7 μm , and various lesser hydrocarbon and carbonyl features from 3.0 to 6.0 μm . In addition this sample shows a hydroxyl feature at 2.7 μm and a very characteristic reststrahlen peak at 9.7 μm whose precise origin is not known. It could be that this polymeric net material contains fiberglass strands which are SiO_2 (quartz) glass fibers. Fiberglass would be expected to provide a strong reststrahlen feature like the one shown. Sample 0113UUUCNT is also the spectral reflectance of a rubberized plastic camouflage net. This sample was noted in the SAL database to be weathered and the presence of surface contaminants due to weathering might be responsible for the subduing of the 9.7 μm reststrahlen feature.

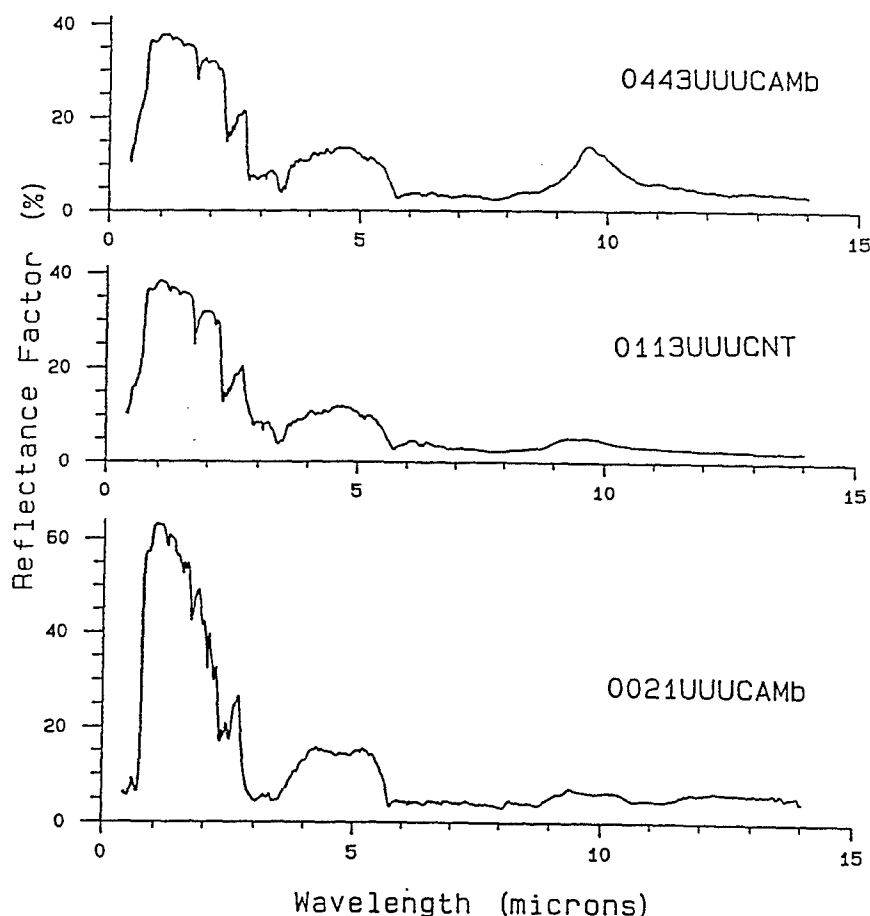


Figure A-35: The Hemispherical Spectral Reflectance of the Brown Component of Two Rubberized Camouflage Nets (0443UUUCAMb and 0113UUUCNT) and a Plasticized Fabric Camouflage Net (0021UUUCAMb). [Taken from the SAL spectral database.]

Sample 0021UUUCAMb shows the hemispherical spectral reflectance of a plasticized fabric camouflage net. This material shows some of the same features seen previously except for the absence of hydroxyl bands near $2.7\text{ }\mu\text{m}$ and an increase in spectral activity from 8 to $14\text{ }\mu\text{m}$. The origin of these features is not known.

A.4.6 Painted Materials

Paints are an important class of materials to understand since they usually provide a protective and low observable coating for most targets of interest. Paints possess a diverse array of spectral features due to their numerous compositional types. All of the full measured paint data presented here, i.e spectral reflectance of both binder and pigments, come from the SAL spectral database. Unfortunately the chemical composition of the paints in the SAL spectral database is not well known. Thus it is more difficult to identify the source of spectral features in paints than it has been for other materials.

Paint pigments are generally used to tailor the visual and near infrared spectrum of paints. At the infrared wavelengths most pigments fail to provide numerous broad band absorption features. Thus it is the paint binder which usually dominates the spectral properties of paints in the thermal infrared.

An older but popular binder for pigments in paint is linseed oil. Figure A-36 shows the infrared reflectance of linseed oil [A.18]. Linseed oil is very transmissive and thus possesses a large bulk reflectance in the infrared. The familiar spectral features of hydrogen absorptions, hydrocarbon stretches, and possibly carbonyl can be seen at 3.0 , 3.5 , and $5.7\text{ }\mu\text{m}$ respectively. The broad feature near $9.0\text{ }\mu\text{m}$ is of unknown origin.

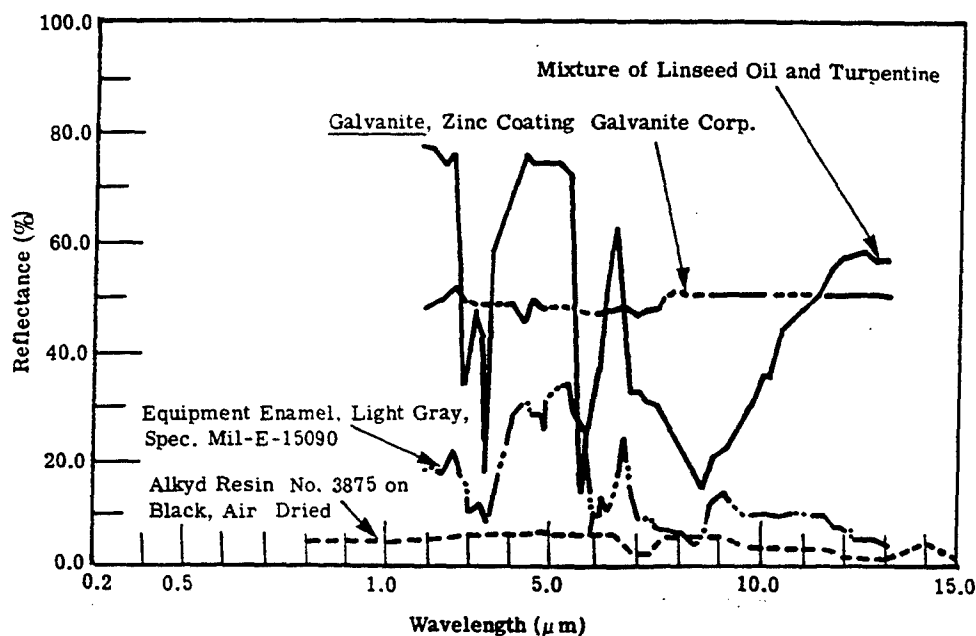


Figure A-36: The Spectral Reflectance of a Linseed Oil Paint Binder [A.18].

Most modern binders are generally polymers because they provide a high quality, lightweight, and durable coating. Table A-5 shows the molecular source of some spectral absorption features in plastics [A.1]. Many of the spectral features already seen in plastic camouflage nets are included in Table A-5.

Table A-5: Some Spectral Absorption Features of Polymers

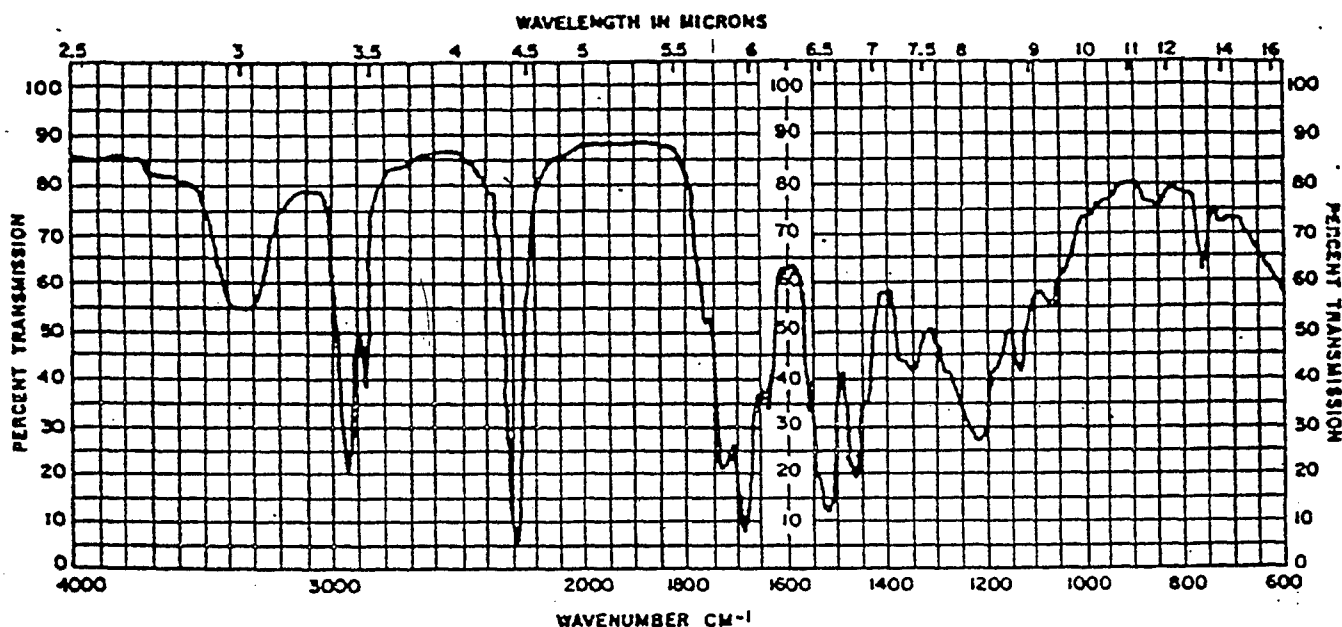
Molecular Group	Feature Location (μm)
O-H	2.8
N-H	3.03, 6.12, 6.46
C-H	3.5, 6.8
Carbonyl	5.75
Methyl	7.26, 7.71
Ester	8.0, 9.75
C-O	9.0 (broad), 13.47

Polyurethanes and fluorocarbons make up most of the polymer binders. Polyurethanes are formed by reacting dihydroxy alcohols with various diisocyanates which results in the formation of many different polyurethanes. Polyurethane binder's spectral absorption features differ considerably depending on the specific constituents used to synthesize the polymer. Figure A-37 (a) shows the spectral transmittance of a polyurethane binder which has been used in airframe applications (Military spec: MIL-C-53039A). This binder shows a water absorption band at 3.0 μm , hydrocarbon bands at 3.42 and 3.5 μm , and a carbonyl band at 5.7 μm . There is a very dramatic feature at 4.4 μm due to the presence of aliphatic polyisocyanates. The large transmittance of this binder in the infrared would be expected to contribute to a large bulk reflectance and would also permit the transmission of spectral features from the underlying bulk material.

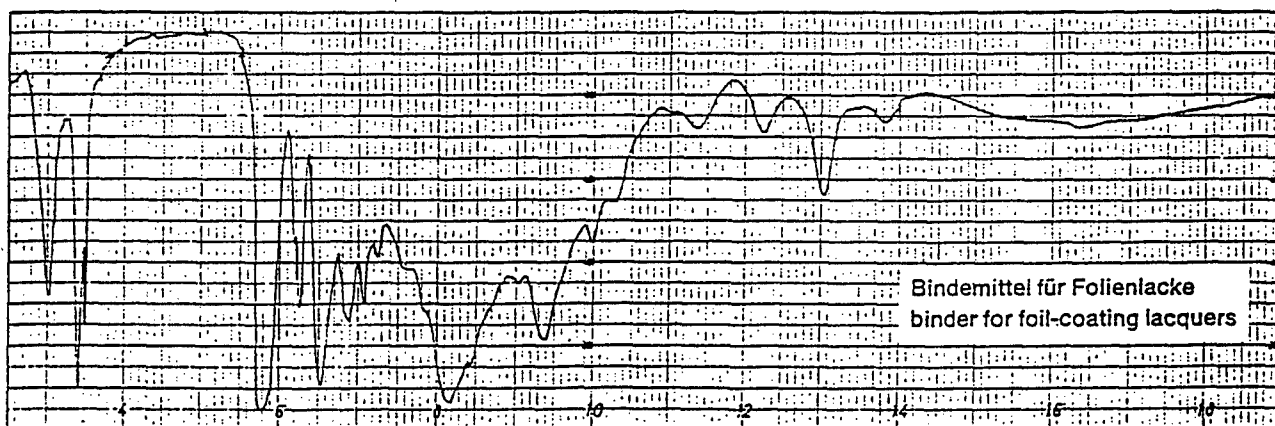
Figure A-37 (b) shows the spectral transmittance of another polyurethane binder. Very little absorption is present from 3.5 to 5.5 μm . We can still see the water, hydrocarbon, and carbonyl features but the strong 4.4 μm feature seen in Figure A-37 (a) is not present in this particular binder. There is a large absorption feature at 8.0 μm presumably due to ester. The other absorption features from 8.0 to 14.0 μm are more difficult to identify.

Another interesting type of polymer binder is fluorocarbon (Teflon). Figure A-38 (a) shows the spectral transmittance of Teflon FEP, a tetrafluorethylene-hexafluoropropane copolymer. The wavenumber axis for this figure is difficult to read so a few reference wavelengths have been added. This binder is interesting since it is practically devoid of spectral features up to about 6.5 μm . The long wavelength thermal infrared (8.0 to 14.0 μm) is also quite featureless

with the exception of an unidentified feature at about 10 μm . The polymer binder shown in Figure A-38 (b) is a cellulose acetate butyrate material (Eastman CAB-171-15s). This binder shows a water feature at 3.0 μm , the hydrocarbon features near 3.5 μm , and the carbonyl feature at 5.7 μm . In addition, features presumably due to esters can be seen at 8.0 and 9.5 μm .

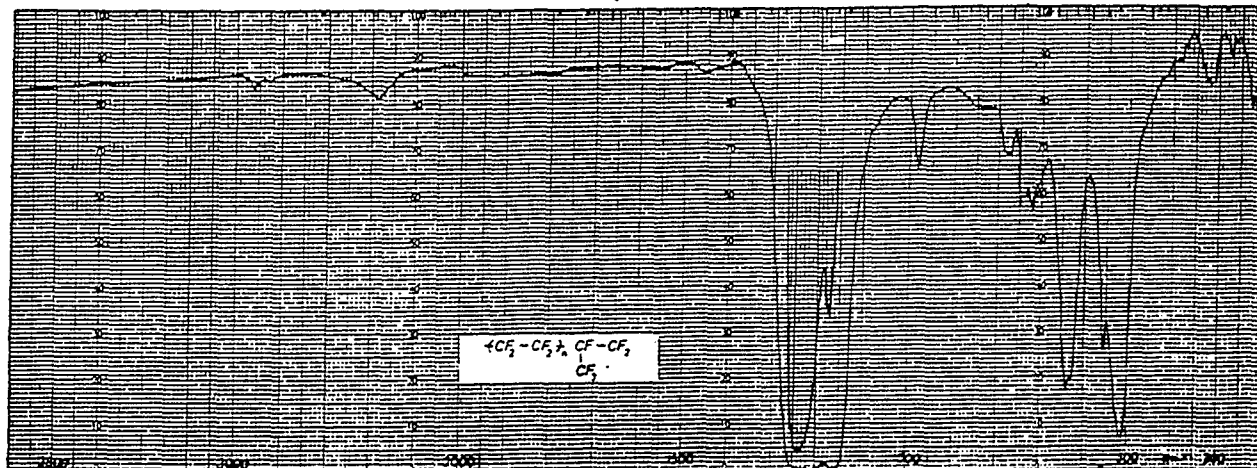


(a)



(b)

Figure A-37: The Spectral Transmittance of Two Polyurethane Binders. a) Aliphatic polyurethane (MIL-C-53039A) and b) another polyurethane binder.

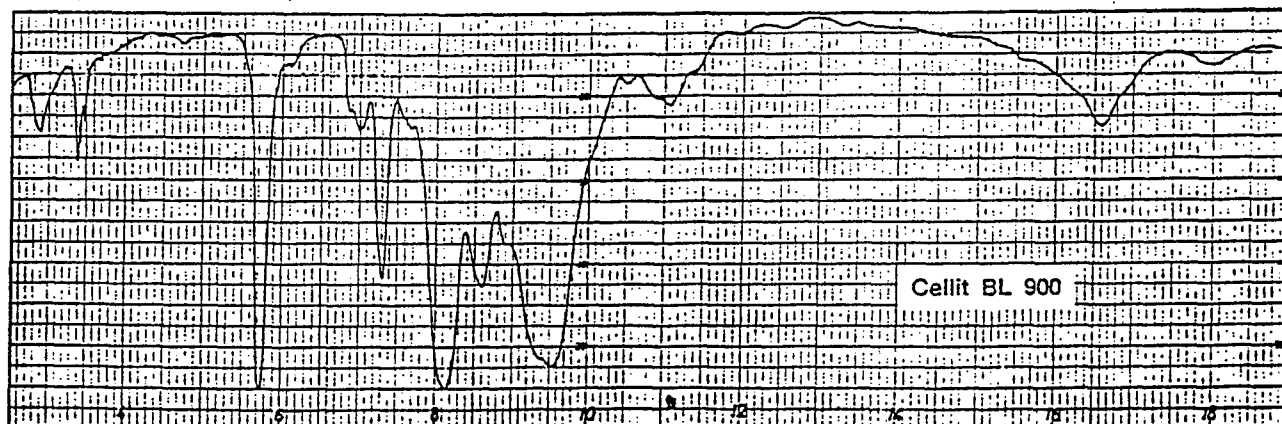


3.5 μ m

6.5 μ m

10.0 μ m

(a)



(b)

Figure A-38: The Spectral Transmittance of Two Polymer Binders. a) Teflon FEP and b) cellulose acetate butyrate (Eastman CAB-171-15s).

Figure A-39 shows the hemispherical spectral reflectance of green paint on steel and green paint on fiberglass. Sample 0418UUUIRN has a single coat of green paint on steel while sample 0419UUUIRN has two coats. Steel is generally quite featureless in the thermal infrared except for possible surface contaminants or impurities in the steel. Thus most of the spectral features are expected to come from the paint. The paint is however translucent enough that a single layer permits significant reflectance off of the steel substrate. The effects of a second coating of paint are evident in sample 0419UUUIRN where the reflectance is dramatically reduced throughout the thermal infrared. Some interesting absorption features that can be seen are a very strong hydroxyl band near $2.7\text{ }\mu\text{m}$, a broader water band near $2.9\text{ }\mu\text{m}$, a very strong C-H stretching vibration complex centered at $3.45\text{ }\mu\text{m}$, and a strong carbonyl band at $5.7\text{ }\mu\text{m}$. The absorption features from 8 to $14\text{ }\mu\text{m}$ are seen as reflectance minima superimposed on the large bulk reflectance due to high binder transmittance. The origin of these the absorption features at 11.0 and $12.5\text{ }\mu\text{m}$ are unknown. The double coated sample 0419UUUIRN has the same spectral features as the single coated sample but their magnitudes have been dramatically reduced.

Sample 0435UUUFIG is a light green paint on fiberglass. The spectral difference in this sample from the painted metal samples is presumably due more to the substrate than the paint. The water, hydrocarbon, and carbonyl bands can still be seen but the fiberglass apparently adds a small reststrahlen band at $9.5\text{ }\mu\text{m}$ due to silica. The partial opacity of the paint has significantly reduced the strength of this reststrahlen feature.

Figure A-40 shows the hemispherical spectral reflectance of three samples of dark green paint on metal. The paint in these samples is presumably multilayered due to the low spectral reflectance compared to sample 0418UUUIRN. The same water, hydrocarbon, and carbonyl features are still present along with a rather large bulk reflectance from 3.5 to $5.5\text{ }\mu\text{m}$ due to the high transmittance of the binders. The broad reststrahlen peak at $9.7\text{ }\mu\text{m}$ is probably due to scattering off of the green pigment, which the writers of the SAL database believed to be $\text{CrPO}_4 \cdot 3\text{H}_2\text{O}$. Many of the smaller features from 5.7 to $8.0\text{ }\mu\text{m}$ are due to hydrocarbon stretches. Sample 0068UUUPNT was reported to be significantly weathered. Thus the presence of surface contaminants, along with reduced first surface reflectance because of increased surface roughness, are probably both responsible for the overall decreased reflectance compared to samples 0059UUUPNP and 0076UUUPNT.

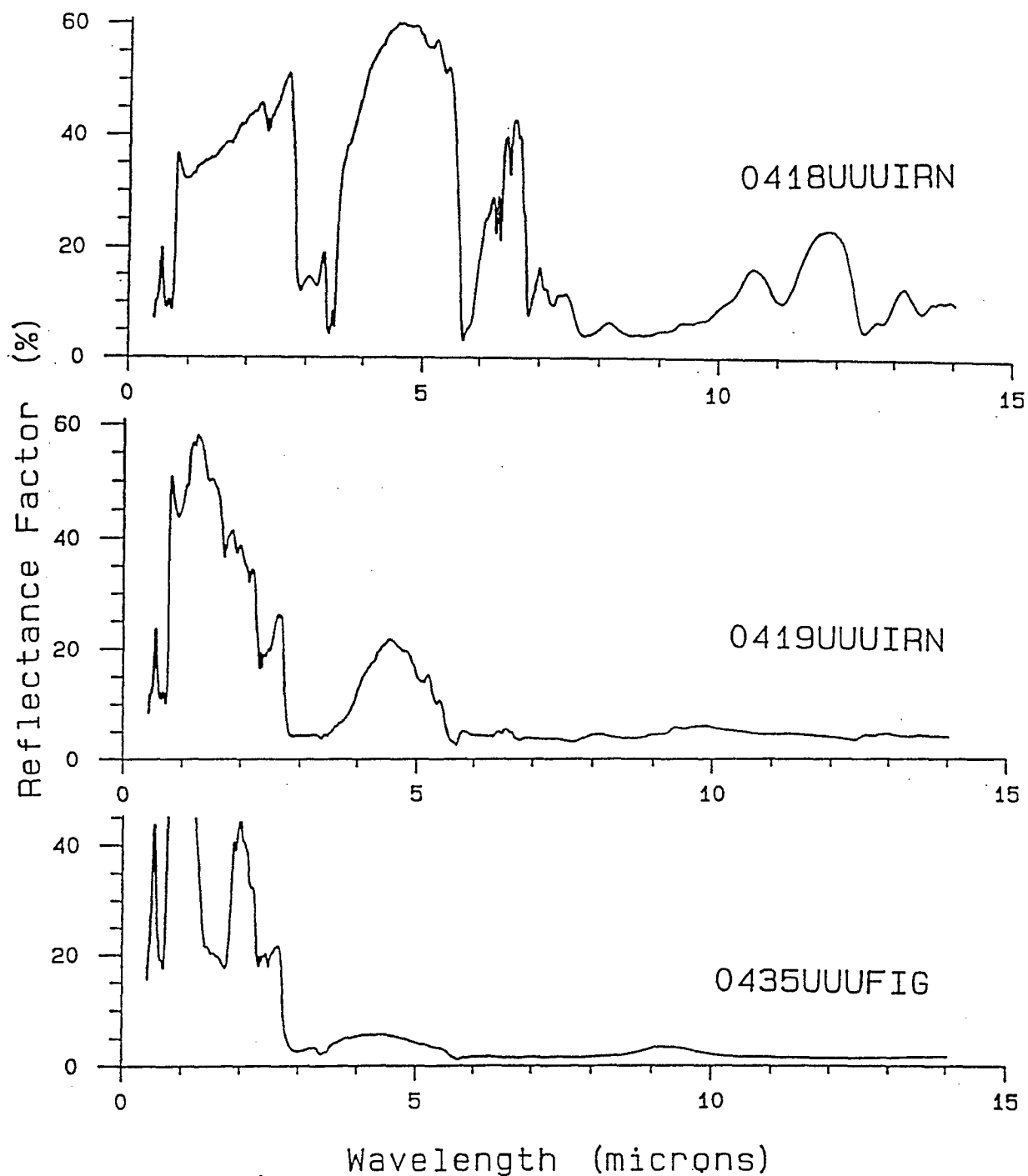


Figure A-39: The Hemispherical Spectral Reflectance of Green Painted Steel and Fiberglass.

Sample 0418UUUIRN is a single coat of green paint on steel.

Sample 0419UUUIRN is two coats of green paint on steel.

Sample 0435UUUFIG is green painted fiberglass.

[Taken from the SAL spectral database.]

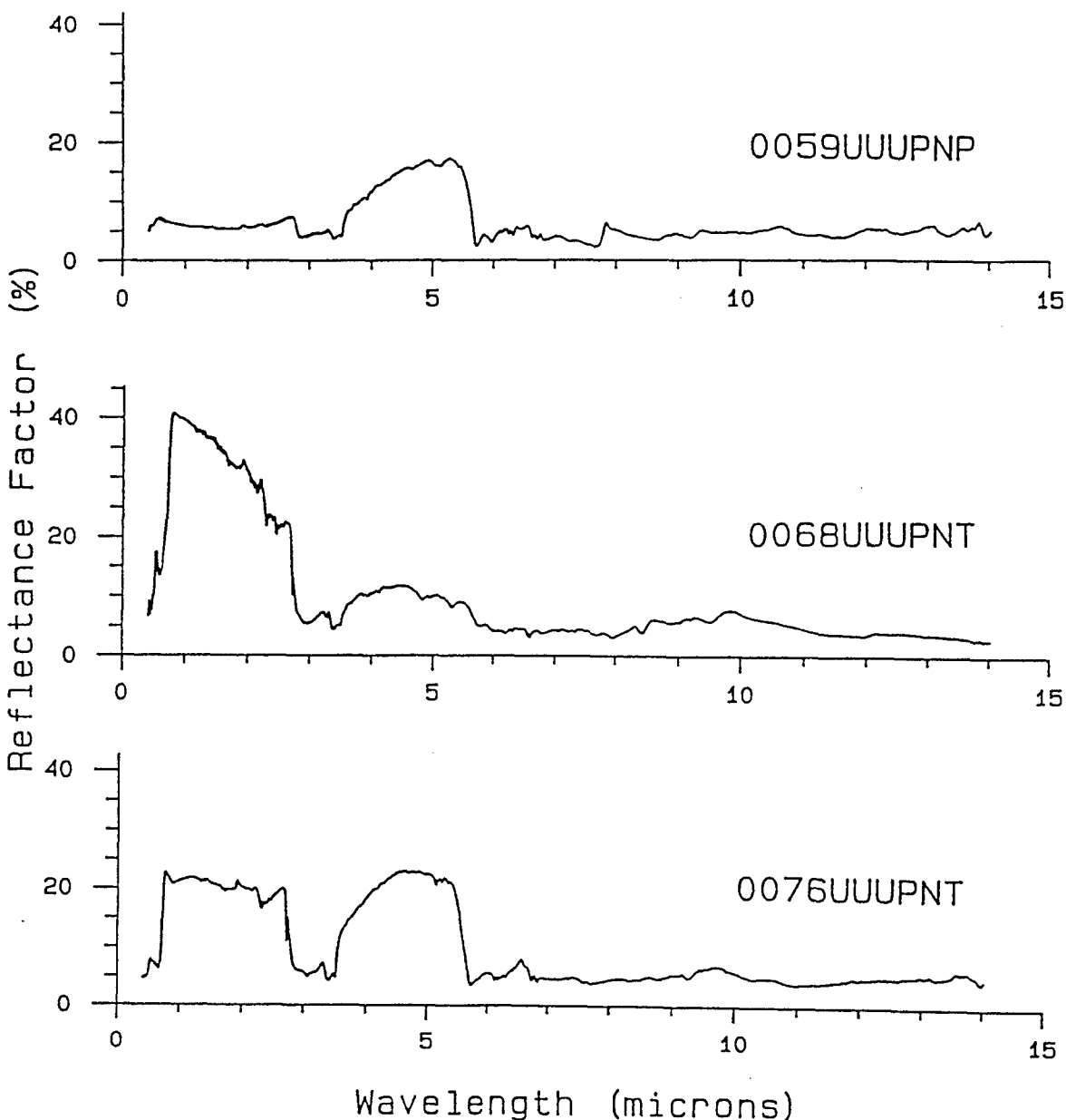


Figure A-40: The Hemispherical Spectral Reflectance of Dark Green Paint on Metal.
[Taken from the SAL spectral database.]

Finally, Figure A-41 shows the hemispherical spectral reflectance of several samples of brown or tan paint on metal. The same general features described in the samples of Figure A-40 (green painted metals) are evident. However the reststrahlen peak at 9.7 μm is much more pronounced in samples 0074UUUPNT and 0075UUUPNT. This reststrahlen feature could be due to the pigment or it could possibly be due to the inclusion of sand or other minerals in the paint. Paint manufacturers have been known to add sand to paint to give it a rough diffuse visible signature.

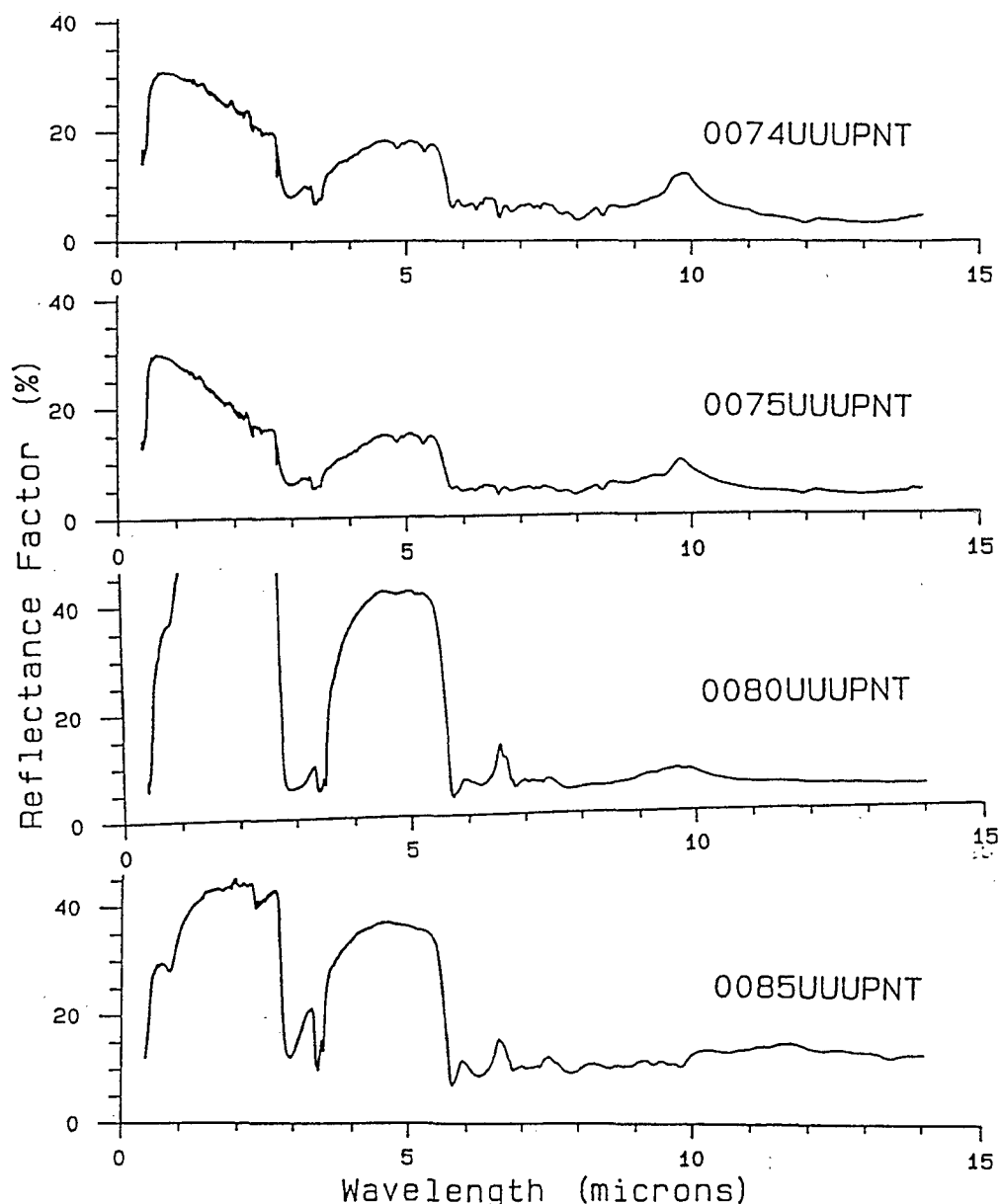


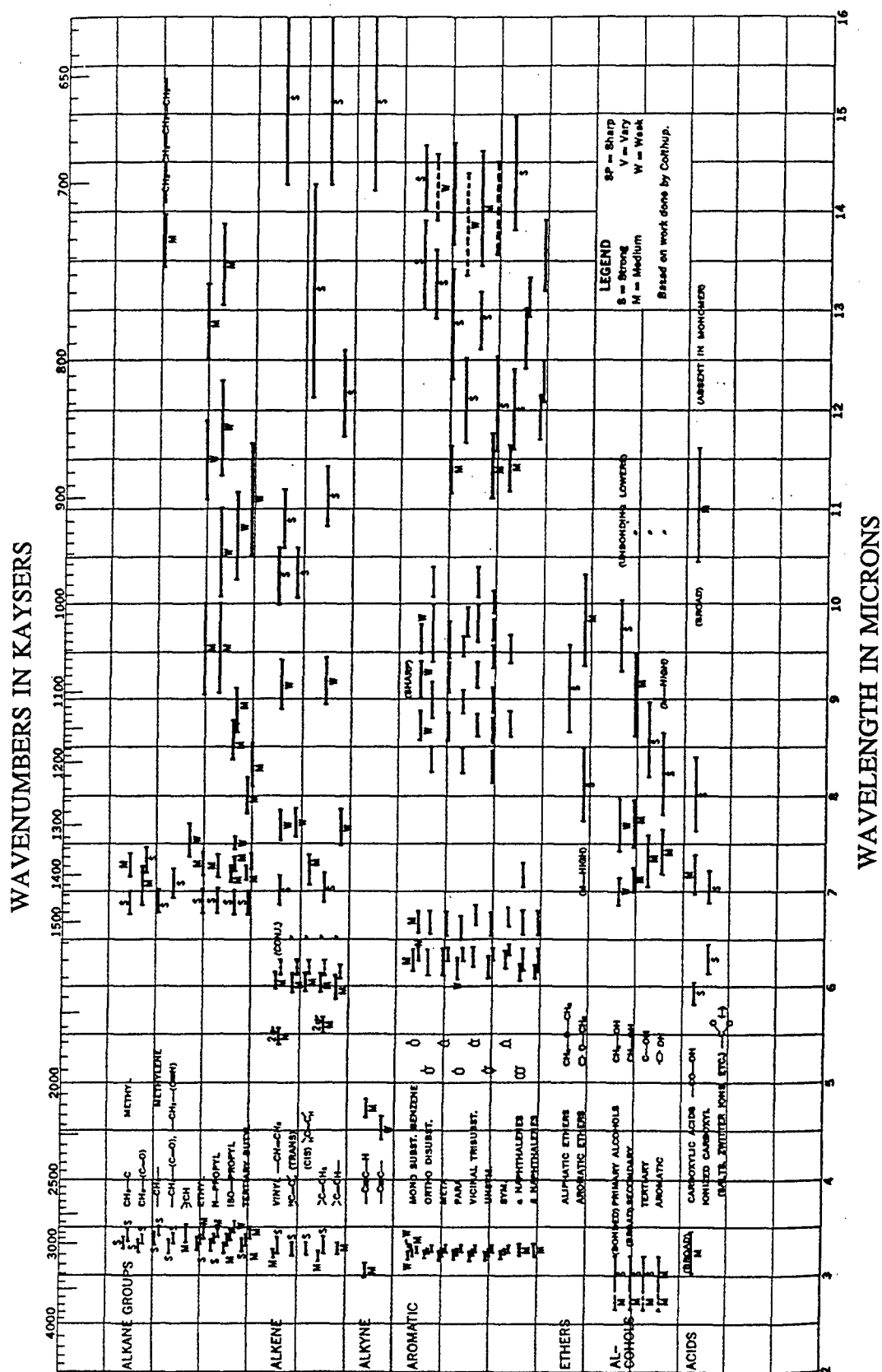
Figure A-41: The Hemispherical Spectral Reflectance of Brown or Olive Tan Paint on Metal. [Taken from the SAL spectral database.]

A.5 Conclusion

Numerous spectral features have been observed and identified in the hemispherical spectral reflectance of some interesting materials. The strength and consistency of these features suggests the possible successful application of multispectral techniques in the thermal infrared. However some spectral features appear too narrow in wavelength extent and too small in magnitude to provide a sufficient signal to noise ratio. Further analysis will be required to determine the practicality of using many of the identified spectral features.

A.6 Additional Spectral Features

Figures A-42 to B-48 contain information from [A.17] pertaining to the spectral location and the relative strength of vibrational absorption features of many molecular structures. All of the vibrational absorption features discussed in this memo are contained in these figures. In addition the figures may provide insight into the spectral features of materials of future interest.



WAVENUMBERS IN KAYERS

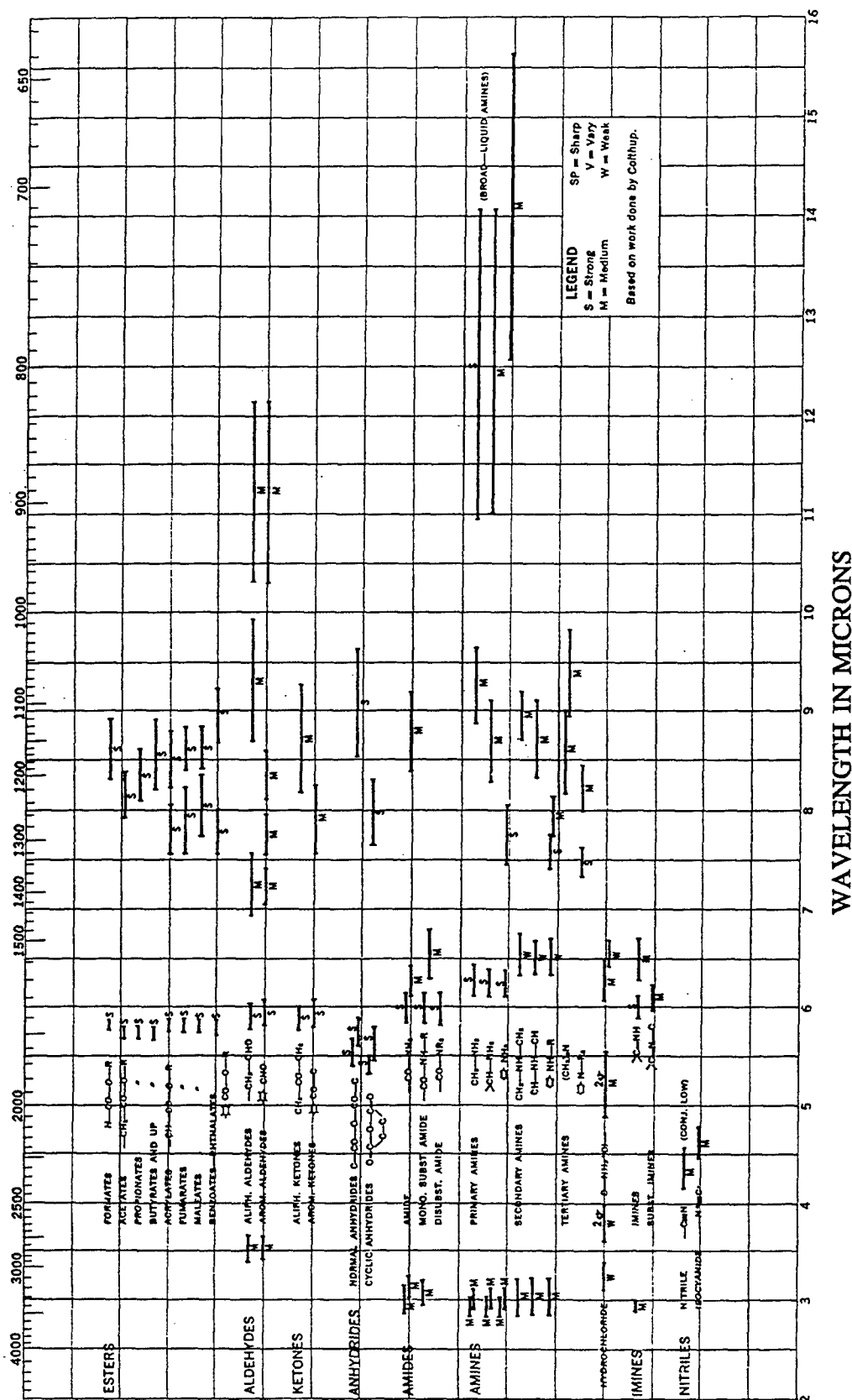
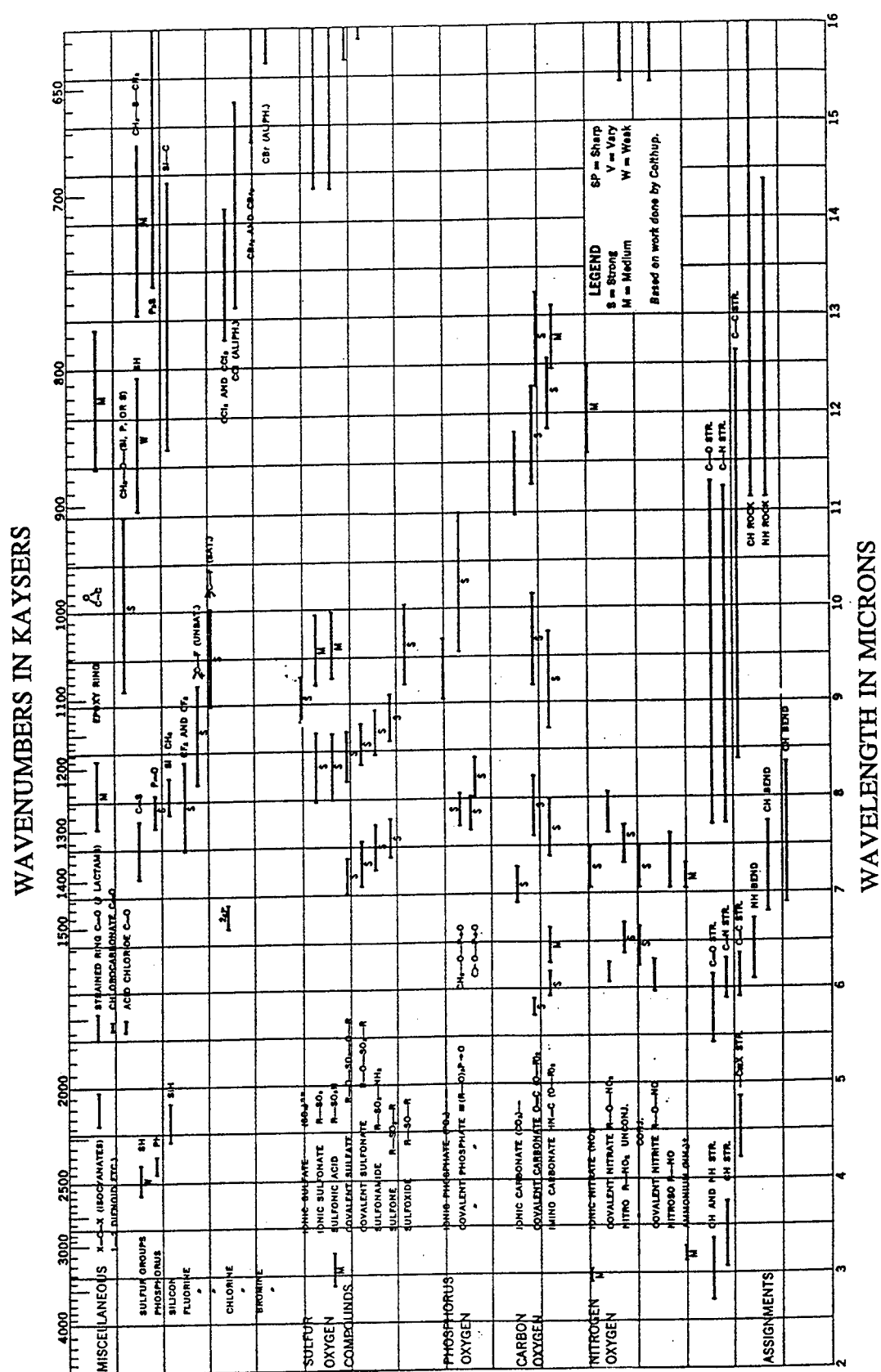
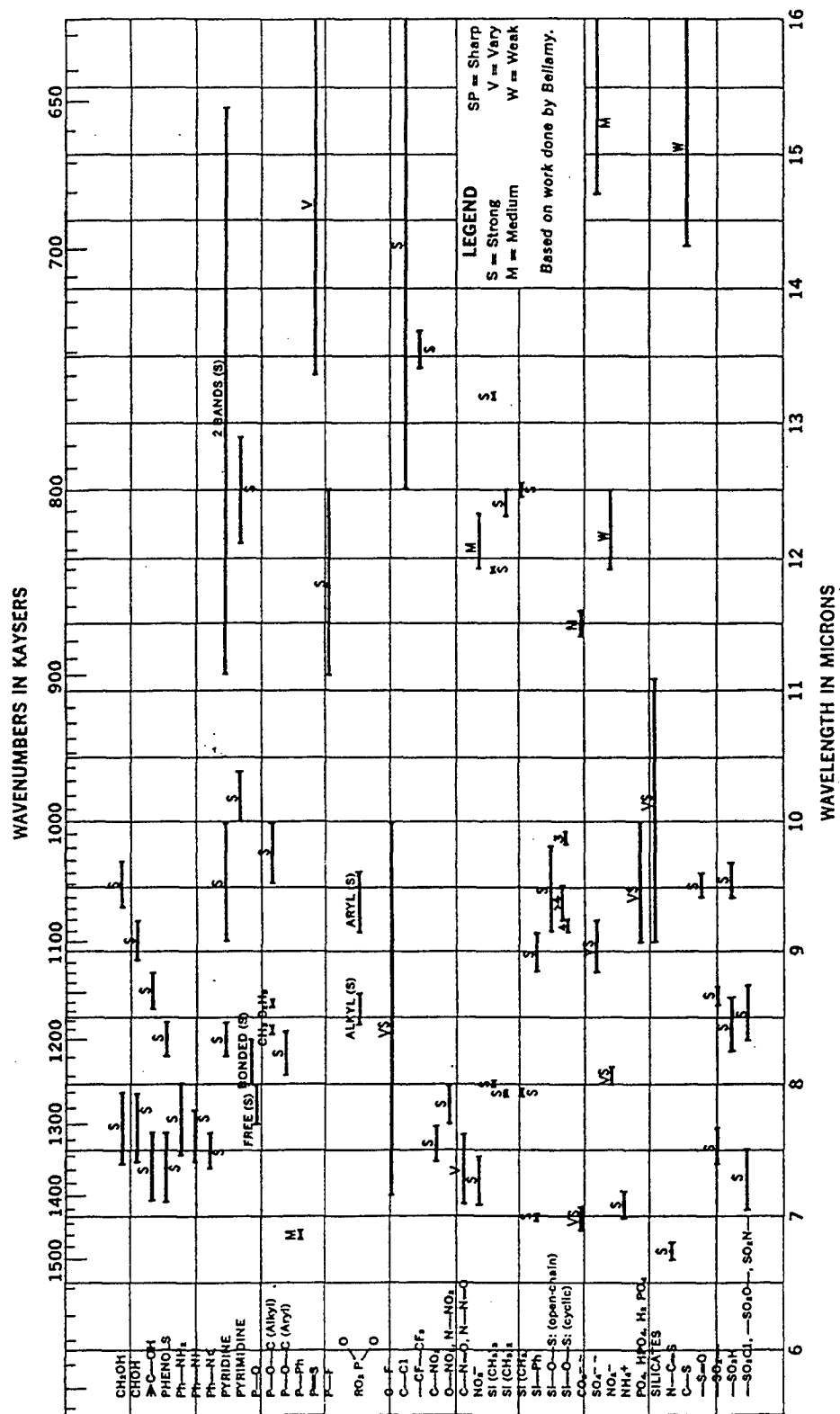


Figure A-43: Vibrational Absorption Features, Part 2 [A.17].





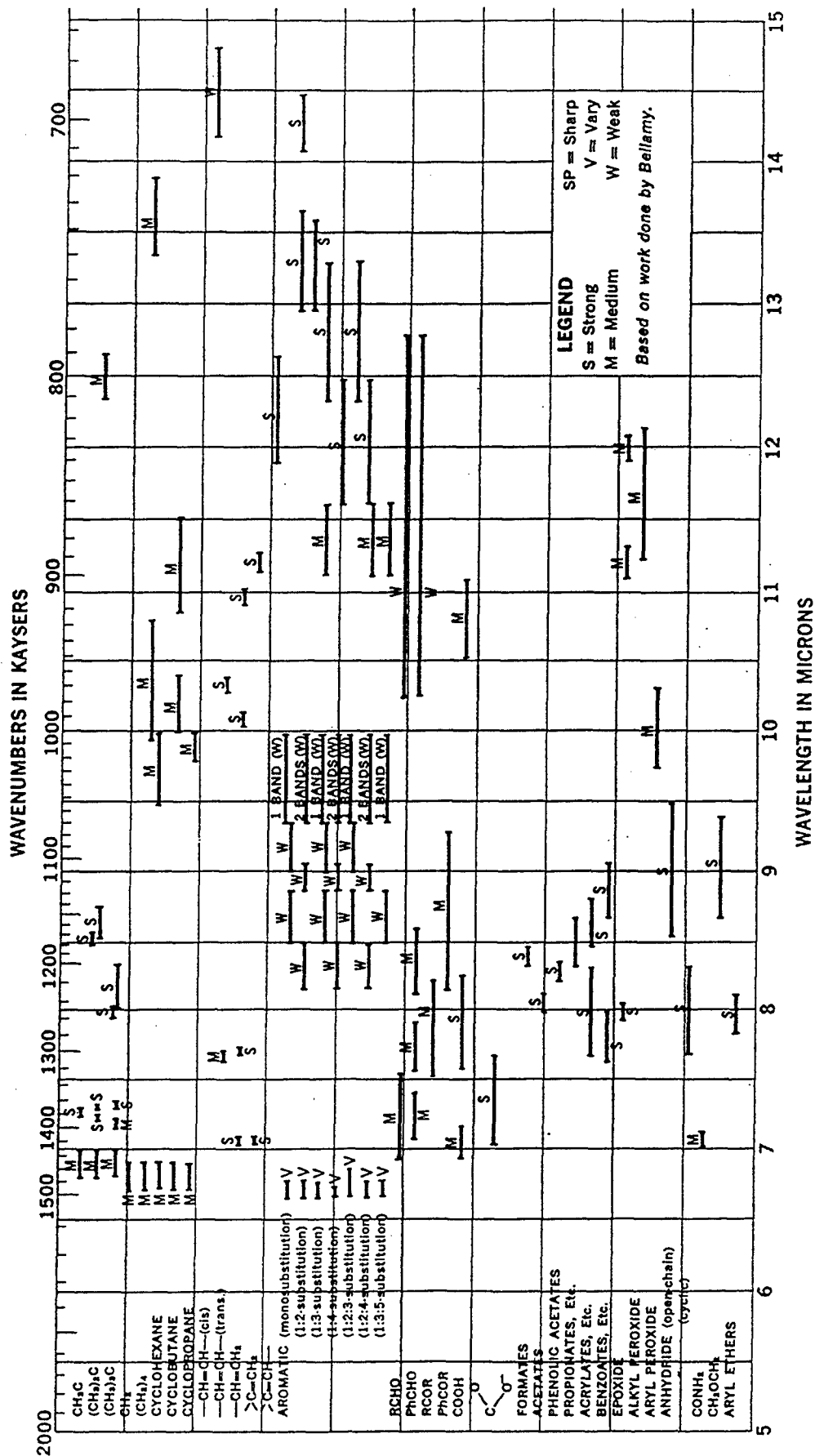


Figure A-46: Single-Bond Vibrations, Part 2 [A.17].



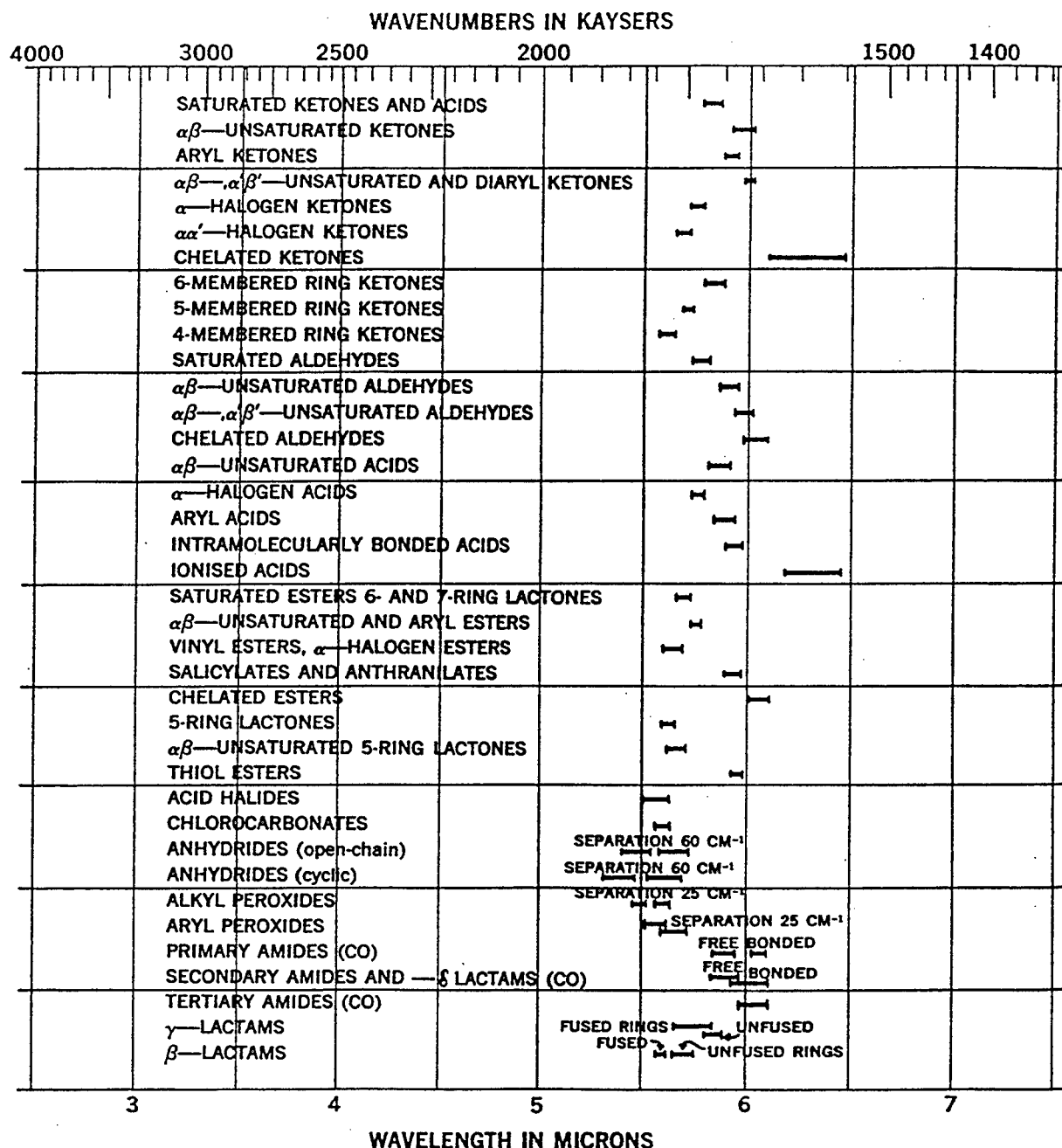


Figure A-48: Carbonyl Vibrations of Some Classes of Organic Compounds. All absorption bands are strong [A.17].

A.7 References

- [A.1] Ballard, S.S, K.A. McCarthy, W.L. Wolfe, "Optical Materials for Infrared Instrumentation," State-of-the-Art-Report, IRIA, The University of Michigan, Willow Run Laboratories, Ann Arbor, MI, 1959.

- [A.2] Bartels, K, "Summary of Spectral Features in the Visible and Infrared Regions for Geologic Minerals," Internal ERIM memo, 1985.
- [A.3] Carmichael, R.S., CRC Handbook of Physical Properties of Rocks, CRC Press, 1982.
- [A.4] Elvidge, C.D., "Thermal Infrared Reflectance of Dry Plant Materials: 2.5-20.0 μm ," Remote Sensing of Environment, 26: pp. 265-285, 1988.
- [A.5] Faulkner, D., R. Horvath, J.P. Ulrich, and E. Work, "Spectral and Polarization Characteristics of Selected Targets and Backgrounds: Instrumentation and Measured Results (3. -14.0 mm)," Work done at ERIM for AF Avionics Laboratory, Wright-Patterson AFB, Technical Report AFAL-TR-71-199, 1971.
- [A.6] Gates, D.M., "Physical and Physiological Properties of Plants," Remote Sensing, Chapter 5, National Academy of Sciences, Funded by NASA, pp. 224-252, 1970.
- [A.7] Gates, D.M., H.J. Keegan, J.C. Schleter, and V.R. Weidner, "Spectral Properties of Plants," Applied Optics, Vol. 4, No. 1, pp. 11-20, 1965.
- [A.8] Gates, D.M., W. Tantraporn, "The Reflectivity of Deciduous Trees and Herbaceous Plants in the Infrared to 25 Microns," Science, Vol 115, pp. 613-616, 1952.
- [A.9] Grant, L., "Diffuse and Specular Characteristics of Leaf Reflectance," Remote Sensing of the Environment, 22: pp. 309-322, 1987.
- [A.10] Hovis, W.A., "Infrared Spectral Reflectance of Some Common Minerals," Applied Optics, Vol. 5, 2:pp. 245-248, 1965.
- [A.11] Knipling, E.B., "Physical and Physiological Basis for the Reflectance of Visible and Near-Infrared Radiation from Vegetation," Remote Sensing of the Environment, 1:pp. 155-159, 1970.
- [A.12] Palik, E.D., Handbook of Optical Constants of Solid, Academic Press, 1985.
- [A.13] Putnam, E.S., "Commercial Applications and Scientific Research Requirements for Thermal-Infrared Observations of Terrestrial Surfaces," A report of the Joint EOSAT/NASA Thermal Infrared Working Group, 1986.
- [A.14] Salisbury, J.W., N.M. Milton, "Thermal Infrared (2.5- to 13.5- μm) Directional Hemispherical Reflectance of Leaves," Photogrammetric Engineering and Remote Sensing, Vol 54, No. 9, pp. 1301-1304, 1988.
- [A.15] Salisbury, J.W., "Preliminary Measurements of Spectral Signatures of Tropical and Temperate Plants in the Thermal Infrared," Fifth Thematic Conference on Remote Sensing for Exploration Geology, ERIM, VOL 1: pp. 131-143, 1986.
- [A.16] Siegal, B.S., and A.R. Gillespie, Remote Sensing in Geology, John Wiley & Sons, 1980.
- [A.17] Weast, R.C., CRC Handbook of Chemistry and Physics, CRC Press, Cleveland, Ohio, 1975

- [A.18] Wolfe, W.L., and G.J. Zissis, The Infrared Handbook, The Infrared Information Analysis (IRIA) Center, ERIM, 1989.
- [A.19] Wong, C.L. and W.R. Blevin, "Infrared Reflectance of Plant Leaves," Australian Journal of Biological Science, Vol 20, pp 501-508, 1967.

Appendix B:

AIRBORNE HYPERSPECTRAL SENSOR SYSTEMS*

RONALD J. BIRK, COMMERCIAL REMOTE SENSING PROGRAM, SVERDRUP TECHNOLOGY, INC.,
STENNIS SPACE CENTER, MS 39529

THOMAS B. McCORD, SETS TECHNOLOGY, INC., 300 KAHÉLU AVE. #10, MILILANI, HI 96789;
HAWAII INSTITUTE OF GEOPHYSICS AND PLANETOLOGY,
UNIVERSITY OF HAWAII, 2525 CORREA ROAD, HONOLULU, HI 96822

ABSTRACT

This paper presents brief profiles of 19 airborne hyperspectral sensor systems currently or nearly available for data acquisition. These systems represent various design concepts and innovations in hyperspectral information collection technology. A number of companies now have the ability to acquire data from these systems. As the scientific and commercial communities become aware of hyperspectral imaging data acquisition opportunities, more applications for this type of data will be investigated and implemented.

INTRODUCTION

An airborne sensor system scans across a line on the ground, generating hundreds of individual pixels in each scan line (the X-axis); the airplane's forward motion generates the Y-axis. The optical system projects data onto several arrays so that all spectral information for a given area is recorded simultaneously (Baker, 1991). Hyperspectral imagers split the spectrum into many separate, narrow channels on a pixel-by-pixel basis, allowing researchers to discern an area's composition through spectral signature discrimination more effectively than is possible with broad-band multispectral scanners.

Airborne hyperspectral imaging represents an additional dimension for remote Earth observations. The technology appears to be advancing faster than applications are being found for the data generated. This paper will help make potential users aware of the available technology by profiling operational Airborne Hyperspectral Sensor Systems (AHSSs) and identifying data acquisition opportunities.

TECHNOLOGY

AHSSs were developed to achieve fine spectral resolution ($\Delta\lambda/\lambda \sim 1\%$), high spatial resolution (1-20m), image spatial

and spectral pattern data base development (30-200 channels), and spaceborne imagery data simulation.

Several types of scanning mechanisms can acquire both spatial and spectral dimensions for an area of coverage on the Earth. Scanning mechanisms include scanning, staring, scanning/staring, and staring arrays. The performance associated with varying these and other parameters of the hyperspectral system design can be modeled to obtain an indication of system characteristics. Performance modeling of system response characteristics, discrimination potential analysis, atmospheric constraints, and spectral signature normalization may be performed with sensor system design software (Jaggi, 1991).

An important system performance specification for many applications is signal-to-noise ratio (SNR) for optimizing peak-to-peak and peak-to-valley discrimination in signature matching algorithms. Current methods for estimating SNR methods include laboratory, dark current, image, and geostatistical procedures (Curran and Dungan, 1989).

SYSTEM PROFILES

AAHIS-1 - SETS Technology, Inc.

The Advanced Airborne Hyperspectral Imaging System - 1 (AAHIS-1) is being developed by SETS Technology, Inc. to demonstrate the value of very high quality hyperspectral imaging data for a variety of land surface and underwater applications. This fully funded system will first fly in May 1994 and should be available as a service starting in the summer of 1994. This first system is optimized for the visible and blue portions of the spectrum (440-835nm, 36 or 73 channels) to concentrate on littoral, vegetation, and underwater applications. The AAHIS-1 uses the latest technology, including a two-dimensional focal plane, to achieve the highest data quality in a pushbroom mode. Performance expected includes 1m ground spatial dimension

*Presented at the 47th National Aerospace and Electronics Conference, Dayton, OH, May 23-27, 1994.

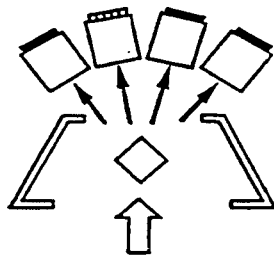
(GSD) at 1km altitude with SNR >500:1 per spectral channel for 20% albedo. The system will first be flown on a Piper Aztec in Hawaii but is available for flight around the world. The compact AAHIS-1 is easily operated and can be carried from place to place as personal baggage. Several applications flights are already planned and funded. Over the next year, the system will be extended to cover the spectral range out to about 2.5µm. The data are collected directly onto a 1.2GB hard drive as measured through a high-speed port at about 0.3MB/s so that approximately a 40km-long swath can be recorded before downloading to Exabyte tape. The data are to be processed by SETS Technology, Inc. using their existing Hyperspectral Image Processing System (HIPS) and its related tools. Several data sets have already been collected and processed using a prototype sensor of similar specifications to prove the technology.

AHS - Daedalus Enterprises, Inc.

The Airborne Hyperspectral Scanner (AHS) (formerly MAS), developed by Daedalus Enterprises, Inc., has been operational since 1991. Applications for this system include environmental studies, mineral exploration, oceanography, satellite simulation, and forest fire environmental impact. The National Aeronautics and Space Administration (NASA) Ames Research Center (ARC) and Goddard Space Flight Center (GSFC) are using Daedalus' spectrometer to develop an airborne simulator for the MODIS-N instrument. When flown with the Thermal Infrared Multispectral Scanner (TIMS), the system can approximate the Advanced Spaceborne Thermal Emission and Reflection Radiometer (ASTER) (Grant and Myers, 1992).

AIS - Geophysical Environmental Research

The Airborne Imaging Spectrometer (AIS) developed by Geophysical Environmental Research (GER) is a 63-channel AHSS. This system began operating in 1987, providing surface mineral direct mapping for commercial use. Between 1987 and 1990, this system was flown over the U.S.A., Australia, Germany, Great Britain, France, Spain, Italy, and Israel (Collins and Chang, 1990). Applications for this sensor include environmental monitoring, oil and mineral exploration, mapping, and military targeting.



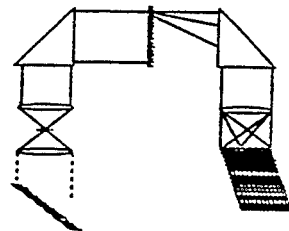
AMSS - Geoscan PTY LTD

The Airborne Multispectral Sensor System (AMSS) was developed by Geoscan PTY LTD of Australia. This AHSS, which was built for commercial mineral exploration, has been operational since 1989. Its applications include mineral, oil, and gas exploration as well as environmental monitoring. The SNR of the AMSS imagery is high enough to enable

band differences to be used for simplified image processing in mineral detection. By use of two or three band differences, the band shapes for specific minerals can be outlined. In addition, single black and white band difference images can show major mineral types directly in an alteration envelope. The minerals can be shown to be present in GER Infrared Intelligent Spectroradiometer (IRIS) ground spectra taken in the scanner-indicated zones (Lyon and Honey, 1990).

ASAS - NASA/Goddard Space Flight Center

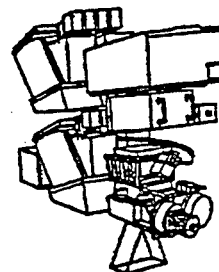
The Advanced Solid-State Array Spectroradiometer (ASAS) was developed by NASA/GSFC. In its current configuration, this AHSS has been operational since 1992.



ASAS is currently the only airborne imaging system with off-nadir pointing capability. Off-nadir pointing imaging devices offer multi-directional observations of bidirectional reflectances and increased temporal coverage potential. With its bidirectional and spectral characteristics, ASAS is ideally suited to provide data for Earth Observing System (EOS) era research: pointing capabilities are proposed for the Multiangle Imaging Spectroradiometer (MISR) on EOS (NASA/GSFC, unpublished). Applications for the sensor include bidirectional reflectance studies, off-nadir viewing, stereo-image analysis, terrestrial ecosystem field experiments, and simulator for EOS spaceborne instruments.

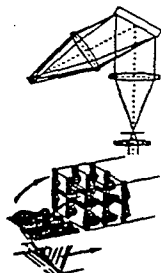
AVIRIS - NASA/Jet Propulsion Laboratory

The Airborne Visible-Infrared Imaging Spectrometer (AVIRIS) AHSS was developed by NASA/Jet Propulsion Laboratory (JPL). This AHSS is designed to measure the upwelling spectral radiance in the region where solar reflected energy from the Earth's surface is dominant. AVIRIS is the first Earth-looking imaging spectrometer to cover the entire solar surface-reflected portion of the electromagnetic spectrum in narrow contiguous spectral channels (Green *et al.*, 1992). AVIRIS is calibrated at better than 5%. The sensor produced its first airborne images in 1986 and its first science data in 1987. The system has been fully operational since 1989. Applications for AVIRIS include imaging spectrometry research and applications, terrestrial land ecology, ocean ecology and bathymetry, geology and soil science, hydrology, atmospheric aerosols and gases, environmental monitoring, and spaceborne system calibration and modeling.



CASI - ITRES Research Ltd.

ITRES Research Ltd. of Canada has developed the Compact Airborne Spectrographic Imager (CASI), which has been operational since 1988. CASI is a highly sensitive pushbroom imager that captures both spatial and spectral information from each line image without any scanning or other mechanical motions. CASI provides programmable spectral band sets and easy switching between spectral and spatial information during data acquisition. Water applications include pollution and algae bloom monitoring, benthic weed surveys, and bathymetry and subsurface feature investigations. Vegetation applications include vitality analysis, species discrimination, cover estimation, right of way surveillance, illicit crop detection, and soil evaluations. In addition, CASI can be used as a tool for providing direct digital input data for Geographic Information Systems (GIS). ITRES is developing a companion system for CASI that will generate the necessary navigation and pointing information to provide direct inputs for GIS (Babey and Anger, 1993).



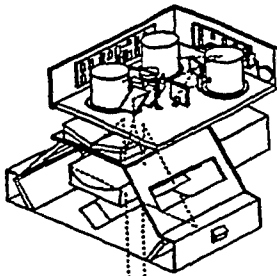
CHRISS - Science Applications International Corporation

The Compact High Resolution Imaging Spectrograph System (CHRISS) developed by Science Applications International Corporation (SAIC) has been operational since 1992. The system features high spectral and spatial resolution, decreased weight, small size, and both digital and analog data recording. CHRISS uses a staring optical design and a high throughput, low aberration spectrograph in a pushbroom imaging format (Speer *et al.*, 1992). Applications include petroleum seepage, vegetation identification, environmental and global change, Department of Defense (DoD) camouflage discrimination and reconnaissance, and NASA forestry and ocean color. SAIC is currently building a new version of CHRISS; parameters for the new system will soon be available.

DAIS-2815 - Geophysical Environmental Research

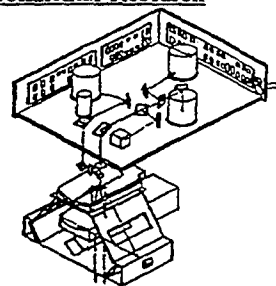
The ASTER Simulator (DAIS-2815) developed by Geophysical Environmental Research has been operational since 1991. This system is designed to simulate ASTER's Visible and Near Infrared (VNIR) band 3 and Thermal Infrared (TIR) bands 10-14.

In addition, the scanner has three Mid-Wavelength Infrared (MWIR) bands between $3\mu\text{m}$ and $5\mu\text{m}$ to investigate this region's use for geological and environmental remote sensing. All data from this instrument can be used in general image processing software, such as ERDAS or GenIsis (Watanabe *et al.*, 1991).



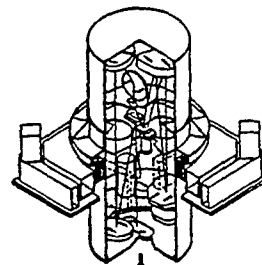
DAIS-7915 - Geophysical Environmental Research

The 79-channel DAIS-7915 was developed by Geophysical Environmental Research for detection, analysis, and mapping. The system is currently under development (Birk, 1992).



HYDICE - Naval Research Laboratory

The HYDICE AHSS is being developed by the Naval Research Laboratory under the Congressional Dual-Use Initiative for transfer of military technology to the civil sector. Researchers are exploring the use of hyperspectral data for problems in agriculture, geology, the environment, coastal ocean processes, ocean optics, the marine atmospheric boundary layer, bathymetry, and water clarity measurements. HYDICE is being built to research the use of an advanced imaging spectrometer to evaluate the data's usefulness and to determine how to build a truly operational system (Rickard *et al.*, 1993).



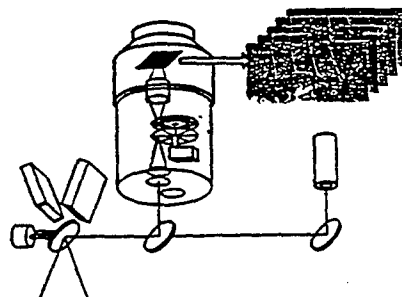
MIVIS - Daedalus Enterprises, Inc.

The Multispectral Infrared and Visible Imaging Spectrometer (MIVIS) produced by Daedalus Enterprises, Inc., has been operational since 1993. MIVIS contains a 10-channel TIR band, a 64-channel spectrometer covering the 2-2.5 μm region, an 8-channel near-infrared (NIR), and a 20-channel visible (VIS) spectrometer. The 102-channel MIVIS is designed primarily for mineral and oil exploration (Baker, 1991). Other applications may include oceanography, environmental studies, plant stress, and thermal mapping applications.

MUSIC - Lockheed Missiles and Space Company, Inc.

The Multispectral Infrared Camera (MUSIC) was developed by Lockheed Missiles and Space Company, Inc. (LMSC) for the Advanced Research Projects Agency (ARPA). The current version has

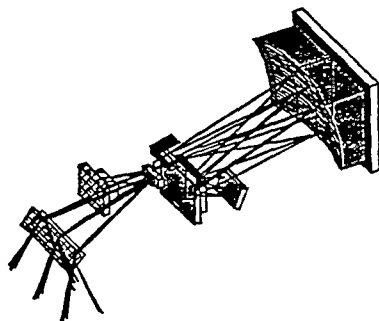
been operational since 1989. MUSIC is a cryogenic staring thermal infrared sensor with dual telescopes. The telescopes produce data frames in two bands simultaneously. Spectral filtering by multi-layer interference filters is provided in each telescope to define the spectral band of radiation reaching the



detectors. Either fixed spectral filters or a circular variable filter can be commanded in each telescope. An on-board computer controls the operation of the sensor, including selection of spectral filters, detector array frame rate, operation of the tape recorders, and pointing of the gimbaled mirror pointing and stabilization system (Kulgein *et al.*, 1992). MUSIC's applications include chemical vapor sensing, plume diagnostics, and target and background spectral signatures.

ROSIS - DLR

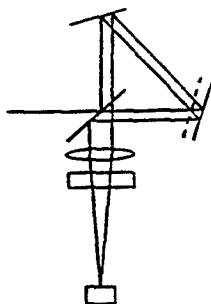
The Reflective Optics Systems Imaging Spectrometer (ROSIS), developed by DLR in Germany, has been operational since 1992. Because of its purely reflective concept, ROSIS extends in



both spectral directions. This system was particularly tailored to measure ocean parameters, including chlorophyll fluorescence, but the range of applications is growing beyond ocean and coastal zones. Water applications for ROSIS include measurement of water pollution, chlorophyll-fluorescence, plankton blooms and biomass, mesoscale eddies and currents, coastal erosion, mapping of flooded areas, and sea-ice mapping. Land and atmospheric applications include mapping of deforestation, crop status, land use, glacier and snow coverage, clouds, and aerosol amount (Kunkel *et al.*, 1991).

SMIFTS - Advanced Research Projects Agency, Office of Naval Research, University of Hawaii

ARPA, Office of Naval Research (ONR), and the University of Hawaii have developed a Spatially Modulated Imaging Fourier Transform Spectrometer (SMIFTS). The instrument is cryogenically cooled, is robust and compact, and provides simultaneous measurement of all spectral channels. SMIFTS uses spatial modulation and a detector array to sample the interferogram and therefore uses no moving parts to obtain data (Lucey *et al.*, 1992). Applications for this system include airborne imaging spectroscopy, plume observations, thermal profiling, Lightsat emulation, and HYDICE data simulation.



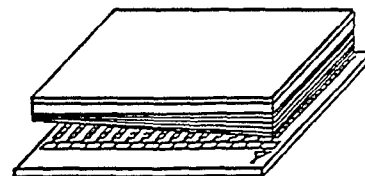
TRWIS-B, TRWIS-SC, TRWIS-II - TRW

TRW is currently flying three models of Imaging Spectrometers: TRWIS-B and TRWIS-SC, which operate in

the VNIR regions (0.46-0.88 μ m), and TRWIS-II, which operates in the short-wave infrared (SWIR) (1.5-2.5 μ m). These instruments have been operated from fixed-wing aircraft, helicopters, and ground platforms. TRWIS-B and TRWIS-II are pushbroom instruments with a swath width of 240 pixels. TRWIS-SC is a cross-track whisk-broom scanner with a swath width of 1000 pixels. All instruments feature simultaneous measurements of all spectral channels to avoid spectral contamination. Extensive software and special-purpose hardware are available to perform sophisticated, rapid processing of data. The data can also be processed in real time in the aircraft to receive immediate identification or quantification of surface material. Applications for these instruments include infrastructure mapping; environmental, agriculture, and forestry monitoring; oil and natural gas exploration; maritime research; and general research (Dr. Donald Davies, personal communication).

WIS - Hughes Aircraft Company/Santa Barbara Research Center

The Wedge Imaging Spectrometer (WIS) developed by Hughes Aircraft Company has been in operation since 1989. This system joins the



spectral separation filters to the detector array, eliminating the need for a complex aft-optics assembly and bringing imaging spectroscopy into an affordable cost range. Its resulting smaller size and weight make it compatible with lightweight satellite or small aircraft use. In addition, its simple, rugged design is well suited to operation by relatively unskilled personnel (Demro and Woody, 1993). WIS sensor data collection is flexible; data acquisition is synchronized with aircraft velocity and focal plane integration times. A wide range of altitudes and velocities are available, and data rectification does not require aircraft attitude information or GPS (Hughes/SBRC, unpublished). Applications for the WIS include hyperspectral imaging, airborne monitoring, environmental observations, terrain and site classification, crop assessment, and identification of specific materials. Hughes is currently building the next generation WIS. Specifications for Hughes' new WIS, as well as for the other systems profiled above, are listed in Table 1.

DATA ACQUISITION

Effective acquisition of hyperspectral imagery to meet environmental monitoring, mineral exploration, agriculture, forestry, and other applications requires accurate geo-location knowledge, good geometric correction capabilities, and traceable reference standards for calibration and digital recording of data for direct transfer to image processing

computer platforms. Sensor system interfaces include Global Positioning System, 3-axis gyro, stabilized mount, digital recorder, and calibration reference sources. Table 2 lists companies currently able to acquire data from specified systems.

Many companies have airborne data acquisition platforms (Table 2). Combining the capabilities of the sensor systems with responsive and reliable deployment and appropriate ancillary data interfaces is key to successful acquisition missions for developing applications to meet end-user needs.

PROCESSING

Hyperspectral imagers produce large amounts of data. To be useful, these data must be reduced to manageable data sets. Image processing systems and software (e.g., ENVI, GenIsis, HIPS, SIPS) are being developed to permit investigators to skim through data quickly in the spectral, spatial, or temporal modes and extract desired information for further analysis. Three-dimensional visualization techniques facilitate this process by permitting anomalies in the data sets or other desired features to be identified quickly for subsequent image processing and analysis (Baker, 1991).

One of the many attributes of hyperspectral data that provides the end-user with significant benefits is the ability to derive atmospheric correction information from the data on a pixel-by-pixel basis (Bruegge *et al.*, 1990).

SUMMARY

Nineteen different airborne hyperspectral sensor systems are currently available for data acquisition, and 14 agencies with data acquisition aircraft have been identified. Advances in hyperspectral imaging technology for remote sensing of the Earth from airborne platforms are accelerating, and greatly enhanced results cannot be far in the future. At present, the number of operational sensors exceeds the number of identified applications for their use. As the scientific and commercial communities become aware of the airborne hyperspectral systems and data options available, more applications for this type of data will be investigated and implemented, providing better data for Earth observation and resources research.

ACKNOWLEDGEMENTS

Work performed by Sverdrup Technology, Inc. personnel on this paper was authorized under NASA Contract NAS13-290. The authors wish to thank Marcia Wise for her assistance in the compilation of information for and editing of this paper.

REFERENCES

- Babey, S. K., and C. D. Anger, 1993. "Compact Airborne Spectrographic Imager (*casi*): A Progress Review," presented at SPIE Conference, April 15, Orlando, FL.
- Baker, William T., 1991. "Hyperspectral Imaging: An Environmental Monitor," *Sensors*, December, pp. 19-24.
- Birk, Ronald J., 1992. "Airborne Hyperspectral Sensor Profiles," Workshop at the International Space Year *International Symposium on Spectral Sensing Research*, Maui, HI, November 15-20, 1992.
- Bruegge, Carol J., James E. Conel, Jack S. Margolis, Robert O. Green, Geoff Toon, Verronique Carrere, Ronald G. Holm, and Gordon Hoover, 1990. "In-situ Atmospheric Water-vapor Retrieval in Support of AVIRIS Validation," SPIE Proceedings, *Imaging Spectroscopy of the Terrestrial Environment*, Orlando, FL, v.1298.
- Collins, William E., and Sheng-Huei Chang, 1990. "The Geophysical Environmental Research Corporation 63-Channel Airborne Imaging Spectrometer and 12-Band Thermal Scanner," SPIE Proceedings, *Imaging Spectroscopy of the Terrestrial Environment*, Orlando, FL, v.1298, pp. 62-71.
- Curran, Paul J., and Jennifer L. Dungan, 1989. "Estimation of Signal-to-Noise: A New Procedure Applied to AVIRIS Data," *Transactions on Geoscience and Remote Sensing*, 27(5):620-628.
- Demro, James C., and Loren M. Woody, 1993. "Flight Demonstration of the Wedge Imaging Spectrometer," Counterdrug Technology Assessment Center's *Tactical Technologies and Wide-area Surveillance International Symposium Proceedings*.
- Grant, Patrick, and Jeff Myers, 1992. "MAS - MODIS-N Airborne Simulator," *International Space Year Proceedings of the International Symposium on Spectral Sensing Research*, Maui, HI, v.I, pp. 350-354.
- Green, Robert O., James E. Conel, and Thomas G. Chrien, 1992. "Airborne Visible-Infrared Imaging Spectrometer (AVIRIS): Sensor System, Inflight Calibration and Reflectance Calculation," *International Space Year Proceedings of the International Symposium on Spectral Sensing Research*, Maui, HI, v.I, pp. 198-214.
- Jaggi, S., 1991. "ATTIRE (Analytical Tools for Thermal Infrared Engineering) - A Sensor Simulation and Modeling Package," Second Annual JPL Airborne Geoscience Workshop, May 20.

Kulgein, Norman G., Stephen P. Richard, Wayne P. Rudolf, and Edwin M. Winter, 1992. "Airborne Chemical Vapor Detection Experiment," *International Space Year Proceedings of the International Symposium on Spectral Sensing Research*, Maui, HI, v.II, pp. 1119-1130.

Kunkel, B., F. Blechinger, D. Viehmann, H. Van Der Piepen, and R. Doerffer, 1991. "ROSIS Imaging Spectrometer and its Potential for Ocean Parameter Measurements (Airborne and Space-borne)," *International Journal of Remote Sensing*, 12(4):753-761.

Lucey, P. G., T. Williams, K. Horton, K. Hinck, C. Budney, J. B. Rafert, and T. B. Rusk, 1992. "SMIFTS: A Cryogenically Cooled, Spatially Modulated, Imaging, Fourier Transform Spectrometer for Remote Sensing Applications," *International Space Year Proceedings of the International Symposium on Spectral Sensing Research*, Maui, HI, v.I, pp. 251-262.

Lyon, R. J. P., and F. R. Honey, 1990. "Direct Mineral Identification (DMI) with Geoscan Mk II Advanced Multi-spectral Scanner (AMSS)," *SPIE Proceedings, Imaging Spectroscopy of the Terrestrial Environment*, Orlando, FL, v.1298, pp. 50-61.

Rickard, Lee J., Robert Basedow, Ed Zalewski, Peter Silvergate, and Mark Landers, 1993. "HYDICE: An Airborne System for Hyperspectral Imaging," *SPIE Proceedings, Imaging Spectrometry of the Terrestrial Environment*, v.1937, p. 173.

Speer, B., C. Coyle, R. Anderson, and G. Mooradian, 1992. "Compact, High Resolution Airborne Hyperspectral Imaging Sensor at SAIC," *International Space Year Proceedings of the International Symposium on Spectral Sensing Research*, Maui, HI, v.II, pp. 948-955.

Watanabe, H., M. Sano, F. Mills, S. H. Chang, and S. Masuda, 1991. "Airborne and Spaceborne Thermal Multispectral Remote Sensing."

Table B-1. System Specifications

SYSTEM	RANGE (nm)	BAND- WIDTH (nm)	CHANNELS	IFOV (mrad)	FOV	PIXEL/ LINE	DIGITI- ZATION	DATA STORAGE	PLATFORMS
AAHIS-1	440-835	11	36 72	1.0	193 mrad	193	12 bits	Mac/Quadra 800, 1.2 GB hard drive, 5.0 GB Exabyte tape	Piper Aztec
AHS #1 #2 #3 #4	430-830 1605-2405 3000-5400 8200-12700	20 50 300 400-1500	20 15 7 6	2.5	85.92°	715	12 bits	Serial to VLDS	NASA/ARC C-130, ER2, ERIM, Caribou
AIS #1 #2 #3	400-1050 1080-1800 2000-2500	25.4 102 15.6	24 7 32	2.5-4.5	90°	512-1024	16 bits	9-track CCT	Piper Aztec, Piper Navajo
AMSS #1 #2 #3	400-1050 2050-2400 8500-12000	20 44 530	32 8 8	2.1 x3	92.16°	768	8 bits	Winchester disks, 600MB optical disks	Light Aircraft
ASAS	420-1037	11	62	0.7	19°	512	12 bits	VLDS	NASA Wallops Island P-3B, NASA/ARC C-130
AVIRIS	400-2500	10	224	1.0	30°	614	12 bits	HDT, 10GB	NASA/ARC ER-2, Altitude 20,000m
CASI	430-870	3.0	<288	1.2	35.4°	578	12 bits	Exabyte 8500 8mm Helical Scan	Helicopter, Light Aircraft, Zeiss Camera Port
CHRISS	425-850	3.4	125	0.17-0.5	10.3°	1024		Digital/Analog Data	Fixed Wing, Helicopter, UAV
DAIS-2815 #1 #2 #3	700-1000 3000-5000 8000-12000	300 600 200	1 3 20	1.0 2.5 5	82°	512-2048	15 bits	IBM 3480	Piper Navajo
DAIS-7915 #1 #2 #3 #4 #5	400-1000 1000-1800 1970-2450 3000-5000 8000-12300	16 100 16 2000 600	32 8 32 1 6	1.1 2.2 3.3	78°		16 bits	IBM 3480 Cartridge	Piper Navajo

Table B-1. System Specifications (Continued)

SYSTEM	RANGE (m)	BAND- WIDTH (nm)	CHANNELS	I FOV (mrad)	FOV	PIXEL/ LINE	DIGITL- ZATION	DATA STORAGE	PLATFORMS
HYDICE	400-2500	3.1 min., 14.9 max., 10.2 avg.	206	0.5	8.94°	312	12 bits		Altitude C141, up to 14,000m
MIVIS #1 #2 #3 #4	430-830 1150-1550 2000-2500 8200-12700	20 50 8 400-500	20 8 64 10	2.0	72°	755	12 bits	Serial to VLDS	Aerial Survey Craft
MUSIC #1 #2	2500-7000 6000-14500	25-70 60-1400	90 90	0.5	1.3° swath width x 2.6°	45	80 frames/s digital PCM		Canberra, U2
RODIS	430-880	5	256	0.55	±16°	512	12 bits	Digital Recorder	Jet Aircraft
SMIFTS	1.0-5.2μm		100	0.66	9.7°	256	12 bits		Helicopter
TRWIS-B	0.46-0.88μm	4.8	90	1	14°	240	8 bits	VHS	Helicopters, Light Aircraft
TRWIS-SC	0.46-0.88μm	4.8	90	1	60°	1000	8 bits	VHS	Helicopters, Light Aircraft
TRWIS-II	1.5-2.5μm	12	85	.5/1	7/14°	240	8 bits	VHS	Helicopters, Light Aircraft
WIS (anticipated)	0.4-0.6μm 0.6-1.0μm 1.0-1.8μm 1.8-2.5μm	12.5 6 30 12.5	17 67 27 45	0.65	20°	512	12 bits	Hard Disk	Light Aircraft

Table B-2. Data Acquisition Opportunities

COMPANY/AGENCY	SYSTEM	COMPANY/AGENCY	SYSTEM
AeroData		GER	DAIS-2815, DAIS-7915
AeroMap U.S., Inc.	ITRES CASI	Innotech Aviation	MEIS, MSS
AeroMet		Intera	
Airesearch Mapping	71-channel CAS	NASA/ARC	AVIRIS, MAS
Atlantic Group		NASA/OSFC	ASAS
Borstad Associates	ITRES CASI	NASA/SSC	CAMS, TIMS, ATLAS
ESA/JRC	DAIS-7915	TRW	TRWIS-B, TRWIS-SC, TRWIS-II